ANSCSE 27

Bangkok

PROCEEDING

The 27th International Annual Symposium on Computational Science and Engineering

📅 30th July – 3rd August 2024

🌐 https://anscse27.com

📍 Faculty of Engineering, Chulalongkorn University, Bangkok, Thailand

CO-ORGANIZERS

Chula Chulalongkorn University

CHULA ΣNGINEERING Foundation toward Innovation

Sasin School of Management

CREA ส.ต.ว. The Catalysis and Reaction Engineering Association

DIAMOND SPONSOR

Chula Chulalongkorn University

RUBY SPONSORS

DELL

MRS-Thailand

SAPPHIRE SPONSORS

DTE

ELSEVIER

JADE SPONSOR

SCIFINITI

WELCOME MESSAGE

Dr. Supawadee Namuangruk

President of Computational Science and Engineering Association
(CSEA), Thailand

Dear Friend and Colleagues,

It is a great pleasure and honor to extend to you a warm invitation to attend the ANSCSE27, which will be held from July 30 to August 03, 2024. This year, the conference is organized by Chulalongkorn University and the Computational Science and Engineering Association (CSEA). As computational methods become increasingly important in science and engineering, the need to collaborate and exchange ideas and experiences becomes more critical. ANSCSE has a long history of being the major forum for computational scientists to communicate their ideas to their fellow scientists. Over 27 years, we have seen many signs of progress and much exciting research conducted in this area. Recently, the use of computational techniques has been extended to a broader domain of problems beyond science, such as attempts to understand the economy, human society, and social networking. Specifically, in sustainable development goals (SDGs), computational science and engineering have become important tools to help us achieve our goals.

This year, in addition to the nine main sessions, we include two new forums: the "Computational Catalysis Southeast Asia Forum" and the "Thailand-Taiwan-Japan Workshop on Computational Science." We expect to have fruitful discussions, establish new collaborations, and strengthen existing collaborations with many interesting international keynote speakers, workshops, and presentations by many exciting researchers. I am confident that with the experience of the organizing team from Chulalongkorn University, we will have a great and fruitful conference. We look forward to seeing all the participants at ANSCSE27.

Best Wishes,

Dr. Supawadee Namuangruk

President of Computational Science and Engineering Association (CSEA), Thailand

WELCOME MESSAGE

Associate Professor Dr. Supareak Praserthdam

Department of Chemical Engineering, Faculty of Engineering,
Chulalongkorn University, Thailand

I am truly honored to chair this prestigious conference that has long been recognized by the computational scientists and engineers' community in Thailand for more than 27 years since first ANSCSE in 1997 at NECTEC. Also, this year, we celebrate 25 years since the first ANSCSE conference at Chulalongkorn University. This year's conference will focus on the achieving of the Sustainable Development Goals or SDG, where all of us, as one of the "computational scientists and engineers" will try our best to achieve these goals. Lastly, I hope that you all enjoy not only the fruitful discussions during the conference with your old and new colleagues, but also enjoy the vibe of this vibrant city of Bangkok or Krung Thep!

Associate Professor Dr. Supareak Praserthdam

Conference Chair

Department of Chemical Engineering, Faculty of Engineering, Chulalongkorn University, Thailand

Committees

Organizing Committee

Conference Chair

- Supareak Praserthdam — Chulalongkorn University, Thailand

Conference Vice-Chair

- Meena Rittiruam — Chulalongkorn University, Thailand
- Tinnakorn Saelee — Chulalongkorn University, Thailand
- Patcharaporn Khajondetchairit — Chulalongkorn University, Thailand

Steering Committee

- Vudhichai Parasuk — Chulalongkorn University, Thailand
- Supa Hannongbua — Kasetsart University, Thailand
- Piyawut Srichaikul — National Electronics and Computer Technology Center (NECTEC), Thailand
- Waraporn Parasuk — Kasetsart University, Thailand
- Wiboonsak Watthayu — King Mongkut's University of Technology Thonburi, Thailand
- Supawadee Namuangruk — National Nanotechnology Center (NANOTEC), Thailand
- Siriporn Jungsuttiwong — Ubon Ratchathani University, Thailand
- Manaschai Kunaseth — National Electronics and Computer Technology Center (NECTEC), Thailand
- Thanyada Rungrotmongkol — Chulalongkorn University, Thailand
- Nawee Kungwan — Chiang Mai University, Thailand
- Bundet Boekfa — Kasetsart University Kampahengsaen campus, Thailand
- Chompoonut Rungnim — National Nanotechnology Center (NANOTEC), Thailand

Scientific Committee Chair

Computational Catalysis (CAT)

- Supareak Praserthdam — Chulalongkorn University, Thailand
- Suwit Suthirakun — Suranaree University of Technology, Thailand
- Tipaporn Patniboon — Mahasarakham University, Thailand

Computational Chemistry (CHE)

- Boodsarin Sawatlon — Chulalongkorn University, Thailand
- Nawee Kungwan — Chiang Mai University, Thailand

Computational Biology (BIO)

- Thanyada Rungrotmongkol — Chulalongkorn University, Thailand
- Rungtiva Pooarporn — King Mongkut's University of Technology Thonburi, Thailand

Computational Physics (PHY)

- Annop Ektarawong — Chulalongkorn University, Thailand
- Pakpoom Reunchan — Kasetsart University, Thailand

Mathematics and Simulations (MAT)
- Poom Kumam — King Mongkut's University of Technology Thonburi, Thailand
- Wutiphol Sintunavarat — Thammasat University, Thailand

Computational Fluid Dynamics (CFD)
- Benjapon Chalermsinsuwan — Chulalongkorn University, Thailand
- Pornpote Piumsomboon — Chulalongkorn University, Thailand
- Saran Salakij — Chulalongkorn University, Thailand
- Somboon Otarawanna — National Metal and Materials Technology Center (MTEC), NSTDA, Thailand

Computational Chemical Engineering (CCE)
- Phuet Praserthcharoensuk — Chulalongkorn University, Thailand
- Supareak Praserthdam — Chulalongkorn University, Thailand

Computational Business and Finance (CBF)
- Pinnaree Tea-Makorn — Chulalongkorn University, Thailand
- Pattanaporn Chatjuthamard — Chulalongkorn University, Thailand
- Sukrit Vinayavekhin — Thammasat University, Thailand

Education and Simulations (EDS)
- Taweetham Limpanuparb — Mahidol University, Thailand
- Ekasith Somsook — Mahidol University, Thailand
- Sarote Boonseng — Mahidol Wittayanusorn School, Thailand

Computational Catalysis Southeast Asia Forum (CCSA)
- Supareak Praserthdam — Chulalongkorn University, Thailand
- Suwit Suthirakun — Suranaree University of Technology, Thailand
- Tipaporn Patniboon — Mahasarakham University, Thailand

Thailand-Taiwan-Japan on computational science (TTJ)
- Siriporn Jungsuttiwong — Ubon Ratchathani University, Thailand
- Supawadee Namuangruk — National Nanotechnology Center (NANOTEC), Thailand

International Scientific Committee
- Sergey Kozlov — National University of Singapore, Singapore
- Tej Salil Choksi — Nanyang Technological University, Singapore
- Wilson Agerico Diño — Osaka University, Japan
- Allan Abraham Padama — University of the Philippines Los Baños, Philippines
- Tipaporn Patniboon — Mahasarakham University, Thailand
- Jose Manuel Ricart Pla — Universitat Rovira i Virgili | The public University of Tarragona, Spain
- James P. Lewis — Institute of Coal Chemistry, China
- Pengju Ren — Synfuels China, China
- Nongnuch Artrith — Utrecht University, Netherlands
- Masanori Tachikawa — Yokohama City University, Japan
- Alexander Urban — Columbia University, USA
- Zhang Ruiqin — City University of Hong Kong, China
- Yi Pei Li — National Taiwan University, Taiwan

- Deva Priyakumar — International Institute of Information Technology, Hyderabad, India
- Ming-Kang Tsai — National Taiwan Normal University, Taipei, Taiwan
- Kenji Iida — Institute for Catalysis, Hokkaido University, Japan
- Azusa Muraoka — Japan woman's university, Japan
- Peter J. Bond — A*STAR's Bioinformatics Institute
- Yasuteru Shigeta — University of Tsukuba, Japan
- Norio Yoshida — Nagoya University, Japan
- Hasashi Okumura — Institute for Molecular Science, Japan
- Satoru Itoh — Institute for Molecular Science, Japan
- Dmitri G. Fedorov — Advanced Industrial Science and Technology, Japan
- Khaled Barakat — University of Alberta, Canada
- Suwipa Sean-oon — Nostrum Biodiscovery, Spain
- Jhih-Wei Chu — National Yang Ming Chiao Tung University, Taiwan
- Jen-Shiang K. Yu — National Yang Ming Chiao Tung University, Taiwan
- Chih-Hao Lu — National Yang Ming Chiao Tung University, Taiwan
- Ian Liau — National Yang Ming Chiao Tung University, Taiwan
- Ovidiu Bagdasar —
- Andrew Gilbert — Q-Chem Inc.
- Wasit Limprasert — Thammasat University, Thailand
- Luciano Andres Abriata — École Polytechnique Fédérale de Lausanne (EPFL), Virtual Presentation
- Chanin Nantasenamat — Snowflake Inc., Virtual Presentation, USA
- Panida Surawatanawong — Mahidol University, Thailand
- Kowit Hengphasatporn — Tsukuba University, Japan
- Tetsuya Taketsugu — Hokkaido University, Japan
- Takayoshi Ishimoto — Graduate School of Advanced Science and Engineering, Hiroshima University, Japan
- Cheng-Chau Chiu — National Sun Yat-sen University, Taiwan
- Mu Jeng Cheng — National Cheng Kung University, Taiwan

The need for a new class of computational tools to tackle the energy-water-environment-food-health nexus"

Rafiqul Gani

PSE for SPEED, Ordrup Jagtvej 42D, DK-2920 Charlottenlund, Denmark
rgani2018@gmail.com

The need for innovative and significantly better solutions than we currently can obtain has become critical and urgent because of the grand challenges of health, food, water, energy and environment that we are facing. The way we convert our resources to the chemicals-based products that we need for the survival of our society is clearly not working as evidenced by the sharp drop of earth's biocapacity, measured in terms of hectares per person. The solution of this complex problem offers the opportunity for fundamental advances in science and technology. However, one area that needs urgent attention is our solution approach where we predominantly either use experiment-based trial and error approaches, or model-based computer aided techniques. While the former guarantees an experimentally verified solution but does not guarantee that better solutions do not exist, the later is able to quickly find the best solution within a defined search space using validated models. Both, however, lack predictive capabilities. That is, ability to find solutions beyond the scope of the technologies they are employing. This paper focuses on issues related to model-based computer aided techniques and what must be done to overcome them, also considering advances in AI, machine learning and computers.

The development and use of the so-called process simulator has without doubt achieved great success. The petroleum and related industries have made significant progress towards achieving reliable design, safer operation, with for example, lower energy consumption and higher profit. This success, however, has lead to a negative trend, that is, replaced the trial and error experiment-based solution approach to the trial and error simulator-based solution approach, which is a faster and less expensive option. However, does it lead to the innovative and significantly better solution that we now need? The current unit-operation based process simulators have an inherent deficiency that they do not have the capability to find new and innovative processing routes involving newly developed technologies. That is, should we look for solution approaches that are not so simulator specific? Are simulators able to solve the current problems we are interested in? If not, should we develop new methods & tools, or, should we wait until the simulators have the needed capabilities, such as the ability to find innovative solutions? A critical issue here is to understand the role of the process simulator – it is by definition, a tool to verify and not to determine the synthesis of a processing route, the actual process design, or the operation design or sustainable process alternatives and many more. They should be used for the purpose they are developed for.

Clearly, a new class of methods and associated intelligent model-based computer aided tools are needed, where predictive and innovative capabilities are provided. Also, the many current and future needs, which may change, must be satisfied. For example, capabilities to synthesize new processing routes; to design chemicals-based products; to integrate resource management-utilization; to synthesize new intensified operations; to generate sustainable process alternatives and many more. Therefore, rather than provide large, complex and rigid process simulators, it could be useful to provide tailor-made problem specific tools configured from a library of different software components (databases, models, design work-flows, analysis tools, solvers, etc.) according to the needs of the user. Note that here, the process simulator is one of many components. The models in the component library needs to have predictive capabilities. It should be possible to generate tailor-made tools of different scales with smooth transition from one scale to the other for similar applications. The paper will highlight the scope and significance of this new class of computer-aided tools and associated methods with several illustrative examples achieving significant improvements and proposing innovative, new and more sustainable solutions.

Improving the Accuracy of Density Functional Theory via Δ-learning and Machine-learning Exact Exchange-correlation Functional

GuanHua Chen

Department of Chemistry, The University of Hong Kong, Hong Kong, China; Hong Kong Quantum AI Lab Limited, Hong Kong, China

Abstract

Density-functional theory (DFT) is a cornerstone of modern computational chemistry. Specifically, Kohn-Sham DFT greatly reduces computational costs by focusing on the real-space electron density rather than the many-body wavefunction in a higher-dimensional space. However, the catch is that the exchange-correlation (XC) functional in Kohn-Sham equation is unknown and needs to be approximated. This leads to the errors that are too large to be predictive. We proposed and developed two approaches to address this problem, *i.e.*, Δ-learning technique to calibrate the results of conventional DFT, and machine learning (ML)-based XC functional.

As approximated XC functional leads to systematic error, a simple ML model with a little extra information will be capable for calibrating the less precise results to better counterparts. Δ-learning is thus designed to learn this error with a small amount of data. Our pioneering work back in 2003 proposed a framework, proving that as simple as a one-hidden-layer neural network, together with several molecular descriptors, is enough for calibrating DFT-level results to experimental level. Later in 2022, we replaced the time-consuming DFT calculation with a graph neural network, enabling the prediction of experimental-level heat of formation in nearly no time. Δ-learning method has also been applied to calibrate photophysical properties, open circuit voltages of lithium-ion batteries, *etc*.

Another solution to improve the accuracy of DFT is to find a better XC functional. In 2004, we refined the three hybrid parameters of B3LYP XC functional to make them depend on molecular descriptors included the number of electrons, dipole moment, quadrupole moment, kinetic energy, and spin multiplicity. The functional exhibits a remarkable alignment with experimental data. Thanks to the holographic electron density theory, in 2019, we further developed a deep-learning-based algorithm that maps quasi-local electron densities to the exact XC potential. This approach not only showed excellent performance on both the training and validation set, but also exhibited transferability and could describe van der Waals interaction. It is shown further that this approach also gives correct dissociation behaviour where conventional DFT functional fails.

References

[1]   "Combined first-principles calculation and neural-network correction approach for heat of formation", L.H. Hu, X.J. Wang, L.H. Wong, G.H. Chen, *J. Chem. Phys.* **119**, 11501 (2003).

[2]   "Predicting experimental heats of formation via deep learning with limited experimental data", G.Y. Yang, W.Y. Chiu, J. Wu, Y. Zhou, S.G. Chen, W.J. Zhou, J. Fan, G.H. Chen, *J. Phys. Chem. A* **126**, 6295 (2022).

[3]   "Predictions of photophysical properties of phosphorescent platinum(II) complexes based on ensemble machine learning approach", S. Wang, C.Y. Yam, S.G. Chen, L.H. Hu, L.P. Li, F.F. Hung, J.Q. Fan, C.M. Che, G.H. Chen, *J. Comput. Chem.* **45**, 321 (2024).

[4]   "A generalized exchange-correlation functional: the Neural-Networks approach", X. Zheng, L.H. Hu, X.J. Wang, G.H. Chen, *Chem. Phys. Lett.* **390**, 186 (2004).

[5]   "Toward the exact exchange-correlation potential: a three-dimensional convolutional neural network construct", Y. Zhou, J. Wu, S.G. Chen, G.H. Chen, *J. Phys. Chem. Lett.* **10**, 7264 (2019).

Interaction between adsorbate and metal alloy systems: Insights from density functional theory and machine learning - based investigations

Allan Abraham B. Padama[1*]

[1]*University of the Philippines Los Baños, Los Baños, Laguna, 4031 (Philippines)*
*abpadama@up.edu.ph

Introduction

From an atomic-scale perspective, analyzing metal alloys for catalytic applications involves a thorough investigation of properties like stability, activity, and selectivity. In such studies, adsorption investigations become relevant due to the reactions that happen on surfaces. The advent of more complex systems, like single-atom alloys (SAA) and high-entropy alloys (HEA), adds complexity to these studies. Nonetheless, these advancements are intriguing as they present opportunities to uncover functional materials for a range of applications. In this presentation, the interactions between atom or molecule and various alloy systems, e.g., SAA and HEA, as studied through density functional theory (DFT)-based calculations and machine learning (ML) techniques will be discussed. The mechanisms of these interactions, as well as the associated phenomena that influence their properties, will be presented. This will offer insights into the applications of these materials from an atomic-scale investigation standpoint.

Methodology

All DFT calculations conducted in the investigations were performed using the Quantum ESPRESSO package.[1] We modeled the surfaces such that the interaction of the adsorbates in the periodic system is minimized. Furthermore, we introduced a vacuum layer to avoid the interactions of the periodically repeated slabs along the direction perpendicular to the surface. Adsorption of various atoms and molecules was performed to determine their stability on the surfaces. ML techniques were applied to predict the energetics and to assist in the analysis of certain mechanisms. In this approach, DFT results (e.g., energetics and electronics properties) and elemental properties of the atoms were used as input features for the models. Depending on the target values, different ML approaches were employed.

Results and Discussion

Figures 1(a) and 1(b) show the top views of the SAA and HEA surfaces, respectively. The SAA surfaces consist of different combinations of the following transition metals: Ag, Au, Co, Cu, Ir, Ni, Pd, Pt, and Rh. On the other hand, the HEA has Co, Cu, Fe, Mn, and Ni as its components. For the SAA surfaces, we found that the O and OH-induced segregation energies are influenced by the formation energy, metallic radius, d-band centers of the dopant, and the difference in the surface energies of the atoms. These factors were obtained by performing analyses using DFT and ML techniques.[2] We also observed that surface facet can influence the segregation of surface atoms of bimetallic systems induced by varying coverages of adsorbates.[3]
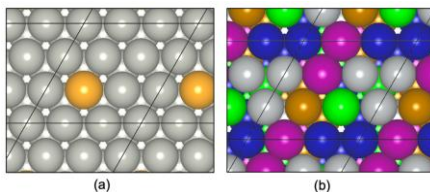

Figure 1. Top views of the (a) single-atom alloy and (b) high entropy alloy surfaces.

On HEA, we calculated the adsorption of H atom using DFT calculations and ML techniques. Figure 2 shows the plots of the ML-predicted versus DFT-calculated H adsorption energies on the fcc-hollow and hcp-hollow sites of CoCuFeMnNi(111) surfaces. We observed a broad range of H adsorption energies on the HEA surface. It signifies the synergy among the elements or a modification of the electronic properties due to the interaction of the constituent elements.
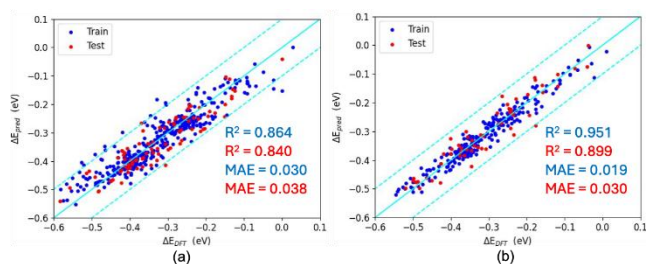
Figure 2. Predicted versus calculated H adsorption energies on (a) fcc hollow and (b) hcp hollow sites of CoCuFeMnNi(111) surfaces. (R2: coefficient of determination, MAE: mean absolute error)

Significance

   This study examines the reactivity and stability of alloy surfaces. Most of the transition metals used in the study are abundant and exploring their applicability as catalysts for various reactions or as sensors would be vital in lowering the costs of devices. Furthermore, HEA are emerging materials that need intensive investigations. Determining their properties would promote their possible applications in industries and would contribute to the generation of knowledge regarding alloys in general.

References

1. Giannozi, P. et al. *J. Phys. Condens. Matter* 21, 395502 (2009).
2. Hipolito, A.N.P. et al. *Comput. Mater. Sci.* 232, 112607 (2024).
3. Palmero, M.A. et al. *Phys. Scr.* DOI 10.1088/1402-4896/ad3f88 (2024)

Reactive force field simulations of catalytic processes on metal surfaces and supported nanoclusters

Josep M. Ricart[1,*], Jordi J. Carbó[1], Gerard Bru[1], Antoni Salom-Català[1],
Evgenii Strugovshchikov[1], Jie Pan[1], Kamila Kaźmierczak[2], and Daniel Curulla-Ferré[2]
[1]*Universitat Rovira i Virgili, Departament de Química Física i Inorgànica, Tarragona, Spain*
[2]*TotalEnergies OneTech Belgium, Feluy, Belgium*
*josep.ricart@urv.cat

Introduction

Supported sub-nanometric metal clusters are considered a singular phase of matter exhibiting many interesting properties that can be used in the design and development of novel catalytic materials. For instance, metal sites on an oxide surface can exhibit high activity combined with enhanced selectivity, and decreased deactivation by undesired products. However, their atomistic simulation requires the consideration of a complex variety of possible active sites at the sub-nanometric level as well as the large number of accessible atomic configurations at reaction temperatures.

The study of such a catalytic system, which is not easily accessible using Density Functional Theory, can be performed by implementing specific Reactive Force Fields capable of performing extensive simulations.

In this talk, we present the development of reactive ReaxFF parameters and their use in simulations of catalytic reactions such as CO_2 valorisation (via the RWGS reaction) or propane dehydrogenation (PDH) on both metal surfaces and nanoclusters. We demonstrate that these ReaxFF parameters can describe the DFT (density functional theory) results and permit using Molecular Dynamics techniques.

Methodology

We have used the ReaxFF method,[1] which employs the so-called bond order formalism and can simulate bond formation/breaking processes in systems of similar size to classical Molecular Dynamics simulations. Each catalytic process requires an assessment of existing parameters or developing new ones, requiring extensive training data for reparametrization. The optimization of force-field parameters relies on a large training set of DFT calculations of metal-catalyzed mechanisms, including geometries, adsorption, relative energies of reaction intermediates, and key bond-breaking/forming profiles. To accelerate and improve the optimization process with large training sets, it is possible to go beyond commercial optimizers. We use an in-house implementation of a machine-learning algorithm GA-ANN, Genetic Algorithm and Artificial Neural Network hybrid method. This method decreases the computational optimization cost and reduces the human participation and supervision of the parametrization process while simultaneously achieving low errors. To obtain the training set we have used DFT calculations using the VASP program.[2] Furthermore, the reparametrization can be accelerated by implementing a second-life application of existing data, such as results from published DFT calculations, to expand the training set. This approach enhances the efficiency and accuracy of the ReaxFF force fields, enabling more effective simulations of complex catalytic systems.

Results and Discussion

As case studies, we present the computational modeling of propane dehydrogenation (PDH) on Pt surfaces, alumina-supported (γ-Al_2O_3) Pt and Pt-Sn sub-nanometric clusters, and the reverse Water-Gas Shift reaction (rWGS) on Ni and NiCu surfaces and clusters.

We demonstrate that the obtained ReaxFF parameters (**2023-Pt/C/H** and **2024-Ni/Cu/C/O/H** can enable large-scale simulations of Molecular Dynamics techniques and describe main features of catalytic processes, see Figure 1.

For PDH on Pt,[3] the measured selectivity as a function of surface topology follows the order Pt(211) > Pt(100) > Pt(111). Simulations at different temperatures on Pt(111) surface allowed building Arrhenius plot to determine computationally the apparent activation energy, 73 kJ mol^{-1}, which is close to that determined experimentally for large nanoparticles ($\sim$5 nm) supported on alumina (75 kJ mol^{-1}).

For rWGS on Ni, the force field accurately reproduces the entire energy profile of the rWGS reaction, including redox and non-redox paths, as well as side reactions such as CO hydrogenation.

Significance

The present results and methodology confirm a way for a more efficient ensemble representation of nanocatalysts. This bridges the gap between atomic-scale modelling and mesoscale experimental techniques, thus offering the possibility of designing a more effective catalyst.
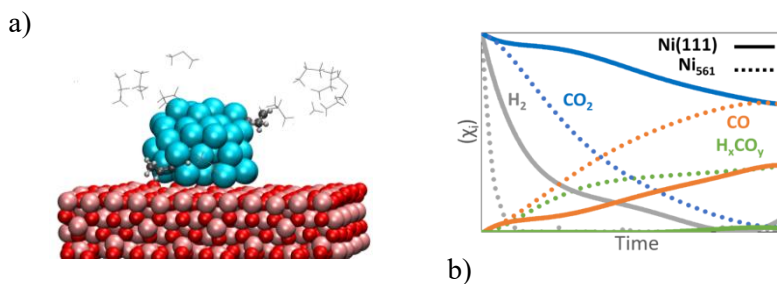
a)

b)

Figure 1. a) Snapshot of a molecular dynamics simulation of PDH on a Pt sub-nanometric cluster supported on γ-Al$_2$O$_3$. b) Evolution of species on different Ni topologies

References

1. Senftle, T.P.; Hong, S.; Islam, S. Md. M.; Kylasa, S.B.; Zheng, Y.; Shin, Y.K.; Junkermeier, C.; Engel-Herbert, R.; Janik, M. J.; Aktulga, J.M.; Verstraelen, T.; Grama. A.; and van Duin, A. C. T.; *npj Comput. Mat*. 2, 15011 (2016).
2. Kresse, G.; and Furthmüller, J.; J. Phys Rev B., 54, 11169 (1996).
3. Salom-Català, A.; Strugovshchikov, E., Kamila Kaźmierczak, K.; Curulla-Ferré, D.; Ricart, J.M., and Carbó, J.J.; J. Phys. Chem. C. 128, 2844 (2024)

Surface as a Playground for Exploring Physical Phenomena and a Foundation for Realizing Designer Materials: Some Hydrogen-Related Case Studies

Wilson Agerico Diño

Dept. of Applied Physics, Osaka University, Suita, Osaka 565-0871(Japan)
wilson@dyn.ap.eng.osaka-u.ac.jp

Introduction

"*... He who controls the spice controls the Universe ...,*" declared Baron Harkonnen in the 1984 film adaptation of Frank Herbert's 1965 novel ***Dune*** [1]. But, what is *the spice*? It can *extend youth... prolong life... increase vitality... heighten awareness... catalyze interstellar travel... use to make paper... plastics... cloths... fibers...* It can be anything. We could have replaced *spice* with *energy... catalyst... platinum...* and no one will be any the wiser. Earl Ward Plummer [2] wrote along the same line, "*... whoever controls complex materials controls science and technology,* i.e., progress is *materials-driven...*" Complex materials exhibit startling properties, reveal new and unexpected insights. Development of methods and models to synthesize and simulate complex systems proved to be extremely useful. But, don't fall into the trap of developing sophisticated experimental and theoretical techniques becoming an end in itself: one better measurement, one better calculation. Remember Ockham's Razor? Philip Warren Anderson [3] wrote, " *... a simplified model throws more light on the real workings of nature than any number of 'ab initio' calculations ..., which, even where correct, often contain so much detail as to conceal rather than reveal reality... After all, the perfect computation simply reproduces nature, it does not explain her ...*" "*Resources are the enemy of imagination,*" quipped Thomas Delavane in the 2012 CBS TV series adaptation of James Patterson's 2012 novel ***Zoo*** [4]. With these in mind, we take the hydrogen-surface reaction as a case study. At the symposium, we will introduce some insights gained from *spice*-related simple model studies (cf., e.g., [5-9]), in our quest to Realize Designer Materials utilizing Surface as a Foundation, and explore some physical phenomena along the way. In the following, we mention two topics related to controlling the dynamics of hydrogen:

Dynamical Quantum Filtering (cf., e.g., [8] and references therein)

Hydrogen plays an important role in a wide variety of applications, e.g., catalysis and metallurgy. H_2 occurs in two spin isomeric forms. *Para*-H have their two proton nuclear spins aligned antiparallel. *Ortho*-H_2 have their two proton nuclear spins aligned parallel. Symmetry requirements forbid spontaneous conversion between these two spin isomers. *Normal*-H_2 have a *para*-H_2 to *ortho*-H_2 ratio of 1/3, at room temperature. Using the surface as a *scattering/filtering media*, we increase the para-H_2 to ortho-H_2 ratio to 4.96 and 16.1 for *normal*-H_2 scattered along the $SrTiO_3(001)[100]$ and $SrTiO_3(001)[110]$ of the TiO_2- and SrO- terminated $SrTiO_3(001)$, respectively [12]. This could find significant applications not only in H_2 storage and transport, but also in realizing materials with pre-determined characteristic properties.

Hydrogen Isotope Separation/Filtering via Tunneling (cf., e.g., [9] and references therein)

Deuterium (D) occurs in natural water, hydrogen, methane, etc., in a D/H molecular ratio of ca. 100-150 ppm. The ratio in hydrogen varies somewhat with the source of the hydrogen. Because deuterium is an isotope of hydrogen, the two cannot be separated by ordinary chemical methods. There are, however, a number of prior processes by which deuterium (heavy water) can be separated from hydrogen (ordinary/natural water). These include distillation, electrolysis, diffusion, normal kinetic isotope effect and various chemical exchange processes. All of these are expensive, requiring either large capital expenditures or large amounts of energy, or both. On an industrial scale, D_2 enrichment with an H/D separation factor of ~1.6 at 25 K involves D_2O electrolytes produced by the Girdler sulfide process and cryogenic distillation. Recently, we reported an H/D separation factor of ~25 at 0.15 V and room temperature [9]. We realized this by polymer electrolyte membrane electrochemical hydrogen pumping (PEM-ECHP) through a heterogeneous electrode consisting of palladium and graphene layers. The hydrogen isotopes tunnel through the one-atom thick graphene layer during the electrochemical reaction. Application of a bias voltage enables one to switch the system from a quantum tunneling (dominant) regime to a classical over-the-barrier (dominant) regime.

Remarks

As in all … problems the governing principle is one of energy [10] … And yet, we still need to know what *Dynamics* would result. *Any sufficiently advanced technology is indistinguishable from magic.* [11] Hence, … *The Quest* (to understand the Magic of Nature) *Continues*!

References

[1] F. Herbert, *Dune* (Chilton Books, 1965).

[2] E.W. Plummer *et al.*, *Prog. Surf. Sci.* **67** (2001) 17-44; *Surf. Sci.* **500** (2002) 1-27.

[3] P.W. Anderson, *Science* **201** (28 July 1978) 307-316.

[4] J. Patterson, M. Ledwidge, *Zoo* (Little Brown, 2012).

[5] W.A. Diño, H. Kasai, A. Okiji, *Prog. Surf. Sci.* **63** (2000) 63-134.

[6] H. Kasai, W.A. Diño, R. Muhida, *Prog. Surf. Sci.* **72** (2003) 53-86.

[7] www.dyn.ap.eng.osaka-u.ac.jp/web/publication.php.

[8] K. Shimizu *et al.*, *Scientific Reports* **10** (2020) 5939.

[9] S. Yasuda *et al.*, *ACS Nano* **16** (2022) 14362.

[10] J.E. Lennard-Jones, *Trans. Faraday Soc.* **28** (1932) 333-359.

[11] A.C. Clarke, *Profiles of the Future: An Inquiry into the Limits of the Possible* (Henry Holt & Co., 1984).

Machine Learning Meets Quantum Mechanics in Catalyst Design

James P. Lewis[1,2,3]*

[1]Institute of Coal Chemistry, Chinese Academy of Science, Taiyuan, Shanxi (China)
[2]Hong Kong Quantum AI Laboratory, Science Park, Hong Kong (SAR China)
[3]Synfuels China Technology Co., Ltd., Beijing, (China)
*james.p.lewis.phd@gmail.com

Introduction

With increases in computational speed, the age of big data enables society to apply machine-learning algorithms to all aspects of life. Recently, even scientists have utilized the age of big data to understand and control nature, whereby to improve our understanding of materials as well as design new materials. Machine learning, a computational dream for decades, has now been realized – or has it?

Methodology

Our research group has endeavored to participate in this exciting direction by applying machine-learning tools to several physical chemistry and materials science - fundamental research problems including catalysts. With machine learning combined with computational density functional methods (FIREBALL2020 developed by our research group), our research has expanded to new directions such as predicting global reaction mechanisms and understanding adsorbate interactions on catalysts. We have also utilized our computational density functional methodologies to generate data for developing machine-learning potentials in a much more efficient manner than what has previously been proposed.

Fast and efficient computational chemistry and materials science software has further enabled rapid accumulation of data from which machine learning algorithms can recognize patterns and make predictions. The application of machine learning tools to catalysis is not as straightforward as one might anticipate, and we will discuss our journey where machine learning meets quantum chemistry in catalysis.

Results and Discussion

We will discuss two prominent examples of our recent success with machine learning: 1) The first example is a machine-learning approach to evaluate global reaction coordinates. We report on a global reaction coordinate (containing all internal coordinates) to thoroughly describe the reaction mechanism for azobenzene photoisomerization. The formalism can be easily applied to any reaction mechanism in catalysis. the role of other proposed reaction mechanisms; 2) The second example is a machine-learning approach to predict adsorbate interactions of alloyed catalysts. Here, we utilize a machine-learning model, based on the random-forest method, to predict CO adsorption in thiolate protected Au-based nanoclusters. One advantage to our machine-learning approach is that correlations in defined features disentangle relationships among the various structural parameters. Our machine-learning adsorbate model is easily extended to other metallic nanocluster catalysts.

Significance

In addition to our previous results using machine learning, we will discuss preliminary results where we are using machine learning to recognize patterns of chemical reactivity. Currently, we are developing a time series convolutional network approach to "forecast" reactivity. This approach will enable us to determine the factors at the quantum level for how reactivity occurs. Pattern recognition of charge and energy flow in materials will enable researchers to explore principles of reactivity. Understanding these patterns at the quantum level will enable us to further enhance the field of catalyst design.
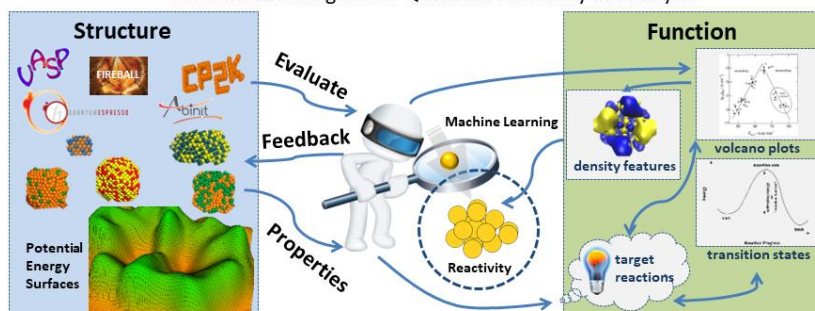
Figure 1. Relating structure and function relationships in catalysis will require an enhanced paradigm that includes machine learning algorithms.

References
1. Tavadze, P.; Avendaño Franco, G.; Ren, P.; Wen, X.; Li, Y.; Lewis, J. P. A Machine-Driven Hunt for Global Reaction Coordinates of Azobenzene Photoisomerization. *J. Am. Chem. Soc.*, *140* (1), 285–290 (2018). https://doi.org/10.1021/jacs.7b10030.
2. Panapitiya, G.; Avendaño-Franco, G.; Ren, P.; Wen, X.; Li, Y.; Lewis, J. P. Machine-Learning Prediction of CO Adsorption in Thiolated, Ag-Alloyed Au Nanoclusters. *J. Am. Chem. Soc.*, *140* (50), 17508–17514 (2018). https://doi.org/10.1021/jacs.8b08800.
3. J.A. Hernandez Zeledon, P. Ren, X. Wen, Y. Li, A.H. Romero, and J.P. Lewis. "Maximizing information stored in machine-learning descriptors for material structure prediction," *J. Appl. Phys.* 127, 215108 (2020). https://doi.org/10.1063/5.0002252.
4. Lewis, J. P.; Ren, P.; Wen, X.; Li, Y.; Chen, G. Machine Learning Meets Quantum Mechanics in Catalysis. *Front. Quantum Sci. Technol.*, *2*, 1232903 (2023). https://doi.org/10.3389/frqst.2023.1232903.

Discovering New Molecules and Materials Using Machine Learning Methods

Jialu Chen, Wenjun Xu and Ruiqin Zhang*

Department of Physics, City University of Hong Kong, Hong Kong SAR 999077 (China)
*aprqz@cityu.edu.hk

Introduction

Optimizing reaction conditions and designing new molecules or materials are crucial in solving energy and environmental challenges in human society. Experimentally testing different reaction conditions or synthesizing new molecules and materials costs a lot of time and resources. High-throughput screening based on theoretical calculations is a practical strategy for making experiments cost-effective. The screening is usually combined with machine learning (ML) methods, which can reduce the costs of theoretical calculations and directly predict experimental results. A key point is constructing descriptors for ML models to recognize molecules and materials.

Methodology

We used various machine learning methods in the discovery of molecules and materials in conjunction with the density functional theory (DFT) calculations which are indispensable in the constructions of descriptors.

Results and Discussion

In our recent work, harmonic vibrational frequencies of several semiempirical methods (the PM6, PM7, and GFN2-xTB methods) were used as the frequency descriptor (FD) in Δ-machine learning (Δ-ML) to reduce the cost in predicting the properties of molecules and materials [1]. The FD generated by the GFN2-xTB method has excellent performance among several semiempirical methods. The chemical accuracy can be achieved with a small training set size according to the combination of single point calculations at density functional theory levels. In addition, we further included infrared intensities to the FD, namely the FD-II. The chemical accuracy of energies can be achieved with a small training set size (3%).

Moreover, a screening framework was implemented for discovering promising photovoltaic materials from double hybrid organic-inorganic perovskites (DHOIPs) [2]. DHOIPs are promising in photovoltaic applications due to their excellent optoelectronic properties and low production costs. Accelerated discovery of DHOIPs has been realized by combining ML techniques, high-throughput screening, and density functional theory calculations. Different from the previous works, the anisotropy of organic cations of DHOIPs was first considered, and Δ-ML was used in high-throughput of DHOIPs to improve the accuracy of ML models further. 19 promising DHOIPs with appropriate bandgaps for solar cells were screened out from 78400 DHOIPs and verified by performing HSE06 calculations.

Further, we combined the steric and electronic effects into a descriptor to construct volcano plots of reaction yields in cross-coupling catalysis [3]. More experiments with other metal catalysts are required to verify the performance of the proposed descriptor, $\% Vbur$ (min) - $3 \cdot$ HOMO–LUMO gap (eV). It has grasped fundamental factors, steric and electronic effects, which influence reaction outcomes together. It is also straightforward with precise physical meanings.

In addition, to allow efficient and reliable transition state (TS) search on a potential energy surface (PES) and thus effectively determine the kinetics and thermodynamics of chemical reactions, we propose a TS search method in accordance with the Q-learning algorithm [4]. Appropriate reward functions are set for a given PES to optimize the reaction pathway through continuous trial and error, and then the TS can be obtained from the optimized reaction pathway. It is demonstrated that the Q-learning method can predict consistent TS and reaction pathway with those by ab initio calculations, offering a simple and reliable Q-learning method to search for all possible TS and reaction pathway of a chemical reaction.

Significance

Machine learning methods are popular and influential in predicting the properties of molecules and materials. Developing effective descriptors plays a critical role in the performance of models. Our work

demonstrates that it is possible to accelerate various property predictions with our approach in the future. Our work also demonstrates an effective method for predicting and discovering hidden novel photovoltaic materials. The concept of volcano plots has universal validity and can act as a predictive tool to accelerate the understanding of cross-coupling catalysis. Our work offers a simple and reliable Q-learning method to search for all possible TS and reaction pathway of a chemical reaction, which may be a new option for effectively exploring the PES in an extensive search manner.

References
1. Chen, J.L., Xu, W.J., and Zhang, R.Q., *New J. Chem.* 45, 20672 (2021)
2. Chen, J.L., Xu, W.J., Zhang, R.Q., *J. Mater. Chem. A* 10, 1402 (2022)
3. Chen, J.L., Zhang, R.Q., "Volcano Plots of Reaction Yields in Cross-Coupling Catalysis", *J. Phys. Chem. Lett.* 13, 520 (2022)
4. Xu, W.J., Zhao, Y.L., Chen, J.L.,, Wan, Z.Y., Yan, D.D., Zhang, X.H., Zhang, R.Q., *J. Comput. Chem.* 45, 487 (2024)

Excess proton/deuteron in light/heavy water solvent using path integral molecular dynamics simulation

Kazuki Tatenuma, Makito Takagi, Tomomi Shimazaki, and <u>Masanori Tachikawa*</u>
Graduate School of NanoBioScience, Yokohama City University,
22-2 Seto, Kanazawa-ku, Yokohama 236-0027 (Japan)
*tachi@yokohama-cu.ac.jp

Introduction

Proton in aqueous solution plays a fundamental role in chemical and biological reactions/materials, and isotope effects have also been reported. However, to our best knowledge, the discussion of the difference between a proton in light water and a deuteron in heavy water is limited. A calculation for deuteron in heavy water based on the first-principles calculations, including NQEs, has not yet been carried out. Significant nuclear quantum effects (NQEs) play a vital role in systems including hydrogen and deuteron due to their light masses. Path integral molecular dynamics (PIMD)[1] is one of the methods that can be considered the NQEs. In this study, thus, we have analyzed the H/D isotope effect between proton/deuteron in light water and heavy water based on the first-principles calculations, including NQEs using the PIMD method.[2]

Methodology

We constructed the two computational models of an excess proton in $32H_2O$ and an excess deuteron in $32D_2O$ in the unit cell with the periodic boundary conditions (PBCs), as shown in Fig. 1. Cell sizes are adjusted for the reasonable density of light water (0.9971 g/cm^3) and heavy water (1.1044 g/cm^3). To consider the nuclear quantum effect, we have carried out path integral molecular dynamics (PIMD) simulations of 100,000 steps, including an initial equilibration process of 5,000 steps. The parameter setting is below; the temperature of this calculation is set to 300 K with Massive Nosé-Hoover chain thermostats. Time step size is set to 0.1 fs/step, and the number of beads is 16. The PIMD simulations were performed using a previously improved house code. Electronic structure calculations were performed using density functional theory (DFT) with the Perdew-Burke-Ernzerhof (PBE) functional and PAW pseudopotentials. Grimme's dispersion correction (D3) is also considered. All the calculations were performed using the Vienna Ab initio Simulation Package (VASP) 5.4.4 program.

Results and Discussion

The radial distribution functions (RDFs) of the O-O distances for the entire system are shown in Fig. 2(a), while the RDFs of O*-O distances around the ions are in Fig. 2(b), where O* represents the oxygen atom in H_3O^+/D_3O^+. We found no significant difference in the O-O RDFs in the entire systems of H-body and D-body. Conversely, we found the H/D isotope effect at the second peak of O*-O RDFs (Fig. 2(b)). The main reason would be the difference in the ratio appearing Zundel structure for H-body and D-body.

We also found double H_3O^+/D_3O^+ in some configurations. These differences in the cations between the H-body and D-body might also affect the mobility of the proton/deuteron.

Significance

We have analyzed the structural H/D isotope effect between an excess proton in light water (H-body) and an excess deuteron in heavy water (D-body), including the nuclear quantum effect by path integral molecular dynamics simulation. We found that the second peak of the H-body is shorter than that of the D-body in the radial distribution function of O^*–O, where O^* is the oxygen atom of H_3O^+/D_3O^+ fragment. The main reason for this would be the difference in the ratio of the Zundel structure with the sp^3-like configuration, where the Zundel structure in H-body (14.0%) is greater than that in D-body (12.0%). We also found rare occurrences of double H_3O^+/D_3O^+ configurations, mainly including the Zundel-Zundel-like structures such as $H_7O_3^+/D_7O_3^+$ and $H_9O_4^+/D_9O_4^+$. The ratios of such configurations appearing in our simulations are 0.89% and 0.20% for the H-body and D-body, respectively.

(a) H-body (b) D-body

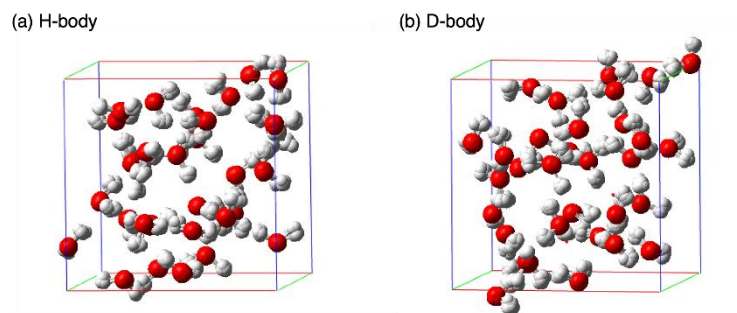**Figure 1.** The two computational models of (a) excess proton in $32H_2O$ (H-body) and (b) excess deuteron in $32D_2O$ (D-body) in the unit cell with the periodic boundary conditions (PBCs).

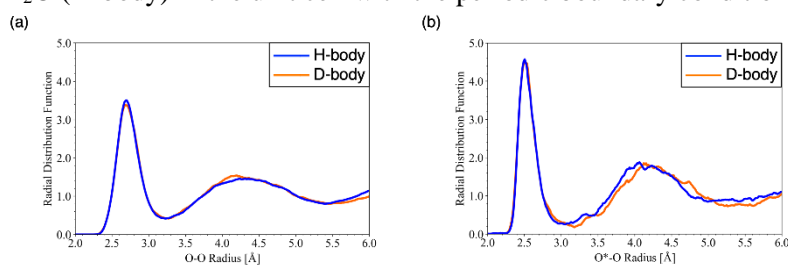**Figure 2.** (a) The O-O RDFs for the entire system and (b) the O-O* RDFs around H_3O^+/D_3O^+.

References

1. M. Shiga, M. Tachikawa, and S. Miura, *J. Chem. Phys*., **115**, 9149 (2001).
2. K. Tatenuma, M. Takagi, T. Shimazaki, and M. Tachikawa, *Bull. Chem. Soc. Jpn*., **97**, uoad009 (2024).

Deep Reinforcement Learning in Chemistry

U. Deva Priyakumar[1]*

[1]*Center for Computational Natural Sciences and Bioinformatics, International Institute of Information Technology, Hyderabad 500 032 (India)*
*deva@iiit.ac.in

Introduction

Deep Learning enjoyed great success in problems like the prediction of molecular properties, where we explicitly provide supervision in the form of input-output pairs, obtained from experimentation or simulation, and use deep learning to generalize these patterns to a set of unseen examples. A few instances of these tasks are predicting the binding affinity, solubility, spectra, etc., given molecular structure. However, in tasks where no such explicit supervision exists, we cannot use these deep learning methods. Furthermore, when the problem cannot be phrased as approximating a function from input-output pairs, deep learning cannot be used. Exploring molecules that have high drug-likeness and low toxicity is one such task. Reinforcement Learning (RL) has been applied to various domains in computational chemistry and has found wide-spread success. In this talk we will take few case studies of using RL in chemistry related tasks such as energy prediction, generative modeling and geometry optimization.

Methodology

RL, an increasingly prevalent category of machine learning algorithms, generally involves two main elements: an agent that takes actions on states present in a "state-space", and a critic in the form of an "environment" that assesses those actions and gives feedback to the agent through rewards or punishments. We can indirectly provide supervision for such tasks which don't have an explicit "correct answer" by rewarding the model based on the properties of intereset such as drug-likeness of output molecules and the diversity of the molecules generated. RL's primary strength lies in handling multi-step decision tasks, where the reward is determined after certain intervals rather than immediately following each decision. This reward is not necessarily directly connected to the last decision made but is, instead, the culmination of decisions made throughout the entire episode.

In each state of our simulation, our agent is tasked with choosing an action. This action choice is represented by the policy function, which gives the probability of each action for a given state. The policy can be deterministic, where the probability for one action in each state will be 1 and for all others, it will be 0; alternatively, it can be stochastic, where all the actions have some probability and we choose actions by sampling from the probability distribution. Now that we know what actions we choose at each state, we can estimate the long-term reward that will be generated under such action choice starting from the given state.

Results and Discussion

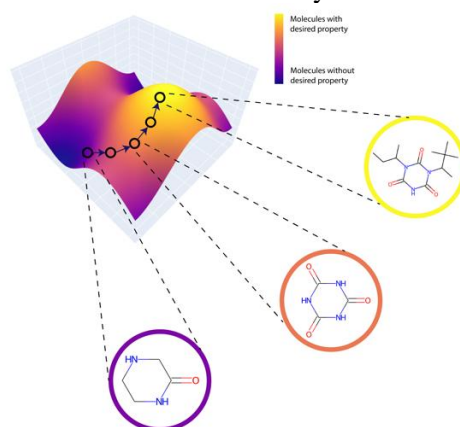We will discuss three main applications of RL in chemistry.

Figure 1. Visualization of any search in a parametrized molecule space being equivalent to ascending a reward function in that space.

(i) Molecular generation: We show that RL along with RNN or GPT can be effectively used to generate molecules de novo that have desired properties such as solubility, QED values, binding affinity, etc.

(ii) Metal cluster generation: We have developed a machine learning potential for gallium metal clusters that will discussed. Followed by this, we will discuss the use of RL for generating three-dimensional structures of low energy gallium clusters. We show that RL makes this more efficient in terms of computational expense and also identifying more clusters than the traditional methods.

(iii) Geometry optimization: One of the primary task in all molecular/material modeling exercises is geometry optimization. We show how multi-agent RL could be used to perform geometry optimization by designing reward functions based on the forces.

Significance

Focused and efficient searching of chemical space is essential to identify molecules and materials that exhibit desired properties and functions. We show that machine learning, specifically, deep reinforcement learning, is efficient in tackling the large chemical space problem effectively making material/molecular design faster and cheaper.

References

1. Sridharan, B., Sinha, A., Bardhan, J., Modee, R., Ehara, M., Priyakumar, U.D., *J. Comp. Chem.* 45, 0000 (2024).
2. Goel, M., Raghunathan, S., Priyakumar, U. D., *J. Chem. Inf. Model.* 61, 5815 (2021).

Machine Learning (ML) for Simulating Complex Energy Materials

Nongnuch Artrith[1*]

[1]*Materials Chemistry and Catalysis, Debye Institute for Nanomaterials Science,
Utrecht University, The Netherlands* *E-mail*: n.artrith@uu.nl

Abstract

Many materials with applications in energy materials, e.g., catalysis or batteries are non-crystalline with amorphous structures, chemical disorder, and complex compositions, which makes the direct modelling with first principles methods challenging. To address this challenge, we developed accelerated sampling strategies based on ML potentials, genetic algorithms, and molecular-dynamics simulations. Here, I will discuss the methodology and applications to amorphous battery materials, including constructing phase diagrams of amorphous phases and correlating their ionic conductivity with local structural motifs. Further, I will show how large computational and small experimental data sets can be integrated for the ML-guided discovery of novel materials. These examples show that the combination of first-principles calculations and ML models is a useful tool for the modelling of complex energy materials and for materials discovery. All data and models are made publicly available.

Nong Artrith is a tenured Assistant Professor in the Materials Chemistry and Catalysis Group at the Debye Institute for Nanomaterials Science, Utrecht University, and a Visiting Researcher at Microsoft Research Amsterdam Lab. Prior to joining Utrecht University, Nong was a Research Scientist at Columbia University, USA, and a PI in the Columbia Center for Computational Electrochemistry. Nong obtained her PhD in Theoretical Chemistry from Ruhr University Bochum, Germany, for the development of machine-learning (ML) models for materials chemistry. She was awarded a **Schlumberger Foundation fellowship** for postdoctoral research at MIT and subsequently joined UC Berkeley as an associate specialist. In 2019, Nong has been named a **Scialog Fellow for Advanced Energy Storage**. Since 2023, Nong is a **member of the NL ARC CBBC** (https://arc-cbbc.nl). She is the main developer of the open-source ML package ænet (http://ann.atomistic.net) for atomistic simulations. Her research interests focus on the development and application of first principles and ML methods for the computational discovery of energy materials and for the interpretation of experimental observations.

Computational Materials and Process Development for a Clean-Energy Future

A. Urban

Department of Chemical Engineering, Columbia University, New York, NY 10027.

Abstract

I will discuss how we use quantum-chemical and data-science methods to advance the understanding of degradation in lithium-ion batteries and metal extraction processes for mining and recovering critical metals.

The electrification of transport and industry requires batteries made from abundant materials. Unfortunately, designing cobalt-free cathodes for high-energy-density Li-ion batteries remains challenging due to the strong dependence of battery lifetime and rate capability on material stability and atomic-scale structural order. Moreover, extracting battery metals such as Cu, Co, Ni, and Li from ores has a significant carbon footprint. Therefore, we urgently need to develop longer-lasting batteries from more abundant materials and carbon-neutral metal-extraction processes.

Toward these objectives, we developed a surface phase diagram methodology that provides insights into cathode degradation via oxygen release and explains stability differences between cathode materials with different compositions. We initiated steps toward engineering battery recycling processes using machine-learning-augmented first-principles calculations, achieving accurate metal oxide reduction and melting temperature predictions.

Bio

Alex Urban is an Assistant Professor of Chemical Engineering and a founding member of the Columbia Electrochemical Energy Center (CEEC) and the Columbia Center for Computational Electrochemistry (CCCE). His group's research focuses on understanding and discovering materials and processes for clean-energy applications using atomic-scale modeling and data science. Alex obtained his Ph.D. from FAU Erlangen-Nuremberg in Germany. He conducted postdoctoral research at MIT and UC Berkeley before becoming an independent University Fellow in the School of Chemistry at the University of St Andrews (UK). He joined the Department of Chemical Engineering at Columbia University in January 2019. In 2019, Alex was named a Scialog Fellow for Advanced Energy Storage by the Research Corporation for Science Advancement. In 2024, he received a National Science Foundation's CAREER award.

An Integrative Modeling & Multiscale Simulation Approach to Targeting Host Innate Immunity

Peter J. Bond[1,2]*

[1]*Bioinformatics Institute (BII), Agency for Science, Technology and Research (A*STAR), 30 Biopolis Street, #07-01 Matrix, Singapore 138671 (Republic of Singapore)*
[2]*Department of Biological Sciences, National University of Singapore, 14 Science Drive 4, Singapore 117543 (Republic of Singapore)*

*peterjb@bii.a-star.edu.sg

Introduction

Infectious diseases are a significant threat to human health. The interaction of pathogens with host cells is critical to infection, the immunological response, and therapeutic interventions. Some bacterial pathogens release toxins from their membranes which can make us ill through interactions with our immune system. We are interested in the mechanisms by which such endotoxic molecules excessively stimulate innate immune receptors, which can lead to sepsis, a condition that kills millions of people globally each year.

Methodology

We build computational models that contribute to our understanding of the mechanisms of disease and host immune responses, with a particular focus on infective pathogens. Our main method of choice is molecular simulation, using multiscale approaches that allow us to access a broad range of spatiotemporal scales, from atomically-detailed systems to highly simplified coarse-grained resolutions. We integrate diverse structural, biophysical, and biochemical data into models that ultimately enable us to work towards novel therapeutic strategies.

Results and Discussion

To better understand the process of bacterial pathogen infection and the host response, we have developed computational models to trace in molecular detail the cascades and intermediates associated with transfer of endotoxins from bacterial surfaces to innate immune receptors. We have subsequently leveraged these models to establish previously undisclosed modes of action of endogenous peptides with anti-inflammatory and antimicrobial activities. Working closely with our experimental collaborators, we have engineered more stable and specific drugs targeting innate immunity and have also shown how such technologies might be adapted for reducing surgical site infections.

Significance

Collectively, this work has unraveled key determinants governing interactions between bacterial pathogens, endotoxins, and host immunity. Furthermore, it is helping towards the development of novel therapeutics to tackle ongoing issues of infectious disease and antimicrobial resistance.

A basic theory for initial value problems of first order ordinary differential equations with L^p-Carathéodory functions and applications to logistic type population models*

Kunquan Lan

Department of Mathematics Toronto Metropolitan University,
Toronto, Ontario, Canada M5B 2K3
E-mail: klan@torontomu.ca https://math.ryerson.ca/~klan/

In this presentation, I shall present a basic theory on the existence and uniqueness of solutions and local solutions for initial value problems (IVPs) of first order ordinary differential equations with L^p-Carathéodory nonlinearities that are not necessarily continuous based on the following paper:

Kunquan Lan, A basic theory for initial value problems of first order ordinary differential equations with L^p-Carathéodory functions and applications, *Journal of Differential Equations*, **386** (2024), 368-403.

The basic theory contains three parts: (*i*) the existence and uniqueness of solutions in $C([a, b], [c, d])$; (*ii*) the existence and uniqueness of local solutions in $C([a, a + h_1(p)]; [c, d])$; (*iii*) the existence and uniqueness of solutions and nonnegative solutions.

The classical results dealt with the above part (*ii*) when f is continuous or an L^1-Carathéodory function, and only obtained the existence of a number h such that the IVPs had local solutions in $C[a, a + h]$.

The results in parts (*i*) and (*iii*) are new. The results in part (*ii*) are new when $p \in (1, \infty]$ and improve the classical results when $p = 1$.

The new basic theory enriches the classical basic theory of initial value problems of first order ordinary differential equations.

As applications of the basic theory, I shall present the existence of solutions and nonnegative local solutions for logistic type population models with heterogeneous environments, where the local rates of changes in the population density are L^p-Carathéodory functions.

Keywords: Initial value problem, first order ordinary differential equation, L^p-Carathéodory function, solution, local solution, uniqueness, fixed point theorem, Bihari inequality

Lexicographic (Robustness) Method for (Uncertain) Multi-objective Optimization of Problems

Petrot N.
Naresuan University, Phitsanulok, 65000 (Thailand)
narinp@nu.ac.th

Introduction

We will focus on (uncertain) multi-objective optimization model problems and the solution concept known as the lexicographic (robustness) solution concept. The concept of lexicographic optimization problems arises naturally when conflicting objectives exist in a decision problem, but for reasons outside the control of the decision-maker, the objectives have to be considered in a hierarchical manner. We will consider both the optimality and algorithms for the lexicographic robust solution concepts in the context of deterministic and uncertain multi-objective optimization problems.

Methodology

We will consider the lexicographic robust solution concepts in the context of deterministic and uncertain multi-objective optimization problems.

Results and Discussion

We will consider both the optimality and algorithms for the lexicographic robust solution concepts in the context of deterministic and uncertain multi-objective optimization problems. Additionally, some concrete problems will be examined as applications of the considered lexicographic (robust) solution concepts.

Significance

Narin Petrot is a mathematician whose contributions significantly advance optimization theory and variational inequalities. His research primarily focuses on the development andvanalysis of algorithms for solving complex mathematical problems, including convex optimization, variational inequalities, and set optimization problems. Petrot's work is noted for enhancing the stability and efficiency of optimization algorithms, particularly in distributed computing. (https://www.scopus.com/authid/detail.uri?authorId=56045120300&origin=AuthorEval)

References

1. P. Boriwan, M. Ehrgott, D. Kuroiwa, N. Petrot, (2020). The lexicographic tolerable robustness concept for uncertain multi-objective optimization problems: a study on water resources management, Sustainability. 12, no. 18, article number 7582.
2. P. Boriwan, M. Ehrgott, D. Kuroiwa, N. Petrot, (2022). On the properties of lexicographic tolerable robust solution sets for uncertain multi-objective optimization problems, Carpathian J. Math, Volume 38 (2022), No. 1, Pages 57 - 66.
3. M. Ehrgott, Multicriteria Optimization (Second Edition), Springer-Berlin Heidelberg (2005).
4. L. Kliemann and P. Sanders (Eds.), Algorithm Engineering (Selected Results and Surveys), Lecture Notes in Computer Science, Springer International Publishing (2016).

Computational Methods: Connecting mathematical theory to Data Science and AI Applications in Healthcare and Education

Bagdasar O.[1]*, Andrica D.[2], Mulgrew D.[1], O'Neill S.[1], Sutton J.[1]
[1]University of Derby, Derby, DE22 1GB (United Kingdom)
[2]Faculty of Mathematics and Informatics, Babeş Bolyai University, Cluj Napoca (Romania)
*o.bagdasar@derby.ac.uk

Introduction

Iterative processes play a fundamental role in mathematics research and practice. Examples include numerical solutions of equations, fixed-point theory, data analysis or machine learning, but also, real-world applications like feedback loops, trial & error, or prototype development.

The first part of the talk presents recursive processes in the complex plane: Horadam sequences which generalize Fibonacci numbers to two dimensions [1], and the dynamic geometry of triangles [2]. We will see how the geometric patterns generated by these iterations can be convergent, divergent, periodic, or dense in 1D curves or 2D annuli of the complex plane, and we will discuss some applications to random number generation. Then we relate some classes of non-expansive mappings to explainable AI and discuss a few recent applications of Data Science to Healthcare datasets and AI-based chatbots used to improve student experience.
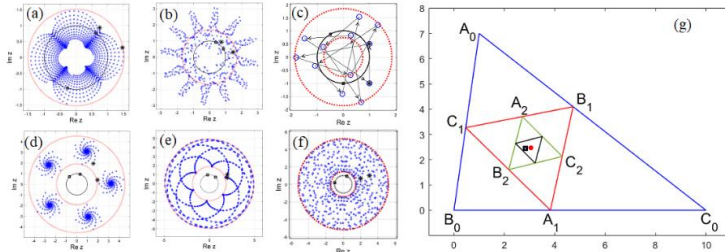
Figure 1. First 500 terms of Horadam sequences whose orbits are (a) convergent; (b) divergent; (c) periodic; (d) k-limit points; (e) dense in 1D; (f) dense in 2D. (g) Nested bisector triangles.

Methodology

The geometric iterative processes are formulated in the framework of complex numbers, which allows the computation of exact formulae for the general terms of the various sequences. This leads to a convenient classification of the patterns, as a function of the initial parameters. The density proofs involve classical results from analysis (Weyl's Lemma), and the performance of a novel pseudo-random number generator (PNRG) was evaluated using the NIST tests [4].

Proofs of convergence related to the sequence of nested triangles involve Cantor's Lemma for Complete Metric Spaces, along with the power curve of a triangle and classical inequalities [2]. The results are visualized using Matlab diagrams, whose application drives the numerical simulations, inspiring generalizations and the exploration of other related dynamic geometries.

Results and Discussion

We provide the classification of the possible dynamics exhibited by complex Horadam in the complex plane and we provide a visual atlas of the resulting geometric patterns. Certain dense patterns were used to build a PNRG which performed well in various NIST tests. Then, we prove the convergence of bisector nested triangle iterations to a point and extend this theory further, to the case of iterations defined by points located on the power curve of a triangle (this contains famous points like the centroid G, incircle I, or the symmedian or Lemoine point K of a triangle). Finally, we present some key aspects related to a recent investigation of healthcare datasets, in which the statistical analysis revealed interesting connections and correlations to power laws [7]. In the end, we discuss the design and application of an AI-based chatbot called DerbyGPT, starting from the concept, technical solutions, applications, impact, and ethical considerations.
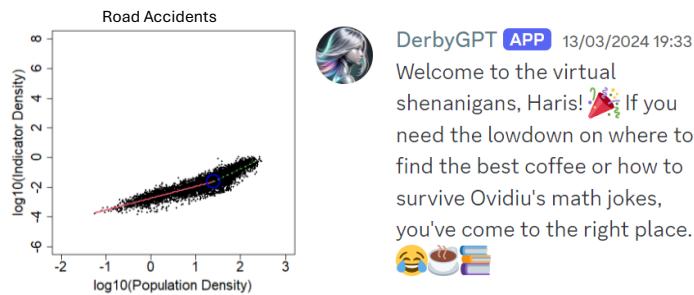
Figure 2. (a) Road Accidents as a function of population density in urban areas; (b) DerbyGPT.

Significance

The results presented in this talk are linked to recent advances linked to geometric patterns of complex recurrent sequences and their applications. In dynamic geometry, the convergence of nested bisectors triangles was proved in a more general setting, closing a conjecture from [5]. The analysis of healthcare datasets provided useful insight [7], currently studied with financial support from NHS, while the DerbyGPT chatbot transformed student and staff experience [6].

References

1. Andrica, D., Bagdasar, O. Recurrent sequences: Key results, Applications and Problems, Springer, (2020).
2. Andrica, D., Bagdasar, O., Marinescu, D.Şt. *Carpathian J Math* 39(3), 605-620 (2023).
3. Artsawang, N., Baiya, S., Ungchittrakool, K., Bagdasar O., Plubtieng, S., Thammasiri, P., *Carpathian J Math.* 40 (2), 243-261 (2024).
4. Bagdasar, O., Chen, M., Drăgan, V., Ivanov, I.G., Popa, I.-L. On Horadam Sequences with Dense Orbits and PR Number Generators. *Mathematics 11*, 1244 (2023).
5. Ismailescu, D., Jacobs, J. *Period. Math. Hung.* 53(1-2), 169-184 (2006).
6. O'Neill S., Mulgrew, D., Bagdasar, O., On the use of LLMs for transforming student and staff experience in Higher Education, in *Proceedings of PPIC'24*, July 4-5, 2024, Porto.
7. Sutton, J., Shahtahmassebi, G., Ribeiro, H.V., Hanley, Q.S. *Sci. Rep.*10(1), 16863 (2020).

Digital & Green Transformation Toward Smart and Sustainable Industry in Thailand

Chawalit Jeenanunta[1]*
[1] Sirindhorn International of Technology, Thammasat University,
Phatum Thani, 12120 (Thailand)
*chawalit@siit.tu.ac.th (corresponding author designated with a star)

Abstract

The talk titled "Digital & Green Transformation Toward Smart and Sustainable Industry in Thailand" will explore the pivotal role of Cyber-Physical Systems (CPS) in achieving Sustainable Development Goals (SDGs), with a particular focus on the context of Thailand. CPS, integrating AI and IoT, is essential in advancing sustainable practices across various sectors, particularly in the green transformation of manufacturing. Emphasizing lean and kaizen methodologies, this talk will discuss how sustainable CPS can drive efficiency and innovation in energy systems and manufacturing. The presentation will highlight case studies and innovative approaches, including using Digital Twins to enhance the sustainability and efficiency of manufacturing processes, ensuring they contribute effectively to the SDGs. Additionally, the talk will cover the synergy between digital and green transformations, demonstrating how digital innovations can facilitate a smart, resilient, and sustainable industrial landscape in Thailand.

Leveraging Analytics for Strategic Decision Making in the Age of Big Data

Thanachart Ritbumroong
National Institute of Development Administration (NIDA), Thailand

The advancement of technology allows businesses to collect more data, not only financial records but also customer behaviors and web clickstreams. This so-called Big Data enables businesses to monitor closely how every activity interacts and collaborates. Instead of asking broad questions such as "How is our profitability?", more detailed data can guide executives to understand each unit's profitability level. Executives can then make prompt decisions on devising strategies for each business unit.

This keynote will share how various companies leverage computational abilities to turn their data into business value. The session will explore business computation and how data is processed to gain business value, including:

- The landscape of technology and managerial decisions
- The evolution of business reporting, business intelligence, data mining, data science, and AI
- Case studies and real-world examples showcasing how data is utilized to solve complex business problems

The aim of this session is to demonstrate how computational abilities can help staff at any level gain a deeper understanding of their internal operations and external environment, enabling a company to react more effectively and gain a competitive advantage.

Integrating Artificial Intelligence in Education to Foster Environmental Sustainability in Thailand

Wasit Limprasert*

Data Science and Innovation Program, interdisciplinary college, Thammasat University, 12120 (Thailand)
*wasit@staff.tu.ac.th

Abstract

We explore the transformative potential of artificial intelligence in revolutionizing Thailand's educational landscape, particularly through the lens of environmental sustainability as conceptualized in the Gaia Theory and the Biotic Pump. Drawing parallels to James Lovelock's view of Earth as a self-regulating organism, the talk proposes the integration of AI-driven tools like encyclopedias and knowledge graphs to enhance the comprehension and application of complex environmental concepts. These tools are tailored to fit Thailand's unique cultural and ecological context, aiming not only to improve educational outcomes but also to empower students to address pressing environmental challenges effectively. By embedding AI in environmental education, we envision a future where Thai students are not merely passive learners but active participants in fostering a sustainable planet. This integration represents a critical step towards aligning technological advancements with ecological stewardship, embodying Lovelock's holistic vision of Earth's interconnectedness.

New techniques for understanding chemical reactions: a reaction space projector and a natural reaction orbital

Tetsuya Taketsugu[1,2]*

[1]*Department of Chemistry, Faculty of Science, Hokkaido University, Sapporo, 0600810 Japan*
[2]*Institute for Chemical Reaction Design and Discovery (WPI-ICReDD), Hokkaido University, Sapporo, 001-0020 Japan*
*take@sci.hokudai.ac.jp

Introduction

In quantum chemistry, the Intrinsic Reaction Coordinate (IRC) is crucial for understanding the fundamental processes of chemical reactions. Defined by the potential energy surface, the IRC has historically guided research into reaction mechanisms. Recent advances in automated reaction path search technologies now allow us to investigate these mechanisms through networks that include multiple reaction paths [1,2]. These networks facilitate a more detailed and interconnected discussion of reaction mechanisms. Each reaction path within the network is represented as a one-dimensional curve in a coordinate space of $3N$-6 dimensions for a system of N atoms, forming a complex web of paths across a multidimensional space. Additionally, trajectories from ab initio molecular dynamics (AIMD) simulations provide dynamic pathways across this network. In this presentation, I will introduce the Reaction Space Projector (ReSPer) method [3-7], which employs dimension reduction techniques to analyze and project these networks and trajectories onto a unified, lower-dimensional space. I will also discuss the natural reaction orbital (NRO) method [8,9], which reveals the evolution of chemical bonds along a reaction path by mixing specific pairs of occupied and virtual orbitals.

Methodology

Dimensionality reduction is widely used across various fields to classify large and complex datasets. In theoretical chemistry, both linear methods like Principal Component Analysis (PCA) and Classical Multidimensional Scaling (CMDS), as well as nonlinear methods such as Locally Linear Embedding (LLE) and Isometric Feature Mapping (ISOMAP), are employed to capture the chemical and structural features of data with minimal loss of information. The disconnectivity graph, which visualizes the topology of high-dimensional potential energy surfaces (PESs), is particularly useful for depicting the free energy landscapes of proteins, preserving information about reaction barriers. CMDS offers a reduced-dimensional subspace while striving to maintain as much of the original multidimensional data's dissimilarity as possible. It can also project out-of-sample data, which were not included in the initial dataset, through an extended version of CMDS. In molecular chemistry, dissimilarity is typically quantified by the Euclidean distance between pairs of molecules. Although mathematically similar to PCA, CMDS is particularly effective at optimizing the distances between molecule pairs, making it a superior method for dimensionality reduction in certain contexts. To facilitate the visualization and analysis of molecular structures in a $3N$–6 dimensional space, and to explore dynamic reaction behaviors in a reduced-dimensional subspace, we developed ReSPer, a Python-based program [3-7]. The ReSPer method involves three steps: (1) pre-processing, (2) dimensionality reduction of the original data, and (3) projecting out-of-sample data onto the reduced-dimensional space, if necessary.

NRO offers a novel approach for analyzing chemical reactions from the perspective of electronic theory [8,9]. This method hinges on the automatic extraction of a pair of occupied and virtual NROs, which are crucial in characterizing electron transfers in response to shifts in nuclear coordinates along a reaction path. These orbitals are derived from solving the coupled-perturbed self-consistent-field (CPSCF) equations, which consider the perturbation due to nuclear displacement. Applied to various chemical reactions, the NRO-based method demonstrates that the sum of squares of the singular values, obtained from the CPSCF solutions, exhibits distinct peaks near transition state structures and along the potential energy curve's shoulders. These peaks not only underline a new interpretation of transition states from an electronic perspective but also highlight asynchronous reaction processes that are not readily apparent in traditional potential energy analyses. The robustness and universality of the NRO-based reaction analysis make it a promising tool for broad and fundamental reaction analyses grounded in electronic theory. This approach is poised to offer

insightful perspectives on reaction mechanisms, potentially standardizing reaction analysis within the electronic theory framework.

In the presentations, I will introduce the methodologies of the ReSPer and NRO techniques and provide several demonstrations of their applications.

Significance

This presentation will highlight innovative new approaches for analyzing the elementary processes of chemical reactions through quantum chemical calculations and dimension reduction techniques. In ReSPer, the reaction path network is projected into a reduced-dimensionality reaction space. Dynamic trajectories are also projected into this reaction space, allowing for the extraction of dynamic routes within the reaction path network. In NRO, the movement of electrons along the reaction path is depicted through a pair of occupied and virtual NROs, allowing for the identification of regions where bond rearrangement or electron transfer occurs.

References

1. Maeda, S., Harabuchi, Y., Ono, Y., Taketsugu, T., and Morokuma, K. *Int. J. Quantum Chem.* 115, 258 (2015).
2. Maeda, S., Harabuchi, Y., Takagi, M., Taketsugu, T., and Morokuma, K. *Chem. Rec.*, 16, 2232 (2016).
3. Tsutsumi, T., Ono, Y., Arai, Z., and Taketsugu, T. *J. Chem. Theory Comput.*, 14, 4263 (2018).
4. Tsutsumi, T., Ono, Y., Arai, Z., and Taketsugu, T. *J. Chem. Theory Comput.*, 16, 4029 (2020).
5. Tsutsumi, T., Ono, Y., and Taketsugu, T. *Chem. Commun.* 57, 11734 (2021).
6. Tsutsumi, T., Ono, Y., and Taketsugu, T. *Top. Curr. Chem. (Z)*, 380, 19 (2022).
7. Tsutsumi, T., Ono, Y., and Taketsugu, T. *J. Chem. Theory Comput.*, 2022, 18, 7483.
8. Ebisawa, S., Hasebe, M., Tsutsumi, T., Tsuneda, T., and Taketsugu, T. *Phys. Chem. Chem. Phys.* 24, 3532 (2022).
9. Ebisawa, S., Tsutsumi, T., and Taketsugu, T. *J. Chem. Phys.* 157, 084118 (2022).

Oxide and sulfide-based catalysts for CO_2 reduction to methanol

Sergey M. Kozlov[1*]

[1]*Department of Chemical and Biomolecular Engineering, College of Design and Engineering, National University of Singapore, Singapore 119260, Singapore*

*sergey.kozlov@nus.edu.sg

Introduction

Annual production of methanol through CO_2 and CO hydrogenation currently exceeds 100 million metric and is expected to increase further since methanol is considered a promising green fuel. Cu-ZnO catalysts are most commonly used for methanol synthesis in industry, although they suffer from rapid agglomeration of Cu particles in the presence of water produced during CO_2 hydrogenation. As a result, significant scientific attention is focused on improving Cu-ZnO catalysts for methanol synthesis or developing alternatives for them.

Methodology

In this talk, I will discuss our recent studies combining experiments and density functional (DFT) simulations exploring how the engineering of the nanostructure of catalysts can help improve their activity in CO_2 reduction. In our computational approach, we devote particular attention to the generation of realistic catalyst models that are in equilibrium with the reaction environment and accurately reflect the nanostructuring of the catalysts in experimental studies.

Results and Discussion

In particular, I will show how designing nanoreactors based on mesoporous silica can help stabilize highly active CuZn alloy nanoparticles as small as 2 nm under methanol synthesis conditions [1]. Besides the presence of the alloy phase, Cu-ZnO catalysts are known to develop during ZnO overlayers on Cu surfaces during the catalytic reaction. In this presentation, I will discuss how the interactions between Cu and ZnO overlayers alter the electronic structure of the latter and make them more active in hydrogenation reactions [2].

$ZnZrO_x$ was proposed as a much more stable and selective catalyst for CO_2 hydrogenation to methanol, despite their lower activity. Our recent studies show that the activity of $ZnZrO_x$ can be increased by doping them with Pd single atoms [3]. Curiously, our simulations show that Pd single atoms do not participate in CO_2 hydrogenation directly, but rather facilitate the dissociation of H_2 molecules on the $ZnZrO_x$ surface. Moreover, our simulations revealed that the slow rate of diffusion of H atoms on the $ZnZrO_x$ surface limits their availability at the active sites for CO2 reduction to methanol. To address this problem, we proposed engineering a distribution network for H atoms in the form of carbon nanotubes (CNT) inside the catalyst [4]. The methanol yield on the obtained $PdN/CNT/ZnZrO_x$ was shown to be 3 times higher than on $Pd_1/ZnZrO_x$ and 8 times higher than on pristine $ZnZrO_x$.

Finally, I will discuss our recent studies of CO_2 reduction to methanol on MoS2-based catalysts [5]. In this study, we fabricate MoS_2 nanospheres without highly active but unselective edge sites through the sulfidation of molybdenum oxide particles. The curved morphology of the produced MoS_2 spheres induces strain in the active sites and makes them more active in CO_2 reduction or facilitates their regeneration under catalytic conditions. Moreover, we show how MoS_2 catalysts with monolayer thickness are more active in methanol production compared to multilayer catalysts due to altered active site structure [6].

Significance

The presented studies highlight how DFT simulations can help the understanding of chemical processes on heterogeneous catalysts and facilitate the rational design of catalysts for societally important reactions. They also illustrate how nanostructuring of catalysts can be considered in DFT simulations and its importance for the activity of applied catalysts.

References

1. Kosari, M., Anjum, U., Xi, S., Lim, A. M. H., Seayad, A. M., Raj, E. A. J., Kozlov, S. M., Borgna, A., Zeng, H. C. *Adv. Funct. Materials.* 31, 2102896 (2021).
2. Song, Y., Mendes, P. C. D., Kozlov, S. M. *J. Mater. Chem. A* 11, 13665 (2023).
3. Lee, K., Anjum, U., Araújo, T. P., Mondelli, C., He, Q., Furukawa, S., Pérez-Ramírez, J., Kozlov, S. M., Yan, N. *Appl. Catal. B: Environ.* 304, 120994 (2022).
4. Lee, K., Mendes, P. C. D., Jeon, H., Song, Y., Dickieson, M. P., Anjum, U., Chen, L., Yang, T.-C., Yang, C.-M., Choi, M. et al. *Nat. Commun.* 14, 819 (2023).
5. Zhou, S., Ma, W., Anjum, U., Kosari, M., Xi, S., Kozlov, S. M., Zeng, H. C. *Nat. Commun.* 14, 5872 (2023).
6. Zhou, S., Ma, W., Kosari, M., Lim, A. M. H., Kozlov, S. M., Zeng, H. C. *Appl. Cat. B* 349, 123870 (2024).

Understanding the Impact of Electrolyte Anions on Single Metal Atom Coordinated N-Doped Carbon for ORR and CO$_2$RR

Tipaporn Patniboon[1]* and Heine Anton Hansen[2]
[1]Faculty of Science, Mahasarakham University, *Maha Sarakham, Thailand*
[2] *Department of Energy Conversion and Storage, Technical University of Denmark, Denmark*
*tipaporn.p@msu.ac.th

Introduction

The single metal atom coordinated N-doped carbon (M/N/C) is a highly efficient electrocatalyst with two-dimensional properties, allowing for adsorption on one side while the other remains available for reaction. This adsorption modifies electronic states, affecting catalytic activity and stability. Investigating how electrolyte anions impact stability and activity informs the design of stable, active catalysts. In this study, we explore the effect of electrolyte anion adsorption on single metal atoms incorporated into graphene for ORR and CO$_2$RR, suggesting optimal combinations for catalyst performance [1, 2].

Methodology

Density functional theory (DFT) calculations were conducted using the Vienna ab initio simulation package (VASP). The projector augmented wave (PAW) method described core electrons, while a plane-wave basis with a kinetic energy cutoff of 600 eV defined valence electrons. The BEEF-vdW functional accounted for exchange and correlation energies. Solvent effects were considered during relaxation, utilizing implicit solvation with a water medium dielectric constant through VASPsol. A dipole correction perpendicular to the catalyst surface was applied to decouple electrostatic potentials. Brillouin zone sampling employed a 3x3x3 Monkhorst Pack k-point mesh. Stability under electrochemical conditions was thermodynamically assessed by evaluating the likelihood of metal center atom dissolution from M/N/C structures [3]. Reaction free energies for ORR and CO$_2$RR steps were calculated based on adsorbate adsorption energies. Catalytic activity was approximated using the computational hydrogen electrode (CHE) model [4].

Results and Discussion

During the Oxygen Reduction Reaction (ORR), different electrolyte anions can vie with water for adsorption on the single metal site, influenced by the metal atom's nature and the local carbon structure surrounding it. This anion adsorption can either poison or modify ORR activity. When an electrolyte anion adsorbs on the single metal site, it can enhance stability against dissolution in acidic environments compared to pure water. Considering both acid stability and ORR activity, single metal sites based on Ir, Cu, Rh, Zn, Au, Os, Cr, and p-block elements (Sb, Sn, and Bi), particularly on graphene edges, exhibit comparable ORR performance and stability to those based on Fe and Co. In the Carbon Dioxide Reduction Reaction (CO$_2$RR), most electrolyte anions don't interact with single metal sites, but water and gas molecules can form ligands. Interestingly, the reduction activity of CO2 to CO on single metal sites with ligands from the solution aligns with experimental trends. Apart from Fe, Co, Mn, and Ni-based single-atom catalysts, promising single metal sites (Cr, Ru, W, Re, Os, Rh, Bi, Sb, Mo, Zn, and Ir) are suggested, considering the adsorbate ligand from the solution.

Significance

In ORR, electrolyte anions compete with water for the metal site, stabilizing it. In CO2RR, they're less involved, but water and gas affect activity. By considering stability and activity, we can suggest effective electrolyte-metal pairings for durable catalysts in both reactions.

References

1. Tipaporn Patniboon and Heine Anton Hansen, *ACS Catalysis* **2021** *11* (21), 13102-13118
2. Tipaporn Patniboon, Heine Anton Hansen; Effects of electrolyte anion adsorption on the activity and stability of single atom electrocatalysts. *Chem. Phys. Rev.* 1 March 2023; 4 (1): 011401.
3. Edward F. Holby, Guofeng Wang, and Piotr Zelenay, *ACS Catalysis* **2020** *10* (24), 14527-14539
4. J. K. Nørskov, J. Rossmeisl, A. Logadottir, L. Lindqvist, J. R. Kitchin, T. Bligaard, and H. Jónsson, *The Journal of Physical Chemistry B* **2004** *108* (46), 17886-17892

Machine-Driven Explore the Distribution of Active Site on Catalyst

Pengju Ren[1,2]*, Hui Yang[1,2], Rongrong Jin[2,3], Xueqian Pang[1,2], James P. Lewis[1,2,4] , Yong- Wang Li,[1,2] and Xiao-Dong Wen[1,2]

[1]Institute of Coal Chemistry, Chinese Academy of Sciences, Taiyuan, 030001 (China)
[2]Synfuels China Co., Ltd, Beijing, 101400 (China)
[3]Beijing University of Chemical Technology, Beijing, 100029, China (China)
[4]Hong Kong Quantum AI Laboratory, Ltd., Hong Kong (China)
*renpengju@synfuelschina.com.cn

Introduction

The rational design of catalysts relies on a deep understanding of the structure-activity relationship. Obtaining the activity distribution on the catalyst surfaces is essential to gain the quantitative structure-activity relationship of catalysts. Characterizing and recognizing the structure of active centers are the main targets of fundamental research in catalysis, which remains great challenges both for experimental and theoretical researches. One of the main challenges is the diversity and inhomogeneity of surface sites. Even the well-defined model surfaces may also possess multiple distributions of reaction sites and may change due to surface fluctuation under different reaction conditions. The essence of the problem of surface activity distribution is statistical sampling. The ML-driven adequate sampling (MLAS) method, was developed for comprehensive analysis of the site chemical environment and activity distribution on surface, including both the adsorption and transition state. Various ML-based strategy algorithms and surface characteristics were adopted to greatly improve the efficiency of the entire process.

Methodology

The ML algorithms, such as K-Means for clustering, PCA analysis for reducing dimensionality, Gaussian Process Regression, were all carried out by scikit-learn package. The overall workflow for MLAS starts from sampling space definition through decomposition of degrees of freedom based on the symmetry analysis of surface and reactants. And then perform clustering analysis on the vector representation of the chemical environment of sites transformed from Cartesian coordinates. Then, the initial sampling process is performed based on the clustering results, followed by constraint optimization to obtain the minimum energy for adsorption or transition state at sampled site. The following GPR analysis gives the regression functions and error distribution. Based on the error distribution, the supplementary sampling and GPR process will be further iteratively performed until the setting criteria are reached. All electronic structure and geometry optimization were calculated by VASP and ASE.

Results and Discussion

This MLAS method was applied to the N2 activation process, the most important step in NH3 synthesis, to revisit the active centers and the activity distribution over the Ru catalyst surfaces. This activity distribution heat-map and the activity population function provide holistic understanding of active centers beyond the estimation from a few special sites (Fig. 1). This approach can be applied to other more complicated catalyst materials and reaction networks, such as interfaces and defects surfaces, and can be strengthened and extended with advanced sampling and potential energy surface exploration methods.
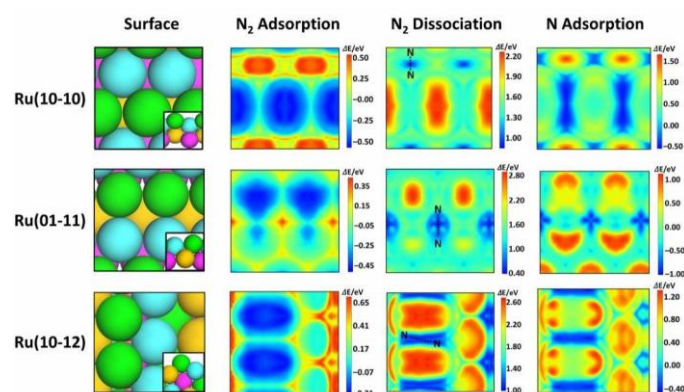
Figure 1. Structures of Ru facets and energy distributions for adsorption and transition state.

Significance

We developed the extensible ML-driven adequate sampling method for highly efficient active site sampling on catalyst surface, which can generate activity distribution and provide *holistic* understanding of active centers beyond the estimation from few special sites.
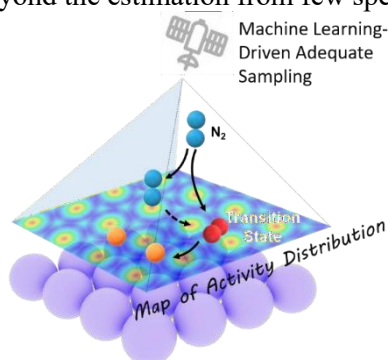

Figure 2. Activity distribution of N2 activation by MLAS on Ru catalyst.

References

1. Yang, H., Ren, P., et al. *J. Phys. Chem. Lett.* 15, 4384 (2024).
2. Lewis, J. P., Ren, P., et al. *Front. Quantum. Sci. Technol.* 2, 1232903 (2023).

From Molecules to Mechanisms: Leveraging Simcenter Culgiand Simcenter STAR-CCM+ for Comprehensive EngineeringSimulations

Tanongsak Sukkasem [1*], Walaikorn Wongpramot [1]

[1]*Digital Transformation Engineering Co., ltd., Chamnan Phenjati Business Center Building Floor 23, Huaykwang, Bangkok 10320, Thailand*
*tanongsak@dtethai.com

Introduction

In the rapidly evolving landscape of engineering and scientific research, the ability to accurately simulate complex systems is paramount. From the molecular-level interactions that govern material properties to the intricate mechanisms of macroscopic systems, comprehensive simulations offer invaluable insights that drive innovation and enhance efficiency. Simcenter Culgi and Simcenter STAR-CCM+ stand at the forefront of this technological frontier, providing robust platforms for detailed and integrated simulations. These tools enable researchers and engineers to bridge the gap between molecular phenomena and large-scale mechanical processes, ensuring a thorough understanding and optimization of various engineering challenges.

Simcenter Culgi excels in molecular modeling and computational chemistry, offering advanced capabilities for simulating molecular dynamics, quantum chemistry, and materials science. Its sophisticated algorithms allow for the exploration of molecular interactions, reaction mechanisms, and material behavior at the atomic scale. On the other hand, Simcenter STAR- CCM+ is renowned for its powerful computational fluid dynamics (CFD) and multiphysics simulation capabilities, enabling the analysis of fluid flow, heat transfer, and structural mechanics in complex geometries.

Together, these tools provide a seamless integration of molecular-level insights with macro-scale engineering simulations, creating a comprehensive framework for tackling multifaceted engineering problems. This paper explores the synergistic capabilities of Simcenter Culgi and Simcenter STAR-CCM+. Through detailed case studies and practical examples, we will demonstrate how leveraging these advanced simulation platforms can lead to groundbreaking discoveries, optimized designs, and accelerated product development, ultimately driving the next generation of engineering innovation.

Methodology

- *Simcenter Culgi software*
- *Simcenter STAR-CCM+*

Result and Conclusion
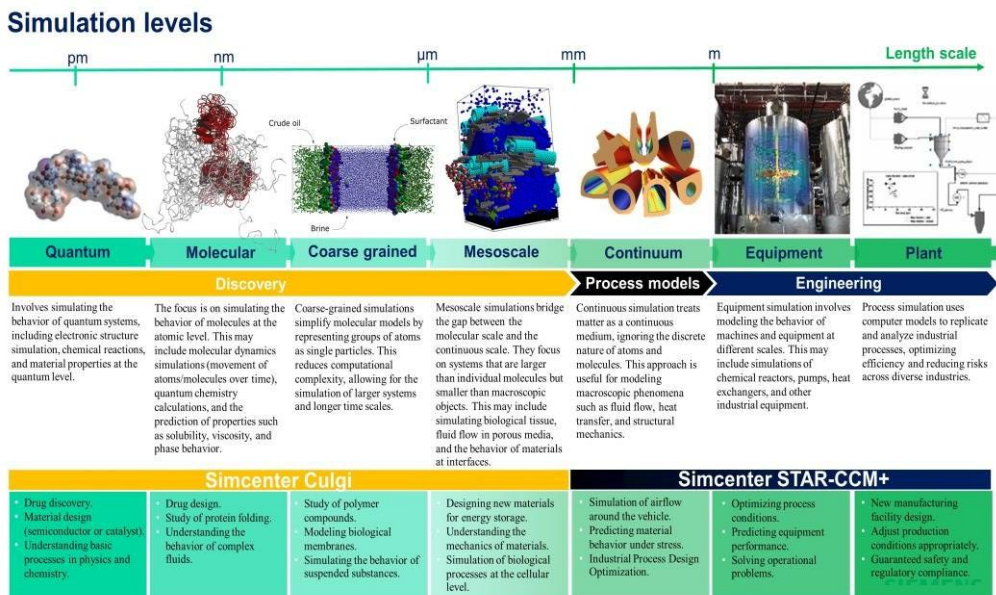
Understanding the impact of promoter induced restructuring in metal nanoparticles on methylcyclohexane dehydrogenation.

Asmee M. Prabhu[1], Chuhong Lin[1], and Tej S. Choksi[1]*
[1]Nanyang Technological University, Singapore, 637459 (Singapore)
*tej.choksi@ntu.edu.sg

Introduction

Central to the affordability and success of liquid organic hydrogen carriers is the search for a dehydrogenation catalyst that selectively dissociates the C-H bonds while preserving the C-C bonds. Dehydrogenation selectivity is increased using p-block promoters like sulphur. These promoters sterically block & electronically modify the certain active sites. Hence, it is necessary to establish the type of active sites blocked by promoters, and whether promoters alter nanoparticle morphologies. Equilibrium morphologies of promoted nanoparticles are determined by Wulff constructions- which require surface energies of promoter-decorated crystal planes as inputs. Computing the surface energies of these promoter-decorated crystal planes with density functional theory is challenging because of the large configurational space, especially at high promoter coverages. We present a surrogate model to estimate the surface energies of arbitrary (hkl) planes decorated with promoters and hence predict equilibrium morphologies of promoted nanoparticles on-the-fly. Further, due to trade-offs between selectivity and reactivity in these promoted nanoparticles, there is a need to systematically screen different promoters and determine how their coverage influences reaction rates & selectivity. Using our surrogate model combined with a micro-kinetic model for methylcyclohexane (MCH) dehydrogenation on S*-Pt nano-catalysts, we determine effect of S* coverage on the rate & selectivity to toluene (TOL).

Methodology

DFT calculations were performed using Quantum ESPRESSO in the Atomic Simulation Environment. Core electrons were represented by Vanderbilt ultra-soft pseudopotentials. Self-consistent total energies were determined using the PBE-D3 functional at a plane-wave energy cutoff of 500 eV and a density cut-off of 5000 eV.

Results and Discussion

The surface energy in the presence of adsorbates (Ω) is deconstructed into contributions from the metal-metal interactions, metal-adsorbate interactions, adsorbate-adsorbate interactions, and temperature/pressure terms. Instead of DFT calculations, we employ surrogate models to estimate each term in, thus yielding Ω on-the-fly. Surface energies of bare Pt slabs are predicted using coordination-based models like the alpha-scheme. Adsorption energies of S* at infinite separation, on active sites of arbitrary coordination numbers are estimated by site-specific scaling relations. To account for S*-S* interactions we employ a pair-wise interaction model inspired by prior studies. With this framework in place, we determine Ω for all possible S* coverages and configurations on the (111), (100), and (211) surfaces (**Figure 1a**). We input the Ω values of the most stable S* coverage and configuration on each (hkl) facet to generate Pt Wulff nanoparticles having different diameters. By tracking the densities of edge (unselective) and terrace (selective) sites before and after promoter adsorption, we verify that promoters introduce morphological changes altering the surface densities of selective and unselective active sites (**Figure 1b**). To analyze the effect of S* on reactivity, we map out the potential energy surface of MCH dehydrogenation species across the most stable active sites on Pt-55 CUBO clusters and S*-Pt-55 clusters. We observe that the elementary reaction barriers relatively lower compared to TOL desorption (**Figure 1c**). Next, we compare microkinetic models for MCH dehydrogenation on bare Pt vs S*-Pt to determine the enhancement in rate and selectivity per mass of Pt in the presence of promoters.

Significance

We present a surrogate model to determine the morphology of nanoparticles modified by promoters. Using potential energy diagrams, we identify the most stable reaction pathways and subsequently build to microkinetic models, to determine the change in reaction kinetics in the presence of promoters. Our

approach for improving the selectivity of nano catalysts is transferable to reactions beyond MCH dehydrogenation where competition between product desorption and secondary reactions exist.
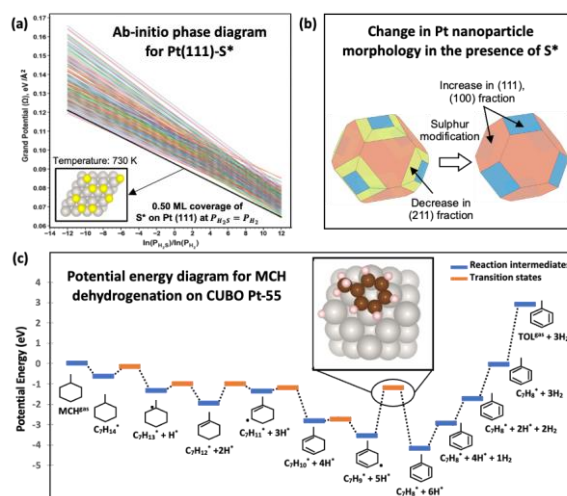

Figure 1. **a.** Ab-initio phase diagram for S*-Pt (111) surface using the surrogate model **b.** Change in S*-Pt nanoparticle morphology **c.** Potential energy diagram for MCH dehydrogenation to TOL on CUBO Pt-55.

References

1. Prabhu, A. M., and Choksi, T. S. *J. Phys. Chem. C* https://doi.org/10.1021/acs.jpcc.3c08106 (2024).

Advancing Molecular Design: Uncertainty-Integrated Optimization for Enhanced Prediction

Lung-Yi Chen,[1] Chu-I Yang,[1] and <u>Yi-Pei Li</u> [1,2]*

[1]*Department of Chemical Engineering, National Taiwan University, No. 1, Sec. 4, Roosevelt Road, Taipei 10617, Taiwan.*
[2] *International Graduate Program on Sustainable Chemical Science and Technology (TIGP-SCST), No. 128, Sec. 2, Academia Road, Taipei, 11529, Taiwan.*
*yipeili@ntu.edu.tw

Introduction

The effectiveness of machine learning models in molecular property prediction is often limited by the noisy and limited training data. To overcome these challenges, this study presents innovative algorithms that incorporate uncertainty quantification (UQ) methods into both single- and multi-objective optimization tasks, allowing for more robust and accurate molecular design processes. Moreover, an explainable UQ framework further attributes uncertainty to specific atoms, providing deeper chemical insight and refining confidence intervals.

Methodology

Utilizing the Tartarus platform,[1] which enables physical validation of molecular properties, this study rigorously compares UQ-integrated optimization methods with traditional approaches. Surrogate models like the direct message-passing neural network (D-MPNN)[2] predict molecular properties, while UQ techniques such as deep ensembles and evidential learning quantify aleatoric and epistemic uncertainties. These UQ methods guide genetic algorithms and other optimization strategies in various design tasks involving organic emitters, protein ligands, and reaction substrates. As shown in Figure 1, to further improve the interpretability of the model, we propose an explainable UQ framework, which offers a novel approach to attribute uncertainty at the atomic level, identifying specific chemical components prone to prediction noise. This model also introduces a post-hoc calibration method to fine-tune the confidence intervals and improve calibration.

Results and Discussion

The UQ-integrated optimization tasks significantly improve property distributions compared to traditional approaches when surrogate models are properly calibrated. In single-objective optimization tasks, the models with well-calibrated uncertainties consistently produced enhanced property distributions. However, poor calibration reduced the benefits of UQ integration. For multi-objective optimization, the UQ-guided approach strategically directed exploration to meet specific application thresholds, improving the reliability and robustness of the design process as listed in Table 1. The explainable UQ framework, with its atomic-level analysis, effectively identifies unseen chemical structures and chemical species prone to noise. The post-hoc calibration further enhances confidence intervals and provides a reliable attribution method.

Table 1. Comparison of top-k hit rates for multi-objective optimization results across various methods.

Dataset	Method	Top-10 hit rate	Top-50 hit rate	Top-100 hit rate
Organic emitters	Weighted sum	0	0	0
	Manhattan	0.60	0.36	0.35
	Hybrid	0	0.20	0.29
	Uncertainty	0.80	0.56	0.36
Reaction substrates	Weighted sum	0.20	0.08	0.07
	Manhattan	0.10	0.10	0.10
	Hybrid	0.40	0.16	0.11
	Uncertainty	0.40	0.22	0.22

Significance

This work advances computational molecular design by embedding UQ into the optimization framework, making uncertainty a strategic component rather than a minimizable factor. Incorporating UQ enhances predictive reliability and aligns closely with practical, real-world application demands. The explainable UQ model provides a deeper understanding of uncertainties at a granular level, allowing for accurate identification and refinement of high-risk areas. These findings mark a significant leap in computational-aided molecular design (CAMD) methodologies, paving the way for more robust optimization strategies and accurate predictions across a range of scientific disciplines.
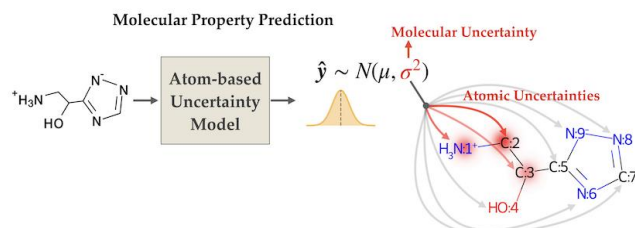
Figure 1. An explainable UQ method for deep learning-based molecular property prediction. This atom-focused UQ approach offers an additional layer of chemical insight into estimated uncertainties. By analyzing individual atomic uncertainty values, it allows for the identification and diagnosis of specific chemical components contributing to prediction uncertainty.[3]

References

(1) Nigam, A.; Pollice, R.; Tom, G.; Jorner, K.; Willes, J.; Thiede, L. A.; Kundaje, A.; Aspuru-Guzik, A. arXiv October 11, 2023.
(2) Heid, E.; Greenman, K. P.; Chung, Y.; Li, S.-C.; Graff, D. E.; Vermeire, F. H.; Wu, H.; Green, W. H.; McGill, C. J. *J. Chem. Inf. Model.* **2024**, *64* (1), 9–17.
(3) Yang, C.-I.; Li, Y.-P. *J. Cheminformatics* **2023**, *15* (1), 13.

Theoretical and Computational Study on Heterogeneous Interfaces Under Light and Voltage Bias

Kenji Iida[1]

[1]*Institute for Catalysis, Hokkaido University, Sapporo, 001-0019 (Japan)*
k-iida@cat.hokudai.ac.jp

Introduction

Heterogeneous interfaces between nanoparticles and surrounding materials have been extensively investigated to develop photo and electrode catalysts. For example, the interface region between a noble metal nanoparticle and a semiconductor reportedly facilitates the plasmon induced electron transfer. The electric double layer (EDL) between a heterogeneous electrode-catalyst and an electrolyte solution often governs the electrode catalysis. Therefore, the atomic-scale insights into the interface regions are required. However, it is difficult to apply theoretical methods to these complex systems because of the large computational cost.

We have performed first-principles simulation of the photoinduced electron dynamics of nanomaterials using the SALMON program[1,2] and have revealed the novel mechanism of optical response governed by the interface region.[3,4] We have also developed a theoretical and computational method in which a heterogeneous material is calculated with SALMON and the solvation effect is evaluated using a statistical mechanical theory for molecular liquids (3D-RISM). The developed method has been applied to complex solid-liquid interfaces under light and voltage bias.[5,6]

Methodology

In the SALMON program, the 3D grid points are used as the basis set for the DFT calculation. Because of the simple algorithm, the program has high parallel efficiency and can be applied to nanomaterials. The solvation effect is evaluated using 3D-RISM theory, which is an analytical formula for molecular liquid and can be applied to dilute electrolyte solutions. After the ground state electronic structure is obtained, the photoexcited electron dynamics is simulated using the real-time time-dependent Kohn-Sham equation.

Results and Discussion

Recent studies have indicated that interface states between a noble metal nanoparticle and semiconductor can facilitate the plasmon induced electron transfer. In this context, we investigated the photoexcited charge transfer at the interface between TiO_2 and an Ag nanocluster. Figure 1 shows the change in the electron occupation number by photoexcitation of a heterostructure consisting of an Ag_{20} nanocluster and TiO_2. The z-direction is perpendicular to the TiO_2 surface, and the horizontal direction is the band energy relative to the Fermi level. The red and blue distributions indicate that the occupation numbers are greater and less than those in the ground state, respectively. In the Ag_{20} moiety (z > 13 Å), the electron occupation is not found in the conduction band, indicating that the excited electrons directly transfer from Ag_{20} to TiO_2 without passing through the conduction band of Ag_{20}. We revealed that the photoinduced electronic interaction at the interface region governs the direct electron transfer.[3]

We have further investigated the solvation effect on the photoexcitation of nanomaterials because protic solvents are widely used for photocatalysts and cause local intermolecular interactions such as hydrogen bonding. Figure 2 shows the carrier density distribution of an Au_{147}-H_2O complex after the 2.3 eV laser irradiation. The yellow and green distributions indicate that the electron density increases and decreases by photoexcitation, respectively. In the H_2O moiety adsorbed on the top of Au_{147}, the carrier density decreases owing to the electron transfer from H_2O to Au_{147}. By analyzing the solvation structure, we showed that the electron transfer was enhanced by the microscopic hydration.[5]

The developed method can also be applied to electrochemical systems. Recent studies address to develop complex electrode-catalysts, for instance, used in fuel cells.[7] However, it is difficult to understand the atomic-scale details of a heterogeneous EDL between an electrolyte solution and a complex electrode catalysis. Therefore, using the developed method, we investigated an EDL between a Pt_{13}-graphite heterostructure and a 1 M KCl aqueous solution to reveal the EDL structure. Figure 3 shows the color map of the density distribution of Cl^- near the positively charged heterostructure. The heterogeneous distribution indicates that the EDL structure is governed by the atomic-scale details of the surface structure.[6]
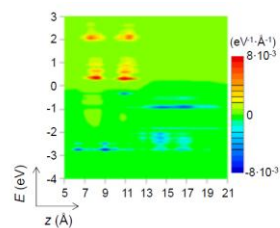
Figure 1. Change in the electron occupation number by photoexcitation of an Ag_{20}-TiO_2 heterostructure.[3]
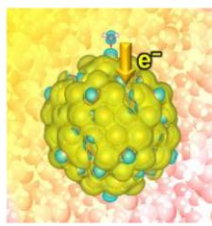

Figure 2. Carrier density distribution of an Au_{147}-H_2O complex in aqua by photoexcitation.[5]
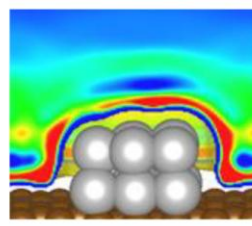

Figure 3. The density distribution of Cl^- near the Pt_{13}-graphite surface.[6]

Significance

We have investigated the response of heterogeneous interfaces to light and voltage bias using our original theoretical and computational method and have revealed the novel mechanisms governed by the atomic-scale details of the interface region. The direct electron transfer revealed in this study is, for instance, valuable for improving the efficiency of light-energy conversion. Our method can be applied to nanomaterials that are too large to calculate with a conventional theoretical method, and thus, is expected to contribute to understanding and designing of their optical and electrochemical properties.

References

1. Noda, M., et al., *Comput. Phys. Commun.* 235, 356 (2019).
2. Iida, K., Noda, M., Ishimura K., Nobusada, K. *J. Phys. Chem. A* 118, 11317 (2014).
3. Iida, K., Noda, M. *NPJ Comput. Mater.* 6, 5 (2020).
4. Takekuma, H. et al., *Adv. Sci.* e2307055 (2024).
5. Iida, K., *J. Phys. Chem. C* 126, 7492 (2022).
6. Iida, K., *J. Phys. Chem. C* 126, 9466 (2022).
7. Kawawaki, T. et al., *Nanoscale*, 15, 7272 (2023).

Molecular Property Prediction Using the Featurized Low-Dimensional Representations with Message Passing Neural Network Framework

Ming-Kang Tsai[1]*

[1]*Department of Chemistry and Intelligent Computer for Sustainable Development Research Center, National Taiwan Normal University, Taipei, Taiwan (ROC)*
*mktsai@ntnu.edu.tw

Introduction

Organic fluorescent molecules play the critical roles in the fluorescence inspection, biological probes, and labeling indicators. Learning the design principle of these molecular architectures always attracts the scientific interests of the synthetic and theoretical communities. In this talk, two tasks of predicting molecular electronic properties will be demonstrated using 10k-plus real world experimental and 100k-plus theoretical datasets, being represented by the chemical knowledge or physical structural information. An assessment of modifying the SchNET models for the predictions of molecular electronic properties, including absorption energy (ΔE_{abs}), emission energy (ΔE_{emi}), and photoluminescence quantum yield (PLQY), is reported. The sample molecules are embedded through the low-dimensional bondstep representation for the purpose of accelerating the dataset preparation. The solution environment is properly introduced outside the interaction layers of SchNET. Two featurization schemes under the framework of the Schnet-bondstep approach, with featuring the concepts of reduced-atomic-number and reduced-atomic-neighbor, will be demonstrated.

Methodology

We combined the low-dimensional bondstep representation and the reduced atomic number (RAN) featurization scheme for describing the complex atom connectivity in the dataset of organic fluorescent molecules. Bondstep representation does not require the prerequisite information of atomic coordinates, and can be simply derived from SMILES files based upon the valence bond theory. The RAN featurization scheme provides the functionality of learning the neighboring electronic effect. Incorporating the bondstep and RAN into message-passing type SchNET model can well capture the electronic energetics between HOMO and LUMO orbitals. Solvation effect was introduced to bypass the interaction blocks and fused to the molecular contribution before atom-wise decomposition for appropriately balancing the ratio of molecule/environment contributions to determine the experimental observables.

Results and Discussion

Two datasets – QM9 and deep4chem are investiagted using the modified SchNET-bondstep approaches. These featurized models can consequently provide fine predictions for experimental ΔE_{abs} and ΔE_{emi} with errors less than 0.1 eV. The corresponding predictions of PLQY (log scale Φ) are shown to be comparable to the published graph convolution network model with the root-mean-square-error at < 0.4. The introduction network scheme for the solvation effect also provides the distinguishable behavior in terms of electronic adsorption vs. electronic emission.

Table 1. Mean-absolute-error (in eV) and R2 values of testing sets using QM9 and deep4chem datasets

QM9	E_H	E_L	ΔE_{HL}
Original SchNET	0.041 (NA)	0.034 (NA)	0.063 (NA)
redo Schnet	0.051 (*0.985*)	0.041 (*0.998*)	0.076 (*0.992*)
Schnet-bs-RANe	0.070 (*0.969*)	0.069 (*0.993*)	0.097 (*0.986*)
deep4chem	ΔE_{abs}	ΔE_{emi}	**logΦ**
Schnet-bs-sol	0.083 (*0.942*)	0.084 (*0.903*)	0.324 (*0.630*)
Schent-bs-RANe	0.079 (*0.946*)	0.080 (*0.908*)	0.263 (*0.718*)

[1]R2 values are reported in parentheses.

Significance

These studies provide a systematic demonstration of using low-dimensional bondstep representation and chemical knowledge based featurization methods for quantitatively predicting the complicated molecular electronic properties. Such an approach can be efficiently used for the high throughput screening on the discovery of new organic fluorescent molecules.
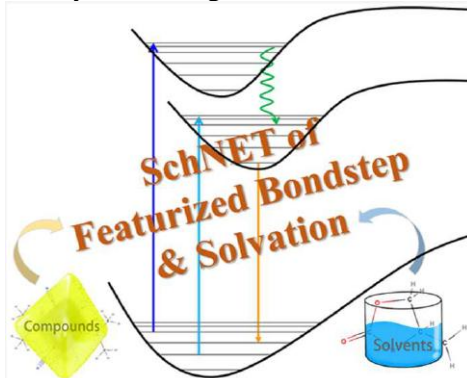

Figure 1. The schematic representation of featured SchNET models for molecular electronic properties predictions.

References

1. Ye, Z.-R., Hunag, I-S., Chan, Y.-T., Li, Z.-J., Liao, C.-C., Tsai, H.-R., Hsieh, M.-C., Chang, C.-C., Tsai, M.-K., *RSC Adv.* 10, 23834-23841 (2020).
2. Ye, Z.-R., Hung, S.-H., Chen, B.,Tsai, M.-K., *ACS Engineering Au*, 2, 360-368 (2022).
3. Hung, S.-H., Ye, Z.-R., Cheng, C.-F., Chen, B., Tsai, M.-K. *J. Chem. Theory Comput.* 19, 4559-4567 (2023).

Influence of vibronic interaction of charge transfer excitons in nonfullerene organic solar cells

Azusa Muraoka[1]*
[1] Japan Women's University, 2-8-1, Mejirodai, Bunkyo-ku, Tokyo, 1128681 (Japan)
*muraokaa@fc.jwu.ac.jp

Introduction

Organic thin-film solar cells consist of acceptor (A) molecules and donor (D) molecules that transport electrons and holes generated by photoabsorption to electrodes. Recently, nonfullerene organic thin-film solar cells (OSCs) with π-conjugated small molecules or polymers as acceptors have attracted attention because of their highly visible light absorption efficiency in the D/A active layer and their effectiveness in increasing the short-circuit current. When an electron in a donor or acceptor molecule absorbs light, it is excited to a higher energy level, leaving behind a positively charged hole. The electrons and holes combine via the Coulomb force to form excitons. The excitons diffuse to the D/A junction interface, and the diffused excitons dissociate into free charge carriers (electrons and holes). The generated free charge carriers are transported toward the electrode and extracted from the external circuit. Therefore, efficient exciton dissociation into separated free carriers leads to an increased photocurrent, enhancing the power conversion efficiency (PCE) of OSCs when considering higher efficiency. The dynamic process of excitons at the D/A interface is crucial, and it is important to clarify the formation and dissociation of excitons and the diffusion process of free carriers[1]. Two hypotheses have been proposed for the process by which photo-induced excitons generate free carriers (electrons and holes). One is the "cool process," in which the excitons generated on the D-side relax to the charge transfer (CT) state at the D/A interface, and the CT state is thermally unbound to generate a charge-separated (CS) state or free carrier; the other hypothesis is the "hot process" in which the exciton does not relax in the CT state at the D/A interface and generates directly free carriers.

Methodology

We investigated the charge dissociation process of excitons in nonfullerene OSCs with BTAx (x = 1 and 3), a nonfullerene acceptor molecule, and PTB7, a typical polymer donor molecule with high external quantum efficiency in a bulk heterojunction structure, using DFT. The electronic structure and electron–hole distance of CT excitons in the excited states of the D/A complexes were analyzed using time-dependent DFT (TD-DFT) calculations, ωB97XD/6-31G(d). We calculated the excitation energy transfer (EET) in the photoexcited initial state and analyzed the nonadiabatic processes owing to the vibronic interaction in the CT exciton state and the structurally relaxed electron–hole polaron paired CT state. From this point of view, we focus on the Huang–Rhys (HR) factor, which indicates the strength of the exciton–phonon coupling and nonadiabatic processes.

Systematic theoretical analysis of the D/A complex will provide insights into the dynamics of CT excitons, that is, the role of vibronic interactions in CT exciton states with respect to the selectivity of hot and cool processes, as well as the control of short-circuit current density and electron–hole recombination.

Results and Discussion

Focusing on the PTB7/BTA1 and PTB7/BTA3, we compared the theoretical results for the excitation energy transfer and CT distance for PTB7/BTAx (x = 1 and 3) with experimental reports. We show the absorption spectra of both PTB7/BTA1 and PTB7/BTA3 complexes. This indicates that in both complexes, only the A-A transition is present at 450 nm, but the oscillator intensities at other wavelengths are dominated by the D-D and D-A transitions. Structural optimization of the excited states of the D/A complex showed that PTB7/BTA3, which had a higher short-circuit current density, also had a larger CT distance and electron coupling, whereas PTB7/BTA1, which had a lower short-circuit current density, had a larger CT distance and greater electron coupling. While comparing PTB7/BTA1 and PTB7/BTA3, electron–hole distance is larger for PTB7/BTA3, which had more D/A transitions. PTB7/BTA1, with a Jsc, has a larger HR factor because of the low-wavenumber vibrational modes in the CT state of the D/A complex and might undergo nonadiabatic relaxation to the ground state.

We found that the Frenkel exciton generated on the D-side becomes a CT exciton at the interface, and its size, that is the electron–hole distance[2], is correlated with the conversion efficiency of organic

solar cells with higher PCE. We also consider that the process by which this initially formed CT exciton dissociates into a free electron and hole polarons without relaxing to the more stable weakly bound electron and hole polaron paired CT states corresponds to the hot process. Therefore, the factor that selects the cool and hot processes can be considered as the nonadiabatic process owing to the vibronic interaction in the initial CT excitonic state [3].
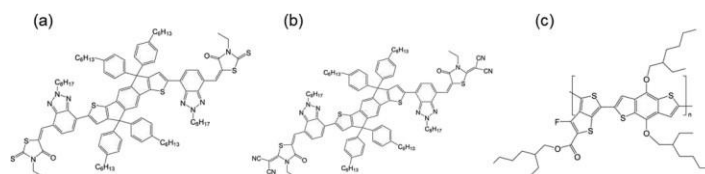
Significance

The significance of the investigation is: (i) the role of vibronic interactions in charge transfer exciton states with respect to the selectivity of hot and cool processes, (ii) the diffusion processes of electron polarons and hole polarons in organic solar cell materials, and (iii) the construction of D/A phase interfaces that exhibit high power conversion efficiency. Based on the concept, i.e., the control of electron and spin behavior by the motion of individual nuclei constituting the system and their collective motion, it is desirable to clarify photochemical phenomena essential for energy conversion devices and electronic devices.

Reference

1. H. Imahori, et. al., *Acc.Res.*, 2, 501 (2021).
2. A. Muraoka, et. al., Phys. Chem. Chem. Phys., 20, 12193 (2018).
3. S. Ikeyama, et. al., *J. Chem. Phys.,* 159, 044307 (2023).

Mechanical Codes of Nucleic Acid and Protein Dynamics

Jhih-Wei Chu*

Institute of Bioinformatics and Systems Biology, National Yang Ming Chiao Tung University,
Hsinchu, (Taiwan, ROC)
*jwchu@nycu.edu.tw

Introduction

The sequence and chemical structure of nucleic acids carry specific functional properties for proper execution of intricate biological processes. Our research aims to resolve how does such vital behaviors arrive from the sequence composition and chemical-scale interactions. Although it has been recognized that mechanical properties are essential in the sequence-structure-dynamics-function relationship of biomolecules, the articulation of which, particularly at the chemical moiety level, remains elusive. In this talk, our development of structure-mechanics statistical learning method that takes the data of all-atom molecular dynamics (MD) simulations as input of graph-theory based machine learning is discussed to addressing the aforementioned issue. The biomolecular systems demonstrating that this approach could be used to gain novel mechanistic insight of the functional behaviors include the mechanical code in transcriptional regulatory sequences of DNA (polyA (A-tract), polyG, CpG, and TpA), solvation of mismatched RNA structures, and binding with exonucleases.

Methodology

In structure-mechanics statistical learning, all-atom MD simulation is conducted and the trajectory is used as input data. Next, an elastic network model is devised as the vehicle for machine learning, for which the fluctuation matching protocol is used to compute the spring constant parameters. The chemical-scale mechanical properties in a structural network, the rigidity graph, is then represented based on the calculated spring parameters. A scheme is also devised to extract statistically prominent patterns of mechanical couplings in the MD trajectory.

Results and Discussion

For the DNA systems with the sequences relating to transcription regulation, mechanical codes are identified that demonstrate the compensatory competition between base pairing and base stacking as the most discriminative feature of the mechanical code. This chemical-scale rigidity can also be used to understand the mechanical property based on the overall shape of the biopolymer, such as persistence length that has been measured experimentally. For the protein systems, we found that mechanical coupling network in the structure exhibits scale-free properties and is sparse comparing to the structural contact network. For long-range communication in the protein structure in responding to substrate or inhibitor binding, a mechanical relay mechanism is identified through the rigidity graphs of MD trajectories. Furthermore, functionally important residues identified in experimental characterization and multiple sequence alignment are found to exhibit specific features in the rigidity graph.

Significance

Structure-mechanics statistical learning provides a useful platform to learn about the mechanism of functional properties in complex molecular systems. The mechanical code concept developed by studying DNA and RNA enables a direct reading of the physical interactions encoded in the sequence. Such intuitive picture is expected to shed new light on DNA allostery and DNA-binding drugs, albeit further development would be necessary. In protein systems, the mechanical-relay picture provides a mechanistic underpinning for conformational changes, long-range communication, and inter-domain allostery. A key advantage is that the responsive mechanical hotspots are mostly residues having important biological functions or significant mutation sensitivity, hence revealing the chemical mechanism of functionally important sites.

References

1. Chen, Y.-T.; Yang, H.; Chu, J.-W., **Mechanical codes of chemical-scale specificity in DNA motifs**. *Chem. Sci.* (2023) *14*, 10155-10166.

2. Raj, N.; Click, T.; Yang H.; Chu, J.-W., **Structure-Mechanics Statistical Learning Uncovers Mechanical Relay in Proteins**, Chem. Sci. (2022) *13*, 3688-3696.
3. Yu, C.-C.; Raj, N.; Chu, J.-W., **Edge weights in a protein elastic network reorganize collective motions and render long-range sensitivity responses**, J. Chem. Phys. (2022) *156*, 245105.
4. Huang, K.-W.; Wu, C.-Y.; Toh, S.-I.; Liu, T.-C.; Tu, C.-I; Lin, Y.-H.; Cheng, A.-J.; Kao, Y.-T.; Chu, J.-W.; Hsiao, Y.-Y., **Molecular insight into the specific enzymatic properties of TREX1 revealing the diverse functions in processing RNA and DNA/RNA Hybrids**. *Nucleic Acids Res.* (2023) *51*, 11927-11940.
5. Sun, X.; Alfermann, J.; Li, H.; Watkins, M.B.; Chen, Y.-T.; Morrell, T.E.; Mayerthaler, F.; Wang, C.-Y.; Komatsuzaki, T.; Chu, J.-W.; Ando, N.; Mootz, H.D.; Yang, H., **Sub-Domain Dynamics Enable Chemical Chain Reactions in Nonribosomal Peptide Synthetases**. *Nature Chem*. (2024) *16*, 259-268.

Development of In-Silico Material Design Tool Based on the Molecular Theory of Solvation

Norio Yoshida[1*]

[1] *Graduate School of Informatics, Nagoya University, Nagoya 464-8601 (Japan)*
*noriwo@nagoya-u.jp

Computer assistance has become indispensable in contemporary endeavors aimed at designing medicines and materials beneficial to humanity. Material molecules exhibit specific structures and properties, necessitating a profound understanding of molecular behavior at the atomic level to tailor molecules that fulfill these criteria. Hence, computational methodologies capable of delineating intricate hierarchical molecular chemical processes are imperative. Our research group has pioneered a multiscale theory based on the 3D-RISM theory, a solvation theory for complex molecular systems, integrated with quantum chemical calculation methods and molecular simulations. This innovative approach empowers us to dissect essential chemical processes pivotal for material molecular design.

Molecular Recognition

Molecular recognition, the non-covalent binding of a host molecule to a specific guest molecule, stands as a cornerstone in the design of drug molecules and materials. Leveraging the 3D-RISM method, we can prognosticate the binding site, affinity, and selectivity of molecules. (Fig 1.) [2]
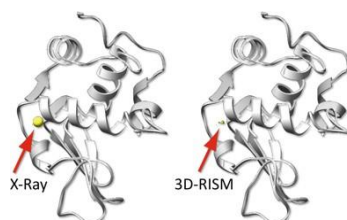
Fig. 1. Ca2+ ion binding site detected by the 3D-RISM method, left, compared with those by experimental observation, right.

Structure Formation and Self-Assembly

The genesis of higher-order structures in biomolecules and material molecules, such as proteins and DNA, parallels the molecular recognition process. Our proposed hybrid Monte Carlo 3D-RISM method allows meticulous consideration of solvent effects.[3]

Chemical Reactions

Chemical reactions, encompassing the formation and dissociation of covalent bonds between atoms, constitute pivotal aspects of molecular design. Accurate depiction of such reactions necessitates quantum chemical methods. We advocate for the QM/MM/3D-RISM

method, a fusion of QM/MM and 3D-RISM approaches, to delineate chemical reactions in intricate molecular systems.(Fig.2.)[4] This methodology enables prediction and analysis of chemical reactions in large, complex molecules within solution environments.
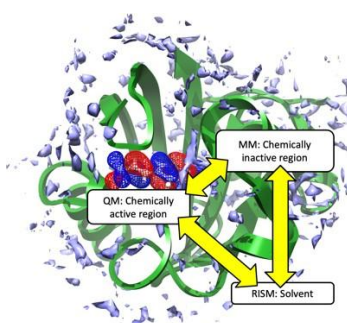

Fig. 2. Schematic illustration of the QM/MM/3D-RISM method.

Photoreaction

The QM/MM/3D-RISM method facilitates the description of photoexcited states of molecules and analysis of the photoreaction mechanisms of target molecules.

These methodologies are encapsulated within RISMiCal, a software package developed by our group. This open-source program is accessible for utilization by the scientific community freely. (Fig.3) [5]

Fig. 3. Logo of the RISMiCal package and QR code for the program access.

References

1. N. Yoshida, J. Comput. Info. Model 57, 2646 (2017).
2. N. Yoshida, S. Phongphanphanee, Y. Maruyama, T. Imai and F. Hirata, J. Am. Chem. Soc. (Communication), 128, 12042-12043, (2006)
3. N. Yoshida, T. Yamaguchi, J. Mol. Liquids, 385, 122418 (2023)
4. N. Yoshida, Y. Kiyota, F. Hirata, J. Mol. Liquids, 159, 83 (2011)
5. Y. Maruyama, N. Yoshida, J. Comput. Chem. 45, 1470 (2024)

Aggregation process of amyloid-β peptides using the replica-permutation method

Satoru G. Itoh[1,2,3]*
[1]*Institute for Molecular Science, National Institutes of Natural Sciences, Okazaki 444-8787(Japan)*
[2]*Exploratory Research Center on Life and Living Systems (ExCELLS), National Institutes of Natural Sciences, Okazaki 444-8787 (Japan)*
[3]*SOKENDAI (The Graduate University for Advanced Studies), Okazaki 444-8787 (Japan)*
*itoh@ims.ac.jp

Introduction

Alzheimer's disease is thought to be caused by the aggregates of amyloid-β peptides (Aβ), such as oligomers and insoluble amyloid fibrils. There are mainly two isoforms of Aβ: Aβ42, consisting of 42 amino-acid residues, and Aβ40, consisting of 40 amino-acid residues. It is known that Aβ42 forms aggregates more easily than Aβ40. However, it is not clear what role the two additional amino-acid residues in the C-terminal region play in the Aβ aggregation.

To investigate the differences in the dimerization processes of Aβ40 and Aβ42, Coulomb replica-permutation molecular dynamics (MD) simulations were performed on Aβ40 and Aβ42 peptides. The Coulomb replica-permutation method is a simulation technique that I have recently developed. This method can be used to efficiently sample both aggregation and dissociation states of biomolecules [1-3]. In addition to the Coulomb replica-permutation MD simulations, aggregation experiments on Aβs were conducted to validate the simulation results.

Methodology

The Coulomb replica-permutation method is a form of the Hamiltonian replica- permutation method (HRPM) [2,3]. HRPM combines the advantages of the replica-permutation method (RPM) [1] and the Hamiltonian replica-exchange method (HREM) [4,5]. RPM is a better alternative to the replica-exchange method (REM). In RPM, temperature permutations among more than two replicas are performed with the Suwa-Todo algorithm [6], as shown in Fig. 1. In HREM, by exchanging the parameters that are related only to limited degrees of freedom, the number of replicas can be decreased in comparison with REM.

In this study, a scaling parameter λ was introduced only for the intermolecular electrostatic interactions as follows:

$$V_{ij}^{\lambda}(q) = \frac{1}{4\pi\varepsilon_0}\frac{(\lambda Q_i)(\lambda Q_j)}{r_{ij}},$$

where q shows the coordinates of atoms in peptides, r_{ij} is the distance between atoms i and j, ε_0 is the dielectric constant. By varying the value of λ, it is possible to efficiently form and break intermolecular hydrogen bonds.
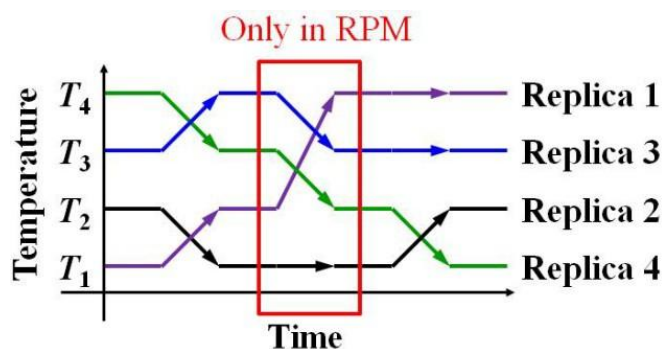

Figure 1. Time series of temperatures in RPM.

Results and Discussion

The simulation results show that Aβ42 forms a more stable dimer compared to Aβ40. This is due to the intramolecular structure of Aβ42, which tends to form a β-hairpin, and the electrostatic interactions between the residues in the C-terminal and N-terminal regions play an important role to stabilize this β-hairpin. Aggregation experiments were also performed on Aβs with mutated residues in the N-terminal region. The results showed that aggregation was suppressed in the mutated Aβs, as predicted by our simulation [7].

Significance

Amyloid-β peptide (Aβ) has two isoforms Aβ42 and Aβ40. The only difference between the two peptides is the two residues at the C-terminus, but Aβ42 forms aggregates more easily than Aβ40. This study has elucidated the reasons why Aβ42 forms aggregates more easily. It also succeeded in identifying the amino-acid residue that is key to aggregation.

References

1. S. G. Itoh and H. Okumura., *J. Chem. Theory Comput.* 9, 570 (2013).
2. S. G. Itoh and H. Okumura, *J. Comput. Chem.* 34, 2493 (2013).
3. S. G. Itoh and H. Okumura, *J. Phys. Chem. B* 118, 11428 (2014).
4. Y. Sugita et al., *J. Chem. Phys.* 113, 6042 (2000).
5. H. Fukunishi et al., *J. Chem. Phys.* 116, 9058 (2002).
6. H. Suwa and S. Todo, *Phys. Rev. Lett.* 105, 120603 (2010).
7. S. G. Itoh et al., *ACS Chem. Neurosci.* 13, 3139 (2022).

Understanding interactions in large molecular systems

Dmitri G. Fedorov

CD-FMat, National Institute of Advanced Industrial Science and Technology (AIST), Japan

Quantitative data on interactions between parts of molecular systems provide valuable information for analyzing molecular binding and chemical catalysis,. Using contributions of parts of molecular subsystems to the binding energies or activation barriers one can improve efficiency of drugs and catalysts in drug or material design.

There are various energy decomposition analyses (EDA) based on quantum-mechanical methods. In order to apply EDA to large molecular systems, such as proteins, it is necessary to combine EDA with a low scaling QM method, for which purpose fragmentation approaches are very suitable.

There are several binding and interaction energy analyses based on the fragment molecular orbital method [1,2]. Pair interaction energy decomposition analysis (PIEDA) and partition analysis (PA) are useful for analyzing binding. Conformational sampling in MD can be analyzed with the fluctuation analysis (FA) and the free energy decomposition analysis (FEDA). Partition analysis of the vibrational energy (PAVE) can be used to take into account temperature effects on binding via thermodynamical partition functions. .Subsystem analysis (SA) can be used to define polarization, desolvation, and interaction contributions to binding energies.

As an example, individual hydrogen bonds in a complex (PDB: 2o8b) of a DNA with a protein [3] were analyzed (Fig. 1).
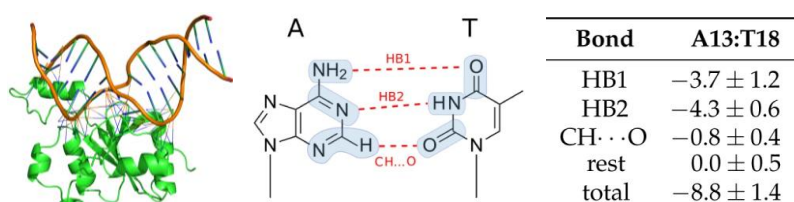

Bond	A13:T18
HB1	-3.7 ± 1.2
HB2	-4.3 ± 0.6
CH$\cdots$O	-0.8 ± 0.4
rest	0.0 ± 0.5
total	-8.8 ± 1.4

Fig. 1. Definition of segments for computing hydrogen bond energies (kcal/mol) in a protein-DNA complex, where "rest" means the remainder of nucleotides (DFTB/PCM).

[1] D. G. Fedorov, J. Chem. Phys. 157 (2022) 231001.
[2] D. G. Fedorov, J. Comp. Chem. 2024, DOI: 10.1002/jcc.27345.
[3] V. Sladek, D. G. Fedorov, Int. J. Mol. Sci. 23 (2022) 13514.

Trends in molecular dynamics simulation research of amyloid-βaggregates

<u>Hisashi Okumura</u>[1, 2, 3]*
[1]Exploratory Research Center on Life and Living Systems, Okazaki, 444-8787 (Japan)
[2]Institute for Molecular Science, Okazaki, 444-8787 (Japan)
[1]Graduate Institute for Advanced Studies, SOKENDAI, Okazaki, 444-8787 (Japan)
*hokumura@ims.ac.jp

Introduction

The cause of Alzheimer's disease is related to aggregates such as oligomers and amyloid fibrils consisting of amyloid-β (Aβ) peptides. Molecular dynamics (MD) simulation studies have been conducted to understand the molecular mechanism of the formation and disruption of Aβ aggregates. In this talk, the MD simulation studies in the following categories are reviewed: aggregation of Aβ peptides in bulk solution, Aβ aggregation at the interface, and nonequilibrium MD simulation of Aβ aggregates. More details can be found in a recent Perspective paper by the author [1].

Aggregation of Aβ peptides in bulk solution

Several studies focused on the initial process of Aβ aggregation, that is, the formation of Aβ dimers and small oligomers. We performed Hamiltonian replica-permutation MD simulations for the dimerization of Aβ42 and Aβ40 peptides [2]. The results showed that both Aβ tend to aggregate when they form a β-hairpin structure. We found that the β-hairpin structure is stabilized by the electrostatic attraction between a positively-charged residue, Arg5, and the C-terminus, which has COO^-, in Aβ42. This β-hairpin promotes dimer formation with the formation of intermolecular β-bridges. On the other hand, in the case of Aβ40, the C-terminal region is shorter by two residues, and the β-hairpin is not stabilized. This is the reason why Aβ42 aggregates more than Aβ40. From these simulation results, we predicted that the key residue is Arg5. They confirmed that the aggregation of Aβ42 is remarkably suppressed when Arg5 was mutated to Glu or Gly. Their theoretical prediction was approved by the experiments in this way.

Aβ aggregation at the interface

Aβ tends to aggregate at hydrophilic/hydrophobic interfaces, such as the surface of cell membranes and the interface between aqueous solution and air. We performed all-atom MD simulations of 100 Aβ(16–22) fragments at an air-water interface. We showed that the existence probability of the peptides at the interface is higher than in bulk water [3]. This is because the Aβ(16–22) fragment has both hydrophilic and hydrophobic amino acid residues and is more likely to be present at hydrophilic-hydrophobic interfaces, such as cell membrane surfaces and the air-water interface. This tendency is also true for full-length Aβ peptides. We also showed that Aβ40 forms more β-hairpin structures at the interface than in bulk water [4]. The β-hairpin structures promote oligomer formation. The higher concentration of Aβ peptides at the interface and the tendency of β-hairpin structure at the interface are the reasons why oligomers are more likely to be formed at the interface than in the bulk water.

Nonequilibrium molecular dynamics simulation of Aβ aggregates

Several experiments have been conducted to destroy Aβ aggregates by applying external forces such as ultrasonic wave or infrared laser. In response to these experiments, nonequilibrium MD simulations have been performed to simulate these external forces and to clarify the molecular behavior during the disruption process. We performed MD simulations of the disruption process of Aβ amyloid fibrils by ultrasound irradiation [5]. We applied time-varying sinusoidal pressure. It was observed that when the pressure was positive, there was no significant change in the structure of the amyloid fibril and water. However, when the pressure became negative, a bubble was formed around the amyloid fibril. When the pressure became positive again, the bubble collapsed, and the water droplet attacked the amyloid fibril as a jet flow, destroying the amyloid fibril.

We also performed nonequilibrium MD simulations to elucidate the role of water molecules in laser-induced destruction of Aβ amyloid fibrils [6]. We showed that laser pulses frequently break intermolecular hydrogen bonds between C=O and N–H even before the Aβ peptides dissociate, as shown in Figs. 1(a)–1(b). The intermolecular hydrogen bond is often reformed after the laser pulse and

before the next laser pulse, as in Fig. 1(c). However, water molecules sometimes enter between the C=O and N–H and inhibit the reformation of intermolecular hydrogen bonds between Aβ peptides (Fig. 1(d)). When this phenomenon occurs, water molecules successively enter between Aβ peptides (Fig. 1(e)), disrupting the intermolecular β-sheet of Aβ amyloid fibrils (Fig. 1(f)).
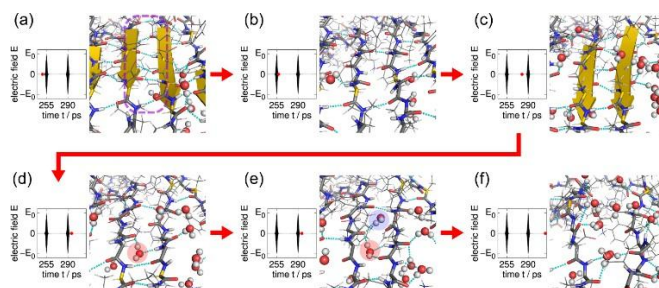

Figure 1. Disruption process of the hydrogen bonds between the Aβ peptides and electric field pulses. Reproduced from Ref. [6]. Copyright 2021 American Chemical Society.

References

1. H. Okumura, J. Phys. Chem. B 127 (2023) 10931.
2. S. G. Itoh, M. Yagi-Utsumi, K. Kato, and H. Okumura, ACS Chem. Neurosci. 13 (2022) 3139.
3. H. Okumura and S. G. Itoh, J. Chem. Phys. 151 (2020) 095101.
4. S. G. Itoh, M. Yagi-Utsumi, K. Kato, and H. Okumura, J. Phys. Chem. B 123 (2019) 160.
5. H. Okumura and S. G. Itoh, J. Am. Chem. Soc. 136 (2014) 10549.
6. H. Okumura, S. G. Itoh, K. Nakamura, and T. Kawasaki, J. Phys. Chem. B 125 (2021) 4964.

Dynamical Interaction Analysis of Protein Interaction by Machine Learning Method

Yasuteru Shigeta
Center for Computational Sciences, University of Tsukuba, Japan.
*shigeta@ccs.tsukuba.ac.jp

Introduction

Computational methods such as quantum chemical calculations and molecular simulations are used in both basic and applied research in a wide range of fields, including physics, chemistry and pharmaceutical sciences. One of the advantages of using these methods is that they enable efficient analysis of phenomena at the molecular level, which cannot be achieved only by experimental analysis. However, the amount of data obtained by these methods for large-scale systems such as proteins is often too large to be analyzed manually. In recent years, the approach to scientific research has begun to shift from conventional working hypothesis-driven science to data-driven science, and it has become important how to extract useful information from big data. Thus, the development of analysis tools using machine learning has attracted attention.

Methodology

By combining the Random Forest (RF) method, with quantum chemical interaction analysis based on the fragment molecular orbital (FMO) method, we have established a method for efficiently discovering important amino acid residues and their interactions (RF-FMO) [1]. The scheme of RF-FMO analysis, which requires input trajectory data from MD simulations of two states of the protein (denoted as Form A and Form B). First, RMSD and their standard deviation were calculated using the trajectories of form A and Form B as inputs to determine representative structures for them. From the trajectories we randomly sampled two hundred structures for each A and B to estimate interaction energies by FMO methods. Finally, the Gini importance values for each amino acid residue and each interaction energy with respect to the state either A or B were calculated by random forest using the interaction energy values among amino acid residues obtained by the FMO calculation as training data. In a decision tree, a value called a Gini index is calculated as a measure of an important feature. The Gini index implies the impurity of the data in a node among nodes classified by a certain feature. When the Gini index is closer to 1 (0), the purity of the data is higher (lower), indicating that the features are (less) important.

Results and Discussion

The RF-FMO was performed on Src-Kinase, for which the functional expression mechanism has been clarified at the molecular level through a wide range of previous studies. Finally, we succeeded in automatically extracting 32 important amino acid residues (extraction rate: 5.1%) and 61 residue pairs (extraction rate: 0.2%) that control the active-inactive transition from a total of 623 residues and 34453 amino acid residue interaction energies. This result shows that the method can automatically extract important interactions for conformational change from a large amount of interaction energy data, instead of the manual FMO interaction analysis conducted so far [1].

It has been assumed that dimer formation is responsible for the functional expression of human C-terminal binding protein 2 (hCtBP2), which suppresses the DNA expression. So far, the conformational change of hCtBP2 at the molecular level is unknown. In this study, we focused on the conformational changes of hCtBP2 itself (Open and Closed states) and analysed the regulation mechanism by RF-FMO. The analysis of hCtBP2 by RF-FMO revealed that 25 out of 1324 amino acid residues and 57 out of 875826 interactions are crucial for the structural transition. Analysis of the extracted pair interaction energies revealed that several interactions with His321 were extracted. This result suggests that the His321-mediated interaction network is important in hCtBP2, which can be confirmed in their representative structures (**Figure 1**). Further analysis of the interaction network of His321 in the open and closed states revealed that the switching between the open and closed states is mediated by changes in the interaction network formed by His83, Glu301 and His321. This indicates that the detailed mechanism of the structural change was successfully elucidated [2].
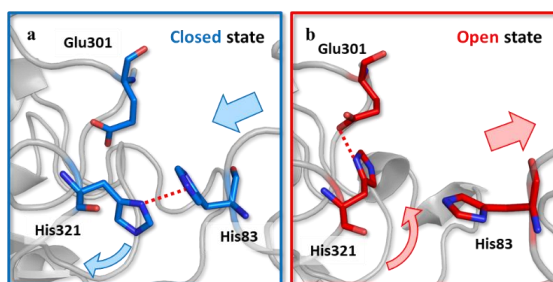
Figure 1. Interaction network nearby His321 in Closed (a) and Open (b) states.

Significance

In this study, computational analysis was carried out on several proteins using interaction analysis based on the FMO method, revealing new scientific knowledge about these proteins. In addition, a novel analysis method (RF-FMO method) combined with machine learning was successfully established to overcome the weaknesses of the previous analysis methods. The RF- FMO method established in this study can be used to analyse not only Src-Kinase and CtBP2 analysed in this paper, but also various other proteins. In the future, it is expected that the RF- FMO method will be used to elucidate the functions of proteins whose detailed molecular mechanisms have not yet been clarified.

References

1. Y. Yamamoto, S. Nakano, Y. Shigeta, *Bull. Chem. Soc. Jpn* 96(1), 42-47(2023).
2. Y. Yamamoto, Y. Shigeta, *Chem Lett* 52(2), 120-123 (2023).

Metal ion-binding site prediction and modeling

Chih-Hao Lu [1,2,3,*]
[1]*Institute of Bioinformatics and Systems Biology,*
National Yang Ming Chiao Tung University, Hsinchu, Taiwan
[2]*Department of Biological Science and Technology,*
National Yang Ming Chiao Tung University, Hsinchu, Taiwan
[3]*Center for Intelligent Drug Systems and Smart Bio-devices (IDS2B),*
National Yang Ming Chiao Tung University, Hsinchu, Taiwan
*chlu@nycu.edu.tw

Introduction

Interactions between proteins and specific metal ions are crucial for many physiological activities. Identifying metal ion-binding sites is essential for understanding the mechanisms underlying the biological interactions of metal ion-binding proteins. However, experimental identification can be challenging and time-consuming due to the complex steps and specialized techniques required. In contrast, computational methods may offer a relatively easier and faster way to analyze metal-binding sites.

Methodology

We have developed a method for predicting metal ion-binding sites by comparing local structures between the query proteins and metal ion-binding templates [1]. All metal ion binding templates are extracted from the Protein Data Bank structures of protein and metal ion complexes. The fragment transformation method [2] attempts to align fragments of the query protein and templates and evaluate their sequence and structure conservation. We have created a comprehensive and user-friendly web tool called MIB [3] for reliable prediction of metal ion-binding sites, which can dock metal ions in protein, including Ca^{2+}, Cu^{2+}, Fe^{3+}, Mg^{2+}, Mn^{2+}, Zn^{2+}, Cd^{2+}, Fe^{2+}, Ni^{2+}, Hg^{2+}, Co^{2+} and Cu^+. An updated version of MIB, MIB2 [4] aims to overcome the limitation of structure-based prediction approaches and utilizes both the $(PS)^2$[5, 6] method and the AlphaFold [7, 8] protein structure database to acquire 3D information for performing metal ion docking and predicting binding residues. A reliable protein structure model can be built with a total of 18 metal ion types (Au^+, Ba^{2+}, Pb^{2+}, Pt^{2+}, Sm^{3+} and Sr^{2+} were added).

Results and Discussion

Our research uncovered specific preferences of different metal ions, showing that they not only favor particular residues, but also specific atoms involved in their binding. MIB2 improves the accuracy of predicting metal ion binding sites by taking into account the unique characteristics of both residues and atoms, considering their preferences for different metal ions. Out of the 18 types of metal ions studied, ten showed sensitivities of over 50%, and seven showed sensitivities of over 75% at a specificity threshold of over 95%.

Significance

MIB2 is a cutting-edge server with more accurate and reliable prediction performance compared to MIB. By helping to identify metal-binding sites in proteins, our research could potentially enhance the findings of proteomics studies.
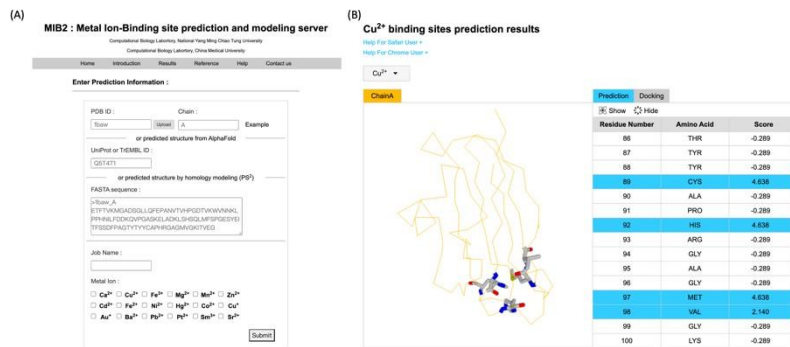
Figure 1. (A) MIB2 server, http://combio.life.nctu.edu.tw/MIB2/. (B) The example of Cu^{2+} binding site prediction results from MIB2.

References

1. Lu, C.H., et al., *Prediction of metal ion-binding sites in proteins using the fragment transformation method.* PLoS One, 2012. **7**(6): p. e39252.
2. Lu, C.H., et al., *The fragment transformation method to detect the protein structural motifs.* Proteins, 2006. **63**(3): p. 636-43.
3. Lin, Y.F., et al., *MIB: Metal Ion-Binding Site Prediction and Docking Server.* J Chem Inf Model, 2016. **56**(12): p. 2287-2291.
4. Lu, C.H., et al., *MIB2: metal ion-binding site prediction and modeling server.* Bioinformatics, 2022. **38**(18): p. 4428-4429.
5. Chen, C.C., J.K. Hwang, and J.M. Yang, *(PS)2: protein structure prediction server.* Nucleic Acids Res, 2006. **34**(Web Server issue): p. W152-7.
6. Chen, C.C., J.K. Hwang, and J.M. Yang, *(PS)2-v2: template-based protein structure prediction server.* BMC Bioinformatics, 2009. **10**: p. 366.
7. Jumper, J., et al., *Highly accurate protein structure prediction with AlphaFold.* Nature, 2021. **596**(7873): p. 583-589.
8. Varadi, M., et al., *AlphaFold Protein Structure Database: massively expanding the structural coverage of protein-sequence space with high-accuracy models.* Nucleic Acids Res, 2022. **50**(D1): p. D439-D444.

QM/MM Simulation in Pyruvate Systems: Mercaptopyruvate Sulfurtransferase and Pyruvate Class II Aldolase

Gou-Tao Huang[1] and Jen-Shiang K. Yu[123]*

[1]*Department of Biological Science and Technology, National Yang Ming Chiao Tung University, Hsinchu City, 300 (Taiwan)*
[2]*Institute of Bioinformatics and Systems Biology, National Yang Ming Chiao Tung University, Hsinchu City, 300 (Taiwan)*
[3]*Center for Intelligent Drug Systems and Smart Bio-devices (IDS²B), National Yang Ming Chiao Tung University, Hsinchu City, 300 (Taiwan)*
*jsyu@mail.nctu.edu.tw

Introduction

Theoretical studies[1,2] employing multiscale molecular simulation in the pyruvate systems of mercaptopyruvate sulfurtransferase (MST) and pyruvate class II aldolase, respectively, are presented. The processes of sulfur transfer in human MST are investigated using quantum mechanics combined with molecular mechanics (QM/MM) to elucidate its reaction mechanism.[1] The aldol cleavage processes catalyzed by pyruvate class II aldolase that transforms the substrate of 4-hydroxy-2-ketoacid into pyruvate and aldehyde through the aldol cleavage are studied by QM/MM metadynamics.[2]

Methodology

In the simulation of MST, density functional theory (DFT) of M06-2X employing Pople basis sets is used as QM along with MM force field of Amber99SB. The energetics are confirmed by wavefunction theory at CCSD(T) level. For the study in aldolase, DFT of ⬜B97X-D is utilized to locate the transition states through the metadynamics approach and to determine the rate-limiting step in reaction kinetics.

Results and Discussion

The sulfur atom (S^0) transfer process in MST goes through a transition state with an activation free energy of 14.9 kcal mol^{-1}, much lower than that of the –SH transfer route at 43.2 kcal mol^{-1}; in addition, the formation of a loop composed of residues of CGSGVT is found crucial to promote the transfer according to electrostatic potential analysis. For the aldolase, metadynamics simulations demonstrate that the C–C bond cleavage is the rate-determining step, with a barrier of approximately 13.7 kcal mol^{-1} that reasonably agrees with the experimental catalytic rate constant.

Significance

Structural computations in the MST system exhibit that the hydrogen atoms of the amide groups in the CGSGVT loop tend to construct a positively-charged environment to stabilize the persulfide anion of cysteine, and the Coulomb repulsion between the anions could be reduced by the support of this loop shown in Figure 1. Around the active site of pyruvate class II aldolase, histidine is relevant to the deprotonation and substrate binding, and the metal-bound hydroxide is a transient species in the course of the deprotonation. The reactive alkoxide could be further stabilized by a salt bridge composed of arginine and aspartic acid illustrated in Figure 2.
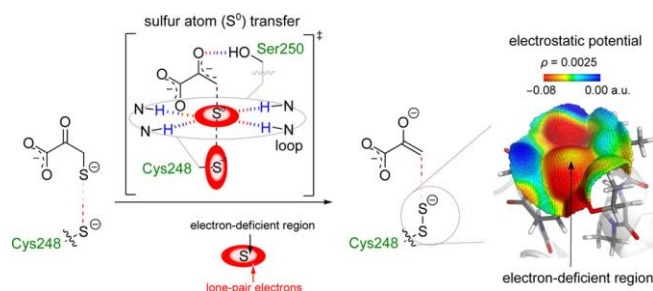

Figure 1. The loop that stabilizes the persulfide anion of cysteine in MST.
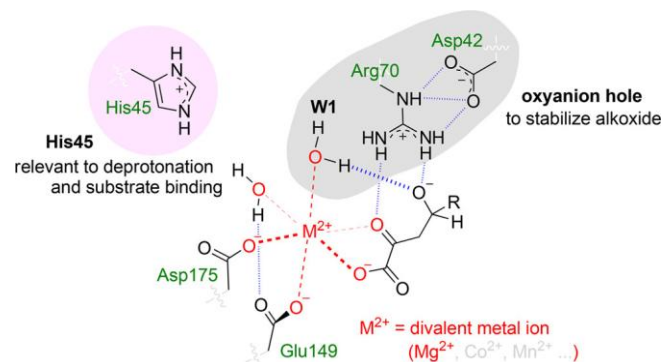
Figure 2. The active site of pyruvate class II aldolase.

References

1. Huang, G.-T., and Yu, J.-S.K. *J. Phys. Chem. B* 120, 4608 (2016).
2. Huang, G.-T., and Yu, J.-S.K. *ACS Catal.* 7, 8130 (2017).

Dynamic 3D cardiac imaging of zebrafish heart enabled by light-sheet imaging and image-processing algorithm

Yu-Kai Chao,[1] Yu-Cheng Chuang,[1] and <u>Ian Liau</u>[1,2,3]*

[1]Department of Applied Chemistry, National Yang Ming Chiao Tung University,
Hsinchu City, 300 (Taiwan)
[2]Department of Biological Science and Technology, National Yang Ming Chiao Tung University,
Hsinchu City, 300 (Taiwan)
[3]Center for Emergent Functional Matter Science, National Yang Ming Chiao Tung University,
Hsinchu City, 300 (Taiwan)
*ianliau@nycu.edu.tw

Introduction

Calcium ions are essential for excitation-contraction coupling and significantly influence cardiac electrophysiology and contractile functions. Disturbances in calcium homeostasis are associated with a range of cardiovascular disorders, including arrhythmias, heart failure, and drug-induced cardiotoxicity. Zebrafish, with hearts functionally similar to those of mammals and transparent during their embryonic stage, are ideal for cardiac research. However, their rapid heart rate, often exceeding 150 beats per minute, presents substantial challenges for traditional confocal microscopes in capturing 3D cardiac images in vivo. To address these issues, we have developed a novel imaging technique and algorithm specifically designed for dynamic cardiac calcium imaging in zebrafish.[1,2,3]

Methodology

Our approach involves a dual-channel light-sheet imaging system, augmented by image- processing algorithms, to enable 4D (3D + time) cardiac calcium imaging. Additionally, we have employed 1D scanning multiphoton imaging to investigate the mechanistic impacts of calcium dysregulation in doxorubicin (DOX)-induced cardiotoxicity, further enhancing our understanding of its cellular effects.

Results and Discussion

Our innovative system has facilitated 4D imaging and the simultaneous quantification of cardiac mechanical function and calcium dynamics in zebrafish. We found that atrial calcium transients are significantly narrower than their ventricular counterparts. Notably, calcium transients in non-beating (silent) hearts were extensively prolonged, especially during the diastolic phase, underscoring the importance of cautious data interpretation when using the silent heart model. Moreover, DOX exposure alters cell morphology and significantly prolongs calcium transients and sarcomere contractions, culminating in arrhythmia-like contractile disorders. The restoration phase of calcium transient dominated the overall prolongation, indicating that DOX perturbed primarily the protein functions responsible for recycling cytosolic calcium ions.

Significance

Our innovative imaging technology significantly enhances cardiac electrophysiological research and drug screening for cardiac-active compounds. By clarifying the intricate relationship between calcium dynamics and cardiac function, our work promises to improve understanding and inform targeted interventions in cardiac health, potentially leading to better therapeutic strategies.
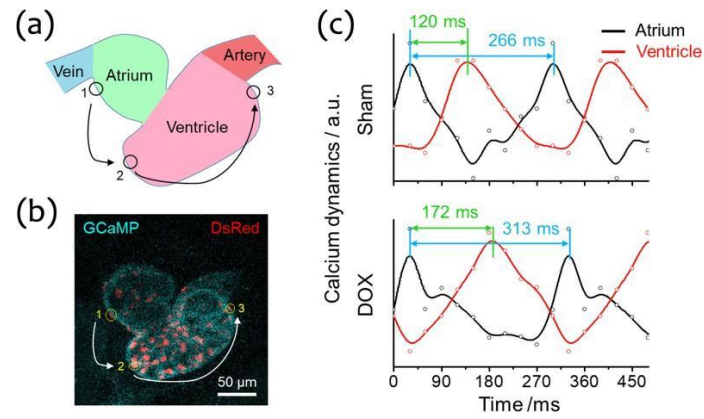
Figure 1. Calcium signaling propagation in zebrafish hearts. (a) Schematic illustration of a zebrafish heart. (b) Representative image capturing a moment in the cardiac cycle of a beating zebrafish heart. (c) Comparison of localized calcium transients in the atrium and ventricle between control and DOX-treated larval zebrafish, demonstrating the impact of DOX on calcium dynamics.

References

1. Lin, K.-Y., Chang, W.-T., Lai, Y.-C., and Liau, I., *Anal. Chem.* 86, 2213 (2014).
2. Tu, W.-M., Huang, X.-C., Chen, Y.-L., Luo, Y.-L., Liau, I., and Hsu, H.-Y. *Anal. Chim. Acta* 1095, 129 (2020).
3. Chao, Y. K., and Liau, I. *Biomed. Opt. Exp.* 12, 7162 (2021)

Cutting-edge technology from the laboratory to the drug discovery marketplace

Dr. Suwipa Saen-oon
Deputy Director of Drug Design, Nostrum Biodiscovery, Barcelona, 08029, Spain
suwipa.saenoon@nostrumbiodiscoery.com

Introduction

This talk will share insights on how technology development in the laboratory can contribute to the real drug development markets. Computational simulations, molecular modelling, bioinformatics, machine learning (ML), and artificial intelligence (AI) have played a significant role in the process of drug discovery, from the early stage of finding new chemical entities (hits) to Hit-2-Lead and Hits optimisation as well as the properties predictions using AI or ML. Nostrum Biodiscovery is a leading provider of customised services and cutting-edge *in silico* technologies to biopharmaceutical and biotechnology companies, contract research organisations (CROs) and academic institutions, enabling them to perform rational drug design. Our company's strength lies in the application of computational chemistry tools, which facilitate the acceleration, streamlining, and optimization of small molecule design in the early stages of discovery. Our technology is unique in that it is based on Monte Carlo-based biomolecular modelling, which we refer to as "Protein Energy Landscape Exploration" (PELE). We have created a software platform that combines multiple proprietary modelling solutions, including PELE, FragPELE, AquaPELE, Adaptive-PELE, and AI tools. These core technologies are designed to address a series of current limitations in the field of chemoinformatics and computer-aided drug design.

References

1. Borrelli, K. W., Vitalis, A., Alcantara, R., Guallar, V. "PELE: Protein Energy Landscape Exploration. A Novel Monte Carlo Based Technique." *J. Chem. Theory Comput.* 2005, 1 (6), 1304–1311.
2. International Journal of Molecular Sciences 23 (24), 16090 (2022): "Recent PELE Developments and Applications in Drug Discovery Campaigns"
3. Diaz, L., Soler, D., Tresadern, G., Buyck, C., Perez-Benito, L., Saen-oon, S., Guallar, V., Soliva, R. "Monte Carlo simulations using PELE to identify a protein–protein inhibitor binding site and pose" *RSC Adv.* 2020, 10, 7058-7064.
4. L Serneels, R Narlawar, L Perez-Benito, M Municoy, V Guallar, DDries T'Syen, M Dewilde, F Bischoff, E Fraiponts, G Tresadern, PWM Roevens, HJM Gijsen, B De Strooper. "Selective inhibitors of the PSEN1–gamma-secretase complex". *J. Biol. Chem.* 6, 299, 2023.
5. J Rullo-Tubau, M Martinez-Molledo, P Bartoccioni, I Puch-Giner, A Arias, S Saen-Oon, C Stephan-Otto Attolini, R Artuch, L Díaz, V Guallar, E Errasti-Murugarren, M Palacín, O Llorca, "Structure and mechanisms of transport of human Asc1/CD98hc amino acid transporter" *Nat Commun.* 15, 2986 (2024). https://doi.org/10.1038/s41467-024-47385-3
6. Kossatz E, Diez-Alarcia R, Gaitonde SA, Ramon-Duaso C, Stepniewski TM, Aranda-Garcia D, Muneta-Arrate I, Tepaz E, Saen-Oon S, Soliva R, Shahraki A, Moreira D, Brea J, Loza MI, de la Torre R, Kolb P, Bouvier M, Meana JJ, Robledo P, Selent J. G protein-specific mechanisms in the serotonin 5-HT2A receptor regulate psychosis-related effects and memory deficits. *Nat Commun.* 15, 1, 4307 (2024). doi: 10.1038/s41467-024-48196-2

Advancing Material Simulations: Machine Learning Potentials for Anharmonic Effects and Thermal Properties

Ittipon Fongkaew[1]

[1]*School of Physics, Institute of Science, Suranaree University of Technology, 30000 (Thailand)*

Abstract

Machine learning methods for developing interatomic potentials offer near-experimental accuracy for simulating materials at finite temperatures. However, their effectiveness in representing anharmonic effects—key for thermal conductivity and phase transitions—is under scrutiny. This presentation explores a new on-the-fly learning approach combining molecular dynamics with Bayesian inference to create precise force fields for thermodynamic predictions. Using examples like hydroxyapatite, nickel, negative thermal expansion materials, and zirconia, it's shown that these potentials accurately predict temperature-driven phase changes before melting and enable detailed heat transport analysis through Green-Kubo theory, incorporating all levels of anharmonic effects. Additionally, a novel machine learning method is introduced for cost-effective training of potentials using advanced beyond-density functional theory, enhancing the prediction of materials' finite-temperature behaviors.

Molybdenum-based MXenes under biaxial strain: Structural Property and Some Promising Applications *via* First-principles Calculation

Satchakorn Khammuang, Sirinee Thasitha, <u>Komsilp Kotmool</u>*

College of Advanced Manufacturing Innovation, King Mongkut's Institute of Technology Ladkrabang, Bangkok 10520, Thailand
*komsilp.ko@kmitl.ac.th

Introduction

MXenes are a group of 2D materials that can be obtained from MAX materials. The letter M represents a transition metal, A represents an element from either IIIA or IVA groups, and X is either N or C. When the A atom of a MAX phase is removed, an MXene can be formed. The discovery of MXene was first reported by Naguib et al. in 2011. MXenes can be represented by the chemical formula $M_{n+1}X_n$, where n is an integer ranging from 1 to 4, resulting in over 30 variations. MXenes based on Mo_2X (where X can be C or N) have gained significant attention due to their outstanding properties, such as visible-light photocatalysis for hydrogen production, thermoelectricity, electrochemical catalysis, and energy storage. Additionally, theoretical reports suggest that Mo_2C and Mo_2N MXenes exhibit superconducting properties with a notably high T_c among other MXene members.

This presentation discusses the stable atomic structures and potential applications of Mo-based MXenes under biaxial strain using a first-principles calculation method. The 1T and 2H phases of Mo_2XT_2 (where X = C and N, and T = O, F, Cl, or H) are evaluated to determine their energetic and dynamic stability. Mechanical and electronic properties are also analyzed to guide possible applications. Additionally, we introduce and investigate the Janus MoWC in this work.

Methodology

The study focused on analyzing the energetic stability of two phases (1T and 2H) of Mo_2X MXenes. To ensure sufficient distance between the layers of the MXene and terminate the van de Waals interaction, the vacuum-slab model with over 20 Å vacuum thickness was utilized. Functional groups (T) were added to the surface of Mo_2X MXenes at different symmetric points to determine their ideal atomic configurations. The calculations were performed using density functional theory under the plane-wave basis set, ultrasoft pseudopotentials with convergent energy cut-off and k-point meshes. The dynamic stabilities of the low-energy structures were verified by the results of phonon dispersions. An *ab initio* molecular dynamics (AIMD) simulation was performed to confirm the existence of calculated MXenes at practical temperatures. Mechanical properties were evaluated by considering the profile of stress-strain response. Electronic band structures and partial density of states (PDOS) were analyzed accurately for bringing to the potentially suitable implementations of calculated MXenes. The two main applications presented in this work consist of Li-battery anode and superconductivity. The first application is evaluated by theoretical storage capacity and average open circuit voltages (OCVs). Meanwhile, electron-phonon coupling based on isotropic Eliashberg theory was used to investigate phonon-mediated superconductivity.

Results and Discussion

By analyzing their energetic stabilities, we discovered that the 2H phase is more stable than the 1T phase for all pristine Mo2C, Mo2N, and MoWC, with relative energies of 63 meV, 90 meV, and 100 meV, respectively. Figures 1a and 1b illustrate the atomic configurations of 1T and 2H phases. The centrosymmetric configuration induces more covalent bonds between M and X atoms obtained from the electron localization function (ELF), as shown in Figures 1c and 1d (for Mo2N). This finding is evidence of the preferable 2H phase. As for functional groups, only Cl termination on Mo2C produces the 1T phase, which is more stable than the 2H phases.
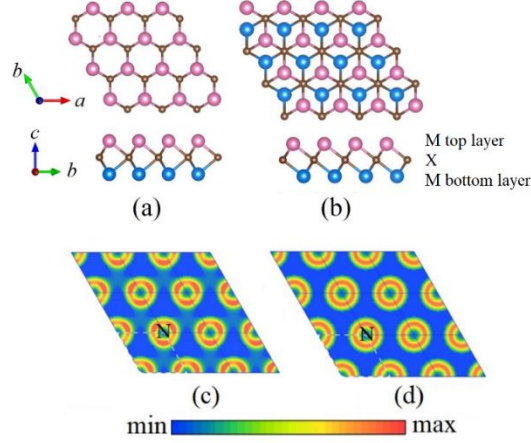
Figure 1. Top and side views of atomic arrangements of 2H (a) and 1T (b) phases and ELF at the (001) plane of 2H (c) and 1T (d) phases.

To access the mechanical properties of the Mo-based MXenes, stress-strain response are presented in Figure 2a and 2b for Mo2N and MoWC, respectively. The elasticity and elastic modulus of 2H phase of all considered Mo-based MXenes are higher than their 1T phase which are listed in Table 1.

Table 1. Mechanical parameters of 1T and 2H phases of Mo-based MXenes.

MXene	Elastic moduli (E, GPa)		Ideal ultimate strength (σ_{max}, GPa) at the highest strain (ε_{max}, %)	
	1T	2H	1T	2H
Mo_2C	312	480	20.8 ($\varepsilon_{max} = 8\%$)	38.0 ($\varepsilon_{max} = 11\%$)
Mo_2N	292	438	19.0 ($\varepsilon_{max} = 7\%$)	37.0 ($\varepsilon_{max} = 12\%$)
MoWC	298	456	4.9 ($\varepsilon_{max} = 2\%$)	33.4 ($\varepsilon_{max} = 12\%$)
Mo_2CO_2	-	507	-	52.0 ($\varepsilon_{max} = 20\%$)

Figure 2. Stress-strain responses of the Mo2N (a) and MoWC (b), and the inset shows the linear fitting for evaluating elastic modulus.

Mo$_2$C and Mo$_2$CO$_2$ were chosen to be studied as electrodes of Li-ion batteries because of their superior strength. The study examines the diffusion of Li ions between the first two most favorable adsorption sites. It is observed that the energy barrier decreases with biaxial strain refinement under compressive strain, but increases with the induction of tensile strain for both MXenes as shown in Figures 3a-d. The energy barriers of Li-ion adsorption on the surfaces of Mo$_2$C and Mo$_2$CO$_2$ are in the range of 31-57 meV and 177-229 meV, respectively. Notably, the storage capacity of Li can reach three layers, corresponding to a theoretical capacity of 788.61 mAhg^{-1} for Mo$_2$C and 681.64 mAhg^{-1} for Mo$_2$CO$_2$.

Additionally, by screening in superconductivity of these MXenes, we found that the Mo_2N is a promising 2D superconductor with exhibiting strong electron-phonon coupling (EPC) under biaxial stress. EPC and corresponding T_c are elucidated upon the dynamically stable strain range. For strain-free Mo_2N, the EPC constant (λ) and T_c are 1.32 and 22.7 K, respectively. The obvious strong EPC with λ over 2.0 occurs at strains of -4%, -2.5%, and 5%, yielding T_c's of 37.8, 35.4, and 28.9 K, respectively, as depicted in Figure 4. The findings suggest that the strain-dependent feature and energy levels of electronic bands play an essential role in enhancing EPC. Moreover, the impact of functional groups (i.e., H and O atoms) on the superconductivity of Mo_2N is investigated. The λ (T_c) values of Mo_2NH_2 and Mo_2NO_2 are found to be reduced in comparison to the original Mo_2N, with values of 0.96 (20 K) and 0.34 (0.9 K), respectively.

Significance

This collection of research highlights significant discoveries regarding the atomic structures of Mo-based MXenes and their potential applications. Mo_2C, Mo_2N, and MoWC exhibit the 2H atomic configuration, which has lower energies than the 1T phase. The diffusion of Li-ion on both Mo_2C and Mo_2CO_2 suggests that the refinement of biaxial strain under compressive stress decreases the energy barrier, whereas the induction of tensile strain increases it. Mo_2N is a strong electron-phonon coupling material that performs well under biaxial strains, with a superconducting temperature of 38 K. These findings imply that Mo_2C-based MXenes may possess promising mechanical and electronic properties under biaxial strain, which could guide their potential use in modern strain engineering devices.
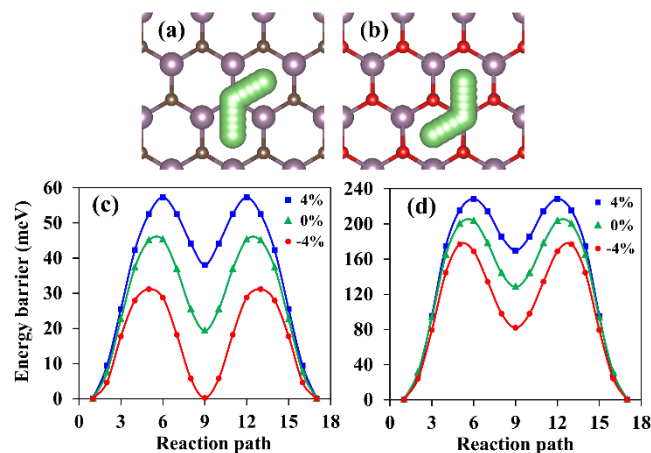

Figure 3. Energy barriers with corresponding paths of (a,c) Mo_2CLi_8 and (b, d) $Mo_2CO_2Li_8$ at certain strains.
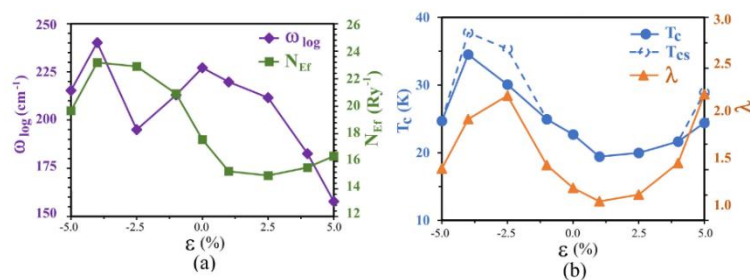

Figure 4. The ω_{log} and N_{Ef}, and (b) the T_c, T_{cs}, and λ of 2H-Mo_2N as a function of strain.

References

1. Kotmool, K., *et al*. *Phys. Chem. Chem. Phys*. 24(29), 17862 (2022).
2. Khammuang, S., *et al Phys. Chem. Chem. Phys*. 25(29), 19612 (2023).
3. Kotmool, K., *et al*. *arXiv* :2207.10863 (2022).
4. Thasitha, S., et al. *Phys. Chem. Chem. Phys*. (Under review).

Investigation of impurity formation and their influence on ion intercalation and phase transition in spinel-LiMn$_2$O$_4$ cathode upcycled from primary battery waste

Teeraphat Watcharatharapong[1]*, Adisak Boonchun[1], Weekit Sirisaksoontorn[2],
Rajeev Ahuja[3,4], Wei Luo[4]

[1] Department of Physics, Faculty of Science, Kasetsart University, Thailand,
[2] Department of Chemistry, Faculty of Science, Kasetsart University, Thailand,
[3] Department of Physics, Indian Institute of Technology (IIT) Ropar, India,
[4] Condensed Matter Theory Group, Materials Theory Division, Department of Physics and Astronomy, Uppsala University, Sweden
[*]teeraphat.wat@ku.th

Introduction

Amongst rising global demand for energy, battery upcycling is a necessary process to tackle environmental issues due to a huge number of spent primary batteries and generate economic benefits. In this study, we have focused on the upcycling of spinel-LiMn$_2$O$_4$ (LMO) from alkaline battery, which is the most used battery type and contains significant amounts of Mn element. However, there are also other metals, especially Zn residues, that possibly contaminate and affect the overall performance of upcycled LMO. Thus, calculations of density functional theory with Hubbard-U correction (DFT+U) were performed to explore the thermodynamics of defect formations in LMO, namely, native and metal contaminants (X = Zn, Al, Fe) and their plausible effects on ion intercalation kinetics and phase transition.

Methodology

All calculations have been performed using DFT as implemented in VASP code. To calculate defect formation energy, we demonstrated atomic chemical potential relation for elements in LMO and its thermodynamic boundary condition. Nudge elastic band method was used to determine migration energy of ion interaction. To study intercalation mechanism, a global minima structure of delithiated LMO configurations was searched from a number of sampled structures generated by Random Swapping Algorithm. Then, a convex hull method was used to identify meta-stable configurations that play a role in the prediction of voltage profiles for each doped LMO compound.

Results and Discussion

Based on the thermodynamic boundary condition, we have found that, besides Mn$_2$O$_3$, Mn$_3$O$_4$ and Li$_2$MnO$_3$, competing phases including Fe$_2$O$_3$, Li$_2$Si$_2$O$_3$, ZnO and Al$_2$O$_3$ could also define the stability region when impurities X are present in sample synthesis. The results of chemical potentials have been used to calculate defect formation energy under several conditions. For example, under X-rich condition, X substitution for Mn (Al$_{Mn}^0$ and Zn$_{Mn}^0$) and Zn substitution for Li (Zn$_{Li}^0$) was revealed to likely exist in contaminated LMO due to the low sdefect formation energies. The ion intercalation associated with these predicted dominate defects was studied based on vacancy-assisted diffusion using nudged-elastic band method. Migration energy of Li ion in the pristine LMO is in a range of 0.08-0.56 eV, which are dependent to the degree of Mn-O octahedral distortion in the corresponding migration channel. The results show that the presence of the impurities does not severely affect the power density of the cathode and even suggests an unblocked capacity of Zn/Li anti-site. We also investigated phase transformation of pristine and defective Zn-LMO during charge/discharge. Our results suggest an improved structural stability which may enable the utilization of extra capacity.
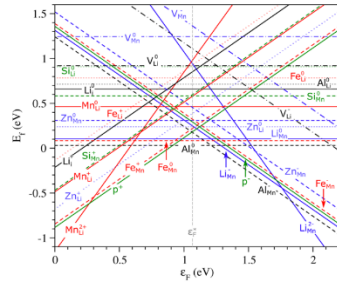
Figure 1. Formation energy (E_f) of native and metal impurities X in LMO under X-rich condition plotted against the Fermi level (ε_F) which is referenced to the valence band maximum of LMO corrected via band alignment. Slopes of each line indicates a charge state of defects.
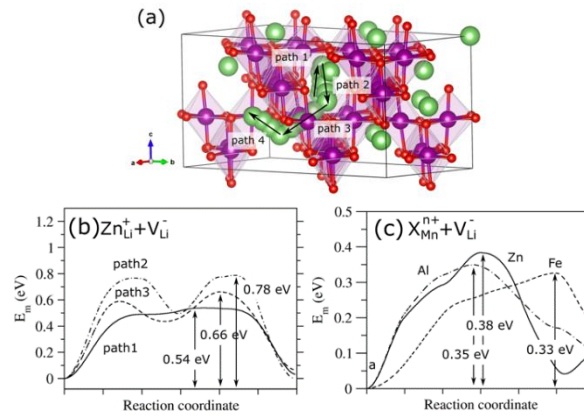

Figure 2. (a) Ion migration pathways in supercell LMO and migration energy of (b) Zn ion diffusion associated with Zn_{Li} formation in LMO and (c) that of Li ion diffusion in LMO with the presence of X_{Mn}.

First-principles Demonstration of Electronic Band Filling-induced Improvement in Thermodynamic Stability and Mechanical Properties of Tantalum Diboride

Annop Ektarawong

Abstract

In this presentation, I highlight how the stability as well as the elastic properties of metal diborides - promising alternatives for hard and protective coating materials for cutting tools - can feasibly be improved through the presence of structural defects and the alloying process, focusing particularly on tantalum diboride. The studies based on the first-principles calculations combined with the cluster-expansion method reveal the enhancement of the stability, stiffness, shear strength, and hardness of the diboride can be interpreted in terms of electronic band filling.

Why is the Reconstruction of Titania Surfaces So Complex?

Wutthikrai Busayaporn[1]* and Robert Lindsay[2]
[1]Synchrotron Light Research Institute (Public Organization),
Nakhon Ratchasima, 30000, Thailand
[2]Corrosion and Protection Centre, School of Materials,
The University of Manchester, Sackville Street, Manchester M13 9PL, United Kingdom
*wutthikrai@slri.or.th

Introduction

Titania remains one of the most well-known oxide surfaces in research for decades. Not mention only its primitive surfaces, but the study extended to the surface reconstruction, till the physisorption and chemisorption of the surfaces. While hundreds of the publications focused on more complicity of their surfaces e.g. the study of heterogeneous catalyst, on the other side, single-atom catalysis tends to be recently in spotlight. To understand the mechanism of any surface interactions, insightful of titania surface structures needs to be clearly determined.

Methodology

Low Energy Electron Diffraction in IV mode (LEED-IV) has been employed as this technique not only reveal the symmetry of the surface but also provide information of surface atomic structures via a set of IV-curves. To interpret the IV-curves, modified version of SATLEED code has been utilized to optimize the initial guess structure of the surfaces to the experimental IV-curves. Indicated by Pendry R-factor (R_p), the best fit structure will be nominated as the actual surface structure reconstruction. In the modified version of SATLEED, n terminations have been allowed to include into the optimization. This subversion of the program widens the opportunity to design the surface to the higher complexity but lower the symmetry. The controversial of this matter will also be discussed in the talk. Finally, the physisorption and chemisorption of the adatoms are predicted via the first principle calculation using the Density Functional Theory (DFT) with CRYSTAL package.

Results and Discussion

In the case of TiO_2 (110)(1x1) single row model of bridging oxygens has been concluded. However, TiO_2 (1x2) thermal transformation is still in debates. Comparison with various surface reconstruction models, Ti_2O_3 added row confirmed to be the dominant surface structure of simple (1x2) reconstruction of TiO_2 (110) reported in [1] as in Fig. 1 (a). However, the structure and formation of X-linked TiO_2 (110)(1x2) has not been validated. The simple and x-link reconstruction can be shown in the STM images in Fig. 1 (b). Hence, even the same LEED-IV technique as in [1], we found that Ti_2O_3 added row model can just make R_p reach to fair value at 0.36. Furthermore, two optimized Ti_2O_3 structures have been found with slightly differences in the heights of the topmost O atoms with R_p are 0.36 and 0.37. Also, the Ti_2O_3 added row structure can lead to consistent STM images just in double strands area but not yet in x-linked area. Lately, asymmetric surface structure of Ti_2O_3 added row has been proposed in [2]. In [2], the Total-reflection High-energy Positron Diffraction (TRHEPD) has been used to investigate the transformation of TiO_2 (110) from (1x1) to be (1x2) reconstruction. The TRHEPD showed that the asymmetric Ti_2O_3 added row model exhibits to be a good candidate of TiO_2 (110)(1x2)
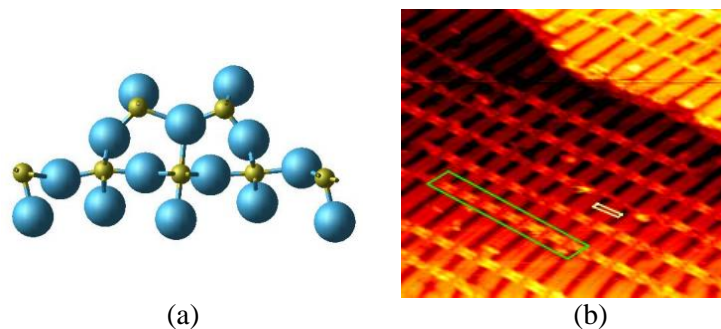
<div align="center">(a)   (b)</div>

Figure 1. (a) Model of the Ti_2O_3 added row represented to be the best candidate of the simple TiO_2 (110)(1x2) reconstruction and (b) STM image (176 $\mathring{A}^2$) of the x-linked TiO_2(110)(1x2) surface. A segment of x-links are marked by a green rectangle. The yellow rectangle indicates the (1x2) unit cell.

reconstruction. This discovery also is consistent with the calculation result from the evolutionary method using in [3]. The result of asymmetric model of Ti_2O_3 added row leads to possibilities that our previous two best-fit added rows might exist together on the surface simultaneously. Therefore, the modified SATLEED has been used with each half of the two best-fit models combine to be the new asymmetric model. Then LEED-IV has been optimized with this model. Result with the best Rp = 0.287 (from combination of structures with Rp = 0.36, 0.37).

Significance

This discovery leads to more understanding of the various existences of the TiO_2 (110)(1x2) surface reconstructions. Emphasize with asymmetric model which is in good agreement with experimental and theoretical conclusions, our work also reveal how these asymmetric structures appear together. This phenomenon can be summarized that the surface of titania may be "extensively soft" than our previous understanding.

References
1. M. Blanco-Rey, J. Abad, C. Rogero, J. Méndez, M. F. López, E. Román, J.A. Martín-Gago, and P. L. Andrés, Phys. Rev., B75, 081402(R) (2007). Einstein, A.B., Alex, A.H., and Glen, R. *Appl. Catal. A: General* 122, 289 (2000).
2. I. Mochizuki, H. Ariga, Y. Fukaya, K. Wada, M. Maekawa, A. Kawasuso, T. Shidara, K. Asakurab and T. Hyodoa, Phys. Chem. Chem. Phys, 18, 7085-7092 (2016).
3. Q. Wang, A. R. Oganov, Q. Zhu, and X. F. Zhou, Phys. Rev. Lett., 113, 266101, (2014)

# Computational Fluid Dynamics Simulation and Redesign of an Absorber Feed Tank

Yotsakorn Pratumwal[1] and <u>Somboon Otarawanna</u>[1]*
[1]National Metal and Materials Technology Center (MTEC),
National Science and Technology Development Agency (NSTDA),
*Pathum Thani 12120, Thailand*
*somboono@mtec.or.th

Introduction

In a wet-type flue gas desulfurization (FGD) system [1], SO_2 in the flue gas is absorbed by the limestone ($CaCO_3$) slurry in the desulfurization absorption tower. After that, the SO_2-containing slurry is transferred to the absorber feed tank (AFT) for removing SO_2. The absorbed SO_2 reacts with the dissolved $CaCO_3$ in the slurry and then $CaSO_3 \cdot 1/2\, H_2O$ is formed by the reaction:

$$SO_2 + CaCO_3 + 1/2\, H_2O \rightarrow CaSO_3 \cdot 1/2\, H_2O + CO_2 \qquad (Eq.1)$$
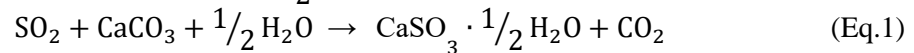
In the AFT, oxidation air is dispersed into the slurry to convert $CaSO_3 \cdot 1/2\, H_2O$ to gypsum ($CaSO_4 \cdot 2H_2O$) by the reaction:

$$CaSO_3 \cdot 1/2\, H_2O + 1/2\, O_2 + 1.5H_2O \rightarrow CaSO_4 \cdot 2H_2O \qquad (Eq.2)$$
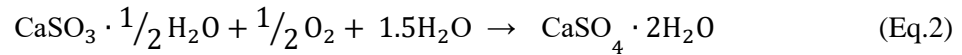
In this work, we studied an AFT experiencing a problem of relatively low SO_2-removal efficiency. The preliminary study suggested that the efficiency problem was due to the lack of O_2 in the reaction shown in Eq.2. In order to enhance the O_2 amount supplied for the reaction, this research focused on redesigning the AFT. Computational fluid dynamics (CFD) was utilized as a main tool in the redesign process.

Methodology

Ansys-CFX software was employed for performing CFD simulation. The CFD model setup was adapted from Ref.[2]. The original condition in the AFT was simulated to study the flow behavior. After analyzing the original condition, modification ideas were evaluated by CFD results. Subsequently, some modifications were implemented to the AFT system and tested for the **SO_2**-removal efficiency.

Results and Discussion

One of the main problems found in the existing system (Fig. 1) was the fact that the inlet and outlet locations of the slurry in the AFT were inappropriate. This led to the flow behavior that the slurry went into the AFT and then quickly left the AFT (Fig. 1). This means that the slurry was in the AFT for a relatively short time period. Consequently, there was not enough time for the slurry to effectively absorb oxygen for the desulfurization reaction. To remedy this problem, we adjusted the slurry inlet location in the AFT (Fig. 2). This change was aimed to promote the slurry circulation in the AFT. Apart from this change, the air dispersion holes were redesigned for increasing the activation area and alleviate the hole blockage problem. A number of CFD simulations were performed to find optimal configurations of the slurry inlet location and the air dispersion hole locations. After making the mentioned changes in the real system, the SO_2-removal efficiency significantly increased. This exemplifies the benefit of CFD simulation in analyzing the flow behavior in the AFT.

Significance

The AFT studied in this work has been operating in a coal-fired power plant in Thailand. The low SO_2-removal efficiency of the AFT led to hefty losses to the power plant. This is because sometimes the power plant had to lower the production capacity to avoid the over-limit SO_2 concentration in the environment or added a costly chemical into the slurry for improving the desulfurization reaction. The AFT redesign by the aid of CFD in this work has substantially improved the **SO_2**-removal efficiency. Consequently, the power plant has been able to save millions baht per annum since the AFT-redesign implementation.
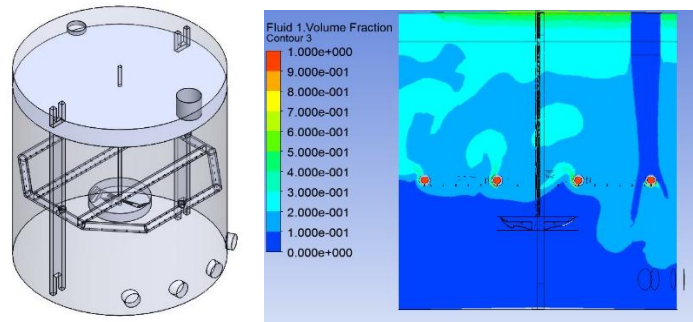
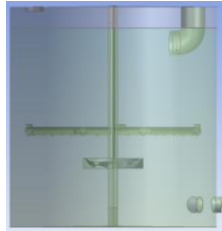**Figure 1.** Geometry of the AFT (left) and CFD result showing the air volume fraction (right)

Figure 2. Geometry of the redesigned AFT

References
1. Suarez-Ruiz, I. and Crelling, J.C. *Applied Coal Petrology: The Role of Petrology in Coal Utilization* (2018).
2. Kerdouss, F., Bannari, A. and Proulx, A. *Chem. Eng. Sci.* 61, 10 (2006).

Multidisciplinary Utilization of Computational Simulations in Acetylene Black Production and Development

Tarabordin Y. [1]*, Jirath S. [1], Piyanut I. [1], and Benchawan P. [1]
[1]IRPC Innovation center, Rayong, 21000 (Thailand)
*Tarabordin.yu@irpc.co.th

Introduction

IRPC Public Company Limited, a leader in Southeast Asia's petrochemical industry, has been manufacturing Acetylene Black (ACB) for over two decades. This study focuses on the multidisciplinary use of Computational Fluid Dynamics (CFD) and Process Simulation to optimize ACB production. By enhancing fluid dynamics understanding and improving process parameters, IRPC aims to increase efficiency, reduce downtime, and elevate product quality. Practical case studies will demonstrate these advancements, providing guidelines for other manufacturers in the industry.

Methodology

This study utilized both Process Simulation and Fluid Dynamics Simulation to optimize the production of Acetylene Black (ACB). The scale-up methodology is shown in Figure 1. Aspen Plus, a robust chemical process simulation software, was employed for Process Simulation. The chemical reactions and operational conditions, including pressure, temperature, and energy inputs, were modeled to predict material and energy balances. For Fluid Dynamics Simulation, ANSYS Fluent, a leading CFD software, was used. Detailed 3D models of the cracking furnace components, specifically the nozzle, were created to simulate fluid flow patterns. Accurate plant data were integrated to enhance the reliability of the simulations. Preliminary results included flow visualizations and quantitative parameters, which helped identify optimal operating conditions and potential risks. Lab-scale experiments and sample testing validated simulation predictions. This iterative process ensured that real-world conditions were closely matched, leading to successful scale-up and implementation in the production environment.

Results and Discussion

The application of advanced computational simulations has yielded significant improvements in the production of Acetylene Black (ACB). Firstly, a new high-dispersibility ACB grade with enhanced crystallinity was developed, leading to superior performance in end products. The refined microstructure allowed for denser packing and easier powder handling, which accelerated the mixing process and reduced overall processing time. Additionally, a 10% increase in electrical conductivity was achieved, which is crucial for applications requiring precise electrical performance. Production capacity was increased by 20% through process optimization, accomplished without the need for additional infrastructure. Furthermore, energy efficiency was significantly enhanced, with a reduction of 100 kWh per metric ton of product, thereby lowering production costs and reducing environmental impact.
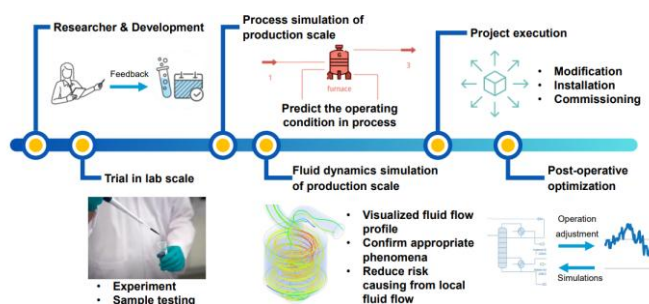

Figure 1. Methodology for Multidisciplinary Utilization of Computational Simulations

Figure 2. High-dispersibility ACB production by cracking furnace improvement

Significance

The integration of advanced computational simulations in ACB production has significantly enhanced product quality and operational efficiency. The development of a new ACB grade with better crystallinity and increased electrical conductivity opens new market opportunities. Production capacity increased by 20% without additional major implementation, while energy consumption was reduced by 100 kWh per metric ton, lowering costs and environmental impact. These advancements underscore the transformative potential of multidisciplinary computational approaches in industrial processes.

References

1. Nadimpalli, N. K. V., Buddhiraju, V. S., and Runkana, V. Adv. Powder Technol. 22, 141 (2011).

Improved engine wall models for Large Eddy Simulation (LES)

Chalermpol Plengsa-Ard

Department of Mechanical Engineering, Faculty of Engineering, Kasetsart University, Bangkok, Thailand

Abstract

Improved wall models for LES are presented in this research. The classical Werner-Wengle (WW) wall shear stress model was used along with the eddy viscosity near walls. A sub-grid scale turbulent kinetic energy was employed in a model for the eddy viscosity. To provide heat flux results, a modified classical variable-density wall heat transfer model, which includes the variation of the turbulent Prandtl number in the boundary layer, was also used. The fully turbulent developed flow in a square duct with constant wall temperature was used to validate the model and the friction factor and Nusselt number predictions are in good agreement with experimental results. The resulting time and spatially averaged velocity and temperature wall functions from the new wall models match well with the law-of-the-wall experimental data. Additionally, the model was validated using experimental data from a Caterpillar engine operated with conventional diesel combustion. The computational pressure and heat release are well predicted when comparing with the experimental measurements. There is successful matching between the predicted and measured wall heat fluxes of ten points on the piston surface. Compared with the previous RANS-based wall models, the new models generate more accurate predictions, which agree better with experimental data.
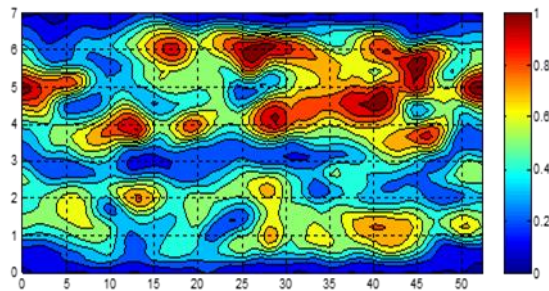
Contour plot of wall heat fluxes from LES (space average*)* based wall model in a square duct.
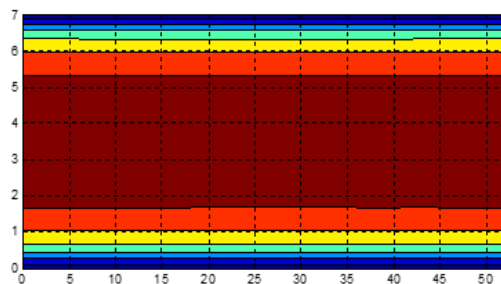
Contour plot of wall heat fluxes from RANS (time average) based wall model in a square duct

Ancient Mural Painting Deterioration Preservation using Computational Fluid Dynamics Approach: A case Study of Historical Temple In Ayutthaya, Thailand

Mongkol Kaewbumrung [1], Wasan Palasai[2] and Plengsa-Ard **Plengsa-Ard [*,3]**

[1] *Department of Mechanical Engineering, Faculty of Engineering and Architecture, Rajamangala University of Technology Suvarnabhumi,*
Phranakhon Si Ayutthaya 13000, Thailand.
[2] *Department of Mechanical Engineering, Faculty of Engineering,*
Princess of Naradhiwas University, Narathiwat, Thailand
[3] *Department of Mechanical Engineering, Faculty of Engineering,*
Kasetsart University, Bangkok, Thailand
[1]*(Italics, 8pt) Thailand University, Anytown, 55555 (Country)*
[2]*Fundamental Research Laboratory, Anytown, 44444-2222 (Country)*
*somchai.a@thaiuniversity.ac.th (corresponding author designated with a star)

Abstract

The preservation of ancient mural paintings is crucial for maintaining cultural heritage, particularly in historically significant sites like the temples of Ayutthaya, Thailand. These murals face various environmental challenges that contribute to their deterioration, including fluctuating temperature, humidity, and the presence of airborne pollutants. This study explores the use of Computational Fluid Dynamics (CFD) as an innovative approach to analyze and mitigate these adverse conditions, thereby aiding in the preservation of these invaluable artworks. The research begins with an extensive collection of environmental data within the temple, including temperature, humidity, and airflow patterns, alongside the physical characteristics of the temple structure and mural locations. A detailed 3D model of the temple is created, capturing all essential features that influence internal airflow. Using CFD software, simulations are set up to model the internal climate under various conditions. These simulations help in visualizing the airflow, temperature distribution, and pollutant dispersion, pinpointing areas where environmental factors are most detrimental to the murals. The analysis of CFD results reveals specific zones within the temple where conditions are conducive to mural deterioration. Based on these findings, preservation strategies are proposed. These include the implementation of climate control systems to regulate temperature and humidity, the use of physical barriers to protect murals from pollutants, and regular monitoring protocols to maintain optimal conditions. By accurately simulating and analyzing the environmental dynamics within the temple, targeted interventions can be designed and implemented, significantly enhancing the preservation of the ancient murals. The findings underscore the potential of CFD as a valuable tool in the ongoing battle to protect and preserve cultural heritage sites worldwide.

Enhanced Particle Dynamics Simulation in Pollution Control Systems: Integrating Electrostatic Modeling with Multiphase Flow Analysis

Ratchanon Piemjaiswang[1],*

[1]*Environmental Research Institute, Chulalongkorn University, Bangkok 10330 (Thailand)*
*ratchanon.p@chula.ac.th

Introduction

The seek for efficient pollution control in industrial processes has led to the development of sophisticated technologies designed to mitigate the release of particulate matter into the environment. Among these, cyclones and electrostatic precipitators have become pivotal in curbing emissions. However, the complexity of particle-fluid interactions within these systems presents significant challenges in predicting performance and optimizing design. To address this, the present study leverages advanced computational fluid dynamics (CFD) by employing the Euler-Euler multiphase flow model, augmented with the kinetic theory of granular flow. This approach enables a more nuanced simulation of particle behavior, particularly with the integration of electrostatic forces—a critical factor in the efficiency of electrostatic precipitators. By synthesizing these computational techniques, the study provides a comprehensive framework for improving the understanding of particle dynamics and enhancing the efficacy of pollution control mechanisms.

Methodology

The study utilized the Euler-Euler multiphase flow model, integrated with the kinetic theory of granular flow, to explore the intricate interactions and behavior of particles within the three-dimension electrostatic precipitator domain. To incorporate the effects of electrostatic forces, the study calculated the electric potential by solving the Poisson equation. Subsequently, the forces derived from the electric potential were applied to the particles as a momentum source term within the system. This modeling of particle behavior made use of Maxwell's equations, which include Gauss's law for electricity, Gauss's law for magnetism, Faraday's law of induction, and Ampere's law, to accurately simulate the influence of both electric and magnetic fields. The numerical implementation of the model was carried out using ANSYS Fluent 2023R2 to compare the flow patterns and particle behavior within the electrostatic precipitator, both with and without the influence of electrostatic forces.

Results and Discussion

The introduction of electrostatic model marked a substantial shift in the observed particle dynamics within the pollution control equipment, particularly in the behavior of particles in relation to the collecting plates of electrostatic precipitators. Prior to the inclusion of the electrostatic force model, the simulation results indicated that particles would travel through the system, make physical contact with the collecting plates, and subsequently fall into the collector below due to gravity. While the result of particle collection aligned with the expected outcomes of the equipment's operation, the mechanism by which particles reached the collectors was predominantly through direct collision and physical contact with the plates. This approach, while yielding correct end-state results, did not accurately reflect the nuanced process of electrostatic induction that is critical to the actual function of electrostatic precipitators. With the electrostatic force model integrated, the results showcased a different trajectory for the particles. Rather than solely relying on collision, the particles experienced forces due to the electric fields generated by the electrodes. This led to a significant alteration in the path of the particles; they were now actively influenced by the electrostatic attraction toward the collecting plates. The model demonstrated that the behavior of particles was predominantly governed by the electrostatic forces, which is a more accurate representation of the physical phenomena at play. The particles were induced to move towards the plates before physically contacting them, mirroring the real-life behavior within electrostatic precipitators where charged particles are drawn to oppositely charged surfaces. The

observed shift in particle dynamics underscores the importance of incorporating electrostatic forces in the simulation models for pollution control systems.

Significance

The inclusion of electrostatic forces in the simulation reflects a nuanced approach to modeling the behavior of charged particles. By solving for the electric potential using the Poisson equation, the study accounts for the influence of electrostatic phenomena on particle dynamics enhancing the model's fidelity and enabling a more realistic representation of particle behavior within the pollution control equipment. This capability is crucial for the design and improvement of electrostatic precipitators, which rely on electrical forces to remove particulate matter from exhaust gases. The implications of this work extend beyond pollution control, offering potential applications in various fields where the manipulation of particulate matter through electromagnetic forces is relevant. Overall, the study approach enhances the predictive capabilities of multiphase flow models and contributes to the development of more effective pollution control technologies.
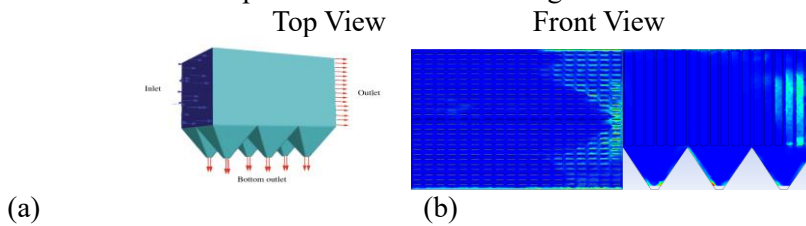

Figure 1. (a) 3D computational domain of the electrostatic precipitator, and (b) volume fraction contour of solid particle in the where bright solid green color indicated high volume fraction.

References

1. Rokkam, R.G., R.O. Fox, and M.E. Muhle, Computational fluid dynamics and electrostatic modeling of polymerization fluidized-bed reactors. Powder Technology, 2010. 203(2): p. 109-124.

Response Surface Methodology and Artificial Neural Network for Low-Temperature Spray Drying of *Saccharum Sinensis* Roxb.

P. Bumroongsri[1]*

[1]*Department of Chemical Engineering, Faculty of Engineering, Mahidol University, Phuttamonthon 4 Road, Nakhon Pathom 73170, Thailand*
*pornchai.bum@mahidol.ac.th

Introduction

In the case that there are numerous factors affecting bioactive compounds, it is essential to select the most effective factors for the optimal extraction of target compounds. Empirical models such as response surface methodology (RSM) and artificial neural network (ANN) can be used for determining the best operating condition based on experimental data. In this paper, low-temperature spray drying conditions of sugarcane (*Saccharum sinensis* Roxb.) were studied. RSM and ANN were applied to determining the optimal operating condition of the low-temperature spray drying process. The optimization was performed to obtain optimal bioactive properties (Igwilo et al., 2022; Molina-Cortés et al., 2023).

Methodology

The research methodology is given in Fig. 1. Response surface methodology (RSM) and artificial neural network (ANN) were applied to determining the optimal operating condition of low-temperature spray drying process that gave the highest values of sucrose yield, total phenolic content, total flavonoid content and antioxidant activity. Low-temperature spray drying process was performed under varying conditions of inlet air temperature for spray drying (70-90 °C), outlet air temperature for spray drying (40-60 °C), encapsulating agent concentration (30-50%) and total soluble solids (10-30%). Sucralose, a non-caloric sweetener, was then synthesized from sucrose.
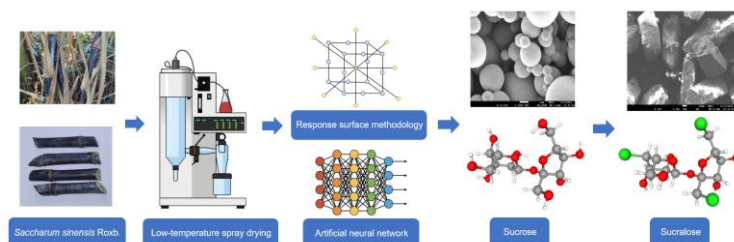

Figure 1. Research Methodology.

Results and Discussion

Figure 2 shows SEM images of dried powder obtained at the optimal operating condition of inlet air temperature 80 °C, outlet air temperature 50 °C, encapsulating agent concentration 40% and total soluble solids 20%. Particles of dried powder with smooth surface morphology could be obtained. This was in contrast with the high-temperature spray drying in which the formation of cracks in the dry skin occurred.
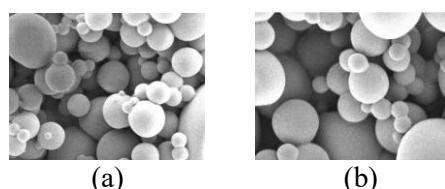

(a)　　　　　　(b)

Figure 2. SEM images of dried powder obtained by low-temperature spray drying at magnification of (a) 7,500 times and (b) 10,000 times.

Figure 3 shows effects of low-temperature spray drying conditions. Bioactive compounds were susceptible for thermal degradation during spray drying so too high temperature resulted in lower antioxidant activity. The addition of encapsulating agent was beneficial to protect sensitive compounds. However, too high encapsulating agent concentration resulted in the reduction in bioactive components. The maximum antioxidant activity was 6.47 mg Trolox equivalents (TE)/g dry weight.
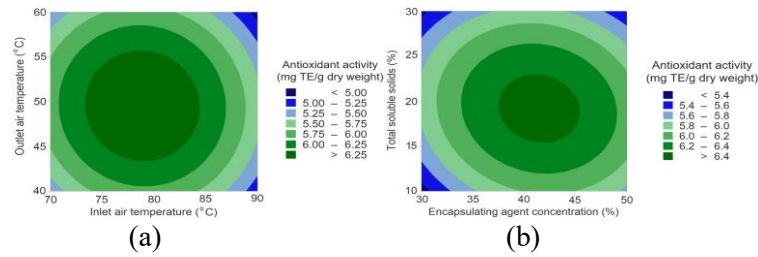
Figure 3. Contour plots for low-temperature spray drying conditions of (a) inlet and outlet air temperature and (b) encapsulating agent concentration and total soluble solids.

Significance

This paper proposes response surface methodology and artificial neural network for low-temperature spray drying of sugarcane (*Saccharum sinensis* Roxb.). The proposed method can predict output variables in order to obtain optimal bioactive properties.

References

1. Igwilo, C.N., Ude, N.C., Onoh, I.M., Enekwe, C.B., and Alieze, B.A. *Bioresource Technol. Rep.* 18, 101056 (2022).
2. Molina-Cortés, A., Quimbaya, M., Toro-Gomez, A., and Tobar-Tosse, F. *Heliyon* 9, e13276 (2023).

Molecular Simulation of Concurrent Natural Gas Production and Decarbonization in Unconventional Shale Reservoirs

Htet Myet Tun[1], Woranart Jonglertjunya[1], Sira Srinives[1], and <u>Poomiwat Phadungbut</u>[1]*

[1]*Department of Chemical Engineering, Faculty of Engineering, Mahidol University, Phuttamonthon, Nakhon Pathom, 73170 Thailand*
*poomiwat.pha@mahidol.edu

Introduction

In the face of pressing global concerns, the energy sector is at a crossroads, attempting to strike a balance between the need to reduce greenhouse gas emissions and the increasing demand for energy. This fine balance is particularly challenging to achieve in the context of natural gas production and decarbonization in unconventional shale reservoirs. To achieve this goal, it is vital to investigate the characteristics of pore structure in shale complex media. Various methods are used to evaluate the shale gas and CO_2 sequestration capacity throughout the process, from initial exploration and production. Volumetric and gravimetric adsorption are two approaches commonly used in the laboratory to explore adsorption behaviors under *in situ* temperature and pressure conditions. Experimental approaches, on the other hand, are typically costly and time- consuming, and the results are often subject to human error. As a result, experimental approaches are more likely to yield macroscopic information about adsorption under certain conditions. Therefore, our work aims to deepen the understandings of "microscopic" CO_2-enhanced shale gas recovery in organic shale reservoirs by molecular simulation. The findings shed light another perspective on the importance of raising awareness about the microporous shale formation as a potential source for shale gas retention and CO_2 capture.

Methodology

In this work, we were carried out a kinetic Monte Carlo (kMC) simulation since its advantage is rejection-free movement and accurate chemical potential (μ) without any extra computation like Widom insertion technique. In simulation, three ensembles of kMC (NVT, NPT, and μVT) were employed during first and second pressure drawdown of shale gas recovery. For the solid model, we chose an atomistic structure of graphitic slit pore with different nano- sized widths to mimic the ideal pore structure of organic shale matrix. All the solid-fluid and fluid-fluid interactions were modelled as combined Lennard-Jones 12-6 and Coulombic potentials. Apart from the CH_4 production and CO_2 storage capacities, the spatial distribution of molecules within the pore space were also analyzed to statistically disclose the preferred location.
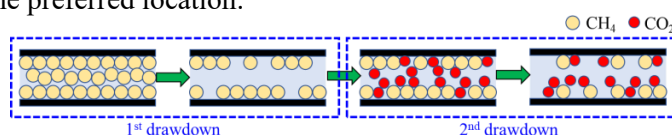

Figure 1. A simplified flow diagram of CO_2-enhanced shale gas recovery in the slit nanopore.

Results and Discussion

As presented in Figure 1, our work is divided into three sub-sections based on a flow process of CO2-enhanced shale gas recovery.

The first is associated with the primary production of shale gas via pressure drawdown. The μVT-kMC mode was utilized in this step. As expected, the left panel of Figure 2 shows that the lower the wellbore pressure, the less CH_4 storage capacity, indicating a higher production capacity. Interestingly, the storage capacity has peaked around ultramicropore-sized shale because the molecular distribution within the pore forms a tightly ordered monolayer packing. As a result, injecting CO_2 gas into the depleted shale ultramicropore would improve shale gas production while also permanently sequestering CO_2.

At the injection stage, we employed NVT-kMC simulation to mimic the CO_2 injection into the shale pore, followed by the computation of bulk-phase pressure with NPT ensemble. We raise the question to the audience whether CO_2 molecules compete for adsorption sites with CH_4 molecules or not?

After CO_2 is injected into shale pores, the secondary production occurs by pressure drawdown to the same wellbore pressure as primary production. At this stage, we assume that the bulk gas composition after CO_2 injection and after 2nd drawdown is identical, leading to the applicability of μVT-kMC ensemble again. It is obvious that it improves shale gas recovery by 15-50%, depending on pore width. However, we further ask the audience when CO_2 molecules partially leave the pore or additionally occupy the vacant location left by CH_4 desorption.
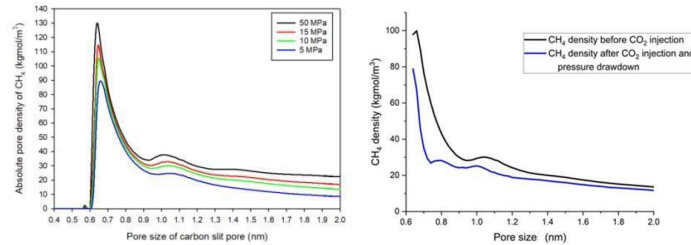

Figure 2. CH_4 adsorption capacity in graphitic slit pores with varying pore sizes for the primary and secondary production.

Significance
- A kMC scheme is newly developed for studying CO_2-enhanced shale gas recovery.
- From a chemical and petroleum engineering perspective, this work explores an alternative approach for improving shale gas recovery from depleted ultramicroporous reservoirs using CO_2 gas.
- From a chemical and environmental engineering perspective, this work proposes an alternative approach for deep underground CO_2 storage technology in ultramicroporous rock formations.

Utility Elicitation and Maximization from Uncertain Certainty Equivalents

Napat Rujeerapaiboon[1]* and Chunling Luo[2]*
[1]National University of Singapore (Singapore)
[2]Hangzhou Normal University (China)
*napat.rujeerapaiboon@nus.edu.sg

Introduction

We extend the literature on utility elicitation using an optimization approach taking as input certainty equivalents of the lotteries offering random payoffs. Unlike other known elicitation methods, ours is non-parametric and is always feasible even if reported certainty equivalents are erroneous. Suitable for all risk-averse individuals, the output of our elicitation method is an approximate utility function that is increasing, concave and piece-wise linear. We then demonstrate how our approximate utility functions lend themselves to data-driven expected utility maximization in both ambiguity-neutral and ambiguity-averse setups. Our findings are not only theoretical, but they are also supported by various experiments based on both synthetic and real-world data.

Examining Influences of Firm-level Employee E-voice on Firm-level Outcomes with Machine Learning Techniques

Tai, J.[1]*, Nguyen, H.[2], Kim, S.[3], Tea-makorn, P.[4]
[1]*University of Sydney Business School, Work & Organisational Studies (Australia)*
[2]*University of Sydney Business School, Work & Organisational Studies (Australia)*
[3]*University of Sydney Business School, Work & Organisational Studies (Australia)*
[4] *Sasin School of Management, Data Analytics Center (Thailand)*
*jewel.tai@sydney.edu.au

Introduction

Rapid development of web-based technologies and communication platforms in the workplace has sparked great scholarly interest in employees' use of digital tools like social media as important channels through which employee voice is expressed (Thornthwaite et al., 2020). Due to global exogenous shocks (e.g., COVID-19 pandemic), voice expressed online, or 'e-voice' (Walker, 2021) has become more prominent as employees and leaders quickly adopted social media tools to communicate remotely. Although it is well-known that employees often use e-voice channels to speak up and provide organizations with suggestions for improvements, we lack knowledge of firm-level e-voice and its outcomes. Text formats for e-voice are dominant in these channels, but severely underexamined in multiple dimensions of e-voice quantity, e-voice sentiment, and e-voice content heterogeneity at firm level. This study addresses numerous calls for more research into the use of technology and e-voice channels (Townsend et al., 2022) and engaging large volumes of firm-level data to examine this phenomenon. We focus on public and anonymous e-voice by analyzing employer reviews from Glassdoor. Hypothesis 1: There is a positive relationship between the interactive effects of firm-level dimensions of e-voice (quantity, content, sentiment) on firm-level satisfaction. Hypothesis 2: Firm-level satisfaction mediates the positive relationship between the interactive effects of firm-level e-voice dimensions and firm performance. (See Fig. 1 for research model)

Methodology

We chose three dimensions of e-voice to examine for interactive effects – (i) quantity, (ii) sentiment, and (iii) content heterogeneity. Our sample consisted of 309 firms across 12 years. Individual employer reviews from employer review platform Glassdoor were collected, where the textual content in the 'Advice to Management' section of reviews was operationalized as e-voice. We obtained firm-level data of the number of employees, assets, common equity, outstanding common shares, and annual price close data from Compustat, a standardized North American and global financial statement and market archival database of publicly traded companies. To measure e-voice quantity, we created a standardized e-voice ratio (E-voice ratio = No. of employees / No. of Reviews per year). We used Tobin's Q to measure firm performance. To measure sentiment of textual content, we applied machine learning techniques using the Python library *tweetnlp* to identify sentiment that involves natural language processing to determine and categorize the sentiment or emotional tone in the review and obtain sentiment scores for individual reviews. Subsequently, scores were aggregated to firm-level by year. To measure e-voice content heterogeneity, we first conducted topic modeling using the BERTopic language model to extract meaningful topics from text data. BERTopic analyzed the semantic relationships between words and the online context of e-voice to obtain meaningful topic clusters from textual conduct per 'Advice to Management'. From the results obtained through topic modeling, we followed Corritore et al.'s (2020) operationalization of heterogeneity in a firm to measure voice diversity. This is calculated as the mean Jensen-Shannon divergence between the topic probability distributions for all unordered pairs of reviews for that firm/year.

Results and Discussion

We obtained 338,157 reviews, which added up to 618,324 sentences. BERTopic identified 255 topics that were used to measure firms' content diversity. We conducted a fixed effects panel data analysis using STATA to highlight intra-firm variations over time. We found a significant three-way interaction between the dimensions of e-voice on firm performance ($\beta = .7786$(p<.05), supporting Hypothesis 1. We also found a significant indirect relationship between the interactive effects of e-voice dimensions and firm performance via firm-level employee satisfaction. These results supported Hypothesis 2.
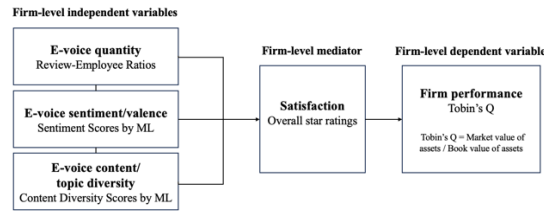
Figure 1: Hypothesized research model

Significance of our research

Our findings support resource-based theoretical perspectives of firm-level e-voice as a highly valuable resource that influences a firm's competitive advantage and improve firm performance. Employees' e-voice can be a social capital resource that has yet to be maximized, although it is easily accessible. We recommend future research into examining other similar platforms with different cultural contexts and affordances.

References

1. *Corritore, M., Goldberg, A., & Srivastava, S. B. (2020). Duality in Diversity: How Intrapersonal and Interpersonal Cultural Heterogeneity Relate to Firm Performance. Admin. Sci. Q., 65(2), 359–394. https://doi.org/10.1177/000183921984417 5*
2. *Thornthwaite, L., Macmillan, C., and Barnes, A. (2020) The internet, the web and social media: the promise and practice of e-voice. In: Wilkinson, A., Donaghey, J., & Dundon, T. (eds.), Handbook of Research on Employee Voice (pp. 509–523). Edward Elgar Publishing. https://doi.org/10.4337/9781788971188.00038*
3. *Townsend, K., Wilkinson, A., Dundon, T., & Mowbray, P. K. (2022). Tracking employee voice: developing the concept of voice pathways. Asia Pac. J. Hum. Resour., 60(2), 283–304. https://doi.org/10.1111/1744-7941.12271*
4. *Walker, M. (2021). Peer-to-peer online voice as emergent collective action. J. Ind. Relat., 63(5), 777–797. https://doi.org/10.1177/00221856211031940*

The BigTech-Bank Lending Ecosystem

Yiyao Wang and Ben Charoenwong[†]

Abstract

We develop a lending model featuring banks with low funding costs and bigtech lenders with superior data for screening borrowers. We derive and characterize the bigtech-bank lending ecosystem and show that a collaborative model featuring data sales dominate joint lending contracts and other collaboration models. Bigtech lenders serve as an on-ramp to the financial system by lending to risky borrowers and then selling borrowers' credit history data to banks, who take over subsequent lending. Bigtech-bank collaborations improve financial inclusion but reduce bigtech investment in screening technology, which has an ambiguous effect on social welfare. Regulatory restrictions on bigtech-bank collaborations can improve welfare when banks' funding costs are significantly lower than bigtech lenders.

JEL Classifications: G21, G23, G33, O32, O34, L84
Keywords: data selling, asymmetric information, relationship lending, fintech

A Short Story of Value Factors: Evidence from Thailand

Kanis Saengchote[1]* and Sampan Nettayanun[2] [1]
Chulalongkorn Business School, Bangkok, 10330 (Thailand) [2]Naresuan University, Phitsanulok, 65000 (Thailand)
* kanis@cbs.chula.ac.th (corresponding author)

Introduction

This study investigates the performance of equity factor investing using Thai stock data from July 2001 to April 2024. Equity factors are specific characteristics or attributes of stocks that can explain differences in returns. Common examples include value, momentum, and size [1]. Motivated by the need to optimize investment strategies, we examine the effectiveness of taking long and short positions in these equity factors [2], specifically focusing on value factors, which identify undervalued stocks. Long-short investment strategies involve taking long positions (buying stocks expected to increase in value) and short positions (selling stocks expected to decrease in value). This approach aims to profit from both rising and falling stock prices, balancing risks and returns, and has been documented to work well in Thailand [3].

The research is motivated by the need to understand how these strategies perform, especially considering the challenges and costs associated with short selling. By examining the added value of different equity factors, the study finds that most benefits come from long positions. These insights are crucial for investors and portfolio managers aiming to optimize their strategies and enhance investment performance. The objective is to provide practical guidance for constructing efficient portfolios that maximize returns while managing risks effectively.

Methodology

This study utilizes computational methods to analyze equity factors in the Thai stock market using data July 2001 to April 2024. The analysis is conducted using R. The primary data source is the Stock Exchange of Thailand's database, which provides comprehensive financial and market data. The value portfolios are constructed using a 2x3 sorting method [1] based on size and financial ratios, representing different aspects of the company leading to different versions of value factors. Specifically, we use eight versions: book-to-market ratio (bm), enterprise book-to-price ratio (ebp), sales-to-price ratio (sp), cash flow-to-price ratio (cfp), operating cash flow-to-price ratio (ocp), earnings-to-price ratio (ep), dividend-to-price ratio (dp), and EBITDA multiple (em).

To calculate excess returns, the average return of the long positions (large-cap and small- cap combined) and the average return of the short positions are calculated. These averages are then used to create a hedging portfolio, which neutralizes the market and size effects, isolating the performance attributable to the specific financial ratios [2]. Specifically, the long positions excess returns deduct the return of the hedging portfolio, while the short positions begin with the hedging portfolio and deduct the return of the short positions.

This method helps to assess the risk-adjusted returns of both long and short positions, providing more insights into the drivers of these investment strategies.

The t-statistic is a measure used to determine the statistical significance of excess returns. It is calculated by dividing the mean of the excess returns by the standard error for each strategy. The Sharpe ratio is then calculated by dividing the mean excess return by the standard deviation.

Results and Discussion

The long legs of value factors show robust performance with excess returns over the hedging portfolio ranging from 0.0014 to 0.0036 and Sharpe ratios between 0.25 and 0.77. In contrast, short legs, despite having higher Sharpe ratios in some cases (0.34 to 0.72), demonstrate significant t-statistics and Sharpe ratios up to 0.77, indicating enhanced risk-adjusted returns. These findings suggest that short positions for five out of eight value strategies offer better diversification and more stable returns, highlighting the potential challenges and limited effectiveness of short selling in factor-based portfolios.

Table 1. Excess returns of value strategies

Excess return	bm	ebp	sp	cfp	ocp	ep	dp	em
Long	**0.0028**	**0.0033**	**0.0029**	**0.0033**	**0.0036**	**0.0014**	**0.0019**	**0.0014**
t-statistic	2.15	2.36	2.23	2.54	3.60	1.27	1.73	1.17
Sharpe ratio	0.47	0.48	0.48	0.54	0.77	0.27	0.36	0.25
Short	**0.0029**	**0.0029**	**0.0029**	**0.0026**	**0.0032**	**0.0019**	**0.0026**	**0.0019**
t-statistic	3.63	3.22	3.22	2.36	2.67	1.46	2.17	1.58
Sharpe ratio	0.72	0.68	0.69	0.49	0.55	0.31	0.45	0.34
Long-short	**0.0057**	**0.0062**	**0.0059**	**0.0059**	**0.0067**	**0.0033**	**0.0045**	**0.0033**
t-statistic	3.00	3.10	3.28	2.95	3.72	1.74	2.50	1.65
Sharpe ratio	0.63	0.65	0.67	0.62	0.77	0.36	0.53	0.34
Short leg %	**50.9%**	**46.8%**	**49.2%**	**44.1%**	**47.8%**	**57.6%**	**57.8%**	**57.6%**

Significance

This study reveals that while long positions in factor-based portfolios offer superior returns, the short positions offer greater diversification and stability. However, short positions are constrained by higher costs and practical difficulties. This finding can reassure investors and portfolio managers that focusing on long legs in their value strategies can still offer reasonable excess returns over the hedging portfolio. By highlighting the limitations of short selling, this research provides practical guidance on constructing more efficient portfolios, ultimately leading to enhanced risk-adjusted performance and better investment outcomes.

References

1. Fama, E.F., and French, K.R. *Journal of Financial Economics*, 128(2), 234-252 (2018).
2. Blitz, D., Baltussen, G., and Vliet, P. v. *Financial Analysts Journal* 76(4), 73-99 (2020).
3. Charoenwong, B., Nettayanun, S., and Saengchote, K. *Pacific-Basin Finance Journal*, 69, 101647 (2021).

Text Analysis, Corporate Innovation Culture and ESG Performance in Emerging Markets

Stefano Starita
Chulalongkorn University, Thailand

Using Li et al.'s (2021b) culture dictionary, developed through word embedding machine learning models, we investigate the influence of corporate innovation culture on ESG performance. This process enabled us to assess several different text analysis techniques applied to the Thai language as well as to learn about the challenges of working with financial reports. After an extensive data cleaning process, aimed at addressing issues stemming from inconsistencies in reporting and incompatibilities with Thai fonts, we obtained a large dataset of listed companies over a time period between 2000 and 2021. Differing from previous research, our study focuses on companies listed on Thailand's stock exchange. Thailand's distinct economic and cultural contexts provide essential insights into the impact of innovation culture on the ESG performance of firms in emerging markets. Our findings reveal a statistically significant positive relationship, where a one-unit standard deviation increase in innovation culture corresponds to a 21.1% rise in ESG scores. This result is economically significant, underscoring the substantial benefits of nurturing an innovative culture within organizations in emerging economies like Thailand. Additionally, our results hold true across various econometric estimation techniques and align with stakeholder, institutional, and legitimacy theories.

Important Role of CO_2 in C-N and C-C Bond Formation via Copper- Catalyzed Electrochemical Reduction

Mu-Jeng Cheng

Department of Chemistry, National Cheng Kung University, Tainan, Taiwan
*E-mail: mjcheng@mail.ncku.edu.tw

Abstract

The electrochemical reduction of CO_2 (CO_2ER) presents a promising pathway to carbon neutrality and offers innovative strategies for fossil fuel utilization. While the majority of studies have emphasized C–C formation via *CO and its coupling with *C_1 intermediates, the capability of direct CO_2 coupling with *C_1 intermediates is less charted. Our DFT calculations examining CO_2 + *C_1 interactions on copper reveal CO_2's superiority over *CO for C–C bond creation. Additionally, co-electrolysis of CO_2 with nitrogen compounds generates valuable C–N bonds. In our examination of C–N bond formation during CO_2 and NO_3^-/NO_2^- co-reduction on copper, we identified that the C–N bond originates directly from gaseous CO_2 coupling with surface-bounded *N_1 intermediates, following the Eley–Rideal mechanism. This discovery challenges conventional perspectives that depended on CO_2ER intermediates, notably *CO. Collectively, our DFT insights underscore CO_2's pivotal role in both C-C and C-N bond formations.

Keywords: C-C Formation, C-N Formation, CO_2 Reduction, Co-Electrolysis, Urea

References:

1. Li et al. "Linking CO to Urea Production from CO_2 and NO_3^-/NO_2^- Co-Electrolysis on Transition Metals" *J. Phys. Chem. C* **2024**, 128, 1058.
2. Lin et al. "Identification of CO_2 as a Reactive Reagent for C-C Bond Formation via Copper-Catalyzed Electrochemical Reduction" *ACS Catalysis* **2023**, 13,11697.
3. Shin et al. "Copper with an atomic-scale spacing for efficient electrocatalytic co- reduction of carbon dioxide and nitrate to urea" *Energy Environ. Sci.* **2023**, 16, 2003
4. Yang et al. "Gaseous CO_2 Couplings with N-Containing Intermediates for Key C-N Bond Formation during Urea Production from Co-Electrolysis over Cu" *ACS Catalysis* **2022**, 12, 11494.

Mechanisms and the Role of Lewis Acids in Transition Metal Catalysts for C-O, C-F, and H-H Activation

Panida Surawatanawong,[1,*] Thanapat Worakul[1], Kajjana Boonpalit[1], and Chayapat Uthayopas[1]

[1]*Department of Chemistry and Center of Excellence for Innovation in Chemistry, Faculty of Science, Mahidol University, Thailand*
*panida.sur@mahidol.ac.th

Introduction

The development of transition metal catalysts for the transformation and functionalization of organic compounds is crucial for the pharmaceuticals and fine chemical industry. Density functional calculations were performed to give insights into the mechanisms and the role of Lewis acids in transition metal catalysts for C-O, C-F, and H-H activation.

Methodology

Density functional calculations of all structures were optimized in gas phase in Gaussian 16. Frequency calculations were carried out to obtain thermodynamic properties and to verify that the optimized geometries containing no imaginary frequency correspond to minima and those with one imaginary frequency correspond to transition states. The intrinsic reaction coordinate (IRC) calculations were performed to verify that the transition state structure leads to the expected intermediates in the reaction. The continuum solvation model with the solvent parameters was used to calculate the solvent-corrected relative free energies.

Results and Discussion

In the C-O activation process, nickel complex with N-heterocyclic carbene (Ni-SIPr) has been shown to selectively catalyze C−O bond hydrogenolysis of aryl methyl ether to obtain arene and alcohol as the only products. The Lewis acid $AlMe_3$ was found to facilitate aryl C–O bond activation via the five-centered transition state by forming a Lewis acid/base adduct with 2-methoxynaphthalene (NaphOMe) with the interaction from the Me group of $AlMe_3$ to Ni.

Then, we investigated the C-F activation in the hydrodefluorination of CF_3-substituted aniline derivatives, $CF_3(C_6H_4)NMe_2$, by the Ru–S complex, $[(PEt_3)Ru(DmpS)]^+$ (DmpS = 2,6-dimesitylphenyl thiolate) with $HSiMe_2Ph$ and with HAl^iBu_2. The Si-H activation on Ru-S generates Ru–H with thiosilane ligand, in which the Si-S bond must be cleaved to generate the active silylium moiety for the fluoride abstraction. In contrast, the Al-H activation of HAl^iBu_2 leads to the formation of Ru–H with the alumenium ($^+Al^iBu_2$), stabilized by the donation from both $\Box$(Ru–H) and sulfur lone pair.

For the H_2 activation, the nickel-borane complex, $Ni[(Mes)B(o-Ph_2PC_6H_4)_2]$, has been reported as an efficient catalyst for styrene hydrogenation. Following the H_2 activation, the resulting *trans*-dihydride nickel-alane complex has higher negative charges on both terminal and bridging hydrogen atoms than the corresponding nickel-borane complex. With the higher hydricity of hydrogen, nickel−alane is expected to be more reactive toward hydrogenation of styrene than nickel-borane.

Significance

The role of Lewis acids in forming different types of interaction with transition metals affects their catalytic activities toward C-O, C-F, and H-H activation. The insights into the difference in the structures and activities will assist with the development of transition metal catalysts.

References

1. Worakul, T. and Surawatanawong, P. *Organometallics* 42, 896 (2023).
2. Boonpalit, K., Uthayopas, C., and Surawatanawong, P. *Organometallics* 41, 259 (2022).
3. Uthayopas, C. and Surawatanawong, P. *Dalton Trans.* 48, 7817 (2019).
4. Wititsuwannakul, T., Tantirungrotechai, Y., and Surawatanawong, P. *ACS Catal.* 6, 1477 (2016).
5. Sawatlon, B., Wititsuwannakul, T., Tantirungrotechai, Y., and Surawatanawong, P. *Dalton Trans.* 43, 18123 (2014).

Preferential Door for Ligand Binding/Unbinding Pathways toward Organophosphate-Inhibited HuAChE

**Kowit Hengphasatporn[1]*, Nalinee Kongkaew[2], Thanyada Rungrotmongkol[2,3],
Ryuhei Harada[1], Yasuteru Shigeta[1]**
[1]*Center for Computational Sciences, University of Tsukuba, Tsukuba, Ibaraki, Japan.*
[2] *Program in Bioinformatics and Computational Biology, Graduate School, Chulalongkorn
University, Bangkok, Thailand.*
[3] *Center of Excellence in Structural and Computational Biology, Department of Biochemistry,
Faculty of Science, Chulalongkorn University, Bangkok, Thailand.*
kowith@ccs.tsukuba.ac.jp

Introduction

The widespread use of organophosphate (OP) pesticides, driven by global population growth and increasing food demands, poses significant health and environmental risks. These pesticides disrupt human acetylcholinesterase (HuAChE) and nerve impulse regulation. The FDA-endorsed antidote, 2-Pralidoxime (2-PAM), effectively detoxifies OP-inhibited HuAChE [1]. In this study, the binding pathways of 2-PAM are unveiled for the first-time using the Ligand-Binding Parallel Cascade Selection Molecular Dynamics (LB-PaCS-MD) technique [2].

Methodology

In the trajectory analysis of LB-PaCS-MD binding and unbinding trials, the routes of 2-PAM and phosphorylated 2-PAM (2-PAM-POX) within HuAChE were determined by calculating distances to specific residues representing different doors of the enzyme. Distances from the center of mass (COM) of these compounds to key residues (Y341 for acyl door, V73 for side door, and Y133 for back door) were normalized, smoothed, and graphed using Origin software. During unbinding, a 2D plot illustrated exit pathways of the product based on distances between its COM and representative amino acids (Y341, V73, Y133) as well as to the hydroxyl O atom of S203. Binding modes were discerned by measuring distance (d_{OP}) between the oxime O atom of 2-PAM and the P atom of S203-POX, and by calculating the angle (θ_{OPO}) among the oxime O atom, P atom of S203-POX, and O atom of S203. This analysis revealed two binding conformations: in-line ($120° < \theta_{OPO} < 180°$) and adjacent ($\theta_{OPO} < 120°$). The CPPTRAJ program was used for distance measurements throughout.

Results and Discussion

The results indicate that 2-PAM predominantly enters the inhibited HuAChE through the acyl door, accounting for approximately 81%. Additionally, there are minor occurrences of entry through the side door (10%) and back door (8%). Although these alternative pathways are observed, their lower frequencies suggest that the acyl door is the primary route for 2-PAM entry into the enzyme, while the side and back doors may serve as supplementary pathways. After 2-PAM approaches S203-POX, two observed binding modes, in-line and adjacent, are identified. The binding conformation with an in-line mechanism via the acyl door is present at 64%, while side and back doors exhibit adjacent binding conformations. Obviously, the in-line binding mode was mainly found when 2-PAM entered through the acyl door. In contrast, the adjacent mode was observed regardless of the entrance door utilized. Conformational shifts in key residues (W86, Y341, and Y449) and the Ω loop influence door dynamics and binding conformation. These insights provide a promising guide for future oxime design, effectively addressing challenges posed by OP pesticides.

Significance

In conclusion, the LB-PaCS-MD technique effectively computationally elucidates both ligand-binding and ligand-unbinding pathways in HuAChE. In addition, the hybrid conformation search, LB-PaCS-MD/OFLOOD, can be used to calculate FELs, allowing one to elucidate ligand-binding/unbinding pathways quantitatively and search for extremely rare binding/unbinding pathways that may be difficult to observe using traditional MD simulations. Our analyses revealed the three potential entrances (acyl, side, and back doors) and two (in-line and adjacent) modes for 2-PAM binding. Notably, the acyl door was a preferential entrance of 2-PAM and facilitated the in-line binding conformation and release of the

final product, 2-PAM-POX. Quantitatively, both structural and energetic assessment suggest that 2-PAM can cause the nucleophilic attack with the P atom of 2-PAM-POX. Additionally, the analysis of the dynamics of the conserved AAAs suggests that they play a pivotal role in the ligand-binding and unbinding processes. Although ligands can enter HuAChE through three doors, this study demonstrated that only the acyl and back doors could potentially serve as exit doors for this product. The release of the product through the back door could be observed using an advanced hybrid enhanced sampling method in future studies.
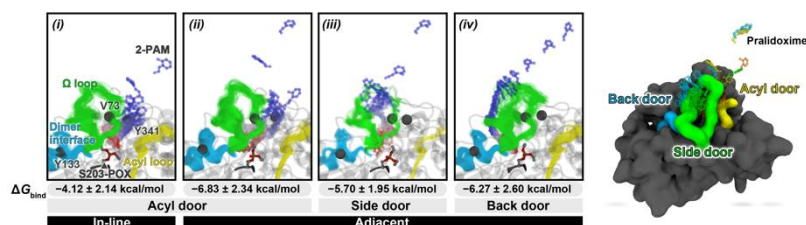

Figure 1. Reaction mechanism of catalyst XYZ. Note format of figures, text wrapping may be used.

References

[1] J.E. Chambers, H.W. Chambers, K.E. Funck, E.C. Meek, R.B. Pringle, M.K. Ross, Efficacy of novel phenoxyalkyl pyridinium oximes as brain-penetrating reactivators of cholinesterase inhibited by surrogates of sarin and VX, Chem Biol Interact 259 (2016) 154-159.

[2] H. Aida, Y. Shigeta, R. Harada, Ligand Binding Path Sampling Based on Parallel Cascade Selection Molecular Dynamics: LB-PaCS-MD, Materials (Basel) 15 (2022).

Theoretical Study of Metal-Hydrogen Interaction in Metal Nanoparticles

Takayoshi Ishimoto[1]
[1]Hiroshima University, Hiroshima, 739-8527 (Japan)
*tishimo@hiroshima-u.ac.jp

Introduction

The behavior of hydrogen (H) in the material has extensively attracted attention in the proton conduction, hydrogen absorption, and so on. In particular, the interaction between hydrogen and transition metals is dominant factor to control the absorption and diffusion properties of H in the metal. In these analyses, the deuterium (D) substitution from H are used to obtain the detailed information of the difference of H/D behavior. The H/D isotope effects are extensively studied by both experimental and theoretical approaches to understand the quantum mechanical principles. Generally, H/D isotope effects are induced by the difference of quantum nature of proton and deuteron. The quantum effects are clarified, such as zero-point energy, nuclear tunneling, vibrational excitation, and so on. The H/D isotope effects are observed in the various fields in chemistry, biochemistry, physics, and other related fields.

Palladium (Pd) is well-known as a hydrogen storage metal under ambient temperature and pressure. Pd-H systems have been extensively studied, not only for their industrial applications but also for their physicochemical properties. Pd, having a face-centered cubic (fcc) structure, has two possible types of hydrogen absorption sites, that is octahedral (O) and tetrahedral (T) sites. It is known that the hydrogen atoms are located only at the O site at ambient temperature and H_2 pressure in Pd bulk. Recently, many important experimental observations have been reported about the hydrogen storage in metal nanoparticles. These inhomogeneous properties of metal nanoparticles affect the unique hydrogen absorption properties. To understand the new hydrogen absorption properties in metal nanoparticles, we theoretically investigated the hydrogen absorption in Pd nanoparticles, adopting the Pd_{405} model of ca. 2.5 nm by using density functional theory[1].

Methodology

Density functional theory (DFT) calculations were performed using the Vienna ab initio simulation package (VASP) with the projector augmented wave (PAW) method. The Perdew-Burke-Ernzefhof (PBE) exchange and correlation functional was used under generalized gradient approximations. The cut-off energy was set to be 400 eV. 1 x 1 x 1 k-points were sampled by the Monkhorst-Pack grid method. We used the Bader approach to calculate atomic chages based on the VASP results. The Pd nanoparticle structure was put in a cubic cell for DFT calculation. The cell size was determined using PBC from a 10 A vacuum region with particle size of model for all x, y, and z directions to avoid interaction between nanoparticles during the DFT calculation.

Results and Discussion

After geometry optimization of Pd_{405}, we clearly found the inhomogeneous geometric features, especially near the surface region. Next, we placed one hydrogen atom into O and T site of optimized Pd_{405} to consider all possible absorption sites. The hydrogen absorption energy in the Pd_{405} nanoparticle was calculated using following equation:

$$Eabs = E(Pd_{405}H) - (E(Pd_{405}) + 1/2(E(H_2))).$$

We found volume expiation of O and T sites after hydrogen absorption, especially near the surface region. In the core part, the hydrogen absorption energies in O and T sites showed a trend similar to that of Pd balk as shown in Fig. 1. We theoretically demonstrated the possibility of hydrogen absorption in T sites near the surface of the Pd nanoparticle. The flexible volume change near the surface and the difference in hydrogen position are strong indicators of stable hydrogen absorption in T sites in the Pd nanoparticles.

Recently, we are developing new approach, which is the combined plane wave and localized basis sets (CPLB) method, to consider high accuracy in large inhomogeneous system. We will introduce the

theoretical background and some applications for metal-hydrogen interaction systems using CPLB method [2].
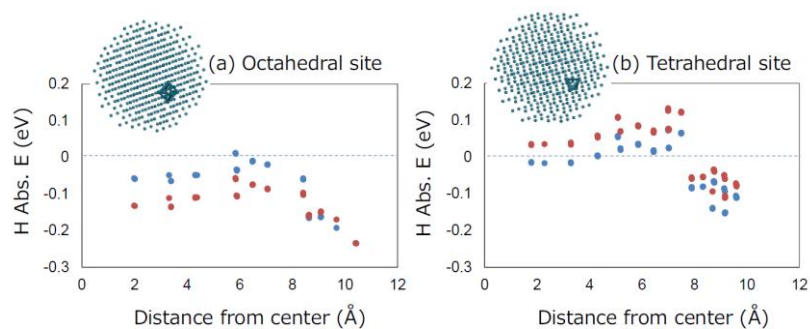

Figure 1. Hydrogen absorption energy of (a) octahedral and (b) tetrahedral sites without (blue) and with (red) zero-point energy (ZPE) correction for $Pd_{405}H$. Examples of octahedral and tetrahedral sites in $Pd_{405}H$ are also shown.

References
1. T. Ishimoto and M. Koyama, *J. Chem. Phys.* 148, 034705 (2018).
2. T. Ishimoto and H. Kai. *Int. J. Quantum Chem.* 118, e25452 (2018).

The Curious Case of Modeling Single File Diffusion

Chia-Yi Lin, Pei-Ying Lin, <u>Cheng-chau Chiu</u>*
National Sun Yat-sen University, Kaohsiung 80424, Taiwan, R.O.C)
*ccchiu@mail.nsysu.edu.tw

Introduction

When a porous material features very narrow channels, the gas diffusion through the material follows a phenomenon called "single-file diffusion" (SFD). The key feature of this phenomenon is that molecules cannot diffuse past each other. In other words, the gas molecules desorb from the permeate side of the channel in the same order as they have entered at the feed side of the channel. This unique behavior can be exploited for gas separation processes: When the channels of porous materials are sufficiently wide, the selectivity for gas separation is typically determined by the selectivity of the gas adsorption and the diffusion processes. A more exothermic adsorption and a higher diffusivity for a gas type typically means that the gas will be enriched in the permeate. However, when SFD occurs, the slowest-moving gas species will limit the diffusivity of all gas molecules moving in a channel. This minimizes the impact of the diffusivity on the selectivity of the gas separation. This phenomenon is, for instance, found in USTA-280, a metal-organic framework (MOF) with one-dimensional channels, which can be used to separate CO_2 and N_2, the main components of flue gas. [1] In the presentation, we will use the CO_2/N_2 separation *via* a USTA-280 membrane as an example to discuss the suitability of different kinetic models to describe SFD.

Methodology

Diffusion barriers and adsorption energies for N_2 and CO_2 have been computed at the DFT-PBE level and used to derive the rate constants for the adsorption/desorption processes as well as for the diffusion of the gas molecules from one unit cell to the next. Based on these values, a kinetic Monte Carlo (kMC) model and a micro-kinetic (MK) model that describes the diffusion of N_2/CO_2 has been set up. In the kMC model, each molecule's position in the channels is explicitly considered, and the diffusion and sorption steps are modeled as stochastic processes. In contrast, the MK model considers the coverage rates of the different gas molecules at the different positions of a channel and describes the gas diffusion with a set of differential equations.

Results and Discussion

Simulations using the kMC method, see Figure 1, can qualitatively reproduce the experimental observation that the CO_2 content in a CO_2/N_2 mixture will be enriched after diffusing through a USTA-280 membrane. It also shows that the composition of the permeate essentially aligns with the adsorbate composition on the feed side of the gas/solid interface. The simulated CO_2 composition in the permeate increases as the width of the modeled membrane increases. This is related to the circumstance that compared to N_2, CO_2 features much higher diffusion barriers in USTA-280. If there is one CO_2 molecule in a channel of the USTA-280 membrane, the diffusion of N_2 through that particular channel will be slowed down significantly, and the number of N_2 molecules that pass through the membrane is limited. However, if the channel is shorter, the probability of having a CO_2 molecule in it is reduced. If there is no CO_2 in the channel, the N_2 molecules can rapidly diffuse through the channel, leading to decreased CO_2 composition in the permeate.

This finding shows the necessity of correctly describing the width of the membrane in the computational model. However, the involved computational costs do not always allow one to set up a kMC model that matches the dimensions of the experimental reference. Thus, we have considered the computationally more affordable MK model. Interestingly, upon using the same DFT data, the MK predicts a fundamentally different behavior: Instead of a high CO_2 selectivity, an enrichment of N_2 in the permeate is predicted, which becomes even more pronounced as the modeled channels become longer. This behavior is because the MK model refrains from explicitly modeling the gas molecules' position, making it impossible to describe the blocking of a channel by the slowly moving CO_2 molecules, which is characteristic of SFD.

Significance

On the one hand, this work provides a better understanding of the limitations of the different models in simulating SFD. On the other hand, the work shows that the kMC model can be a useful tool to visualize the molecular processes that control the selectivity of the gas separation process when SFD occurs.
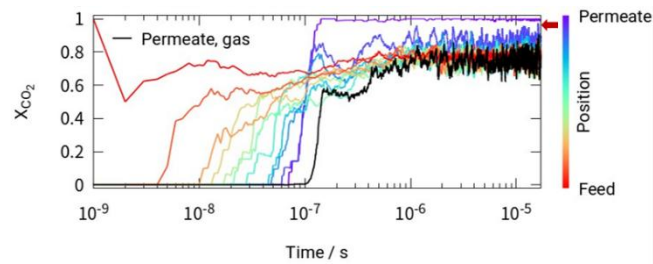

Figure 1. kMC results for the simulation of CO_2/N_2 separation with a USTA-280 membrane. The membrane modes has width of 100 unit cells and the CO_2 mole faction in the feed is set to 0.05. The graph shows the CO_2 mole fraction in the gaseous permeate (black) and at different positions inside the USTA-280 channel. The red arrow marks the experimentally measured CO_2 mole fraction in the permeate.

References

1. Hsu, C.-H., Lin, C.-Y., Lin, P.-Y., Chiu, C.-c. and Kang, D.-Y., **preprint**, DOI:10.2139/SSRN.4731910.

Enhancing Efficiency of Metal-Sulfur Batteries Cathodes using Two-dimensional Materials

Thanayut Kaewmaraya[1,2*], Nipat Thatsami[1], Tanveer Hussain[3], Parinya Tangpakonsab[1], Pornsawan Sikam[4,5]

[1]*Department of Physics, Khon Kaen University, Khon Kaen, Thailand*
[2]*Institute of Nanomaterials Research and Innovation for Energy (IN-RIE), NANOTEC -KKU RNN on Nanomaterials Research and Innovation for Energy, Khon Kaen University, Khon Kaen, 40002, Thailand*
[3]*School of Science and Technology, University of New England, Armidale, New South Wales 2351, Australia*
[4]*Office of Research Administration, Chiang Mai University, Chiang Mai, 50200, Thailand*
[5]*Center of Excellence in Materials Science and Technology, Materials Science Research Center, Faculty of Science, Chiang Mai University, 50200, Thailand*
*thakaew@kku.ac.th

Introduction

Li-ion batteries (LIBs) are currently the mainstream energy storage devices for portable electronics and electric vehicles (EVs). However, the relatively low abundance of lithium resources is one of the major barriers for extended driving range EVs and the ever-increasing large-scale storage. In this regard, alternative battery technologies offering high energy density and cost effectiveness are of importance. Room-temperature metal-sulfur batteries (including Li- S and Na-S batteries) have recently emerged as one of the feasible candidates because of the ultrahigh theoretical energy density and naturally abundant electrode materials (*i.e.*, sodium and sulfur). Nevertheless, the commercial viability of these batteries remains hindered by the shuttle effect, poor electrical conductivity of sulfur, and sluggish electrochemistry. Herein, this talk presents the use of generic two-dimensional (2D) materials as cathode hosting materials to solve the mentioned issues.

Methodology

Density functional theory (DFT) *via* planewave-based Vianna *Ab-initio* Simulation Package (VASP) was utilized to unravel key fundamental aspects namely interfacial interactions of lithium/sodium polysulfides (Li_2S_n and Na_2S_n; $1 \leq n \leq 8$) with cathode hosting 2D materials, electronic properties, electrochemical sulfur reduction reaction (SRR). Additionally, ionic diffusion was probed by the Nudged Elastic Band (NEB) method.

Results and Discussion

Our findings indicate that 2D materials (including nanoporous graphene, transition metal dichalcogenides, MXenes, and As_2S_3) can effectively inhibit the shuttle effect because they bind with lithium/sodium polysulfides stronger than the electrolytes do as shown in Fig. 1. This prominent binding is ascribed to the immense ionic bonds between the 2D materials and polysulfides. Moreover, such materials are excellent electrical conductors which ensure the efficient electrochemical process during the redox reaction. Importantly, they also catalyze the electrochemical reactions by reducing the energy barriers of conversions among the redox intermediates in SRR and diffusion barriers of Na+ and Li+ ions as shown in Fig. 2. Hence, 2D materials conclusively offers the advantages for enhancing the efficiencies of Li-S and Li-S batteries *via* suppressing polysulfide shuttling and promoting electrochemical kinetics.

Significance

Beyond the reported applications of 2D materials as electrodes in ubiquitous LIBs, this work highlights their novel functionality as an electrode material to solve the intrinsic challenges of Li-S and Na-S batteries which are among the promising contenders for extended driving range EVs and grid-scale energy storage devices. Consequently, their technological Readiness Level (TRL) can be lifted.
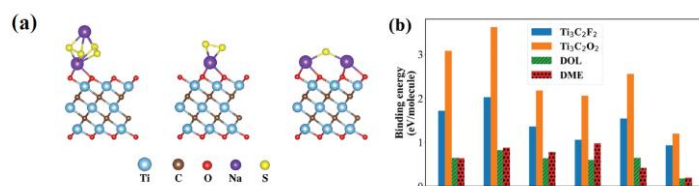
Figure 1. (Left) Relaxed atomic orientations of sodium polysulfides Na$_2$S$_n$ on Ti$_3$C$_2$O$_2$ MXenes and (right) comparative binding energies of Na$_2$S$_n$ on Ti$_3$C$_2$O$_2$ as compared with Na$_2$S$_n$ and conventional electrolytes such as 1,2-dimethoxyethane (DME) and 1,3-dioxolane (DOL).
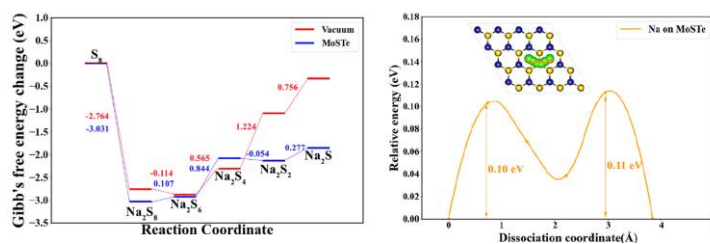

Figure 2. (Left) Gibbs free energy change of the sulfur reduction reaction (SRR) at room temperature 298.15 K and (right) ionic diffusion barrier of a Na$^+$ on Janus MoSTe.

References

1. Kaewmaraya, T., Thatsami, N., Tangpakonsab, P., Klinkla, R., Kotmool, K., Hussian, T., *Journal of Power Sources* 585, 233639 (2023).
2. Thatsami, N., Tangpakonsab, P., Moontragoon, P., Umer, R., Hussain, T., Kaewmaraya, T., *Phys. Chem. Chem. Phys*. 24, 4187–4195 (2022).

Microkinetic Molecular Volcano Plots for Enhanced Catalyst Selectivity and Activity Predictions

Thanapat Worakul[1] **Rubén Laplaza**[1,2]**, Shubhajit Das**[1]**, Matthew D. Wodrich**[1,2] **and Clemence Corminboeuf**[1,2]*****

[1]*Laboratory for Computational Molecular Design, Institute of Chemical Sciences and Engineering, École Polytechnique Fédérale de Lausanne (EPFL), 1015 Lausanne, Switzerland* [2]*National Center for Competence in Research-Catalysis (NCCR-Catalysis), Ecole Polytechnique Fédérale de Lausanne (EPFL), 1015 Lausanne, Switzerland*
**clemence.corminboeuf@epfl.ch*

Introduction

Volcano plots and 2D activity maps,[1] derived from linear free energy scaling relationships, are valuable tools for predicting and rationalizing catalytic properties. By exploiting the Sabatier's principle these tools enable rapid identification of optimal catalysts through visual representations that correlate catalytic performance with a key energetic descriptor representative of the catalytic cycle. This work combines the rapid screening ability of molecular volcano plots with microkinetic modeling to create the next-generation of *microkinetic volcano plots* that predict the concentration of the product(s) at a given reaction time. We also introduce *mikimo*,[3] a lightweight Python program that is seamlessly integrated with our previously released volcano plot/activity map builder, *volcanic*[2] which automates the construction of microkinetic molecular volcano plots and activity/selectivity maps.
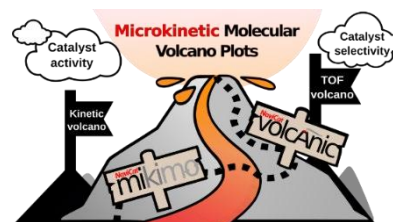
Methodology

For each possible value of the descriptor variable, estimates of the energy barriers associated with all the individual reaction steps can be acquired from the general simulated reaction profile. The corresponding rate constants can then be obtained for every reaction step from the Eyring-Polanyi equation and the kinetic equations constructed. The rate constants for the reverse reactions are obtained simultaneously and included in the preceding steps. For a given reaction time, the equations can then be integrated numerically, and the product concentration at a fixed time plotted as a function of the descriptor. Completing this process using a single descriptor variable gives rise to microkinetic volcano plots, while using two descriptor variables provides microkinetic activity maps.
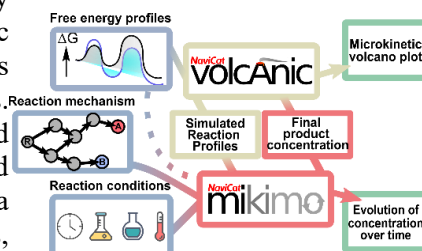
Results and Discussion

With the theoretical framework and the implementation of microkinetic volcano plots in hand, we demonstrate their application for catalytic reactions. Owing to their ability to account for temperature and concentration in complex mechanisms, microkinetic activity maps that use time or temperature as secondary descriptors allow for the simultaneous optimization of both catalyst and reaction conditions. Through these plots/maps, we examine the impact of physical conditions on catalytic performance. Furthermore, we pinpoint the catalysts that perform optimally under the specified physical conditions.

a) Rh-catalyzed hydroformylation

b)

c)
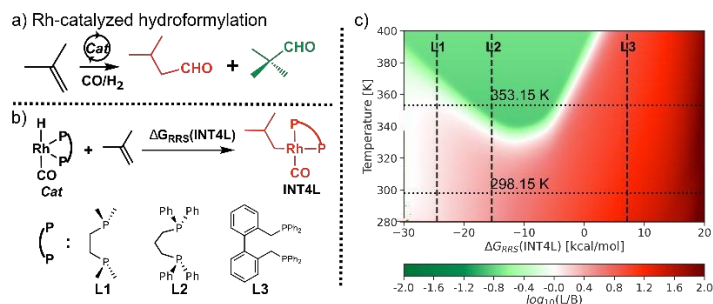
Significance

Microkinetic volcano plots and activity/selectivity maps plots enable not only the rapid screening of catalysts and substrates for reactions involving complicated mechanisms (*e.g.*, intertwined catalytic cycles leading to multiple products), but also the effect of physical conditions (*e.g.*, reaction temperature/length, concentration of reactants) on activity and selectivity. Leveraging these capabilities permits the simultaneous optimization of the catalyst and the reaction conditions, thereby providing a unified theoretical framework for the holistic design of active and selective homogeneous catalysts and reactions. We have also introduced *mikimo*, a Python-based open-source module for microkinetic modeling of homogeneous catalytic reactions. This easy-to-use implementation reproduces experimental results regarding product distribution and is applicable to diverse reaction mechanisms as well as conditions.

References

1.   Wodrich, M. D.; Sawatlon, B.; Busch, M.; Corminboeuf, C., The Genesis of Molecular Volcano Plots. *Accounts of Chemical Research* **2021,** *54* (5), 1107-1117.

2.   Laplaza, R.; Das, S.; Wodrich, M. D.; Corminboeuf, C., Constructing and interpreting volcano plots and activity maps to navigate homogeneous catalyst landscapes. *Nature Protocols* **2022,** *17* (11), 2550-2569.

3.   Worakul T, Laplaza R, Das S, Wodrich M, Corminboeuf C. Microkinetic Molecular Volcano Plots for Enhanced Catalyst Selectivity and Activity Predictions. *ChemRxiv*. 2024; doi:10.26434/chemrxiv-2024-j79s3

Unraveling the mystery of solvation-dependent fluorescence of fluorescein dianion using computational study

**Abheek Roy[1], Suvadip Samanta[1], Soumyadip Ray[1], Sunil Kumar S[1]
and <u>Padmabati Mondal</u>[1]***
*[1]Indian Institute of Science Education and Research (IISER) Tirupati,
Tirupati, Andhra Pradesh, India*
*padmabati.mondal@iisertirupati.ac.in

Introduction

Fluorescein, an organic dye molecule, can exist in seven prototropic forms: one cation, three neutral forms, two monoanions, and one dianion. The fluorescence quantum yield of the dianionic form is the maximum, with a high value of 0.93 in the solvent phase. Therefore, this molecule has a broad range of potential applications, such as a gain medium in certain dye lasers, as a marker in biomedical applications, and as a flow tracer in hydrology. Interestingly, the molecule was found to be non-fluorescent in the gas phase. [1] Despite several studies addressing the fluorescence characteristics of fluorescein dianion, the underlying physical mechanism that dictates the dominance of one channel over the other is not understood. No comprehensive comparison of the mechanism or energetics of electron detachment between the solution and gaseous phases of the dianion has been reported to date.

Methodology

This work aims to provide a deeper insight into the fluorescence characteristics of fluorescein dianion in terms of a systematic investigation of the effect of water addition on its fluorescence properties by calculating two energy parameters, adiabatic detachment energy (ADE) and vertical detachment energy (VDE). For these calculations, the structures of fluorescein dianion and fluorescein monoanion were computed. The vibrationally resolved absorption and emission spectra of fluorescein in aqueous media were calculated and compared with the available experimental spectra. The comparison of different energy components and their role in the stability of one photoproduct over the other was elucidated to illuminate the deactivation pathways both in the gas phase and the solvent phase. All calculations were performed using density functional theory (DFT) and time-dependent DFT at the B3LYP/6-311++G(d,p) level of theory using Gaussian09 software using different solvent models e.g. polarizable continuum model (PCM), conductor-like polarizable continuum model (CPCM), solvation model based on density (SMD), microsolvation and cluster continuum model (CCM).

Results and Discussion

In this work [2], the effect of hydration on the fluorescence property of fluorescein dianion was investigated. In the case of this specific molecule, there exist two major mechanisms of de-excitation after photoabsorption: (a) fluorescence and (b) photodetachment. The detachment energies calculated with continuum solvation models were found to be significantly higher than those in the gas phase. This explains the larger fluorescence quantum yield of fluorescein dianion in the solvent phase as opposed to the gas phase, where it is much easier for an electron to photodetach due to the low electron detachment energy. The VDE calculated under microsolvation was found to gradually increase as more and more water molecules were added to the system, thereby approaching the value obtained using a continuum solvation model. The location of the sites where the water molecules get attached was found to make a difference in the electron detachment energy. However, it is apparent that a collective effect of the solvent environment rather than the task of just a few water molecules causes the VDE to have a high negative value in the solution phase. The higher stability of the dianion in the solvent phase compared to the monoanion is attributed to the higher solvation free energy of the dianion due to its larger negative charge. This contributes to the higher electron detachment energy of the fluorescein dianion in the solvent phase. It is also found that the photodetachment process in the gas phase is followed by vibrational relaxation via some low-frequency vibrational modes involving the xanthene ring. PCM underestimates the stability of fluorescein monoanion in the solution phase when compared to results from microsolvation and CCM gives results that are consistent with the expected trend. However, for fluorescein dianion, an over-stabilization of the structure in the solution phase was noticed as compared to the results from microsolvation.
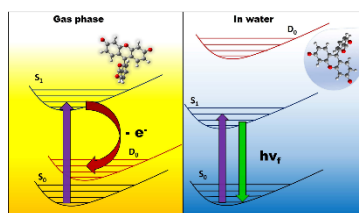
Figure 1: A graphical representation for the dependence of photodetachment and fluorescence phenomena of fluorescein dianion in the gas phase and a solvent, respectively, on their detachment energies.

Significance

The results from the present work indicate that the activation of the fluorescence channel of gas phase fluorescein dianion over the photodetachment channel can be achieved only if a relatively large number of water molecules are added to the system. These findings suggest that activating one deactivation path over the other completely relies on their energetics, which can be tuned via several external or internal factors, e.g., the inclusion of substituting group, light irradiation to the higher excited states, degree of solvation, etc. Therefore, these results provide useful insights into the controlled experiments one might perform on fluorescein dianion, where a particular deactivation path will be favored over another. Furthermore, quantitative understanding of finetuning of fluorescence quantum yield using microsolvation of fluorescein dianion will help in designing controlled fluorescence probe for biomedical applications.

References

*1. P. D. McQueen, S. Sagoo, H. Yao, and R. A. Jockusch, Angew. Chem. Int. Ed Engl.(2010), **49**, 9193.*
*2 .A Roy, S Samanta, S. Roy, Sunil Kumar S, P. Mondal, J Chem. Phys. (2024), **160**, 034302*

Proton Transfer in Polarizable Molecular Dynamics Simulations

Márta Gődény[1,2], Florian Joerg[1,2] and Christian Schröder[1]*

[1]*University of Vienna, Faculty of Chemistry, Department for Computational Biological Chemistry,*
Währinger Str. 17, 1090 Vienna, Austria
[2]*University of Vienna, Vienna Doctoral School in Chemistry (DoSChem),*
Währinger Str. 42, 1090 Vienna, Austria
*christian.schroeder@univie.ac.at

Introduction

Proton transfer reactions are crucial in myriad biochemical and physical processes ranging from enhancing electrolyte conductivity to the regulation of enzymatic activities and ion channel functions. While molecular dynamics (MD) simulations are extensively employed to explore phenomena and mechanisms that influence macroscopic properties at the atomic level, conventional MD approaches fail to model proton transfers since bonds cannot be broken or formed. Alternative methods, such as ab initio MD or reactive force fields, are computationally demanding and impractical for large systems or extended simulation periods. Constant pH simulations are limited to a finite number of protonation sites and do not incorporate explicit protons. We present Protex[1], a Python-based extension for the MD software OpenMM, to overcome these challenges: Protex integrates proton transfer reactions within conventional polarizable MD simulations without significant computational overhead. Additionally, it does not require a proton bath and can accommodate an unlimited number of protonation sites.

Methodology

Protex employs a single topology approach, where each base is modified to include a dummy atom at the potential protonation site. These dummy atoms possess mass but lack partial charges and Lennard-Jones parameters, rendering them inert within the simulation environment. This approach ensures a correct atom mapping between an acid and its conjugate base. During protonation, the force field parameters of the dummy atom and the proton of the donor are changed, effectively transforming the dummy atom into an active proton and vice versa, thus facilitating the reaction without breaking or forming bonds, as shown in Figure 1.
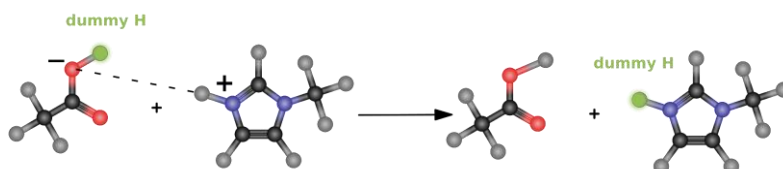

Figure 1. Proton transfer between 1-methylimidazolium and acetate in a single topology approach. Dummy atoms are shown in green.

Protex works by stopping the trajectory production at regular intervals and checking if there are acidic protons within a cutoff radius of a suitable acceptor (illustrated by the dashed line in Figure 1). Protons are then transferred based on predetermined probabilities derived from quantum mechanical scans of the reactants. These probabilities can be adjusted throughout the simulation to maintain the desired ratio of charged to neutral species.[2] Protex is compatible with any force field supported by OpenMM, though it has been specifically developed and validated using the CHARMM polarizable force field. The typical workflow involves setting up and optimizing a simulation box using CHARMM with the CHARMM36 force field, followed by production runs in OpenMM 7.6 utilizing the Velocity Verlet integrator. Analysis of pertinent properties such as diffusion coefficients, conductivity, radial distribution functions, and proton hopping chains is conducted using the MDAnalysis package and custom Python scripts.

Results and Discussion

We conducted a detailed investigation of the protic ionic liquid (IL) 1-methylimidazolium acetate using Protex. Our research demonstrates that while conventional polarizable MD simulations

inadequately capture the conductivity of the system,[3] incorporating proton transfer reactions significantly enhances the correlation with experimental data.[1,4] In a more complex test scenario, we examined the same IL in conjunction with a protic solvent, methanol, and a photoacid. The majority of the system consisted of methanol, which typically received the proton from the photoacid before it was transferred to more stable species such as acetic acid or 1-methylimidazolium. Our simulations successfully depicted proton hopping across multiple protonated methanol ions serving as intermediate carriers. Furthermore, the decay of protonated methanol followed an exponential trend, aligning with the observations of our experimental collaborators. This comprehensive study underscores the utility of Protex in enhancing MD simulations to better match empirical findings, particularly in complex ionic systems involving multiple proton transfer dynamics.

Significance

We believe that Protex offers a cost-effective solution for simulating proton transfer within molecular dynamics frameworks. Currently, our efforts are directed towards expanding Protex's applicability to biological systems, with a particular emphasis on proton-conducting ion channels.

However, Protex is not limited to proton transfer reactions. We plan to broaden its capabilities to include various other phenomena such as charge transfer, tautomerism, ligand exchange in complexes, and straightforward chemical reactions, including chemisorption of CO_2.

References
(1) Joerg, F.; Wieder, M.; Schröder, C. *Front. Chem.* **2023**, *11*, 1140896.
(2) Jacobi, R.; Joerg, F.; Steinhauser, O.; Schröder, C. *Phys. Chem. Chem. Phys.* **2022**, *24*(16), 9277–9285.
(3) Joerg, F.; Schröder, C. *Phys. Chem. Chem. Phys.* **2022**, *24* (25), 15245–15254.
(4) Gődény, M.; Joerg, F.; Kovar, M. P.-P.; Schröder, C. *J. Phys. Chem. B* **2024**, *128* (14), 3416–3426.

Mass spectrometry and machine Learning (MS-ML): A combined tool for medical diagnosis

Koner D.[1*] and Banerjee S.[2]
[1] *Indian Institute of Technology Hyderabad, 502285, (India)*
[2] *Indian Institute of Science Education and Research Tirupati, 517507, (India)*
*debasishkoner@chy.iith.ac.in

Introduction

The desorption electrospray ionization mass spectrometry (MS) imaging (DESI-MSI) is an extensively used ambient ionization MS technique to generate gas phase ions without fragmentation. Several thousands of signals of molecules can be found for biological/pathology samples like tissue sections, blood, and urine from DESI-MSI. Based on the signal intensities, the samples can be classified. However, a significant number of signals in the MS also appear as noises. Finding out the prominent signals from the MSs and sorting out the discriminatory signals within several thousand signals to classify them into different categories is a challenging task. In our recent works, we have developed a protocol using an in-house peak-picking algorithm to build ML models to differentiate the biological samples. Our protocol has been successfully applied to the diagnosis and/or biomarker detection of nephrotic syndrome (NS), breast cancer, and temporal lobe Epilepsies (TLE).

Methodology

In the DESI-MSI technique, highly charged aerosol of microdroplets is sprayed onto a surface, which desorbs and ionizes molecules, and finally analyzes the molecules by MS. Samples are analyzed in their normal conditions with minimal sample preparation, and chemicals, metabolites, and lipids can be rapidly identified from their m/z signals. The mass spectra recorded are then used as a dataset for building ML models. The prominent signals are picked using our own in-house package depending on the abundance of the molecules. The importance signals are then determined using multivariate classifiers e.g. random forest, extra tree. Finally, we have constructed ML models using a few most important (say top 50 or 100) signals. The most important discriminatory signals are the biomarkers which can be further characterized using MS/MS technique.

Results and Discussion

In our first work, we have built a support vector machine (SVM) model which can classify four different types of NSs (IgA nephropathy (IgAN), membranous glomerulonephritis (MGN), and lupus nephritis (LN)) with an average accuracy of 98%. Dysregulation of glycerophospholipids, sphingolipids, and glycerolipids in the kidney appears as prominent biomarkers for diagnosing the NS. In the second work, we have found that a 100% accurate (with 99% average accuracy) ML model can be built to predict breast cancer using only four different types of diacylglycerols. In the third project, we have studied the lipid profile of the human hippocampus obtained from epilepsy surgery for temporal lobe Epilepsies using negative ion mode DESI-MSI and ML which revealed upregulation of anionic/negatively charged phospholipids in the TLE compared to the non-TLE samples.

Significance

Simple 1-min scanning of the renal biopsy specimen by DESI-MSI can be used to find out the metabolic derangement of lipids in different types of nephrotic syndromes, which can be analyzed by machine learning for rapid and accurate classification of NS. Exceptional diagnostic potential of diacylglycerols for accurate discrimination between breast cancer and adjacent normal tissue by mapping their distributions in lumpectomy specimens using DESI-MSI have been reported. Metabolic upregulation of this lipid in breast cancer was observed. Machine learning models revealed striking upregulation of anionic/negatively charged phospholipids in the TLE compared to the non-TLE specimens. The origin and the evolution of the biomarkers (phospholipids etc.) revealed here can be investigated in detail which will open up new avenues for studying those diseases.
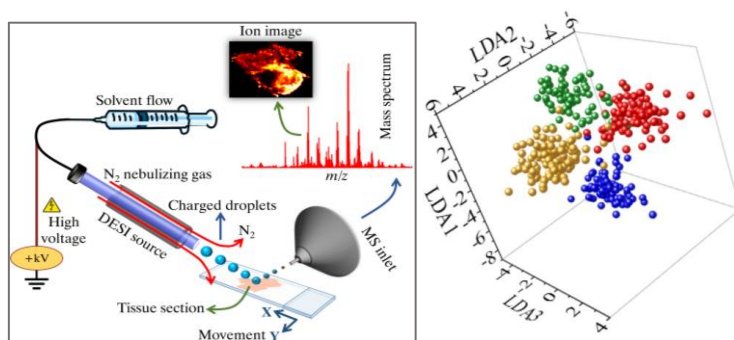
Figure 1. Schematic diagram of DESI-MSI technique (left). Linear discriminant analysis of mass spectra obtained from different types of NS tissue sections.

References
1. Mondal, S., Singh, M. P,; Kumar, A., Chattopadhyay S., Nandy, A., Sthanikam, Y., Pandey, U., Koner, D., Limesh, M., Banerjee, S. *J. Proteome Res.* 22, 967-976 (2023).
2. Mondal, S., Sthanikam, Y., Kumar, A., Nandy, A., Chattopadhyay S., Koner, D., Rukmangadha, N., Narendra, H., Banerjee, S., *Anal. Chem.* 95, 20, 8054-8062 (2023).
3. Mondal, S., Nandy, A., Dande, G., Prabhu, K., Balmiki R. R., Koner, D., Banerjee, S. *ACS Chem. Neurosci.* 15, 983-993 (2024).

Mechanistic Study of Water Splitting Over Doped Barium Titanate with a Machine Learning Potential

Kajjana Boonpalit[1,2] and Nongnuch Artrith[2]*

[1]School of Information Science and Technology, Vidyasirimedhi Institute of Science and Technology (VISTEC), Rayong 21210 (Thailand)
[2]Materials Chemistry and Catalysis, Debye Institute for Nanomaterials Science, Utrecht University, 3584 CG (Netherlands)
*n.artrith@uu.nl

Introduction

Electrocatalytic water splitting, producing hydrogen and oxygen via water electrolysis, stands out as a highly attractive method for generating renewable carbon-free alternative fuels. However, its practical application faces challenges due to the high costs associated with the Pt cathode and Ir/RuO_x anode catalysts. On the search for alternative catalyst materials, barium titanate ($BaTiO_3$) has garnered attention since this inexpensive and non-toxic perovskite oxide can be synthesized from earth-abundant precursors. Its potential for catalyzing the oxygen evolution reaction (OER) has been highlighted by recent studies. [1] Additionally, the introduction of transition-metal dopants, including Fe and Ni, has been explored to enhance the electric conductivity and catalytic activity of $BaTiO_3$. [2] In this work, we delved into the mechanistic details of OER over pristine and Ni-doped $BaTiO_3$ (001). To gain insights into the OER mechanism in dynamics simulation, a neural-network based machine learning potential (MLP) was constructed to enable large-scale and long-time molecular dynamics simulations (MD) of OER with an accuracy close to DFT. [3]

Methodology

Instead of relying on costly and time-consuming ab-initio molecular dynamics (AIMD), the training dataset for the MLP was constructed via the MACE-MP-0 model, a foundational tool for atomistic materials chemistry. MD simulations were conducted with MACE-MP-0 to explore the potential energy surface. Subsequently, single-point density functional theory (DFT) calculations were employed to recalculate the energies and forces of the generated structures to yield a database with the RPBE level of theory, using VASP plane-wave package. Following dataset construction, we evaluated the performance of machine learning models, including MACE and ænet, using our custom $BaTiO_3$ database. These models were then deployed to investigate the OER mechanism through MD and Metadynamics (MetaD) simulations.

Results and Discussion

Our proposed MLP training pipeline offers a significant acceleration in dataset construction, which traditionally consumes substantial time and resources in MLP-related research. Through the adoption of an active learning scheme, we can iteratively refine the performance of the machine learning model, resulting in a more accurate and efficient MLP tailored for stable MD simulations. While AIMD has provided invaluable insights into the interaction of water with oxide surfaces, its limitations in terms of length and time scales often hinder the characterization of the properties of aqueous oxide interfaces. However, our MLP-MD approach has enabled us to delve into water dissociation over $BaTiO_3$ surfaces through nanosecond-scale simulations. Looking ahead, employing MLP-MetaD to study the entire OER reaction profile promises to be a future direction for our study.

Significance

Typically, constructing a database for training an MLP is resource-intensive, necessitating numerous AIMD simulations to capture diverse configurational space. However, in this study, we adopted a more efficient approach by leveraging the MD trajectory obtained from simulations by the MACE-MP-0 model. By doing so, we circumvented the need for extensive AIMD simulations. This strategy enabled us to explore the configurational space through a longer-picosecond MD simulation, while also facilitating parallelization using single-point DFT calculations. The MLP trained with the custom $BaTiO_3$ database has the potential to significantly accelerate MD and MetaD simulations,

thereby facilitating the study of the OER over nanosecond-timescale, which is not practical with conventional AIMD.

References

1. Nasby, R. D., and Quinn, R. K. Mater. Res. Bull. 11 (8), 985-992. (1976)
2. Artrith, N., Sailuam, W., Limpijumnong, S., and Kolpak, A. M. Phys. Chem. Chem. Phys. 18 (42), 29561-29570. (2016)
3. Artrith, N., and Urban, A. Comput. Mater. Sci. 114, 135-150. (2016)

Suzuki-Miyaura Coupling Reaction Using Pd-H-Faujasite Zeolite: A Combined Experimental and Theoretical Study

Phakthira Suwadit[1], Thana Maihom[1], Kanokwan Kongpatpanich[2],
Sasiwadee Boonya-udtayan[1], Piti Treesukol[1] and Bundet Boekfa[1]*

[1]*Division of Chemistry, Department of Physical and Material Sciences, Faculty of Liberal Arts and Science, Kasetsart University, Kamphaeng Saen Campus,*
Nakhon Pathom, 73140, Thailand
[2]*Department of Materials Science and Engineering, School of Molecular Science and Engineering, Vidyasirimedhi Institute of Science and Technology, Rayong 21210, Thailand*
*bundet.b@ku.ac.th

Introduction

Zeolite, a crystalline microporous aluminosilicate, stands out as an exceptional catalyst in green chemistry synthesis. The utilization of Palladium zeolite catalysts in cross-coupling reactions, synthesizing unsymmetrical biaryls from aryl halides and boronic acid, has gained interest. The larger pores of Pd-Faujasite zeolite facilitate efficient encapsulation of aggregated Pd species, thereby enhancing catalytic performance.

In this study, we focus on the cross-coupling reaction between Bromobenzene and Phenylboronic acid using Pd-H-Faujasite zeolite, employing both experimental and theoretical approaches. Pd-H-Faujasite zeolite catalyst was synthesized in our laboratory and underwent characterization using XRD spectroscopy techniques. Suzuki-Miyaura cross-coupling reactions were studied at various conditions. The products were characterized with TLC and NMR spectroscopy. The adsorption and reaction mechanism over Pd-H-Faujasite zeolite were theoretically examined using DFT calculations. The theoretical results provide support for the formation of biphenyl products in the reaction.

Methodology

The coupling reaction involving bromobenzene with phenylboronic acid was synthesized using Pd-H-Faujasite zeolite. Pd was introduced by combining a solution of Pd acetate and H-Faujasite zeolite in THF, allowing the mixture to react for 48 hours at room temperature. The structure of Pd-H-Faujasite zeolite was analyzed using X-ray diffraction (Bruker, D8 ADVANCE, CuKα radiation) and BET analysis. For the reaction, a mixture of Bromobenzene (1.0 mmol), phenylboronic acid (1.2 mmol), ethanol (5 mL), K_2CO_3 2 mmol and 10 mg of Pd-H-Zeolite catalyst was stirred and refluxed at various temperatures and reaction times. All products were carefully characterized using TLC and NMR spectroscopy.

For quantum calculation, the Pd-H-Faujasite zeolite catalyst was modeled with a 34T quantum cluster model to represent the active site. The Pd_4 cluster within the zeolite was located over the Brønsted acid site. The M06-L functional was employed to calculate the coupling reaction over the Pd-H-Faujasite zeolite, using the 6-31G(d,p) and LANL2DZ basis set in this model. All calculations were studied using the Gaussian 09 program.

Results and Discussion

The cross-coupling reaction involving bromobenzene and aryl boronic acid was studied with Pd-H-Faujasite zeolite. The coupling reaction was performed employing Pd-H-Faujasite under various conditions. The highest yield is 63% with Pd-H-Faujasite at 120 C and 4 hr reaction time. The computational analysis of the coupling reaction between bromobenzene and phenyl boronic acid on Pd-H-Beta zeolite was studied by using the M06L functional. The reaction involves three steps: oxidative addition of bromobenzene, transmetallation with phenylboronic acid, and reductive elimination leading to biphenyl, as illustrated in Figure 1. The calculated activation energies with bromobenzene and phenylboronic acid for these steps were found to be 12.0, 31.4, and 15.3 kcal/mol, respectively. These findings indicate that the Pd cluster located within the Brønsted acid site of Faujasite zeolite is well-suited for facilitating the cross-coupling synthesis reaction.

Significance

We studied the cross-coupling reaction between Bromobenzene and Phenylboronic acid using Pd-H-Faujasite zeolite with both experiment and theoretical study.
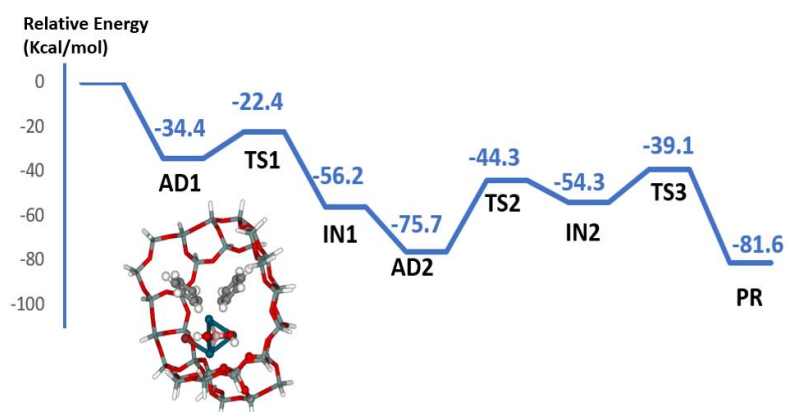

Figure 1. Reaction pathway for the coupling reaction of bromobenzene with phenylboronic acid over 34T Pd-H-Faujasite zeolite. The structures were calculated using the M06L functional. Energies are in kcal/mol.

References
1. Boekfa, B., Maihom, T., Ehara, M. and Limtrakul J., *Scientific Reports* 14, 611 (2024).
2. Srirattanasakunsuk, P., Boekfa, B., Treesukol, P., Jarussophon, N., Maihom, T., Kongpatpanich, K. and Limtrakul. J*., ACS Omega* 8, 49, 46904–46913 (2023)

In silico study on the inclusion complexation of 4, 6-dimethoxyflavone with β-cyclodextrins

Gulzaib Basharat[1], Thanyada Rungrotmongkol[1,2]*, Supot Hannongbua[3]*

[1]*Program in Bioinformatics and Computational Biology, Graduate School,
Chulalongkorn University, Bangkok 10330, Thailand*
[2]*Center of Excellence in Structural and Computational Biology, Department of Biochemistry, Faculty
of Science, Chulalongkorn University, Bangkok 10330, Thailand*
[3]*Center of Excellence in Computational Chemistry (CECC), Department of Chemistry,
Faculty of Science, Chulalongkorn University, Bangkok 10330, Thailand*
* thanyada.r@chula.ac.th, supot.h@chula.ac.th

Introduction

This study explores the pharmacological properties and potential therapeutic applications of the naturally occurring 4,6-dimethoxyflavone (DMF). DMF is a flavonoid derivative regarded as a promising candidate for cancer treatment because of its ability to interact with various cellular components [1]. The presence of methoxy groups at the 4 and 6 positions on the flavone core enhances its lipophilicity and cellular uptake, facilitating more effective interaction with intracellular targets critical for cancer cell proliferation and survival. DMF exhibits anti- inflammatory and anticancer activities, potentially through modulation of various signaling pathways, including those involved in cell proliferation and apoptosis [2]. However, the solubility of DMF is rather low, hindering pharmaceutical applications. To increase the solubility, β-cyclodextrin (βCD) and derivatives were utilized to encapsulate such lipophilic guest molecules into their hydrophobic cavity, while their hydrophilic outer part interacts with surrounding water [3]. βCDs have been extensively used and widely acceptable carriers for improving the physicochemical properties of lipophilic drugs [4].

Methodology

Considering this interest, we select βCD and its hydrophilic derivatives; methyl-β-cyclodextrin (MβCD), dimethyl-β-cyclodextrin (DMβCD), hydroxypropyl-β-cyclodextrin (HPβCD) [5], hyaluronic acid β-cyclodextrin (HAβCD), sulfobutylether-β-cyclodextrin (SBEβCD) to generate inclusion complex with DMF by two different methods: *(i)* molecular docking using the CDOCKER module in Accelrys Discovery Studio 2.5; and *(ii)* parallel cascade selection molecular dynamics (PaCS-MD), a method for sampling rare events that facilitate the generation of transition pathways between a reactant and a product [6]. This technique employs repetitive short-duration MD simulations from key configurations, termed conformational resampling cycles, to sample these pathways. Additionally, the classical MD simulations were performed on each complex for 1μs in triplicates and the last 900 ns are used for analyses [7].

Results and Discussion

The docking study showed that DMF can effectively form inclusion complexes with βCD and derivatives. DMF revealed two favorable conformations, and the interaction energies for A and C conformations are -22 to -28 kcal/mol and -23 to -26 kcal/mol, respectively. RMSD of complex was calculated to assess the system stability. Notably it remained stable for all complexes; however, during the third simulation of the MβCD complex for both conformations, the drug transiently exited and re-entered the cyclodextrin cavity, forming a new inclusion complex. Among the βCD derivatives examined, the DMF/SBEβCD complex demonstrated superior performance, characterized by the highest number of atom contacts and the lowest solvent accessibility in the hydrophobic cavity of SBEβCD. The hierarchy of atom contact numbers across the complexes was observed as follows: DMF-SBEβCD > DMF-HPβCD > DMF- DMβCD > DMF-MβCD > DMF-HAβCD > DMF-βCD. These findings highlight the exceptional capability of modified cyclodextrins, especially SBEβCD, in enhancing the solubility and stability of the lipophilic drug DMF, thereby underscoring their potential as effective molecular encapsulating agents.

Significance

- This study addresses a critical barrier to the clinical utility of DMF poor aqueous solubility. The outcomes open avenues for developing more safer and effective alternatives and enhancing the

anticancer efficacy of DMF.

- The use of βCDs not only improves the solubility of lipophilic drug, but also sets a precedent for using computational methods in drug design and development, paving the way for rapid, cost-effective pharmaceutical innovations.
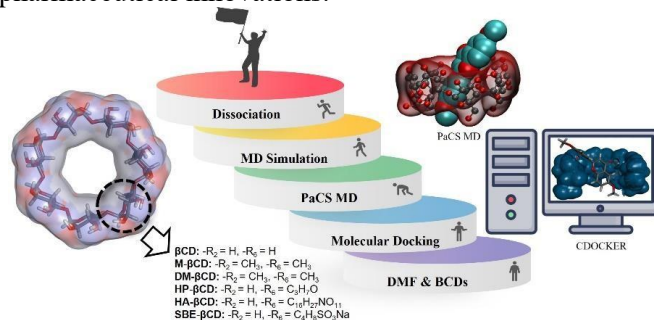

Figure 1: A graphical representation of inclusion complexation study of DMF/βCDs

Keywords: Dimethoxyflavone, β-cyclodextrin, Docking, MD simulation, PaCS-MD

References

1. Songngam, S., et al., AAPS PharmSciTech, 2014. 15(5): p. 1189-96.
2. Li, H., X. Zhang, and W. Wang, Afr J Tradit Complement Altern Med, 2017. 14(4): p. 213-220.
3. Poulson, B.G., et al., Polysaccharides, 2021. 3(1): p. 1-31.
4. Jansook, P., N. Ogawa, and T. Loftsson, Int J Pharm, 2018. 535(1-2): p. 272-284.
5. Mekjaruskul, C., et al., Int J Pharm, 2013. 445(1-2): p. 1-11.
6. Tran, A.K.R.H.Y.N.D.P., AIP Conference Proceedings, AIP Publishing., 2016. 1790(1).
7. Aman, A., et al., RSC Adv, 2023. 13(39): p. 27244-27254.

Performance of Single Atom Supported V_2CO_2 as an Anchoring Material for Aluminum-Sulfur Batteries: A First-Principles Study

Pakuna Panbo[1], Anchalee Junkaew[2], Suwit Suthirakun[1*]

[1]*School of Chemistry, Institute of Science, Suranaree University of Technology, 111 University Avenue, Muang, Nakhon Ratchasima, 30000, (Thailand)*
[2]*National Nanotechnology Center (NANOTEC), National Science and Technology Development Agency (NSTDA), Pathum Thani, 12120, (Thailand)*
* suthirak@sut.ac.th

Introduction

Aluminum-sulfur (Al-S) batteries have recently gained significant attention due to the high earth abundance and theoretical capacity of sulfur as the electrode material (1). However, the shuttle effect of large polysulfide (Al_2S_n) remains a challenge for the development of high-performance Al-S batteries. This can be overcome by using anchoring material that enhances polysulfides adsorption. MXene offers fascinating properties, such as high electronic conductivity and a large specific area (2). Various MXenes have demonstrated performance improvements in batteries. Based on first-principles calculations, 3d-transition metal-loaded V_2CO_2 ($SA@V_2CO_2$) MXene was modeled as an anchoring material to suppress the shuttle effect and improve sulfur reduction reaction at the cathode. The free energy diagrams of the various $SA@V_2CO_2$ can demonstrate the reaction profile the determining step and provide an estimate of the favorable performance for Al-S batteries.

Methodology

All calculations were carried out using spin polarized density functional theory (DFT) method as implemented in Vienna ab initio simulation package (VASP) (3, 4). The projector augmented wave (PAW) method was used to treat the electron-ion interaction. The exchange-correlation functional was approximated by the generalized gradient approximation (GGA) with Perdew-Burke-Ernzerhof (PBE) functional. The DFT-D3 method was employed for corrections of weak van der Waals interactions between S_8 or Al_2S_n and $SA@V_2CO_2$. The cutoff energy was set to 500 eV. Structure optimizations were carried out within the energy and force convergence of 10^{-6} eV and 0.02 eV/Å, respectively. The Brillouin zone integrations were carried out using k-point sampling of the Monkhorst-Pack scheme as 5 x 5 x 1. The vacuum gap is set to 20 Å in the z-direction to avoid interaction between the periodic images.

Results and Discussion

3d-Transition metal atoms (TMs) were placed on V_2CO_2 monolayer and explored the performance of $SA@V_2CO_2$ for Al−S batteries (5). There are two different preferential binding sites. Sc, Ti, Cr, Mn, and Cu atoms prefer to bind at hollow O_{TopC} site, whereas the other 3d-TMs prefer to bind at hollow O_{TopV} site. Various initial structures of S_8 and Al_2S_n molecules were investigated at various binding sites on both bare and $SA@V_2CO_2$ surfaces. For the bare V_2CO_2, Al–O bonds were characterized as the bond formation upon polysulfides adsorption. Al_2S_3, Al_2S_6, and Al_2S_{12} can easily form Al–O bonds and strongly adsorb on the surface. In contrast, S_8 and Al_2S_{18} weakly adsorb on the surface since there is no Al atom in S_8 while Al_2S_{18} is a large cluster where S atoms hinder the formation of Al–O bonds.

For the $SA@V_2CO_2$, S atoms of S_8 and Al_2S_n species can form bonds with TMs on the surfaces. The possible binding sites of S_8 and Al_2S_n molecules were considered by TM–S bonds on the surface. The results suggest that $SA@V_2CO_2$. can suppress the shuttle effect of high order Al_2S_n comparing with bare. Furthermore, the energy profiles of sulfur reduction reaction reveal the potential determining step which can be used to determine the performance of the cathode materials for Al-S batteries.

Significance

The study focuses on the single-transition metal atom (SA) catalysts on V_2CO_2 as anchoring material for Al-S batteries. Adsorption strength was used to investigate the suppression of shuttle effect. Free energy profiles of sulfur reduction reactions provide an estimate of the performance for Al-S batteries.
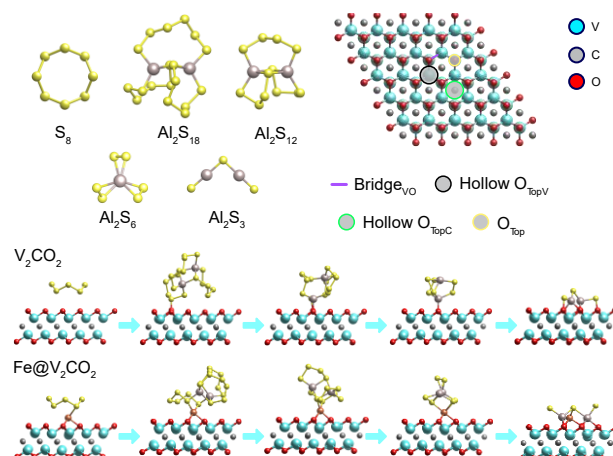
Figure 1. S_8 and Al_2S_n species. Binding site of SAs on V_2CO_2. Sulfur reduction reaction on bare and Fe@V_2CO_2 as an example.

References
1. Klimpel M., Kovalenko M. V., and Kravchyk K. V. *Commun Chem*. 5, 1 (2022).
2. Wang Z., Zheng X., Chen A., Han Y., Wei L., and Li J. *ACS Mater Lett*. 4, 8 (2022).
3. Kresse G., and Furthmüller J. *Physical Review B*. 54, 16 (1996).
4. Kresse G., and Furthmüller J. *Comput. Mater. Sci*. 6, 1 (1996).
5. Ju S., Yuan C., Zheng J., Yao L., Zhang T., and Xia G. *Energy Storage Mater*. 52 (2022).

Theoretical Investigation of Enhanced C_2N through Transition Metal Doping for Sodium-Sulfur Batteries

**Wongsathorn Kaewraung[1], Sirisak Singsen[2], Anchalee Junkaew[3,*],
and Suwit Suthirakun[1,*]**

[1]*School of Chemistry, Institute of Science, Suranaree University of Technology,
Nakhon Ratchasima, Thailand 30000*
[2]*School of Physics, Institute of Science, Suranaree University of Technology,
Nakhon Ratchasima, Thailand 30000*
[3]*National Nanotechnology Center (NANOTEC), National Science and Technology Development
Agency (NSTDA), Pathum Thani, Thailand 12120*
*A. Junkaew: anchalee@nanotec.or.th and S. Suthirakun: suthirak@sut.ac.th

Introduction

Metal-sulfur batteries have been proposed as a next-generation energy storage technology due to their high theoretical capacity and energy density. Among them, sodium-sulfur (Na-S) batteries are particularly promising due to their high theoretical capacity, nontoxicity, environmental friendliness, and low cost. However, Na-S batteries still face challenges in terms of capacity fading and cycling stability due to shuttle effect and sluggish kinetics of sulfur reduction reaction (SRR).[1] Recently, C_2N, a novel 2-dimensional material, has been shown to improve the performance of Na-S batteries, despite its issues of Na-trapping.[2] To solve this problem and enhance catalytic activity, transition metal doping could be a viable method. Herein, we design transition metal doping on C_2N using first-principles methods, focusing on iron (Fe) and cobalt (Co) due to strong interaction with sodium polysulfide (NaPSs) and their popularity in experimental studies. We study and compare the performance of single-atom and dual-atom in suppressing shuttle effect and enhancing the delithiation reaction. Based on the calculated results, we could suggest new transition metal doping C_2N for future high-performance Na-S batteries.

Methodology

All calculations are carried out using the spin polarized DFT method as implemented in Vienna ab initio simulation package (VASP 5.4).[3,4] The frozen-core projector augmented wave (PAW) method was used to describe the electron-ion interaction. The exchange-correlation contributions were approximated by the generalized gradient approximation (GGA) with Perdew-Burke-Ernzerhof (PBE) functional. Weak van der Waals interactions between the adsorbates and $TM-C_2N$ were partially corrected using the DFT-D3 method with Becke-Jonson damping. The surface structures were optimized with a kinetic energy cutoff of 500 eV and k-point sampling of the Monkhorst-Pack scheme as 4 x 4 x 1 for structural optimization and 9 x 9 x 1 for electronic structure calculations. The energy and force convergence criteria were set to 10^{-6} eV and 0.02 eV/Å, respectively.

Results and Discussion

Computations reveal that TM doping improves NaPSs adsorption and prevents Na trapping. In addition, doping with dual-atom show stronger NaPSs adsorption compared to single-atom doping due to the increased number of active transition metal sites that bind with sulfur in NaPSs. However, both same dual-atom transition metal (Fe-Fe and Co-Co) and different dual-atom transition metal (Co-Fe) exhibit similar adsorption energy, suggesting that using different transition metals, when both metal groups are next to each other, does not significantly affect adsorption with NaPSs.

The catalytic activity of SRR can be investigated via construction of Gibbs free energy profile. We find that Co-Fe doping reduces the energy of the potential limiting step in the Na_2S_4 to Na_2S_2 conversion more effectively than the same dual-atom combinations (Fe-Fe and Co-Co) and single-atom doping. This suggests that different dual atom doping on C_2N effectively accelerates the SRR process.

Overall, dual-atom doping, especially Co-Fe doped C_2N, shows better performance. The insights obtained from this work could guide and suggest directions for future research, leading to the discovery of high-performance cathode materials of Na-S batteries.

Significance

This research addresses a significant challenge and improvement in the field of sodium-sulfur (Na-S) batteries by exploring transition metal doping on C_2N monolayers through single-atom and dual-atom transition metals.
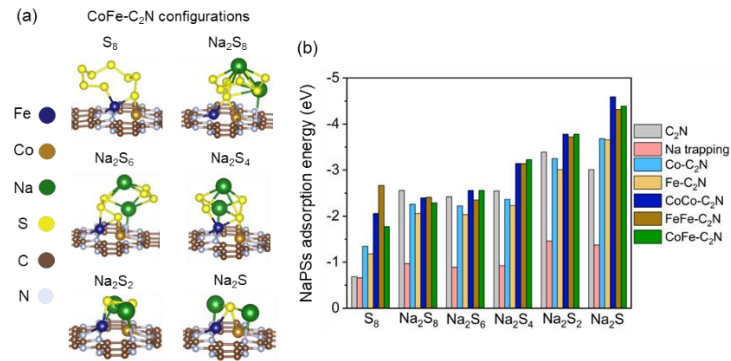

Figure 1. (a) The most stable adsorption configurations of S_8 and NaPSs on CoFe-C_2N. (b) Adsorption energy of S_8 and NaPSs when adsorbed on bare C_2N, Na trapping (Na doped on C_2N), single-atom doping, and dual-atom doping.

References

1. Manthiram, A., Yu, X. *Small* 11, 2108-2114 (2015).
2. Sajjad, M., Hussain, T., Singh, N., and Larsson, L.A. *Langmuir* 36, 13104-13111 (2020)
3. Kresse, G., Furthmüller, J. *Physical Review B* 54 (16), 11169-11186 (1996)
4. Kresse, G., Furthmüller, J. *Computational Materials Science* 6 (1), 15-50 (1996)

Molecular Dynamics Investigation into Solvation and Dynamics of NaClO₄ in Glyme Solvents for Sodium-Ion Batteries

Phitchapa A. and Manaswee S.*

Department of Chemical Technology, Faculty of Science, Chulalongkorn University, 254 Phayathai Road, Wangmai, Pathumwan, Bangkok 10330, Thailand
*manaswee.s@chula.ac.th

1. Introduction

Sodium-ion batteries (SIBs) are an attractive alternative to lithium-ion batteries (LIBs) due to abundance and cost-effectiveness of sodium (Na). With Na being the sixth most common element in the Earth's crust, SIBs offer a more practical and economical solution for large-scale energy storage (Slater et al., 2013). SIBs operate by moving sodium ions (Na^+) between the anode and cathode during charging and discharging cycles. However, the larger ionic radius of sodium compared to lithium leads to unique electrochemical properties, which present specific challenges, especially in the design and performance of electrolytes used in SIBs (Xu, 2004; Kim et al., 2012). Common electrolytes in SIBs include sodium salts such as sodium hexafluorophosphate ($NaPF_6$) and sodium bis(trifluoromethylsulfonyl)imide (NaTFSI). However, the use of fluorinated salts raises significant environmental and safety concerns due to the production of toxic and corrosive byproducts and their potential transformation into Per- and polyfluoroalkyl substances (PFAS) (Rensmo et al., 2023). PFAS are notorious for their persistence in the environment, bioaccumulation, and toxicity (Guelfo et al., 2023). While substances like bis(perfluoroalkyl)sulfonimide (bis-FASI) enhance electrochemical stability, their environmental impact drives the search for safer alternatives. In response, scientists are investigating fluorine-free salts such as sodium bis(oxalato)borate (NaBOB) and sodium bis(salicylato)borate (NaBSB) (Hernández et al., 2022). Additionally, sodium perchlorate ($NaClO_4$) with its notable solubility and ionic conductivity, is considered as a promising electrolyte option (Ponrouch et al., 2012).

The choice of solvent is also critical in determining the properties of the electrolyte, including ionic conductivity, viscosity, and stability. Ether-based solvents known as glymes are promising candidates for SIBs electrolytes because they offer high dielectric constants, low viscosity, and favorable chemical stability. These attributes improve the dissolution and mobility of Na^+, which is crucial for optimal SIB performance. Glymes have been identified as suitable solvents for Li-S and Li-O₂ batteries due to their appropriate volatility, which is beneficial for open cell designs, and their high chemical stability within the cell environment. Salts such as LiTFSI (lithium bis(trifluoromethanesulfonyl)imide), LiTf (lithium triflate), LiFSI (lithium bis(fluorosulfonyl)imide), and LiBETI (lithium bis(pentafluoroethylsulfonyl)imide) when used in glyme-based electrolytes, enhance battery performance by providing high ionic conductivity and stability. These properties make them ideal for both insertion and conversion chemistries, making these salts standout choices for Li-S and Li-O₂ applications. (Di Lecce et al., 2022). Additionally, glymes exhibit lower flammability and a reduced risk of thermal runaway compared to traditional carbonate-based solvents, enhancing safety for large-scale energy storage systems (Li et al., 2022).

Recent research on Na-O₂ battery systems highlights the impact of solvent selection on battery performance. Lutz et al. (Lutz et al., 2016) found that glyme ethers with different chain lengths significantly affect battery performance. Short-chain ethers facilitate solvent removal and precipitation, leading to the formation of large cubic crystals that store substantial amounts of material. In contrast, long-chain ethers result in smaller submicrometric crystallites, reducing system performance. The solvation structure of Na^+ in various solvents is critical for Na-O₂ battery functionality. Studies by Hartmann et al. and McCloskey et al. (Hartmann et al., 2013; McCloskey et al., 2014). have shown that Na^+ ions influence the formation and growth of discharge products, affecting the overall capacity and efficiency of Na-O₂ batteries.

Molecular dynamics (MD) simulations are a valuable tool for investigating the solvation and transport properties of electrolytes at the atomic level. These simulations allow researchers to examine how ions interact with solvent molecules, offering detailed insights into the structural and dynamic characteristics of electrolyte systems. By using MD simulations, researchers can analyze various solvation environments and ion movements, which are often difficult to observe experimentally (Park et al., 2018; Ravikumar et al., 2018; Núñez-Rojas et al., 2023; Gupta et al., 2024; Cheng et al., 2024).

In this study, we employ MD simulations to investigate the solvation and transport behaviors of NaClO$_4$ in different glyme solvents, including monoglyme (G1), diglyme (G2), triglyme (G3), and tetraglyme (G4). Our objective is to compare the solvation structure, coordination number, and diffusion coefficients of Na$^+$ ions in these glymes to determine the most effective solvent for SIB applications.

2. Methodology
2.1 Computational methods

Classical molecular dynamics (MD) simulations were conducted using GROMACS 2023.2 (Abraham et al., 2023; Van Der Spoel et al., 2005) to investigate the solvation and dynamics of NaClO$_4$ in glyme solvents: monoglyme (G1), diglyme (G2), triglyme (G3), and tetraglyme (G4). The OPLS-AA force field (Doherty et al., 2017) was applied to model the interactions between Na$^+$ ions and glyme molecules. Figure 1 illustrates the chemical structures of the ions and glyme molecules. Each simulation system contained 130 NaClO$_4$ molecules and glyme solvents: 1249 G1, 914 G2, 710 G3, and 577 G4 molecules, corresponding to 1 M NaClO$_4$. Periodic boundary conditions were applied in all three dimensions. A cutoff distance of 1.2 nm was used for Lennard- Jones interactions. Long-range electrostatic interactions were managed using the Particle-Mesh Ewald (PME) method. To relax the initial configurations, energy minimization was carried out with the steepest descent algorithm. Following minimization, the systems were equilibrated in two stages. The first stage, NVT equilibration, was conducted at 300 K for 1 ns using the velocity- rescale thermostat with a 0.1 ps coupling time. The second stage, NPT equilibration, was performed at 1 bar for 1 ns using the stochastic cell rescaling (C-rescale) barostat with a 2.0 ps relaxation time. After equilibration, production MD simulations were executed for 10 ns with a 2 fs time step. The duration of these simulations was sufficient to accurately capture the dynamics and solvation characteristics of the equilibrated systems.
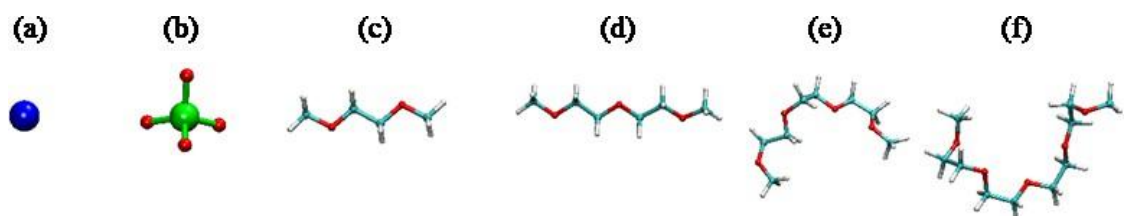

Figure 1. Illustrations of ions and glyme solvents: (a) Na$^+$, (b) ClO$_4^-$, (c) monoglyme (G1), (d) diglyme (G2), (e) triglyme (G3), and (f) tetraglyme (G4).

2.2 Analysis

The radial distribution function (RDF) denotes probability distribution of particle at a distance of r from reference and characterizes the solvation structure (Ravikumar et al., 2018) as follows:

$$g_{x,y}(r) = \frac{n(r)}{4\pi r^2 dr \rho} \tag{1}$$

where $n(r)$ is the number of y atoms at a radial distance r from a reference particle, $4\pi r^2 dr$ is the volume of a shell of thickness dr at r, and ρ is the bulk number density of y atoms.

By integrating the related radial distribution function up to R, the coordination number illustrates the number density of atoms around the reference atom at the distance R, as shown in the following equation:

$$N(r) = \int_0^R g_{x,y}(r)gr \tag{2}$$

where $N(r)$ is the number integral at distance R and $g(r)$ is the radial distribution function.

The transport of ions were measured by the diffusion coefficient (D), which was computed from a least-squares fitting for a straight line in mean squared displacement (MSD) in the diffusive regime (Han et al., 2016) as shown in the following equation:

$$D = \lim_{\Delta t \to \infty} \frac{\langle MSD_i(t) \rangle}{6t} \tag{3}$$

where $MSD_i(t)$ is the mean-square displacement of the center-of-mass of a component i after time t, $<>$ denotes an ensemble average.

The Nernst-Einstein equation can be used to calculate the ionic conductivity (σ) for the system as the following equation:

$$\sigma = \frac{N_{pair}e^2}{Vk_BT}(q_+^2 D_+ + q_-^2 D_-) \tag{4}$$

where N_{pair} is the number of ion pairs, e is electric charge, q_+ and q_- are the total charges on cation and anion respectively, D_+ and D_- are the diffusion coefficient of cation and anion, respectively, V is the simulation box volume, T is the temperature, and k_B is the Boltzmann constant.

3. Results and Discussion
3.1 Structural properties
3.1.1 Solvation structure of Na$^+$

Figure 2 shows the Na$^+$ solvation structures obtained from 1 M NaClO$_4$ in G1, G2, G3, and G4 glyme solvents. **NaClO$_4$/G1:** The Na$^+$ (blue sphere) is closely associated with ClO$_4^-$, forming a contact ion pair (CIP) as shown in Figure 2a. The G1 glyme molecules are positioned around the Na$^+$, but the primary interaction is between Na$^+$ and ClO$_4^-$. This finding is in good agreement with nuclear magnetic resonance (NMR) and Raman spectroscopy (Lutz et al., 2016). The NMR shifts indicated that Na$^+$ ions are significantly coordinated by the ether oxygen atoms of G1. The study found that in NaClO$_4$/G1, Na$^+$ tend to form stable complexes with the solvent molecules, which is indicative of strong ion-solvent interactions. Moreover, the Raman spectra showed distinct vibrational modes corresponding to the Na$^+$-G1 interactions. There was a significant red shift in the C–O–C stretching vibrations and a blue shift in the C–C–O bending/twisting modes upon coordination with Na$^+$. These shifts are indicative of the strong interaction between the Na$^+$ and the ether oxygen atoms of G1, further confirming the formation of CIP (Ortiz Vitoriano et al., 2020).
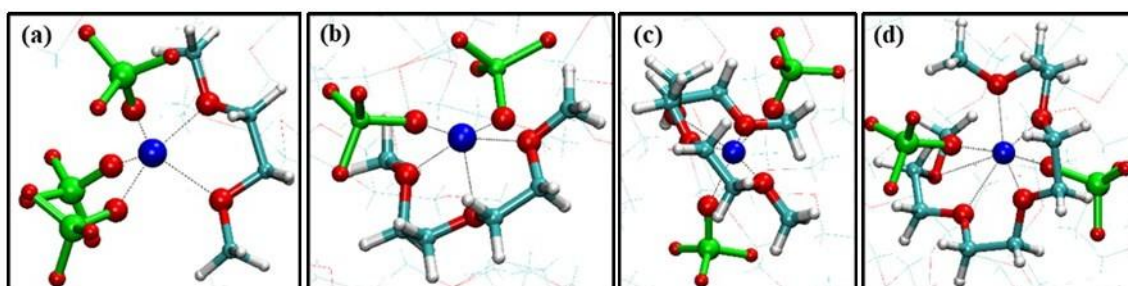

Figure 2. Equilibrium simulation snapshots of the Na$^+$ solvation structure in (a) NaClO$_4$/G1, (b) NaClO$_4$/G2, (c) NaClO$_4$/G3, and (d) NaClO$_4$/G4.

NaClO$_4$/G2: In this system (Figure 2b), the Na$^+$ interacts with ClO$_4^-$, but the interaction is weaker compared to G1. The G2 molecules are more prominently involved in the solvation of Na$^+$, indicating the presence of both CIP and solvent-separated ion pairs (SSIPs). **NaClO$_4$/G3:** As seen in Figure 2c, the Na$^+$ is mostly surrounded by G3 molecules, with ClO$_4^-$ positioned further away, indicating a clear SSIP structure. **NaClO$_4$/G4:** In this panel (Figure 2d), the Na$^+$ ion is well- separated from ClO$_4^-$ and is surrounded by G4 molecules, forming stable SSIP. The solvation shell of G4 molecules around Na$^+$ is more extensive compared to G1, G2, and G3.

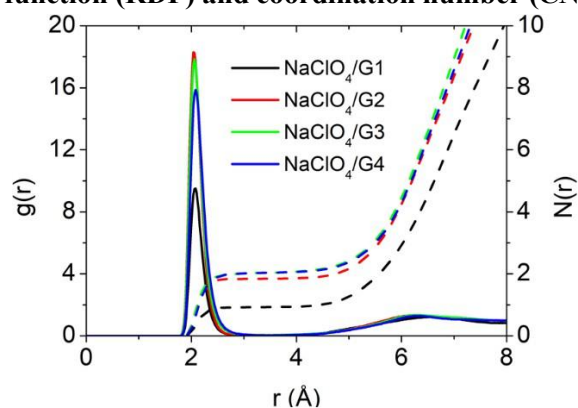### 3.1.2 Radial distribution function (RDF) and coordination number (CN)

Figure 3. RDF (solid lines) and CN (dashed lines) for Na$^+-$O(glymes).

The RDF plot for Na$^+$ and (O)glymes (Figure 3) displays significant peaks around 2 Å for all glyme solvents (G1, G2, G3, and G4). This peak represents the first solvation shell of Na$^+$ ions, indicating the most frequent interaction distance between Na$^+$ and the oxygen atoms of the glymes. Among these, NaClO$_4$/G1 (black line) has the lowest peak intensity which mean the weakest interaction between Na$^+$ ions and G1. This trend suggests that G1 has fewer ether oxygen atoms available to solvate Na$^+$, resulting in direct Na$^+$-ClO$_4^-$ interactions. In contrast, longer glymes (G2, G3, G4), which have more ether oxygen atoms, can coordinate more effectively with Na$^+$, thereby reducing direct Na$^+$-ClO$_4^-$ interactions. The peak intensity increases slightly for NaClO$_4$/G2 (red line), NaClO$_4$/G3 (blue line), and NaClO$_4$/G4 (green line), indicating gradually stronger interactions as the glyme chain length increases. Moreover, coordination number (CN), derived from integrating the RDF peaks, show that the CN for Na$^+$ in G1 is around 2. The oxygen atoms from G1 glyme molecules are likely to coordinate with the Na$^+$, on average in a ratio of 2:1. For longer glymes (G2, G3, and G4), the CN increases to approximately 4, suggesting more extensive solvation shell. Thus, longer glymes provide more coordination environment for Na$^+$ ions, enhancing solvation stability.

The interaction between Na$^+$ and ClO$_4^-$ was considered from the RDF plot for Na$^+$ and (O)ClO$_4^-$. Figure 4a shows significant peak around 2 Å for NaClO$_4$/G1 (black line), indicating strong direct interaction between Na$^+$ and the oxygen atoms of the ClO$_4^-$. This peak is much higher for the system of G1 glyme solvent compared to the other glymes (G2, G3, and G4) which mean the interaction between Na$^+$ and ClO$_4^-$ is strongest in G1. Additionally, the RDF plot for Na$^+$ and (Cl)ClO$_4^-$ (Figure 4b) shows significant peak around 3 Å for NaClO$_4$/G1 (black line), indicating strong direct interaction between Na$^+$ and the ClO$_4^-$. This peak is more pronounced in G1 compared to the other glymes (G2, G3, and G4), suggesting that the interaction between Na$^+$ and ClO$_4^-$ is strongest in G1. In longer-chain glyme molecules, the RDF peaks are less intense and display additional peaks at larger distances, indicating the formation of SSIPs. For the CN of Na$^+$ and (Cl)ClO$_4^-$ in G1 is approximately 3. This higher CN in G1 confirms the formation of contact ion pairs (CIPs). In contrast, for G2, G3, and G4 glymes, CN values decrease, suggesting weaker interactions between Na$^+$ and ClO$_4^-$ and a tendency towards the formation of SSIPs.
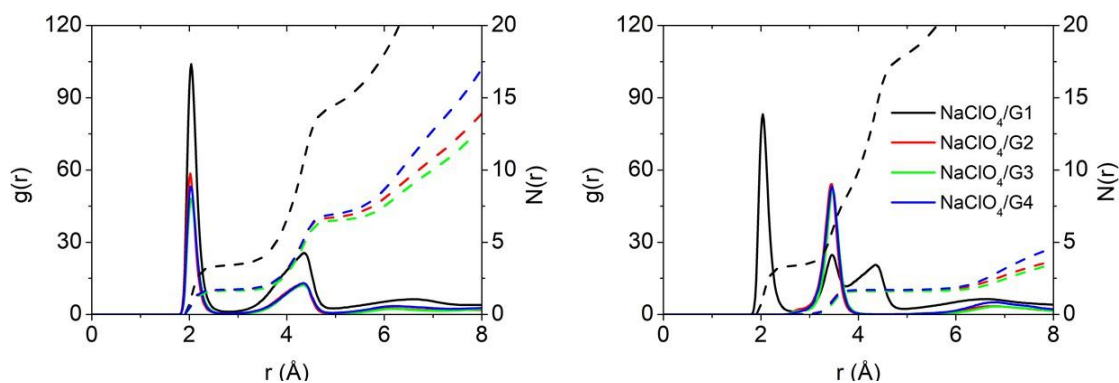
Figure 4. RDF (solid lines) and CN (dashed lines) for (a) $Na^+-O(ClO_4^-)$ and (b) $Na^+-Cl\ (ClO_4^-)$.

Table 1. Lennard-Jones and Coulombic interaction energies (kJ/mol) for Na^+-Glymes and Na^+- ClO_4^-, obtained from simulations of 1 M NaClO₄ in G1, G2, G3, and G4 glyme solvents.

System	LJ Na+-Glymes	LJ Na^+-ClO_4^-	Coul Na^+-Glymes	Coul Na^+-ClO_4^-
NaClO₄/G1	1,226.8	3,567.0	-13,782.6	-52,843.3
NaClO₄/G2	2,867.9	2,091.4	-30,375.2	-26,166.1
NaClO₄/G3	2,886.6	1,712.5	-32,924.7	-24,266.1
NaClO₄/G4	2,489.2	1,924.9	-30,948.6	-26,482.9

The RDF and CN analyses provide detailed picture of the solvation structure, while the interaction energy calculations quantify the stability and strength of these interactions. The Lennard-Jones (LJ) and coulombic interaction energies for Na^+-Glyme and Na^+-ClO_4^-, as well as coulombic interactions, are summarized in Table 1. The LJ interaction energy for Na^+-Glyme is lowest for NaClO₄/G1, indicating weaker van der Waals interactions. This aligns with the RDF data showing weaker Na^+-Glyme interactions in G1. The coulombic interaction energy between Na^+ and ClO_4^- is most negative for NaClO₄/G1, indicating the strongest electrostatic interactions, which supports the observation of CIPs in G1. As the glyme chain length increases (G2, G3, G4), the coulombic interaction energy becomes less negative, indicating weaker Na^+-ClO_4^- interactions and a shift towards SSIP formation. Comparing these trends to the data from Lutz et al. (Lutz et al., 2016), it is observed that the formation of CIPs in short-chain glymes like G1 is characterized by strong Na^+-ClO_4^- interactions and lower coordination numbers. In contrast, longer glymes show weaker Na^+-ClO_4^- interactions, higher coordination numbers, and a tendency towards SSIPs formation. This consistent trend across both studies validates the observed solvation structures and interaction energies.

3.2 Dynamical properties
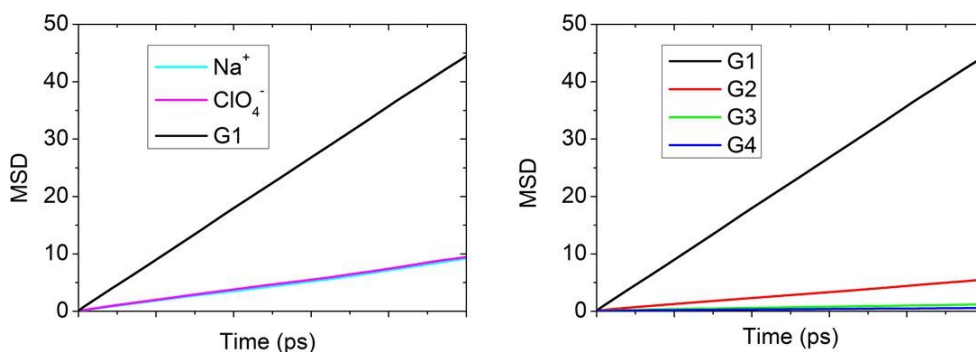### 3.2.1 Mean squared displacement (MSD) and diffusion coefficient (D)

Figure 5. (a) MSD of Na^+, ClO_4^-, and G1 obtained from 1 M $NaClO_4$/G1 electrolyte (b) MSD of various glyme solvents.

The plot of MSD versus time for $NaClO_4$/G1 from Figure 5a shows the movement of cation, anion and solvent. G1 exhibits the highest mobility, followed by ClO_4^- and Na^+. The slopes of ClO_4^- and Na^+ are not significant different, which mean there are nearly similar mobility. The slope of the MSD for G1 is significantly higher, indicating that the solvent molecules are more mobile than the ions. This higher mobility is also reflected in the diffusion coefficients, where G1 has the highest diffusion coefficient compared to the other systems. The parallel and low slopes of Na^+ and ClO_4^- suggest restricted mobility, which can be attributed to the strong interactions between Na^+ and ClO_4^-, leading to the formation of contact ion pairs (CIPs). The high diffusion coefficient of the solvent G1, along with the lower diffusion coefficients for Na^+ and ClO_4^-, confirm this restricted mobility and strong ion pairing.

When comparing the different glyme solvents, the MSD plots show that mobility decreases with increasing chain length of the glymes. For $NaClO_4$/G2, the slopes of the MSD plots are lower than for G1, indicating reduced mobility, which is also reflected in the diffusion coefficients. Specifically, the mobility trend follows the order: G1 >> G2 > G3 ~ G4 (Figure 5b). This indicates that the shorter glyme (G1) provides the highest mobility, whereas the longer glymes (G3 and G4) result in significantly lower mobility. The diffusion coefficients align with this trend, showing the highest values for G1 and the lowest for G4. The low and parallel MSD slopes for G4 indicate restricted mobility, which can be associated with hydrodynamic interactions. The increased chain length in G4 leads to higher viscosity, reducing the overall mobility of the system.

The diffusion coefficients vary significantly across the different components and glyme solvents. For Na^+, the values decrease as the glyme chain length increases: 7.23×10^{-7} cm²/s in $NaClO_4$/G1, 1.81×10^{-7} cm²/s in $NaClO_4$/G2, 0.58×10^{-7} cm²/s in $NaClO_4$/G3, and 0.21×10^{-7} cm²/s in $NaClO_4$/G4. Similarly, the diffusion coefficients for ClO_4^- ions also show a downward trend with increasing glyme chain length: 7.57×10^{-7} cm²/s in $NaClO_4$/G1, 1.82×10^{-7} cm²/s in $NaClO_4$/G2, 0.69×10^{-7} cm²/s in $NaClO_4$/G3, and 0.28×10^{-7} cm²/s in $NaClO_4$/G4. The solvents themselves follow the same pattern, with diffusion coefficients of 95.49×10^{-7} cm²/s in $NaClO_4$/G1, 11.26×10^{-7} cm²/s in $NaClO_4$/G2, 2.67×10^{-7} cm²/s in $NaClO_4$/G3, and 1.23×10^{-7} cm²/s in $NaClO_4$/G4.

These values indicate that the diffusion coefficient for solvent is always higher than that for ClO_4^-, which in turn is higher than that for Na^+ ($D_{solvents} > D_{ClO_4^-} > D_{Na^+}$). The diffusion coefficients show clear trend: $NaClO_4$/G1 > $NaClO_4$/G2 > $NaClO_4$/G3 > $NaClO_4$/G4 (Figure 5a). This pattern suggests that as the glyme chain length increases, the mobility of both ions and solvents decreases. In contrast, $NaClO_4$/G3 and $NaClO_4$/G4 exhibits low and parallel MSD slopes, indicative of restricted mobility due to stronger hydrodynamic interactions which are the effects of ions move through the electrolytes and create a flow that affect to the other nearby particles. These interactions result in coupled motion of ions and solvent molecules, which is reflected in the lower diffusion coefficients for $NaClO_4$/G3 and

NaClO₄/G4 (Figure 5b). The higher interaction energies in NaClO₄/G3 and NaClO₄/G4 further support the presence of significant hydrodynamic effects, which impede the movement of ions and solvent molecules, leading to reduced diffusivity.
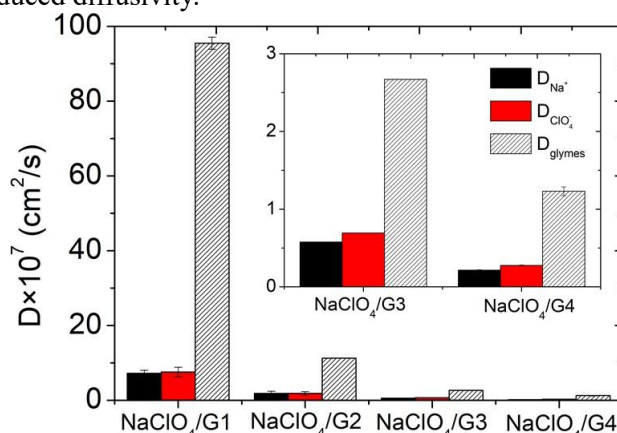

Figure 6. Diffusion coefficients (D) for (a) Na⁺, ClO₄⁻, and glymes, and (b) inset plot of NaClO₄/G3 and NaClO₄/G4 electrolytes.

1.1.1 Ionic conductivity (σ)

Figure 7 shows ionic conductivity of electrolytes. **NaClO₄/G1:** The NaClO₄/G1 system exhibits the highest ionic conductivity at 21.66 mS/cm. This high conductivity can be attributed to the low viscosity (0.42 mPa·s) (Tang & Zhao, 2014) and smaller molecular size of the G1 solvent, which allows for higher ion mobility. The high diffusion coefficients of both Na⁺ and ClO₄⁻ in this system contribute significantly to the overall ionic conductivity. **NaClO₄/G2:** The ionic conductivity for NaClO₄/G2 is 7.17 mS/cm, which is lower than that for G1. This decrease in conductivity is due to the increased viscosity (0.98 mPa·s) (Kodama et al., 2011; Tang & Zhao, 2014) and larger molecular size of the G2 solvent, which restricts ion mobility. **NaClO₄/G3:** The ionic conductivity further decreases to 2.07 mS/cm for NaClO₄/G3. The longer chain length and higher viscosity (1.96 mPa·s) (Kodama et al., 2011; Tang & Zhao, 2014) of the G3 solvent result in even lower ion mobility compared to G2. **NaClO₄/G4:** The lowest ionic conductivity is observed for NaClO₄/G4 at 0.81 mS/cm. The G4 solvent, with the longest chain length and highest viscosity (3.40 mPa·s) (Kodama et al., 2011; Tang & Zhao, 2014), provides the most significant restriction to ion mobility.
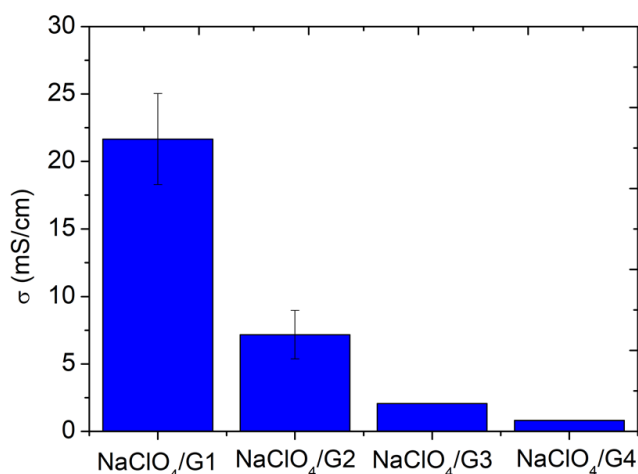

Figure 7. Ionic conductivity (σ) of electrolytes obtained from 1 M NaClO₄ in G1, G2, G3, and G4 glyme solvents. The standard deviation error bars for G3 and G4 are too small to be clearly visible.

4. Conclusion

The study used MD simulations to explore the solvation structure, dynamics, and ionic conductivity of sodium perchlorate ($NaClO_4$) in various glyme solvents: monoglyme (G1), diglyme (G2), triglyme (G3), and tetraglyme (G4), aiming to optimize SIB. It found that 1 M $NaClO_4$ in G1 formed strong contact ion pairs (CIPs) between Na^+ and ClO_4^-, resulting in high ionic mobility and the highest conductivity among the solvents tested (21.66 mS/cm). G1 has fewer ether oxygen atoms available to solvate Na^+, resulting in direct Na^+- ClO_4^- interactions. In contrast, longer glymes (G2, G3, G4) which have more ether oxygen atoms that can coordinate with Na^+. Thus, longer glymes favored to form in solvent-separated ion pairs (SSIPs), leading to reduced ion mobility and lower conductivity due to stronger hydrodynamic interactions. The study concludes that G1 solvent is ideal for high-power applications requiring rapid ion transport, while G2 solvent offers a balance of mobility and stability, making it suitable for long-life cycle batteries.

References

Abraham, M., Alekseenko, A., Bergh, C., Blau, C., Briand, E., Doijade, M., Fleischmann, S., Gapsys, V., Garg, G., & Gorelov, S. (2023). GROMACS 2023.1 Manual. *GROMACS: Groningen, The Netherlands*.

Cheng, H., Ma, Z., Kumar, P., Liang, H., Cao, Z., Xie, H., ... & Ming, J. (2024). Non-flammable electrolyte mediated by solvation chemistry toward high-voltage lithium-ion batteries. *ACS Energy Letters, 9*(4), 1604-1616.

Doherty, B., Zhong, X., Gathiaka, S., Li, B., & Acevedo, O. (2017). Revisiting OPLS Force Field Parameters for Ionic Liquid Simulations. *Journal of Chemical Theory and Computation*, *13*(12), 6131-6145.

Di Lecce, D., Marangon, V., Jung, H. G., Tominaga, Y., Greenbaum, S., & Hassoun, J. (2022). Glyme-based electrolytes: suitable solutions for next-generation lithium batteries. *Green Chemistry, 24*(3), 1021-1048.

Guelfo, J., Ferguson, P., Beck, J., Chernick, M., Doria-Manzur, A., Faught, P., Flug, T., Gray, E., Jayasundara, N., & Knappe, D. (2023). The dirty side of clean energy: Lithium ion batteries as a source of PFAS in the environment.

Gupta, S., Gupta, U., & Sappidi, P. (2024). Molecular dynamics simulation study of sodium ion structure & dynamics in water in ionic liquids electrolytes using 1-butyl-3-methyl imidazolium tetrafluoroborate and 1-butyl-3-methyl imidazolium hexafluorophosphate. *Journal of Molecular Graphics and Modelling, 130*, 108775.

Han, S.-D., Rajput, N. N., Qu, X., Pan, B., He, M., Ferrandon, M. S., Liao, C., Persson, K. A., & Burrell, A. K. (2016). Origin of Electrochemical, Structural, and Transport Properties in Nonaqueous Zinc Electrolytes. *ACS Applied Materials & Interfaces*, *8*(5), 3021-3031.

Hartmann, P., Bender, C. L., Vračar, M., Dürr, A. K., Garsuch, A., Janek, J., & Adelhelm, P. (2013). A rechargeable room-temperature sodium superoxide (NaO2) battery. *Nature Materials*, *12*(3), 228-232.

Hernández, G., Mogensen, R., Younesi, R., & Mindemark, J. (2022). Fluorine-Free Electrolytes for Lithium and Sodium Batteries. *Batteries & Supercaps*, *5*(6), e202100373.

Kim, S.-W., Seo, D.-H., Ma, X., Ceder, G., & Kang, K. (2012). Electrode Materials for Rechargeable Sodium-Ion Batteries: Potential Alternatives to Current Lithium-Ion Batteries. *Advanced Energy Materials*, *2*(7), 710-721.

Kodama, D., Kanakubo, M., Kokubo, M., Hashimoto, S., Nanjo, H., & Kato, M. (2011). Density, viscosity, and solubility of carbon dioxide in glymes. *Fluid Phase Equilibria*, *302*(1), 103-108.

Li, Y., Wu, F., Li, Y., Liu, M., Feng, X., Bai, Y., & Wu, C. (2022). Ether-based electrolytes for sodium ion batteries [10.1039/D1CS00948F]. *Chemical Society Reviews*, *51*(11), 4484-4536.

Lutz, L., Yin, W., Grimaud, A., Alves Dalla Corte, D., Tang, M., Johnson, L., Azaceta, E., Sarou-Kanian, V., Naylor, A. J., Hamad, S., Anta, J. A., Salager, E., Tena-Zaera, R., Bruce, P. G., & Tarascon, J. M. (2016). High Capacity Na–O2 Batteries: Key Parameters for Solution-Mediated Discharge. *The Journal of Physical Chemistry C*, *120*(36), 20068-20076.

Martínez, L., Andrade, R., Birgin, E. G., & Martínez, J. M. (2009). PACKMOL: A package for building initial configurations for molecular dynamics simulations. *Journal of Computational Chemistry*, *30*(13), 2157-2164.

McCloskey, B. D., Garcia, J. M., & Luntz, A. C. (2014). Chemical and Electrochemical Differences in Nonaqueous Li–O2 and Na–O2 Batteries. *The Journal of Physical Chemistry Letters*, *5*(7), 1230-1235.

Núñez-Rojas, E., González, I., Guzmán-González, G., & Alejandre, J. (2023). Molecular dynamics simulations for liquid electrolytes of propylene carbonate with LiTFSI, $LiPF_6$, and $LiBF_4$ salts. Journal of Molecular Liquids, 390, 122983.

Ortiz Vitoriano, N., Ruiz de Larramendi, I., Sacci, R. L., Lozano, I., Bridges, C. A., Arcelus, O., Enterría, M., Carrasco, J., Rojo, T., & Veith, G. M. (2020). Goldilocks and the three glymes: How Na+ solvation controls Na–O2 battery cycling. *Energy Storage Materials*, *29*, 235-245.

Park, C., Kanduč, M., Chudoba, R., Ronneburg, A., Risse, S., Ballauff, M., & Dzubiella, J. (2018). Molecular simulations of electrolyte structure and dynamics in lithium–sulfur battery solvents. *Journal of Power Sources*, *373*, 70-78.

Ponrouch, A., Marchante, E., Courty, M., Tarascon, J.-M., & Palacín, M. R. (2012). In search of an optimized electrolyte for Na-ion batteries [10.1039/C2EE22258B]. *Energy & Environmental Science*, *5*(9), 8572-8583.

Ravikumar, B., Mynam, M., & Rai, B. (2018). Effect of Salt Concentration on Properties of Lithium Ion Battery Electrolytes: A Molecular Dynamics Study. *The Journal of Physical Chemistry C*, *122*(15), 8173-8181.

Rensmo, A., Savvidou, E. K., Cousins, I. T., Hu, X., Schellenberger, S., & Benskin, J. P. (2023). Lithium-ion battery recycling: a source of per-and polyfluoroalkyl substances (PFAS) to the environment? *Environmental Science: Processes & Impacts*.

Slater, M. D., Kim, D., Lee, E., & Johnson, C. S. (2013). Sodium-Ion Batteries. *Advanced Functional Materials*, *23*(8), 947-958.

Tang, S., & Zhao, H. (2014). Glymes as versatile solvents for chemical reactions and processes: from the laboratory to industry [10.1039/C3RA47191H]. *RSC Advances*, *4*(22), 11251-11287.

Van Der Spoel, D., Lindahl, E., Hess, B., Groenhof, G., Mark, A. E., & Berendsen, H. J. C. (2005). GROMACS: Fast, flexible, and free. *Journal of Computational Chemistry*, *26*(16), 1701-1718.

Xu, K. (2004). Nonaqueous Liquid Electrolytes for Lithium-Based Rechargeable Batteries. *Chemical Reviews*, *104*(10), 4303-4418.

AI-Driven Image Processing System for Aquatic Plant Studies: Application to watermeal Detection and Counting

Wuttiphat Ainthongkham[1], Surat Teerapittayanon[2], Tatpong Tulyananda[1*], and Monrudee Liangruksa[2*]

[1]*Faculty of Science, Mahidol University 272 Rama VI Road, Ratchathewi, Bangkok 10400, Thailand*
[2]*National Nanotechnology Center (NANOTEC), National Science and Technology Development Agency (NSTDA), Pathum Thani 12120, Thailand*
* tatpong.tul@mahidol.edu and monrudee@nanotec.or.th

Introduction

Watermeal, also known as Khai Nam or Phum (*Wolffia globosa*), is classified as the smallest flowering plant. It has a diameter of approximately 0.5-1.5 mm [1]. This floating, aquatic plant is easy to propagate and is commonly found in natural reservoirs. Its nutritional composition mainly includes protein, fiber, and phytopigments, with protein content as high as that of beans. Watermeal also contains essential amino acids. In Thailand, this small aquatic plant has gained attention as it can be used in dietary supplements and dishes.

The cultivation of watermeal, presents unique challenges due to its size and sensitivity to environmental conditions like pH and temperature. Traditional methods of measuring growth by direct counting, are inaccurate. The utilization of image analysis software, such as ImageJ, equipped with custom macros and commands written in JavaScript or Python, is more precise to quantify the watermeal population. By leveraging the capabilities of ImageJ, researchers can automate the process, thus enhancing efficiency and reducing the likelihood of human error. Here we integrate image processing techniques and deep learning models like MobileNet-v2 to further refines the detection and counting. This approach not only streamlines the process for watermeal detection, but can also apply for other plant farming systems, potentially revolutionizing farming systems.

Methodology

Convolutional Neural Network (CNN) is a type of neural network used in computer vision and image analysis. CNN models come in various architectures, each influencing their properties and performance. Some examples of pre-trained CNN models include LeNet-5, AlexNet, VGGNet, GoogLeNet, and MobileNet. For this study, we utilize MobileNet-v2, an enhanced version of the MobileNet-v1 CNN model known for its high performance in image processing.

MobileNet-v2 [2] has 53 convolutional layers designed to be less computationally and memory intensive than previous versions. It achieves this by utilizing techniques such as depthwise separable convolutions, inverted residual blocks, and linear bottlenecks to enhance feature generation efficiency. This structure is suitable for image processing on devices with limited computing resources, offering fast processing and efficient image recognition and analysis. The MobileNet-v2 architecture comprises two main components: the inverted residual block and the bottleneck residual block. Within these blocks, there are essential layers, including 1x1 convolution with Relu6, depthwise convolution, and 1x1 convolution without any linearity.

Results and Discussion

We performed three separate techniques for watermeal number using ImageJ, Open Computer Vision 2 (OpenCV**2**) [3] and MobileNet-v2, as shown in Figures 1 and 2, respectively.
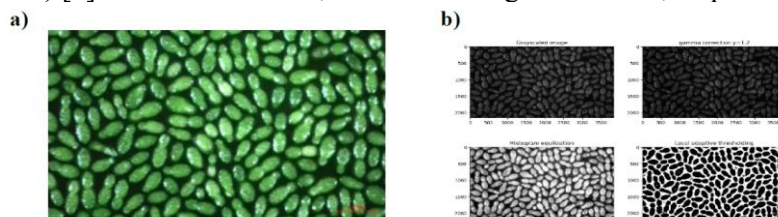

Figure 1: (a) Sample image of watermeal used in image analysis with ImageJ (magnification 10x), and (b) OpenCV2 plots the image with grayscale, gamma correction, histogram, and thresholding tables.

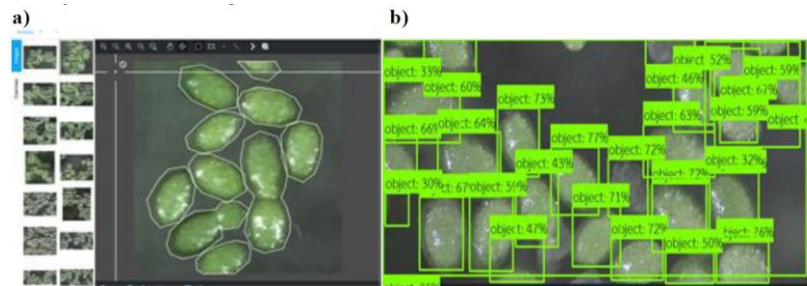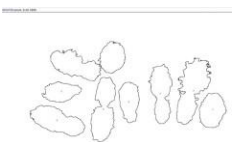Green objects are converted to black and white (thresholding) to distinguish the objects from the background.
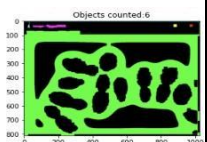

Figure 2: (a) The CNN model development was based on a dataset of watermeal images labeled by the annotation tool (https://annotation.peer-ai.com). (b) Object detection results from MobileNet-v2.

Table 1: Enumeration of the watermeal numbers using techniques: ImageJ, OpenCV (CV2, and MobileNet-v2. Watermeal sample images with counting numbers from different techniques, and the corresponding errors compared with human eye observation. Noting that, the average percentage error of each method = % total error of each method/number of images used in testing.

Table 1: Enumeration of the watermeal numbers using techniques: ImageJ, OpenCV (CV2), and MobileNet-v2.

Images	Watermeal number, average percentage error		
	ImageJ	OpenCV2	MobileNet-v2
11	9,18%	6,45%	9,18%
10	8,20%	1,90%	11,10%

Significance
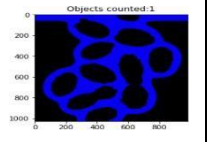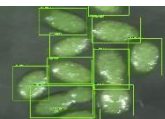
Table 2 presents the counting results and the average percentage errors of the three methods on some test images. The order of lowest average errors is as follows: ImageJ (19.5%), MobileNet-v2 (23.3%), and OpenCV2 (86.6%). To enhance the accuracy of detection and counting using MobileNet-v2, additional images are needed. Notably, the error percentage of OpenCV2 is higher than that of the other two methods. Both ImageJ and MobileNet-v2 exhibit similar error percentages (19.5% and 23.3%, respectively). Consequently, these two techniques are well-suited for detecting and counting the number of watermeal. ImageJ has the advantage of offering a variety of tools, including the ability to calculate the area and size of an object. On the other hand, MobileNet-v2 provides object detection and counting capabilities, which can be further developed for automatic enumeration and tracking of the plant's growth rate. Moreover, MobileNet-v2 is suitable for deployment on resource-constrained devices such as smartphones and cameras.

Table 2: Average percentage errors of all 3 methods (ImageJ, OpenCV2, and MobileNet-v2).

Methods	Average percentage error
ImageJ	19.5%
OpenCV2	86.6%
CNN (MobileNet-v2)	23.3 %

References
1. Saepae, P., (2022), *Available:* https://science.mahidol.ac.th/simple-science/2022/08/02/wolffia/, April 11, 2024.
2. Sandler, M., Howard, A., Zhu, M., et al. Proceedings of the IEEE Conference on Computer Vision and Pattern Recognition, 4510-4520 (2018).
3. Bradski, G., Dr. Dobb's Journal of Software Tools, 120, 122-125 (2000).

DESIGNING SARS-CoV-2 MAIN PROTEASE INHIBITORS USING QSAR-ML TECHNIQUES

Borwornlak Toopradab[1,2], Phornphimon Maitarad[3*], and Thanyada Rungrotmongkol[1,2*]
[1] Program in Bioinformatics and Computational Biology, Graduate School, Chulalongkorn University, Bangkok 10330, Thailand
[2] Center of Excellence in Biocatalyst and Sustainable Biotechnology, Department of Biochemistry, Faculty of Science, Chulalongkorn University, Bangkok 10330, Thailand
[3] Research Center of Nano Science and Technology, Department of Chemistry, College of Science, Shanghai University, Shanghai, 200444 PR China
*maitarad@shu.edu.cn, and thanyada.r@chula.ac.th

Introduction

In response to the global impact of the COVID-19 pandemic, many research groups address the urgent need to develop effective interventions against the virus by focusing on the SARS-CoV-2 main protease (M^{pro}). The M^{pro} enzyme plays a crucial role in the viral replication process, making it an attractive target for drug design. In this work, we focus on small-molecule thioesters that were evaluated against SARS-CoV-2 M^{pro}. To guide in designing potent inhibitors, Quantitative Structure-Activity Relationship (QSAR) was applied to establish a correlation between the structural attributes of small-molecule thioesters and their inhibitory potential against the M^{pro}. The genetic function approximation with multiple linear regression (GFA-MLR), random forest (RF), artificial neural network (ANN), and gradient boosting regression (GBR) models were employed to gain insights into the inhibitory behavior of these compounds.

Methodology

All 33 novel thioesters and their biological activities in Fig. 1 were taken from Pillaiyar *et al.* [1]. The biological activities in terms of IC_{50} values (μM). The IC_{50} values were converted to pIC_{50}, defined as dependent variables (y). The studied small-molecule thioesters were divided into 80% training set and 20% test set according to the Kennard-Stone algorithm, which was achieved by the Python package Kennard-Stone 1.1.2. The independent structural molecular descriptors for the QSAR model were computed using Material Studio software [2]. GFA generates a population of statistical models, focusing on the best one to estimate the relationship between molecular activity and chemical identity. It employs spline-based output equations, increasing model complexity. RF is a popular ensemble method for classification and regression tasks. It creates multiple decision trees to reduce overfitting risk and improve accuracy. ANN is a powerful nonlinear method for model development, and it has a role in feature selection. ANN was used to generate a model of the inhibitory activity data using the function approximation method. GBR was to produce a predictive model from an ensemble of weak predictive models. GBR can be used for regression and classification problems. The fitness of these models was measured by R-squared (R^2), which reflects the fraction of the total variance of the y variable, and the R^2 value close to 1, the better the model.

Results and Discussion

The QSAR concept with GFA-MLR, RF, ANN, and GBR models was used to quantitatively relate the antiviral activity of the small-molecule thioesters to their molecular descriptors. The GBR approach exhibited robust statistical performance, with $R^2_{training}$ set, $RMSE_{train}$, and $RMSE_{test}$ were 0.987, 0.066, and 0.332, respectively. It is interesting to find that the antiviral activity of these compounds appears to be mainly governed by five features of importance, *i.e.* E-state keys (sums): S_aasC, E-state keys (sums): S_aaCH, Shadow area fraction: ZX plane, Shadow area: ZX plane, and Shadow area: YZ plane. The possible mechanism of action of these compounds was analyzed and discussed; in particular, important structural requirements for the thioester with an unsubstituted pyrimidine is the best-leaving group for covalent M^{pro} inhibition.
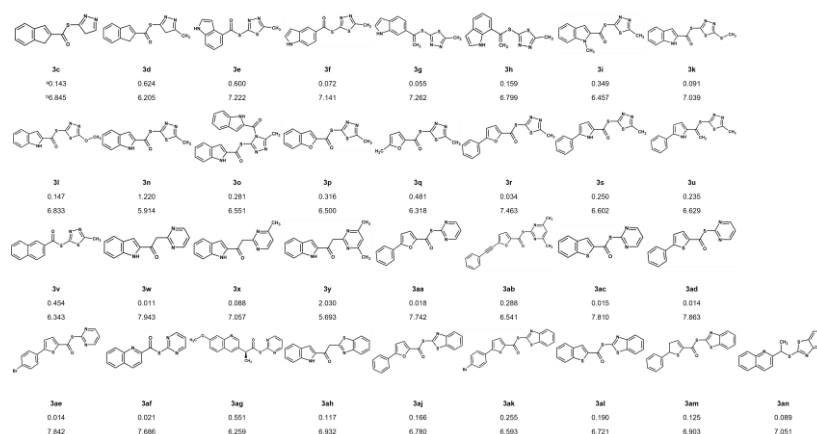
Figure 1. Small-molecule thioesters with their inhibitory activities. Data are expressed in term of the (a) IC_{50} (μM) and (b) pIC_{50}.

Objective: We aimed to determine the relationship between the structural properties of small-molecule thioesters and their biological activities using QSAR-ML models.

Significance

Based on the best proposed QSAR model, some new compounds with higher SARS-CoV-2 M^{pro} inhibitor activity have been theoretically designed. Such results can offer valuable references for future experimental work.

References
1. Pillaiyar T., et al., *J Med Chem 65*, 13 (2022).
2. Fan, X., et al. *Advanced Materials Research*, 706 (2013).

SynProtX: Artificial Intelligence Toward Enhanced Prediction of SynergisticCancer Drug Combinations Using Large-Scale Protein Expression Profiling

Bundit Boonyarit[1], Tisorn Naphattalung[2], Matin Kositchutima[2], Nattawin Yamprasert[3], Thanyada Rungrotmongkol[4,5,*], and Sarana Nutanong[1,*]

[1]*School of Information Science and Technology, Vidyasirimedhi Institute of Science and Technology, Rayong, 21210, Thailand*
[2]*Kamnoetvidya Science Academy, Rayong, 21210, Thailand*
[3]*School of Information, Computer, and Communication Technology, Sirindhorn International Institute of Technology, Thammasat University, Pathum Thani, 12120, Thailand*
[4]*Program in Bioinformatics and Computational Biology, Graduate School, Chulalongkorn University, Bangkok, 10330, Thailand*
[5]*Center of Excellence in Structural and Computational Biology Research Unit, Department of Biochemistry, Faculty of Science, Chulalongkorn University, Bangkok, 10330, Thailand*
*thanyada.r@chula.ac.th (T.R.) and snutanon@vistec.ac.th (S.N.)

Introduction

The effective cancer treatments face significant challenges, primarily the severe side effects of chemotherapy and the emergence of drug resistance in targeted therapies. Combination therapies, which use multiple drugs simultaneously, tackle these issues by targeting the molecular diversity and complexity inherent in cancer, thereby enhancing treatment efficacy, reducing resistance, and minimizing toxicity. Recent advances in deep learning have significantly accelerated the identification of potent drug combinations, traditionally hindered by laborious and expensive laboratory procedures. Despite the focus of existing models on drug molecular structures and cancer cell gene expression, the crucial role of protein interactions in biological processes and phenotype determination necessitates the integration of protein expression data. Therefore, we have developed SynProtX, a deep learning model that employs graph neural networks for the molecular structure of drugs and deep neural networks for gene and protein expressions to predict the effects of drug combinations across cancer tissue datasets.

Methodology

SynProtX employs a comprehensive data integration strategy, leveraging gene expression data with 714 genes from the CCLE database and protein expression data that includes 6,688 proteins from ProCan-DepMap-Sanger. The model also utilizes drug combination data from the DrugComb database, with a specific focus on the FRIEDMAN and ALMANAC studies, to develop models. Our computational approach is underpinned by several network architectures, including graph convolutional networks (GCN), graph attention networks (GAT), Attentive FP, and integration of graph attention networks with molecular fingerprints (GATFP). These models enable a detailed analysis of the molecular structure of drugs and their complex interactions with gene and protein expressions. To benchmark SynProtX against state-of-the-art and baseline models, we compared it with DeepSynergy [1], DeepDDS [2], AttenSyn [3], and XGBoost. Model performance was evaluated using a suite of metrics appropriate for classification tasks—AUROC, AUCPR, F1 Score, Kappa, Accuracy, and Balanced Accuracy—and for regression tasks—Root Mean Square Error (RMSE), Mean Absolute Error (MAE), and Pearson Correlation Coefficient (PCC). We conducted these evaluations through 15 independent tests using triplicated 5-fold cross-validation and implemented Bayesian optimization to fine-tune the model's hyperparameters, ensuring model reliability and robustness.
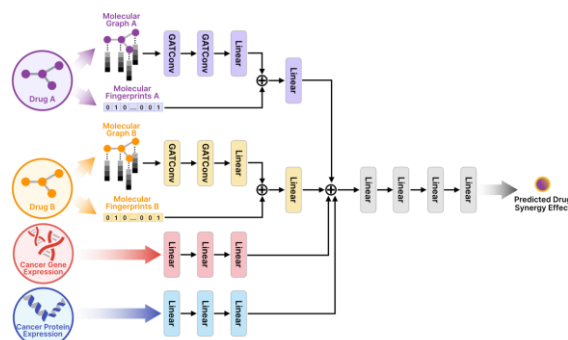
Figure 1. Model architecture of SynProtX-GATFP, leveraging graph attention networks (GAT) and molecular fingerprints for the molecular structure of drugs and deep neural networks for gene and protein expressions to predict drug synergy effect.

Results and Discussion

Our findings demonstrates that SynProtX-GATFP, utilizing both molecular graphs and fingerprints through a graph attention network coupled with deep neural networks, provides robust predictive performance in the FRIEDMAN study. Our model surpasses existing state-of-the-art and baseline models in handling diverse cancer tissue datasets derived from the ALMANAC study, including lung, breast, ovarian, and skin tissues, with accuracy improvements reaching up to 2.5%. Crucially, incorporating protein expression data enhances the prediction accuracy by an additional 0.1% to 4.4% over models relying solely on gene expression. Our model achieves generalizability evidenced by the leave-drug-combination-out validation method, which boosts prediction accuracy across all examined tissues by 2.5% to 3.6%. Moreover, SynProtX reveals key cancer-associated proteins, providing insights into the molecular mechanisms involved and suggesting molecular substructures that are pivotal for the design of effective real-world cancer drug combinations.

Significance

Our strategy facilitates the identification of cancer drug combinations and enhances our understanding of the relationships between drugs and cancer cells, contributing to the exploration of the biological mechanisms underlying synergistic effects.

References

1. K. Preuer, R. P. Lewis, S. Hochreiter, A. Bender, K. C. Bulusu, G. Klambauer, *Bioinformatics,* **2018**, *34*, 1538-1546.
2. J. Wang, X. Liu, S. Shen, L. Deng, H. Liu, *Briefings in Bioinformatics* **2022**, *23*, bbab390.
3. T. Wang, R. Wang, L. Wei, *Journal of Chemical Information and Modeling* **2023**.

Identification of Genes Associated with Alzheimer's Disease in Thai Population using RNA Sequencing Analysis

Monwipha M.[1], Nongluk P.[2], Chinae T.[3], Supatcha L.[3], Supapon C.[4,5], and Weerayuth K.[1,4*]

[1] Bioinformatics and Systems Biology Program, School of Bioresources and Technology, and School of Information Technology, King Mongkut's University of Technology Thonburi, Bangkok 10150, Thailand

[2] Biological Engineering Program, Faculty of Engineering, King Mongkut's University of Technology Thonburi, Bangkok 10140, Thailand

[3] Biochemical Engineering and Systems Biology Research Group, National Center for Genetic Engineering and Biotechnology, National Science and Technology Development Agency at King Mongkut's University of Technology Thonburi, Bangkok 10150, Thailand

[4] Systems Biology and Bioinformatics Research Group, Pilot Plant Development and Training Institute, King Mongkut's University of Technology Thonburi, Bangkok 10150, Thailand

[5] School of Bioresources and Technology, King Mongkut's University of Technology Thonburi, Bangkok 10150, Thailand

*weerayuth.kit@kmutt.ac.th

1. Introduction

Dementia is a syndrome characterized by progressive decline in cognitive function. As a result, patients lose the ability to perform basic activities in daily life. Alzheimer's disease (AD) is the most common cause of dementia, which contributes up to 80% of all dementia diagnoses [1]. There are 50 million AD patients worldwide and this number will increase to 152 million in 2050 [2]. National Institute on Aging-Alzheimer's Association (NIA-AA) classified AD continuum into 5 stages including preclinical AD, AD with mild cognitive impairment (MCI), AD with mild dementia, AD with moderate dementia, and AD with severe dementia [3]. Currently, drugs for AD patients are effective only in treating the symptoms of AD. Thus, there is still no drug for curing and preventing AD [2]. Early diagnosis is important to delay the progression of AD, which can be beneficial to patients, their carers and healthcare systems [4].

AD is characterized by the accumulation of amyloid-beta peptide (Aβ) and Tau protein. The Aβ is generated by cleavage of the transmembrane APP. When monomers of Aβ become oligomer, it will lead to plaques formation. The accumulation of Aβ in the intraneuronal leads to neurotoxic processes. Aβ also plays a role in inducing Tau hyperphosphorylation, which lead to the formation of protein tangles. The accumulation of hyperphosphorylated Tau in neurons lead to protein misfold and aggregation in intracellular neurofibrillary tangles (NFT), which reducing their affinity for microtubules. This results in a disturbance in the structural and regulatory functions of the cytoskeleton in neuronal cells. In addition, other pathological paths play important roles in AD development as well. For instance, neuroinflammation, oxidative stress and autophagy dysregulation [5]. However, the molecular mechanism that contributes to AD is still unclear. Understanding the molecular mechanisms in AD can help us to develop early diagnosis and therapeutic drug, which can delay progression of AD.

High-throughput sequencing technology and bioinformatic tools offer invaluable assistance in the study complex diseased. Transcriptome analysis has been used for studying gene-expression alterations, non-coding RNAs, copy number variants (CNVs), or alternative splicing [6]. The analysis can provide insights into biological pathways and molecular mechanisms of AD. Workflow for transcriptome analysis consist of five steps including preprocessing, read alignment, transcriptome reconstruction, expression quantification and differential expression analysis [7]. Differential expression analysis aims to identify differentially expressed genes (DEGs). Many studies used differential expression analysis to quantify gene expression between biological samples in difference conditions. By using this analysis, the relative expression level of genes can be obtained. Subsequently, the gene expression will be used for statistical tests [8] to find the important genes that may play an important role in AD.

In Thailand, the number of elderly populations is increasing. It was estimated that there will be more than a million people with dementia in 2030 and 2 million in 2050 [9], consistent with the global trend [2]. However, there is still lack of knowledge of AD-specific genes for Thai patients. This

information can be used for studying biological mechanisms underlying AD. In this study, transcriptome analysis was conducted to pinpoint the genes that specifically contribute to AD. Expressed transcripts in MCI patients and healthy controls were identified and quantified. Consequently differential expressed transcripts between MCI patients and healthy controls can be obtained. The results of this study help us understand the function of significant differentially expressed transcripts, which will help to gain insight into pathogenesis mechanism of AD. In addition, we can reveal genes that may play an important role in AD that are specific to Thai MCI patients.

2. Methodology

2.1 Transcriptome data

Whole transcriptome sequencing data of Thai MCI patients (n=51) and healthy control (n=49) were provided by Chulabhorn Royal Academy (CRA). Peripheral blood was collected from all individuals. Preparation of whole transcriptome sequencing library was done by purifying the poly-A containing mRNA molecules using poly-T oligo-attached magnetic beads. Transcriptome data was generated in the form of 100 bp paired-end reads using MGISEQ-2000 platform.

2.2 Reference data

Reference genome and gene annotation GRCh38 of *Homo sapiens* (human) release version 110 was obtained from Ensembl (https://ftp.ensembl.org/pub/release-110/fasta/homo_sapiens/dna/ and https://ftp.ensembl.org/pub/release-110/gtf/homo_sapiens/).

2.3 Transcriptome data analysis

Transcriptome data analysis (Figure 1) workflow used in this study started from quality control of raw sequencng data using FastQC (v0.11.9) and MultiQC (v1.0.dev0). Reads were aligned to reference genome using HISAT2 [10] (v2.2.1). Rseqc (v5.0.2) was used for assessing the quality of alignment results. Transcriptome reconstruction and expression quantification were performed using StingTie [11] (v2.2.1). Before differential expression analysis, principal component analysis (PCA) was used to reveal the difference of transcripts expression between conditions. Then, identification of differentially expressed transcripts between Thai MCI patients and healthy control was performed by using Ballgown [12] in R (v4.2.3) with criteria P-value < 0.01 and |Log2FC| > 0.5. Enrichment analysis of known transcripts to understand biological function insights into the progression of AD using Enrichr [13] was performed. Gene names from a set of known differentially expressed transcripts were used as inputs for enrichment analysis based on gene ontology (GO) and Kyoto Encyclopedia of Genes and Genomes (KEGG) pathways. Significant terms using criteria adjusted P-value < 0.05 were selected. To find important genes specific to patients, a protein-protein interaction (PPI) network of downregulated and upregulated genes was performed using the STRING database [14] and Cytoscape (v3.10.1) separately.
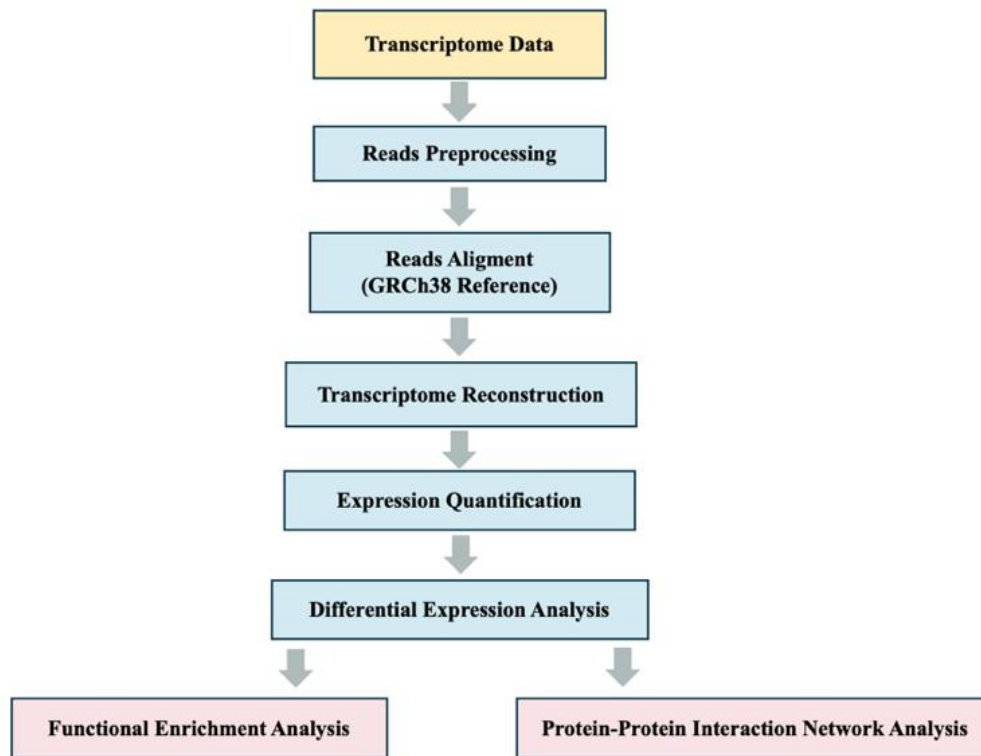
Figure 1. A transcriptome analysis workflow

3. Results and Discussion

3.1 Transcriptome data preprocessing and alignment

Whole transcriptome sequencing (WTS) data of Thai MCI patients (n=51) and healthy control (n=49) were used in this study. The data was divided by AD status as cognitive normal control, mild cognitive impairment (MCI), mild dementia, and moderate dementia. All 100 samples passed quality control with PHRED score of more than 30. The average number of total reads is 77,843,840. For each sample, sequence reads were aligned to reference genome GRCh38 with the average 97.01**%** of alignment rate.

3.2 Differential expression analysis

PCA revealed transcriptome expression differences between case and control groups. The results indicate that the samples from two populations are largely overlapping with one another (Figure 2A), which suggests that transcript expression is very similar between the case and control groups. Ballgown software reported 23,235 expressed transcripts in 100 samples by using cutoff P-value < 0.01 and |Log2FC| > 0.5 to filter significant transcripts. In this study a list of 155 transcripts including 71

downregulated transcripts and 44 upregulated transcripts was obtained (Figure 2B). There are 41 known downregulated and 24 known upregulated transcripts.
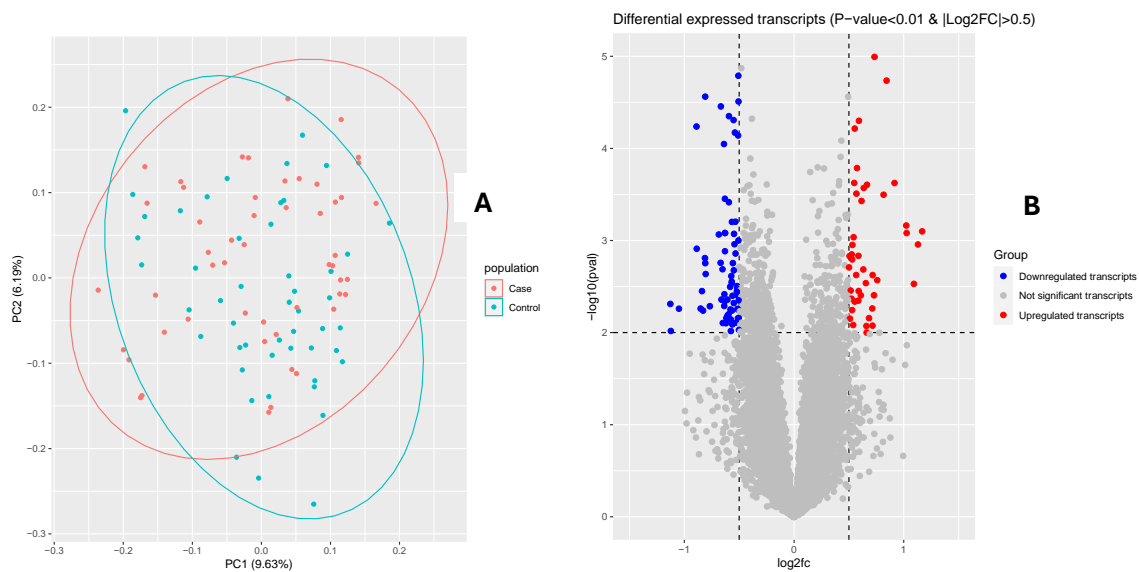

Figure 2. (A) PCA plot of case and control populations
(B) Volcano plot of differential expressed Transcripts

To identify differentially expressed transcripts between cases and healthy controls, transcripts expressed at low levels were filtered out prior to the statistical test in the differential expression analysis to enhance detection power [15]. P-value < 0.01 and |Log2FC| > 0.5 were used as cutoffs to select significantly expressed transcripts. Most of samples from case group are MCI, which is the early stage of AD. Therefore, the transcriptome expression between the case and control groups was largely similar (Figure 2A). In addition, increasing number of replicates of samples can increase the power of detection of significant transcripts [15].

Table 1. Top 5 Downregulated transcripts (Ordered by Log2FC)

	Transcript name	Fold change (FC)	Log2FC	P-value	Gene name
1	ENST00000558506	0.45771392	-1.1274819	0.00488385	EIF5
2	ENST00000502534	0.45907565	-1.1231962	0.00960227	RPL34
3	ENST00000417439	0.48325525	-1.0491427	0.00549904	LTF
4	ENST00000265333	0.53982168	-0.8894452	5.782052753 11161e-05	VDAC1
5	ENST00000424576	0.56272388	-0.8295009	0.00577313	RPL6

Table 2. Top 5 Upregulated transcripts (Ordered by Log2FC)

	Transcript name	Fold change (FC)	Log2FC	P-value	Gene name
1	ENST00000502632	2.24616933	1.16746669	0.00079568	HNRNPH1
2	ENST00000376809	1.8863944	0.91563134	0.00023757	HLA-A
3	ENST00000631943	1.76034842	0.815861	0.00031826	IGHV7-4-1

| 4 | ENST00000397528 | 1.63894966 | 0.71277154 | 0.00546649 | SLC7A7 |
| 5 | ENST00000677726 | 1.58552346 | 0.66495922 | 0.00024788 | DDX5 |

Significant transcripts include ENST00000558506 from the EIF5 gene, which shows the highest downregulated expression (Table 1), and ENST00000502632 from the HNRNPH1 gene, which shows the highest upregulated expression compared to the control group (Table 2).

Ribosomal subunits and translation initiation factors alteration in AD leading to ribosome dysfunction which is an early event of AD development [16]. Abnormal genes encoding ribosomal proteins are regulated leading to altered protein levels of translation initiation factors such as EIF2A, EIF3H and EIF5. Hernandez-Ortega et at. [17] found that CA1 region of the hippocampus of AD cases shows slightly decreasing in EIF5 protein level compared to healthy cases. Consistent with this study, the expression of EIF5 transcripts was found to be lower compared to the healthy control group.

APP is a precursor for amyloid-β peptides. Appropriate expression of APP is essential for maintaining healthy neurons and their connections. Khan et al. [18] found that HNRNPF and HNRNPH1 were significantly upregulated in the hippocampus of APP/PS1 mice, suggesting that overexpression of HNRNPF or HNRNPH1 increases the production of APP. Consistent with this study, the expression of HNRNPH1 transcripts was found to be higher compared to the healthy control group.

3.3 Functional enrichment analysis

Significant GO terms of downregulated transcripts include 18 Biological processes (BP), 10 Cellular component (CC), and 8 Molecular function (MF). Enriched KEGG pathways were spliceosome, ribosome, RNA transport, and coronavirus disease. Downregulated transcripts are involved in decreasing protein formation and macromolecule, promoting apoptotic process, and reducing the activation of the NIK/NF-kappaB signaling as shown in Table 3. In AD, protein synthesis and degradation are altered to maintain cell viability [19]. Decreasing protein synthesis is associated with the impairment in ribosome function, which can lead to development of AD [20]. Accumulation of tau and amyloid protein can cause apoptosis resulting in neural death [21]. The nuclear factor kappaB (NF-kB) pathway is important in the progress of AD. In normal brain function, the role of this pathway is in synaptic plasticity, learning, and memory. In AD, activation of this pathway leads to neuroinflammation, activation of microglia, oxidative stress and apoptosis. This imbalance results in neuron degeneration [22]. However, our results show low activation of this pathway. In addition, a decrease in RNA processing alteration was also found in this study. Transcriptome dysregulation and altered function of RNA binding proteins (RBPs) may lead to modulation of RNAs expression. RBPs are important in the brain involving in neurogenesis, synaptic transmission, and plasticity. Downregulation of RBPs also involved in splicing, polyadenylation and degenerate mRNA [23].

Significant GO terms of upregulated transcripts include 9 BP, and 2 MF. Upregulated transcripts are involved in the disrupted anoikis process, promoting immune response by a T-cell, increasing process involved in the organelle formation, and increasing mRNA processing as shown in Table 4. Anoikis is essentially an apoptosis which is important in preventing inappropriate translocation and attachment of cells [24]. T-cell is immune cells that involved in AD pathogenesis. Activation of T-cell can increase proinflammatory factors leading to neuroinflammation [25]. Increased alternative splicing can produces more mRNA variants affecting proteins that are essential for controlling cellular differentiation and development of AD [26]. In addition, increasing integral proteins of the plasma membrane and promoting mRNA processing were also found.

Table 3. Top 5 significant GO terms of downregulated transcripts

GO terms	Genes
Biological Process	
Cytoplasmic Translation (GO:0002181)	RPS14;EIF3M;RPL34;RPS3;RPL6
Macromolecule Biosynthetic Process (GO:0009059)	EEF1B2;RPS14;RPL34;RPS3;RPL6

GO terms	Genes
Regulation Of Apoptotic Process (GO:0042981)	MORF4L1;DDX3X;HSPA5;RPS3; VDAC1;SGK1;TPT1;LTF
Translation (GO:0006412)	EEF1B2;RPS14;RPL34;RPS3;RPL6
Ribosome Assembly (GO:0042255)	RPS14;DDX3X;RPL6
Cellular Component	
Intracellular Organelle Lumen (GO:0070013)	DDX3X;HSPA5;RPS3;SELENOF; SOD2;MMP8;LTF
Cytosolic Small Ribosomal Subunit (GO:0022627)	RPS14;RPS3
Small Ribosomal Subunit (GO:0015935)	RPS14;RPS3
Large Ribosomal Subunit (GO:0015934)	RPL34;RPL6
Cytosolic Large Ribosomal Subunit (GO:0022625)	RPL34;RPL6
Molecular Function	
Small Ribosomal Subunit rRNA Binding (GO:0070181)	RPS14;RPS3
mRNA Binding (GO:0003729)	RPS14;DDX5;DDX3X;TRA2B;RPS3
Cadherin Binding (GO:0045296)	DDX3X;EIF5;HSPA5;RPL34;RPL6
RNA Binding (GO:0003723)	RPS14;DDX5;DDX3X;EIF5;RPL34; TRA2B;RPS3;RPL6;TPT1
mRNA 5'-UTR Binding (GO:0048027)	RPS14;DDX3X

Table 4. Top 5 significant GO terms of upregulated transcripts

GO terms	Genes
Biological Process	
Negative Regulation Of Anoikis (GO:2000811)	PDK4;ITGA5
T Cell Mediated Immunity (GO:0002456)	BTN3A2;HLA-A
Regulation Of Anoikis (GO:2000209)	PDK4;ITGA5
Positive Regulation Of Organelle Organization (GO:0010638)	TOM1;SORBS3
RNA Transport (GO:0050658)	HNRNPA1;KPNB1
Molecular Function	
Vinculin Binding (GO:0017166)	TLN1;SORBS3
pre-mRNA Binding (GO:0036002)	DDX5;HNRNPA1

3.4 PPI-network analysis

Downregulated transcripts show 21 genes with 46 interactions. Among them, RPS3 has the highest interactions with 10 genes as shown in Figure 3A. The results suggested that RPS3 was important to the pathogenesis of AD patients. Shigemizu et al. [27] identified blood-based biomarkers for early diagnosis of AD by performed RNA-seq. They found that many downregulated genes were enriched in function involving ribosomal subunits including RPL, RPS, and MRP genes. Our results

also found downregulated transcripts in RPL6, RPL34, RPS3 ,and RPS14 genes. Moreover, they reported top-ranked 10 hub genes and one of hub genes is RPS3, which is also the hub gene in our study.

Upregulated transcripts show 9 genes with 8 interactions. Among them, HNRNPA1 and HNRNPH1 have the highest interactions with 3 genes as shown in Figure 3B. The results suggested that HNRNPA1 and HNRNPH1 were important to the pathogenesis of the disease. Heterogeneous nuclear ribonucleoprotein A1 (HNRNPA1) is a protein involving in RNA transcription, pre-mRNA splicing, mRNA transport, protein translation, microRNA processing, telomere maintenance and the regulation of transcription factor activity. Dysregulation of HNRNPA1 in AD may contribute to disease pathogenesis by altered RNA splicing. The splicing will increase longer APP splice variant and amyloid-β formation [28].
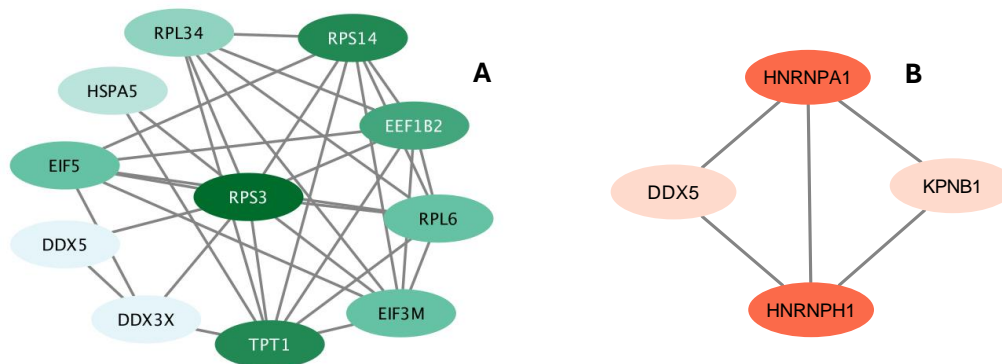

Figure 3. (A) Sub network of RPS3 gene and (B) HNRNP genes. Each dot represented a node. The degree of node was reflected by its color. The deeper color from light to dark (The greater the degree).

PPI-network analysis revealed important genes specific to Thai MCI pateints. RPS3 is the key gene that is downregulated in case group. In contrast, HNRNPA1 and HNRNPH1 are key genes that are upregulated in case group. Interestingly, DDX5 gene was both downregulated and upregulated with different transcripts (Downregulated transcript: ENST00000582326, Upregulated transcripts: ENST00000676969). DDX5 dynamically regulates the processes of transcription, splicing programs, and miRNAs during cell differentiation. The downregulation of DDX5 may inhibit RNA binding [29]. Consistent with our results downregulated transcripts decreased RNA binding process. However, these findings need to be further verified by techniques such as quantitative real-time polymerase chain reaction (qRT-PCR).

4. Conclusion

This study focused on analyzing transcriptome sequencing data of Thai MCI patients. A total of 41 downregulated and 24 upregulated significant known transcripts were identified. The strongest downregulated transcript is ENST00000558506 (EIF5 gene). The highest upregulated transcript is ENST00000502632 (HNRNPH1 gene). The downregulated transcripts were enriched in functions including protein synthesis, apoptotic processes, the NF-kB pathway, and RNA binding. Conversely, the upregulated transcripts were enriched in functions such as anoikis, the immune system, and mRNA processing. Our findings revealed important genes specific to Thai MCI patients, including RPS3, HNRNPA1, HNRNPH1, and DDX5. These genes may play crucial roles in the pathogenesis of AD in the Thai population.

References
1. Duong, S., Patel, T., and Chang, F., Dementia: What Pharmacists Need to Know, *Can Pharm J (Ott)* 150, 118-129 (2017).
2. Breijyeh, Z. and Karaman, R., Comprehensive Review on Alzheimer's Disease: Causes and Treatment, *Molecules* 25, (2020).

3. Porsteinsson, A.P., Isaacson, R.S., Knox, S., Sabbagh, M.N., and Rubino, I., Diagnosis of Early Alzheimer's Disease: Clinical Practice in 2021, *J Prev Alzheimers Dis* 8, 371-386 (2021).

4. Rasmussen, J. and Langerman, H., Alzheimer's Disease - Why We Need Early Diagnosis, *Degener Neurol Neuromuscul Dis* 9, 123-130 (2019).

5. Riscado, M., Baptista, B., and Sousa, F., New Rna-Based Breakthroughs in Alzheimer's Disease Diagnosis and Therapeutics, *Pharmaceutics* 13, (2021).

6. Bagyinszky, E., Giau, V.V., and An, S.A., Transcriptomics in Alzheimer's Disease: Aspects and Challenges, *Int J Mol Sci* 21, (2020).

7. Yang, I.S. and Kim, S., Analysis of Whole Transcriptome Sequencing Data: Workflow and Software, *Genomics Inform* 13, 119-125 (2015).

8. Zhang, Z.H., Jhaveri, D.J., Marshall, V.M., Bauer, D.C., Edson, J., Narayanan, R.K., Robinson, G.J., Lundberg, A.E., Bartlett, P.F., Wray, N.R., and Zhao, Q.Y., A Comparative Study of Techniques for Differential Expression Analysis on Rna-Seq Data, *PLoS One* 9, (2014).

9. Chuakhamfoo, N.N., Phanthunane, P., Chansirikarn, S., and Pannarunothai, S., Health and Long-Term Care of the Elderly with Dementia in Rural Thailand: A Cross-Sectional Survey through Their Caregivers, *BMJ Open* 10, (2020).

10. Kim, D., Paggi, J.M., Park, C., Bennett, C., and Salzberg, S.L., Graph-Based Genome Alignment and Genotyping with Hisat2 and Hisat-Genotype, *Nat Biotechnol* 37, 907-915 (2019).

11. Pertea, M., Pertea, G.M., Antonescu, C.M., Chang, T.C., Mendell, J.T., and Salzberg, S.L., Stringtie Enables Improved Reconstruction of a Transcriptome from Rna-Seq Reads, *Nat Biotechnol* 33, 290-295 (2015).

12. Frazee, A.C., Pertea, G., Jaffe, A.E., Langmead, B., Salzberg, S.L., and Leek, J.T., Ballgown bridges the gap between transcriptome assembly and expression analysis, *Nat Biotechnol* 33, 243–246 (2015).

13. Kuleshov, M.V., Jones, M.R., Rouillard, A.D., Fernandez, N.F., Duan, Q., Wang, Z., Koplev, S., Jenkins, S.L., Jagodnik, K.M., Lachmann, A., McDermott, M.G., Monteiro, C.D., Gundersen, G.W., and Ma'ayan, A., Enrichr: A Comprehensive Gene Set Enrichment Analysis Web Server 2016 Update, *Nucleic Acids Res* 44, 90-97 (2016).

14. Szklarczyk, D., Gable, A.L., Nastou, K.C., Lyon, D., Kirsch, R., Pyysalo, S., Doncheva, N.T., Legeay, M., Fang, T., Bork, P., Jensen, L.J., and von Mering, C., The String Database in 2021: Customizable Protein-Protein Networks, and Functional Characterization of User-Uploaded Gene/Measurement Sets, *Nucleic Acids Res* 49, 605-612 (2021).

15. Conesa, A., Madrigal, P., Tarazona, S., Gomez-Cabrero, D., Cervera, A., McPherson, A., Szczesniak, M.W., Gaffney, D.J., Elo, L.L., Zhang, X., and Mortazavi, A., A Survey of Best Practices for Rna-Seq Data Analysis, *Genome Biol* 17, 13 (2016).

16. Jiang, Y. and MacNeil, L.T., Simple Model Systems Reveal Conserved Mechanisms of Alzheimer's Disease and Related Tauopathies, *Mol Neurodegener* 18, 82 (2023).

17. Hernandez-Ortega, K., Garcia-Esparcia, P., Gil, L., Lucas, J.J., and Ferrer, I., Altered Machinery of Protein Synthesis in Alzheimer's: From the Nucleolus to the Ribosome, *Brain Pathol* 26, 593-605 (2016).

18. Khan, M.I., Zhang, J., and Liu, Q., Hnrnp F and Hnrnp H1 Regulate Mrna Stability of Amyloid Precursor Protein, *Neuroreport* 32, 824-832 (2021).

19. Keller, J.N., Interplay between Oxidative Damage, Protein Synthesis, and Protein Degradation in Alzheimer's Disease, *J Biomed Biotechnol* 2006, 12129 (2006).

20. Ding, Q., Markesbery, W.R., Chen, Q., Li, F., and Keller, J.N., Ribosome Dysfunction Is an Early Event in Alzheimer's Disease, *J Neurosci* 25, 9171-9175 (2005).

21. Kumari, S., Dhapola, R., and Reddy, D.H., Apoptosis in Alzheimer's Disease: Insight into the Signaling Pathways and Therapeutic Avenues, *Apoptosis* 28, 943-957 (2023).

22. Jha, N.K., Jha, S.K., Kar, R., Nand, P., Swati, K., and Goswami, V.K., Nuclear Factor-Kappa Beta as a Therapeutic Target for Alzheimer's Disease, *J Neurochem* 150, 113-137 (2019).

23. Rybak-Wolf, A. and Plass, M., Rna Dynamics in Alzheimer's Disease, *Molecules* 26, (2021).

24. Taddei, M.L., Giannoni, E., Fiaschi, T., and Chiarugi, P., Anoikis: An Emerging Hallmark in Health and Diseases, *J Pathol* 226, 380-393 (2012).

25. Dai, L. and Shen, Y., Insights into T-Cell Dysfunction in Alzheimer's Disease, *Aging Cell* 20, 13511 (2021).

26. Wong, J., Altered Expression of Rna Splicing Proteins in Alzheimer's Disease Patients: Evidence from Two Microarray Studies, *Dement Geriatr Cogn Dis Extra* 3, 74-85 (2013).

27. Shigemizu, D., Mori, T., Akiyama, S., Higaki, S., Watanabe, H., Sakurai, T., Niida, S., and Ozaki, K., Identification of Potential Blood Biomarkers for Early Diagnosis of Alzheimer's Disease through Rna Sequencing Analysis, *Alzheimers Res Ther* 12, 87 (2020).

28. Clarke, J.P., Thibault, P.A., Salapa, H.E., and Levin, M.C., A Comprehensive Analysis of the Role of Hnrnp A1 Function and Dysfunction in the Pathogenesis of Neurodegenerative Disease, *Front Mol Biosci* 8, 659610 (2021).

29. Li, M., Geng, R., Li, C., Meng, F., Zhao, H., Liu, J., Dai, J., and Wang, X., Dysregulated Gene-Associated Biomarkers for Alzheimer's Disease and Aging, *Transl Neurosci* 12, 83-95 (2021).

Enhanced Virtual Screening with Pre-trained Deep Learning Model: SARS-CoV-2 Case Study

Thawanrat S.[1], Jiramet K.[2], Hathaichanok C.[1,3], Kajjana B.[2], Thanyada R.[1,3]*, and Sarana N.[2]*

[1] *Center of Excellence in Structural and Computational Biology, Department of Biochemistry, Faculty of Science, Chulalongkorn University, Bangkok, 10330, Thailand*
[2] *School of Information Science and Technology, Vidyasirimedhi Institute of Science and Technology (VISTEC), Rayong, 21210, Thailand*
[3] *Program in Bioinformatics and Computational Biology, Graduate School, Chulalongkorn University, Bangkok, 10330, Thailand*
*thanyada.r@chula.ac.th; snutanon@vistec.ac.th

Introduction

The COVID-19 pandemic has adversely affected humans in various ways. Despite having vaccinations and FDA-approved drugs, the capability of the coronavirus's rapid mutation poses a challenge to current defences. The main protease (M^{Pro}) plays a crucial role in the lifecycle of the virus, making it a promising target for drug development against SARS-CoV-2. However, significant mutations in M^{Pro}, have been shown to confer severe resistance to the current drug, Nirmatrelvir. To prepare, developing a machine learning (ML) model could accelerate the discovery of promising compounds. Our study focuses on improving the ML model's bioactivity prediction efficiency by incorporating transfer learning techniques before conducting analysis with in silico assays, such as molecular docking and molecular dynamics (MD) simulations, alongside toxicity screening and pharmacokinetics profiling.

Methodology

In this study, we compared numerous ML models, both traditional models and different architecture of deep learning (DL) models pre-trained for chemistry tasks. The construction of traditional models is conducted via scikit-learn and RDKit, applying Fisher's exact test statistical method and ranking Gini importance for feature engineering. DL models are chosen based on different representations and pre-trained model availability, which include both SMILES based and Graph-based model. Each model was implemented following the method of the published studies. The model's performance is evaluated by 100 random splitting of our M^{Pro} target dataset, with 80% being the training set, 10% validation set, and 10% external test set. Models demonstrating the best predictive performance are chosen to screen compounds from ChemDiv database. In order to assess the binding affinity of ML-predicted candidates against M^{Pro}, we conducted molecular docking using GOLD software with parameters set at 6 Å sphere and 100 configurations. Crystal protein structures of SARS-CoV-2 M^{Pro} are retrieved from Protein Data Bank. For toxicity screening, the analysis is conducted via ADMET lab 2.0 platform. The compounds that passed toxicity screening are further evaluated for their pharmacokinetic properties using Egan's BOILED - Egg plot in SwissADME.

Results and Discussion

Here, pre-trained KPGT and CHEM-BERT demonstrated the best predictive performance in our benchmark with mean AUC of 0.88 ± 0.02 and 0.87 ± 0.02, due to its relatively close performance, we employ the model in ensemble by splitting the dataset into 5-fold splitting and finetune each architecture 5 times, resulting in 10 models used for screening. Our ML model rapidly screened out 10,306 candidates from a total of 1.6 million compounds. Molecular docking was conducted on screened compounds against WT SARS-CoV-2 M^{pro} and two major variants, S144A and H172Y. The results indicated 640 compounds with higher fitness scores than Nirmatrelvir, Ensitrelvir, and Bofutrelvir, among all variants. Potent compounds, screened for toxicity, are further analyzed with SwissADME, as shown in **Figure 1**. While our ML models demonstrate effectiveness with an ultra-large library, their predictive capacity is constrained by the applicability domain, thus limiting their potential to predict the bioactivity of compounds with novel chemical structures. This limitation can be improved by enhancing the diversity of chemical structures in the training dataset.

Significance

This research harnesses the power of ML models to optimize the drug screening process. By applying the transfer learning technique, our study significantly enhances the predictive capabilities of ML models, thereby facilitating effective drug screening. In addition, this study contributes to the understanding of potential SARS-CoV-2 M^{Pro} inhibitors against both WT and major variants of the virus, providing comprehensive insights into combatting the evolving threat of COVID-19 and future coronavirus outbreaks. These compounds not only demonstrate potent inhibitory activity but also serve as protection against future coronavirus outbreak. In summary, this study represents an innovative approach towards improving the drug screening pipeline and enhancing preparedness for future pandemics.
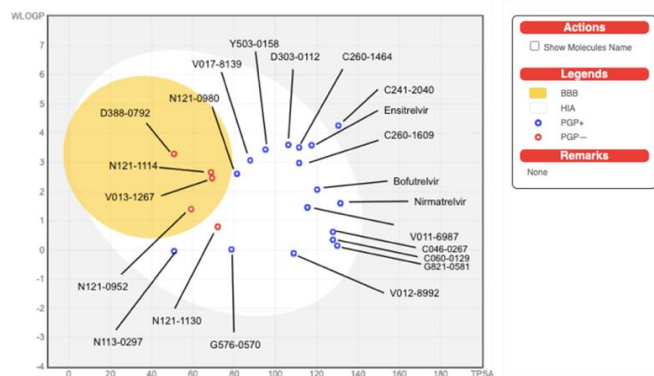

Figure 1. The Egan's BOILED-Egg plot of candidate compounds and reference M^{pro} inhibitors (Nirmatrelvir, Ensitrelvir, and Bofutrelvir).

Photo-dressed states generating unidirectional π-electron rotation in an aromatic ring molecule

Hirobumi Mineo[1*], Quang-Huy Ho[2], Ngoc-Loan Phan[2], Gap-Sue Kim[3], and Yuichi Fujimura[4]

[1]*STAI, Van Lang University, Ho Chi Minh City, (Vietnam)*
[2]*Department of Physics, Ho Chi Minh City University of Education,*
Ho Chi Minh City, (Vietnam)
[3]*Darma College, Dongguk University, Seoul, (Korea)*
[4]*Department of Chemistry, Tohoku University, Sendai, (Japan)*
*hirobumimineo@vlu.edu.vn

Introduction

In this talk we theoretically demonstrate that the helical-photon dressed state determines the direction of rotation of π electron in an elliptically polarized (EP) or circularly polarized (CP) laser. We consider minimum three-electronic states model, which consists of the ground state and a doubly degenerate electronic excited state or two nondegenerate excited states. Three helical-photon dressed states are derived by solving the time-dependent Schrödinger equation. The angular momentum of one of the three helical-photon dressed states represents an intuitive π-electron rotation, and the rest represent the opposite rotation, i.e., counter-intuitive rotation. Intuitive rotation means that the direction of π-electron rotation is the same as that of the given helical electric field vector, i.e., the electron rotation follows the classical equation of motion in the helical electric field. Whereas the counter-intuitive rotation means that the rotational direction of π-electron is opposite to that of the given helical electric field vector, i.e., this is a purely quantum behavior of the π-electron rotations. It is rigorously proved that the sum of the angular momentum of the three dressed states is conserved and zero. To examine the characteristic feature of the helical-photon dressed states mentioned above, benzene (D_{6h}) and toluene (C_S) are adopted as typical aromatic ring molecules with a doubly degenerate, and two nondegenerate excited states, respectively.

Methodology

Consider a three-electronic state model for a two-dimensional aromatic ring molecule in the presence of a helical UV laser. The nuclear motions are assumed to be frozen. The molecule is set on the xy plane in the helical UV laser propagating along the z direction. The interaction between π-electron and electric fields of a helical UV laser with frequency ω is taken into account within the semi-classical treatment. Then, we derive an analytical formula for the π-electron angular momentum for each dressed state. Finally, we prove the conservation of the angular momentum of the π electronic system: the sum of the three angular momenta is zero, .

$$L_z^{\Omega_0} + L_z^{\Omega_1} + L_z^{\Omega_2} = 0$$
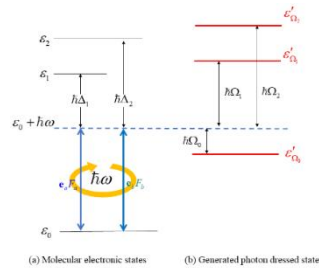
Fig. 1. (a) Creation of the dressed states in a nonresonant helical (circularly or elliptically polarized) laser with frequency ω in a three-electronic-state model. The laser detunings of laser a, b are Δ_1 and Δ_2, respectively. (b) The three helical-photon dressed states generated are denoted by $\Omega = \Omega_0, \Omega_1, \Omega_2$. The dressed energy $\hbar\Omega_j$ (j = 0, 1, 2) is formed with $\varepsilon'_\Omega = \hbar(\omega + \Omega) + \varepsilon_0$ (red solid lines).

Results and Discussion

Fig. 2. Intuitive and counterintuitive induction paths for inducing π-electron rotations in the three photon dressed states formed by a circularly polarized laser.

We have theoeretically studied how the helical-photon dressed states determines the unidirectional π-electron rotation in the applied CP or EP laser within 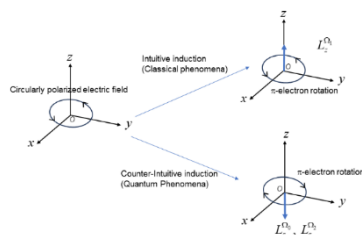the semi-classical treatment of light-molecule interactions and rotating wave approximation. By solving the time-dependent Schrödinger equation in a three-electronic states model under a frozen nucleus assumption, we have analytically obtained forms of wave functions for three helical-photon dressed states. The resultant angular momentum of one of the helical-photon dressed states represents an intuitive rotation following the classical equation of motion, and the rest represent opposite rotation, i.e., counterintuitive π-electron rotation, which is a purely quantum phenomena that has been nearly overlooked until now. It has been rigorously proven that the sum of the angular momentums of all three dressed states is conserved and zero for aromatic ring molecules with high or low symmetry, irrelevant to the laser parameters such as detuning.

Significance

In benzene the dressed state consists of two eigenfunctions, which are the simultaneous eigenfunction of energy and angular momentum, whereas in toluene one of dressed states is an approximately simultaneous eigenfunction of energy and angular momentum.

Utilizing correlation filtering techniques for quality assessment of retinal fundus images in diabetic retinopathy diagnosis

Rapeephat Yodsungnoen[1], Panomsak Meemon[2], and Ittipon Fongkaew[1,2,*]

[1]*School of Integrated Science and Innovation, Institute of Science, Suranaree University of Technology, 30000 (Thailand)*
[2]*School of Physics, Institute of Science, Suranaree University of Technology, 30000 (Thailand)*
*ittipon@g.sut.ac.th

1. Introduction

Diabetes leads to diabetic retinopathy (DR), a serious eye disease caused by high blood pressure and abnormal glucose levels in the blood vessels, potentially leading to blindness if not addressed. The number of individuals affected by DR is expected to increase from 103 million in 2020 to 130 million by 2030, and further to 160 million by 2045 [1]. Despite this growing demand, the global supply of ophthalmologists was just about 230,000 in 2015, including those in Thailand, with a modest annual growth rate of 2.6% [2]. This shortage is anticipated to deepen, resulting in the risk of neglect care for both diabetic patients, who require regular screenings, and for DR patients, who need continuous assessment and precise grading to avert severe consequences. Moreover, the distribution of ophthalmologists in Thailand is highly skewed, with a significant concentration in urban centers. For instance, Bangkok boasts approximately 437 ophthalmologists for 5.5 million individuals, whereas Ubon Ratchathani, a larger province, has only 9 ophthalmologists for 1.8 million individuals. This imbalance impedes timely and accurate diagnoses, compelling nurses and general physicians in rural areas to assume the responsibilities of ophthalmologists, thus increasing the risk of delayed or incorrect diagnoses. Thus, we are interested in developing an end-to-end DR grading system for grading the severity level of DR patients based on deep learning. Thereupon, to train the DR grading model, we decided to gather the retinal images from various hospitals and request that the ophthalmologist label these images. The collected images include a significant proportion of medically unsuitable retinal images (MURI), approximately 23%. As a result, the labelling process has slowed down due to the time required for ophthalmologists to screen out these MURIs from the dataset. Consequently, in this work, we aim to propose an image screening system that automatically screens out MURI from the dataset by adhering to the EyePACS standard protocol [3], [4]. This screening system utilizes an object detection algorithm to fulfil the protocol requirements for medically suitable retinal images (MSRI) in the primary and temporal fields, which must include the optic disc, the macula, and the vascular arch. The optic disc is a circular, bright anatomical structure where the optic nerve converges. The macula is a dark, oval region in the center of the retina, located in a vessel-free area and approximately 2-3 times the optic disc's diameter away from the optic disc. Currently, There is a variety method proposed to localize and segment the optic disc and macula namely: (1) Intensity determining, [5-11]; (2) Hough transform, [12]; (3) Anatomical structure analysis, [5-7, 13, 14]; (4) Morphological operations, [5, 9, 12-14]; (5) Correlation filtering, [5, 10, 15-17]; and (6) machine learning, [18-21]. Eventually, in this work, we propose an image screening system based on the correlation filtering method because of its simplicity, interpretability, and low data requirement for development. Furthermore, our screening algorithm aims to surpass a false discovery rate score of 0.05 [22] and a recall score of 0.90 [23] in classifying MSRI and MURI, ensuring that only images of sufficient quality and rich informational content are retained for subsequent labelling.

2. Methodology

Dataset

We use three datasets to create, develop, and evaluate our screening algorithm including IDRiD dataset, Messidor dataset, and our private dataset. First, IDRiD dataset [24] was curated to support various purposes namely lesion segmentation, DR severity grading, and optic-disc and macula localization. Moreover, this dataset was acquired by using a Kowa VX-10α digital camera with a 50º field of view (FOV) and a resolution of 4288×2848 pixels in jpg file format. The retinal image in this dataset totally contains 516 images, which have been split into a training set (413 images) and a testing set (103 images). Second, Messidor dataset [25] contains a total of 1200 retinal images, which are collected by utilizing CCD color video camera mounted on a Topcon TRC NW6 non-mydriatic retinography device with a 45-degree field of view (FOV) in diverse image sizes, such as 1440×960, 2240×1488, and 2304×1536 pixels. However, there are only 1136 images labelled for macula localization task in this dataset. Eventually, our private dataset consists of 328 positive images and 100 negative images, in a total of 428 images. Annotation of dataset was implemented by a master student by following the EyePACS standard protocol and under the ophthalmologist suggestion. Additionally, in this dataset, the definition of positive image is a medically suitable retinal image (MSRI) in a primary field of EyePACS protocol which should contain the optic disc, the macula, vascular arch, and equal distance between the optic disc and macula from the center Figure. 1 or temporal field of EyePACS protocol which contain significance ocular parts similar to primary field, but the macula should locate at the center of image. We select these field as a positive because these field are comprehensive area including various crucial ocular structure, thereby these field are simple in observing the lesion or the abnormality in retinal, resulting in the ease in downstream task such as DR severity grading. On the other hand, the negative image is an image that does not achieve these requirement Figure. 1.

Figure 1. An example from the private dataset includes images where (a) and (b) represent positive
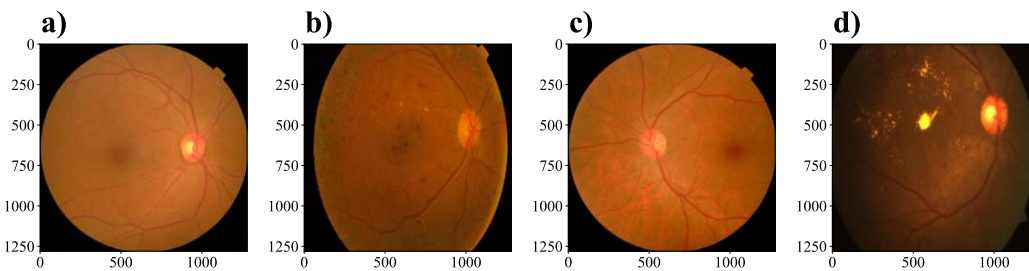

cases, while (c) and (d) are negative cases. The negative classification of these images is attributed to factors such as their depiction of the nasal field of retinal images and the unclear location of the macula, respectively.

Optic disc and macula detection

Due to our screening algorithm relating to apply the correlation filtering technique for detect the existence of optic disc and macula in retinal image. Hence, we initially utilize the training set of the IDRiD dataset to generate reference templates (or mask) for both the optic disc and macula. The process involved resizing the fundus images to a square shape of 1280 pixels and then cropping the resized images around the objectives. For optic disc, the cropping size is varied in the range of 200 to 400 with the step size of 100 in both symmetric and asymmetric shape. For macula, the cropping size is varied in the range of 100 to 300 with the step size of 50 in solely symmetric shape. Currently, we use the cropping dimensions of 200×300 and 200×200 for the optic disc and macula. This cropping procedure was repeated N times, and the resulting cropped images were averaged to create reference templates for the optic disc and macula, respectively, define as,

$$\bar{T} = \frac{1}{N}\sum_{i=0}^{N} T_i \qquad (1)$$

where $\bar{T}$ is a reference template and T_i is a cropped image number i[th]. In the context of ocular detection, we deploy the correlation filtering method on the resized fundus image using an optic disc template to identify the optic disc.
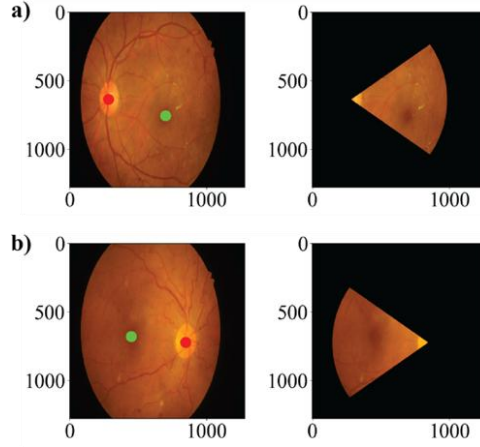
Following this, we delineate the region of interest (ROI) for macula detection by utilizing the determined location of the optic disc as a central reference point and selecting an area that locate to threefold the size of the optic disc within a range of -30 to 30 degrees [9], resulting in the ROI in a like-conical shape, illustrated in above Figure. Subsequently, we employ the correlation filtering technique on the ROI image to locate the macula. Ultimately, thresholding the correspondence space is applied to determine the reliability of the maximum point, which serves as an indicator for locating the optic disc and macula. This process involves establishing a threshold value within the correspondence space, beyond which points are considered reliable. By applying thresholding, we can effectively identify the maximum point that accurately represents the location of these ocular structures. Furthermore, we currently use matching method, named normalized correlation coefficient [Equation. 2], to establish the correspondence space in the correlation filtering.

$$R(x,y) = \frac{\sum_{x',y'}(\bar{T}'(x',y') \cdot I'(x + x', y + y'))}{\sqrt{\sum_{x',y'}(\bar{T}'(x',y')^2 \cdot I'(x + x', y + y')^2)}} \tag{2}$$

$$\bar{T}'(x',y') = \bar{T}(x',y') - \frac{1}{w \cdot h} \cdot \sum_{x'',y''} \bar{T}(x'',y'') \tag{2.1}$$

$$I'(x + x', y + y') = I(x + x', y + y') - \frac{1}{w \cdot h} \cdot \sum_{x'',y''} I(x + x'', y + y'') \tag{2.2}$$

Let I is a retinal fundus image.

Image screening

In this work, we use and develop a method proposed in [26] to be suitable for our task in classifying the MURI and MSRI. We will call the retinal image MSRI if it can pass these criteria: first, the optic disc and macula must locate within the acceptance region, called R1; and second, the optic disc must locate outside the specific region, called R2. R2 is added to become a criterion because we don't need a nasal field of a retinal image. An example of these regions is illustrated in Figure. 2. The R1 is defined by the lower and upper boundaries, following the below equations:

$$L_{R1} = y_c - \varepsilon \tag{3.1}$$

$$U_{R1} = y_c + \varepsilon \tag{3.2}$$

where y_c is a vertical centerline of retinal image, ε is an adjusted parameter, L_{R1} is a lower boundary, and U_{R1} is an upper boundary. Moreover, the lower and upper boundary of R2 is computed as:

$$L_{R2} = x_c - \delta \tag{4.1}$$

$$U_{R2} = x_c + \delta \tag{4.2}$$

where x_c is a horizontal centerline of retinal image, δ is an adjusted parameter, L_{R1} is a lower boundary, and U_{R1} is an upper boundary. In this work, we use grid search on 50 images of private dataset to determine the optimal parameters, thereby ε and δ is 170 and 200 pixels, respectively.

Figure 2. The acceptance region of R1 and R2
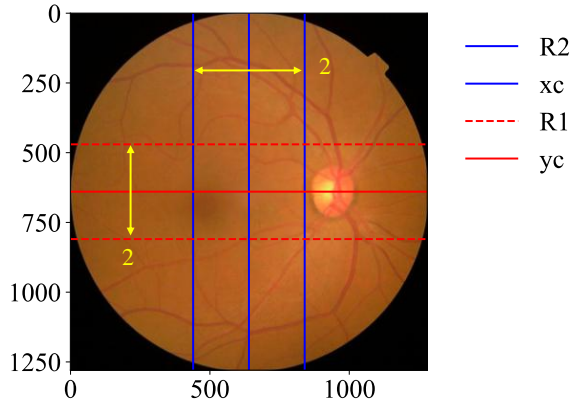
Evaluation

In the optic disc and macula detection, we evaluate the performance of our algorithm using the testing set of IDRiD. Initially, we quantify the accuracy of our algorithm's predictions by measuring the error between the predicted location and the ground-truth location of ocular structures. This analysis is conducted using the Euclidean distance (ED) as define in [Equation. 5], providing insights into the precision of our predictions at the pixel level. Additionally, we calculate the Average Precision (AP) score to measure the accuracy of the algorithm's bounding box predictions. The AP score, a scalar metric, reflects the performance of an object detection algorithm by assessing the precision of predicted boxes relative to actual objects in the image. It is computed by integrating various precisions, being as a function of recall, as described in [Equation. 6]. A higher AP score indicates better algorithm performance in object detection tasks. Moreover, we use a R-criterion score as mentioned in [27], to evaluate the performance of our macula detection on the Messidor dataset and due to the Messidor dataset comprising images of varying sizes, we apply different R values corresponding to each image size: R = 68 for images sized 1440 x 960, R = 103 for images sized 2240 x 1488, and R = 108 for images sized 2304 x 1536. In the context of image screening, we employ various evaluation metrics, including the confusion matrix, false discovery rate (FDR), and recall of positive images, to assess the performance of our screening process on our private dataset. The false discovery rate is utilized to evaluate the proportion of negative samples that remain in the dataset after screening, while recall is used to measure the proportion of positive samples that are retained in the dataset post-screening.

$$ED = \|X_1 - X_2\| \tag{5}$$

where X_1 is the ground-truth location and X_2 is the predicted location.

$$AP = \int_{r=0}^{r=1} p(r)\,dr \tag{6}$$

Let p is a precision and r is a recall.

3. Results and Discussion

Optic disc and macula detection

In Table. 1, the performance of the proposed method reveals that the Euclidean distance (ED) error for the optic disc and macula is 38.9 and 53.8 pixels, respectively. When expressed as a percentage of the image width, these errors are approximately 3.04% and 4.20%, respectively. Additionally, we evaluate the proposed method using various average precision (AP) scores, including AP at an IOU threshold of 0.50 (AP_{50}), AP at an IOU threshold of 0.75 (AP_{75}), and the mean AP score between IOU thresholds of 0.50 and 0.95 with a step size of 0.05. The results indicate that macula detection is highly sensitive to the IOU threshold, as evidenced by the AP score dropping from 0.827 to 0.550. Conversely, optic disc detection shows less sensitivity when comparing AP_{50} with AP, indicating that the template matching method for optic disc detection is relatively stable. Moreover, we calculate the mAP to serve as the representative AP score for the proposed method. The mAP is widely used to compare the performance of object detection algorithms, providing a comprehensive measure of accuracy across different IOU thresholds. Generally, to compare the proposed method with other approaches, the Messidor dataset is used to measure the performance of macula detection algorithms. This measurement is conducted by comparing the predicted macula location with the ground truth location across various sizes of agreement areas and then computing the score, called the R-criterion score, where R represents the radius of the optic disc, being roughly 208 pixels each image. As shown in Figure. 3, an increase in the denominator leads to a reduction in the size of the agreement area. Thus, the R-criterion effectively demonstrates the accuracy, precision, and stability of the algorithm in predicting the macula's location as the agreement area decreases.

Table 1. The general performance of proposed method on IDRiD dataset

Ocular name	ED (pixels)	AP_{50}	AP_{75}	AP	mAP	Runtime (s)
Optic disc	38.9	0.949	0.949	0.778	0.652	0.102
Macula	53.8	0.827	0.550	0.525		

Figure 3. The agreement area of each R-criterion on Messidor dataset

Table. 2 presents the outcomes of the proposed method across different agreement areas. It is notable that the values for R and R/2 are relatively close, indicating that over 90 percent of the predicted macula locations fall within the radius of R/2, which equals 104 pixels, around the ground-truth macula
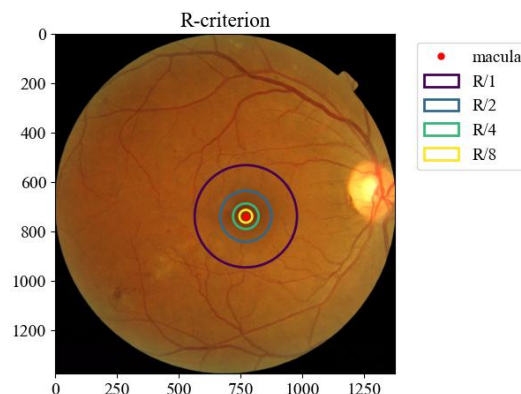
location. Similarly, the predicted macula is distributed around the ground-truth location within the radius of 52 pixels at 77.9 percent and within 26 pixels at 41.9 percent. This demonstrates the proposed method's capability to accurately predict the macula's location with varying levels of precision.

Table 2. The macula detection on Messidor dataset

Ocular name	R/8	R/4	R/2	R
Macula	0.419	0.779	0.912	0.931

The qualitative results of the proposed method are illustrated in Figure. 4 and Figure. 5. Sub-figures a, b, and c demonstrate high-quality predictions, whereas sub-figures d, e, and f show poor-quality predictions. Notably, the IDRiD dataset results highlight frequent false detection of the optic disc, frequently caused by bright lesions and white fibers that obscure the optic disc's location. Additionally, false macula detection is influenced by factors such as medium-sized hemorrhages and dark spots in the retinal image because these dark-like regions can resemble the macula on grayscale images during the matching process. Furthermore, errors in optic disc detection can propagate to macula detection, as the predicted location of the optic disc is used as a reference to delineate the ROI for macula detection. In the Messidor dataset, the proposed method often fails to detect the macula due to the challenges in distinguishing blood vessels from the macula.

Figure 4. The detection results of the proposed method on the IDRiD dataset. The three images above (a–c) showcase good quality predictions, whereas the images below (d–f) exhibit poor quality predictions. Where, cross sign (×) is a predicted location, the dot sign (●) is a ground-truth location, the green color represents the optic disc, and the red color represents the macula.
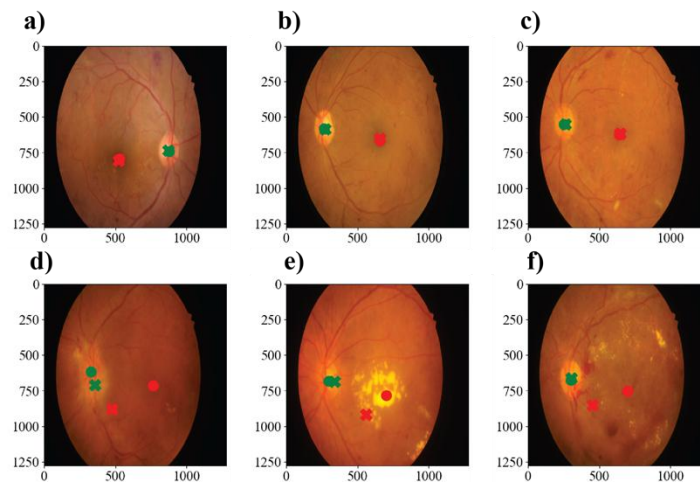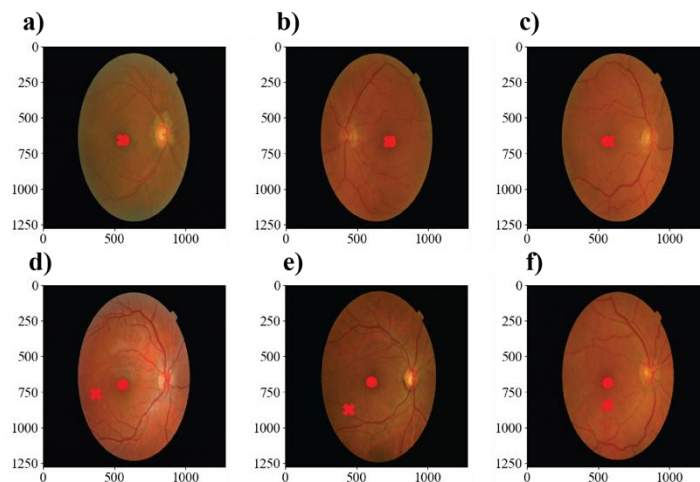

Figure 5. The detection results of the proposed method on the Messidor dataset. The three images above (a–c) showcase good quality predictions, whereas the images below (d–f) exhibit poor quality predictions. Where, cross sign (×) is a predicted location, the dot sign (●) is a ground-truth location, and the red color represents the macula.

Image screening

The performance of the proposed method is demonstrated through the confusion matrix presented in Figure. 6. This matrix illustrates that the algorithm exhibits superior ability in correctly classifying positive images as opposed to negative images. This is evidenced by a lower incidence of false positives compared to false negatives. This discrepancy suggests that the features employed by the algorithm might not be sufficiently robust for accurately distinguishing negative images. Table 3 provides further insight, indicating the high precision score and reliable false discovery rate of the proposed method, which closely align with the goal score of 0.05. Moreover, the method achieves a high recall of 0.875, which deviates by approximately 0.025 from the established goal. In practical terms, the proposed method successfully reduces the proportion of negative images in the dataset to 6 percent while retaining 88 percent of the positive images after screening.
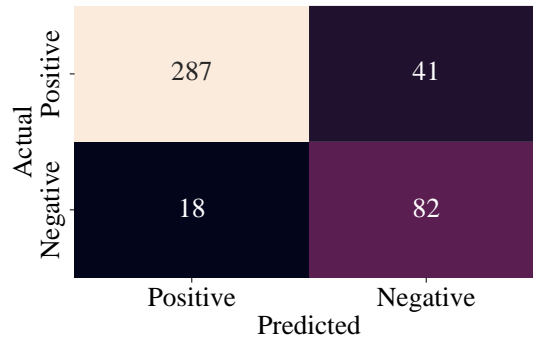
Figure 6. The confusion matrix of proposed image screening method.

Table 3. The performance of proposed image screening

	Accuracy	Precision	Recall	FDR
Goal [22, 23]	-	0.950	0.900	0.050
Proposed method	0.862	0.941	0.875	0.059

The qualitative results of the proposed method, as illustrated in Figure. 7, reveal distinct characteristics associated with each type of prediction. Notably, false-positive cases frequently occur from false detections where lesions or haemorrhages are incorrectly identified as resembling the macula. Similarly, false negatives result from misdetections, as depicted in Figure. 7.e. Conversely, the case shown in Figure. 7.f indicates a scenario where image overcropping causes the macula to be located outside the acceptable region, leading to false negative predictions. These observations suggest that enhancing the stability of the retinal fundus field could potentially improve the accuracy of the screening process. In the true positive case, the proposed method demonstrates the ability to correctly classify an image as positive, even in the presence of abnormal retinal conditions. Additionally, images of the nasal field are accurately identified as true negatives, further validating the method's effectiveness.

Figure 7. Example of image screening results: a) True positive; b-c) False positive; d) True negative; and e-f) False negative.

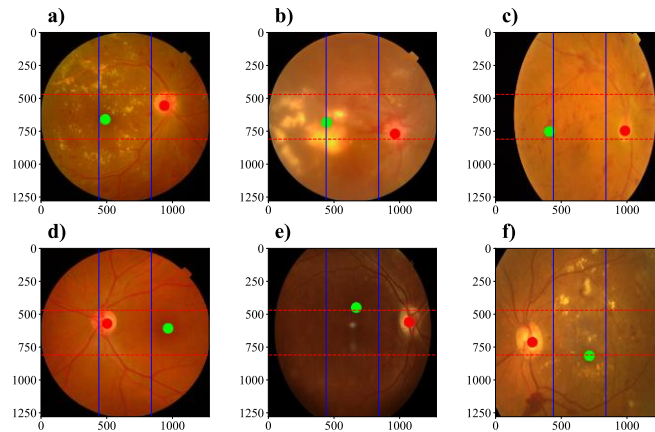## 4. Conclusion

In this study, we successfully developed an image screening algorithm designed to identify medically suitable retinal images within the primary and temporal fields, in accordance with the EyePACS protocol. Our approach integrates two primary components: ocular detection and image screening. The ocular detection utilizes correlation filtering techniques combined with anatomical structure analysis to accurately identify key ocular structures such as the optic disc and macula. The subsequent image screening process then applies specifically defined acceptance regions tailored to these fields to differentiate between medically suitable and unsuitable retinal images. Our results demonstrate that the proposed method achieves reliable detection scores, with the screening process performing well across various evaluation metrics, aligning closely with established medical standards. However, there is room for further refinement, particularly in enhancing macula detection accuracy, improving image acquisition techniques, and adjusting the decision boundaries used in the screening process. Despite these areas for improvement, the proposed screening method represents a promising step towards the development of practical and reliable retinal image screening systems, contributing to more efficient and accurate diagnoses in clinical settings.

References

1.   Teo, Z.L., et al., *Global prevalence of diabetic retinopathy and projection of burden through 2045: systematic review and meta-analysis.* Ophthalmology, 2021. **128**(11): p. 1580-1591.
2.   Resnikoff, S., et al., *Estimated number of ophthalmologists worldwide (International Council of Ophthalmology update): will we meet the needs?* British Journal of Ophthalmology, 2020. **104**(4): p. 588-592.
3.   Bresnick, G.H., et al., *A screening approach to the surveillance of patients with diabetes for the presence of vision-threatening retinopathy.* Ophthalmology, 2000. **107**(1): p. 19-24.
4.   Murgatroyd, H., et al., *Effect of mydriasis and different field strategies on digital image screening of diabetic eye disease.* British journal of ophthalmology, 2004. **88**(7): p. 920-924.
5.   Chalakkal, R.J., W.H. Abdulla, and S.S. Thulaseedharan, *Automatic detection and segmentation of optic disc and fovea in retinal images.* IET Image Processing, 2018. **12**(11): p. 2100-2110.
6.   Fu, Y., et al., *Fovea localization by blood vessel vector in abnormal fundus images.* Pattern Recognition, 2022. **129**: p. 108711.
7.   Medhi, J.P. and S. Dandapat, *An effective fovea detection and automatic assessment of diabetic maculopathy in color fundus images.* Computers in biology and medicine, 2016. **74**: p. 30-44.
8.   Palanisamy, G., P. Ponnusamy, and V.P. Gopi, *An adaptive enhancement and fovea detection technique for color fundus image analysis.* Signal, Image and Video Processing, 2023. **17**(3): p. 831-838.
9.   Sekhar, S., W. Al-Nuaimy, and A.K. Nandi. *Automated localisation of optic disk and fovea in retinal fundus images*. in *2008 16th European Signal Processing Conference*. 2008. IEEE.

10.   Sinthanayothin, C., et al., *Automated localisation of the optic disc, fovea, and retinal blood vessels from digital colour fundus images.* British journal of ophthalmology, 1999. **83**(8): p. 902-910.

11.   Usman Akram, M., et al. *Retinal images: optic disk localization and detection.* in *Image Analysis and Recognition: 7th International Conference, ICIAR 2010, Póvoa de Varzin, Portugal, June 21-23, 2010, Proceedings, Part II 7.* 2010. Springer.

12.   Zheng, S., et al. *Automatic and efficient detection of the fovea center in retinal images.* in *2014 7th International Conference on Biomedical Engineering and Informatics.* 2014. IEEE.

13.   Deka, D., J.P. Medhi, and S. Nirmala. *Detection of macula and fovea for disease analysis in color fundus images.* in *2015 IEEE 2nd International Conference on Recent Trends in Information Systems (ReTIS).* 2015. IEEE.

14.   Welfer, D., J. Scharcanski, and D.R. Marinho, *Fovea center detection based on the retina anatomy and mathematical morphology.* Computer methods and programs in biomedicine, 2011. **104**(3): p. 397-409.

15.   Nayak, J., P.S. Bhat, and U. Acharya, *Automatic identification of diabetic maculopathy stages using fundus images.* Journal of medical engineering & technology, 2009. **33**(2): p. 119-129.

16.   Yu, H., et al., *Fast localization and segmentation of optic disk in retinal images using directional matched filtering and level sets.* IEEE Transactions on information technology in biomedicine, 2012. **16**(4): p. 644-657.

17.   Mvoulana, A., R. Kachouri, and M. Akil, *Fully automated method for glaucoma screening using robust optic nerve head detection and unsupervised segmentation based cup-to-disc ratio computation in retinal fundus images.* Computerized Medical Imaging and Graphics, 2019. **77**: p. 101643.

18.   Sedai, S., et al. *Multi-stage segmentation of the fovea in retinal fundus images using fully convolutional neural networks.* in *2017 IEEE 14th International Symposium on Biomedical Imaging (ISBI 2017).* 2017. IEEE.

19.   Al-Bander, B., et al., *Multiscale sequential convolutional neural networks for simultaneous detection of fovea and optic disc.* Biomedical Signal Processing and Control, 2018. **40**: p. 91-101.

20.   Song, S., et al. *Bilateral-vit for robust fovea localization.* in *2022 IEEE 19th International Symposium on Biomedical Imaging (ISBI).* 2022. IEEE.

21.   He, H., et al., *JOINEDTrans: Prior guided multi-task transformer for joint optic disc/cup segmentation and fovea detection.* Computers in Biology and Medicine, 2024. **177**: p. 108613.

22.   Coyner, A.S., et al., *Deep learning for image quality assessment of fundus images in retinopathy of prematurity.* Investigative Ophthalmology & Visual Science, 2018. **59**(9): p. 2762-2762.

23.   Fleming, A.D., et al., *Automated assessment of diabetic retinal image quality based on clarity and field definition.* Investigative ophthalmology & visual science, 2006. **47**(3): p. 1120-1125.

24.   Porwal, P., et al., *Indian diabetic retinopathy image dataset (IDRiD): a database for diabetic retinopathy screening research.* Data, 2018. **3**(3): p. 25.

25.   Decencière, E., et al., *Feedback on a publicly distributed image database: the Messidor database.* Image Analysis and Stereology, 2014. **33**(3): p. 231-234.

26.   Şevik, U., et al., *Identification of suitable fundus images using automated quality assessment methods.* Journal of biomedical optics, 2014. **19**(4): p. 046006-046006.

27.   Gegundez-Arias, M.E., et al., *Locating the fovea center position in digital fundus images using thresholding and feature extraction techniques.* Computerized Medical Imaging and Graphics, 2013. **37**(5-6): p. 386-393.

On the JC Conjugate Gradient Method for Vector Optimization

Jamilu Y.[1,2] and Poom K.[1]*

[1]*Center of Excellence in Theoretical and Computational Science (TaCS-CoE) and KMUTTFixed Point, Research Laboratory Room SCL 802 Fixed Point Laboratory Science Laboratory Building, Department of Mathematics, Faculty of Science, King Mongkut's University of Technology Thonburi (KMUTT), 126 Pracha-Uthit Road, Bang Mod, Thung Khru, Bangkok 10140, (Thailand).*
[2]*Department of Mathematics, Faculty of Physical Sciences, Ahmadu Bello University Zaria, Kaduna, (Nigeria).*
*poom.kum@kmutt.ac.th (corresponding author designated with a star)

Introduction

Vector optimization problems (VOPs) are extensively utilized across various scientific disciplines to tackle decision-making problems involving multiple conflicting objectives. Notable applications include the location problem [3] and antenna design [4]. The solution to a VOP consists of a set of non-dominated points, commonly known as Pareto-optimal or efficient points. In 2018, Lucambio-Peréz and Prudente [5] introduced a conjugate gradient (CG) algorithm to solve VOPs. Since then, several other CG algorithms have been developed. Among these, the spectral CG (SCG) algorithm is notable, although its search direction is not descent in the vector setting, [2]. The authors introduced the JC CG method which is an SCG algorithm by using the Dai-Kou (DK) CG parameter with JC spectral parameters (JC), this is an extension of the in [1]. In this study, we redefined the DK parameter and JC spectral parameters in a new way (VJC). With these redefined parameters, the descent property and global convergence are established. A numerical experiment is presented to validate our findings, our methods is descent and appear to be the best-performing methods on the number of iterations and CPU time. The JC methods performed better in function and gradient evaluations.

Methodology

Algorithm 1: VJC Algorithm

Step 0: Let $x_0 \in \mathbb{R}^n$ be given. Compute $u(x_0)$ and initialize $k \longleftarrow 0$.
Step 1: Compute $u(x_k)$. If $|v(x_k)| \le \bar{e}$, where $\bar{e} > 0$, then stop.
Step 2: Compute the spectral parameter $\bar{\vartheta}_k$, and set $\bar{\vartheta}_k := \min\{10, \max\{\vartheta_k^{VJC}, \frac{1}{2}\}\}$.
Step 3: Compute

$$d_k := \begin{cases} u(x_k), & k = 0, \\ \bar{\vartheta}_k u(x_k) + \beta_k s_{k-1}, & k \ge 1, \end{cases} \quad (1.1)$$

where

$$\bar{\vartheta}_k^{JC+} := 1 - \frac{1}{\bar{\tau}_1}\left(\bar{\tau}_2 \frac{\bar{\tau}_1 + \bar{\tau}_3}{\bar{\tau}_2 - \bar{\tau}_4} - \alpha_{k-1}\bar{\tau}_2\right),$$
$$\bar{\vartheta}_k^{JC-} := 1 - \frac{1}{\bar{\tau}_1}\left(\bar{\tau}_2 \frac{\bar{\tau}_1 + \bar{\tau}_3}{\bar{\tau}_2 - \bar{\tau}_4}\right). \quad (1.2)$$

and $\beta_k = \max\{\beta_k^{DK^*}, 0\}$ with

$$\beta_k^{DK^*} := \frac{1}{\alpha_{k-1}(\bar{\tau}_2 - \bar{\tau}_4)}\left(\bar{\tau}_1 - \bar{\tau}_2 \frac{\|JF(x_k) - JF(x_{k-1})\|_{2,\infty}^2}{\bar{\tau}_2 - \bar{\tau}_4}\right). \quad (1.3)$$

Again, $\bar{\tau}_1 := -\phi(x_k, u(x_k)) + \phi(x_{k-1}, u(x_k))$, $\bar{\tau}_2 := \phi(x_k, d_{k-1})$, and $\bar{\tau}_4 := \phi(x_{k-1}, d_{k-1})$.
Step 4: Compute $\alpha_k > 0$ s.t strong Wolfe condition is satisfies.
Step 5: Set $x_{k+1} = x_k + \alpha_k d_k$, for $k \longleftarrow k + 1$ and move to **Step 1.**

Results and Discussion

We validate our theoretical findings by utilizing some benchmark test problems sourced from various multi-objective optimization (MOO) literature. The algorithms were coded in MATLAB R2023b. For numerical purposes, we utilize a scaled processing approach for VOP:

$$min_{x \in R^n}(\lambda_1 F_1(x), \cdots, \lambda_m F_m(x)),$$

where $\lambda_i = \frac{1}{max(1, \|\nabla F_i(x_0)\|_\infty)}$, $i = 1, 2, 3, \cdots, m$, and $x_0 \in R^n$.

Based on the considered test problems, the performance profile of the presented result as seen in Figure 1, shows that the proposed VJC- method is promising.
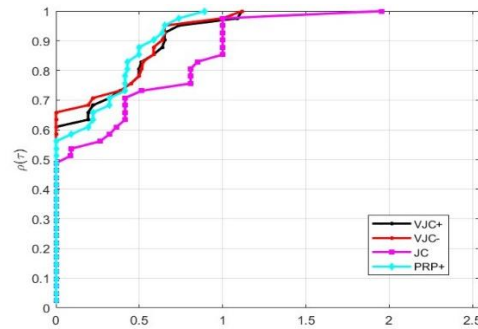
Figure 1. Number of Iterations

Significance

It is well-established that a conjugate gradient (CG) direction that satisfies the descent property is more desirable than one that does not. In light of this, we propose an alternative JC SCG method that ensures the descent property. Consequently, our proposed method is preferable to the JC SCG method described in [2].

References

1. Jian J. Chen Q. Jiang X. Zeng Y.and Yin J. A new spectral conjugate gradient method for large-scale unconstrained optimization. *Optim. Methods Softw.* 32(3):503—515 (2017).
2. He Q.R. Chen C.R. and Li S.J. Spectral conjugate gradient methods for vector optimization problems. *Comput. Optim. Appl.* 86:457–489 (2023).
3. Wang S.C. and Chen T.C. Multi-objective competitive location problem with distance-based attractiveness and its best non-dominated solution. *Appl. Math. Model.* 47:785-795 (2017).
4. Jahn J. Kirsch A. and Wagner C. Optimization of rod antennas of mobile phones. *Math. Methods Oper. Res.* 59:37-51 (2004).
5. Lucambio~Pérez L. R. and Prudente L.F. Nonlinear conjugate gradient methods for vector optimization. *SIAM J. Optim*. 28(3):2690-2720 (2018).
.

Numerical Simulations of Carbon Emission-Absorption Model with Data From Thailand

Hongsuda Hongsresawat[1], Dussadee Somjaiwang[2]* and Parinya Sa Ngiamsunthorn[3]

[1,2]*The Demonstration School of Kanchanaburi Rajabhat University, Kanchanaburi, 71000 (Thailand)
[3] Department of Mathematics, Faculty of Science, King Mongkut's University of Technology Thonburi (KMUTT), Bangkok, 10140 (Thailand)
*dsdsjw17@gmail.com

1. Introduction

In the summer of 2024, between the months March and May, many environmental anomalies occurred within Thailand, such as, rising temperatures which exceeded 40 degrees Celsius for more than a week. Another example would be unexpected thunderstorms beginning from early March and lasting the entire duration of summertime (https://www.tmd.go.th, online accessed on 2024). This shows that Thailand's current weather conditions are extremely variable. These variabilities in weather conditions are one of many results of global warming, which is caused by the great amount of greenhouse gases in the atmosphere. Though this research is focused solely on Thailand in a closed environment, the greenhouse effect is a problem faced worldwide. Therefore, global warming is a dilemma that has gained a lot of attention universally and has been a common point for countries to band together and set goals aiming to reduce greenhouse gas emissions. Such movements are led by leading countries such as, China, who put forward a dual carbon target that aims to reduce the total amount of carbon emissions in China by 65% within the year 2030. This declaration has raised concerns in terms of the reality of carbon emissions in China, causing many researchers to find ways to accurately calculate carbon emissions. Such as ,(Leilei Han et al., 2022),who analyzed China's carbon emission stability according to current changes in industrial structure and (Haokun Sui et al., 2022), who did a dynamic analysis of delayed carbon emissions influenced by China's urbanization and population. Apart from China, other countries see the importance of this increasingly critical issue. For example, (Pita Donald et al., 2024), who used a mathematical model to explain carbon dioxide emissions for vehicles. In this paper, we use the numerical method with a delayed differential equation model of carbon emission-absorption under the influence of Thailand's urbanization to analyze carbon neutrality.

The structure of this research consist of as follows; The modeling of Carbon Emission- Absorption is presented in section 2. The result and discussion of numerical simulations of Carbon Emission-Absorption model with data from Thailand is investigated in section 3. Finally, the concluding remarks are in the conclusion in section 4.

2. Methodology

The carbon emission-absorption model under the influence of urbanization (Fei et al., 2023) show in (1.1) ,and the description of each compartment is given Table 1.

$$\frac{dx}{dt} = r_1 x - \frac{r_1 x^2}{N_1} + \alpha \frac{r_1 xy}{N_2}$$

$$\frac{dy}{dt} = r_2 y - \frac{r_2 y^2}{N_2} + a - a \frac{y(t-\tau)}{M} \qquad (1.1)$$

Table 1. Descriptions of variable in the model (1.1)

Parameter	Description	unit
x	Total carbon absorption at time t	billion tons
y	Total carbon emissions at time t	billion tons
r_1	The annual growth rate of carbon absorption	-
N_1	The maximum value of carbon absorption in a certain space	billion tons
α	The absorption coefficient of carbon emissions corresponding to carbon absorption	-
r_2	The annual growth rate of carbon emissions	-
N_2	The maximum environmental capacity of carbon emissions	billion tons
a	The influence coefficient of the speed of urbanization on the growth of carbon emissions	-
M	The maximum value of urban carbon emissions	billion tons
τ	Time of urban ecological process adapting to population migration	years

Table 2. Thailand's per capita carbon emissions (2010-2021)

Year	2010	2011	2012	2013	2014	2015
Metric ton per capita	3.527	3.478	3.706	3.804	3.736	3.825
Annual growth rate	-	-0.014	0.066	0.026	-0.018	0.024
Year	**2016**	**2017**	**2018**	**2019**	**2020**	**2016**
Metric ton per capita	3.794	3.768	3.718	3.849	3.714	3.794
Annual growth rate	-0.008	-0.007	-0.013	0.035	-0.035	-0.008

(https://data.worldbank.org/indicator/EN.ATM.CO2E.PC?locations=TH, *CO2 emissions (metric tons per capita) - Thailand,* accessed on 21 March 2024)

In table 2, we can see an obvious increase in carbon in the year 2020 compared to the year 2010, with a slight decrease from the previous year, 2019. This decrease is most likely affected by the Covid-19 pandemic. Even then, the decrease is miniscule, meaning that global events have very little impact on decreasing carbon emissions as opposed to increasing them.

Table 3. Thailand's annual carbon emissions (2010-2021)

Year	2010	2011	2012	2013	2014	2015
Values/ million ton	248.7	249.3	266.7	268.4	275.3	275.5
Annual growth rate	-	0.002	0.070	0.006	0.026	0.001
Year	**2016**	**2017**	**2018**	**2019**	**2020**	**2021**
Values/ million ton	280.8	286.7	284.7	279.1	264.6	279.2
Annual growth rate	0.019	0.021	-0.007	-0.020	-0.052	0.055

(https://www.bp.com, *bp Statistical Review of World Energy 2022 | 71st edition,* accessed on 25 November 2023)

From table 3, we further reinforced the fact that though a minute change, carbon emissions can decrease with a certain rate. We will refer to this decrease in carbon emissions as carbon absorptions.

3. Results and Discussion

We choose a group of parameters to make each parameter as close as possible to the current situation in Thailand. In 2021, the amount of carbon emission is 0.28 billion tons (BP. ,2022) and the amount of carbon absorption is 0.11 billion tons. Thus we choose $(x(t), y(t)) = (0.11, 0.28)$ for $t \in (-\tau, 0)$ let $r_1 = 0.01$, $r_2 = 0.017$, $N_1 = 0.02$, $\alpha = 0.09$, $N_2 = 0.02$, $a = 0.075$ and $M = 1.57$.
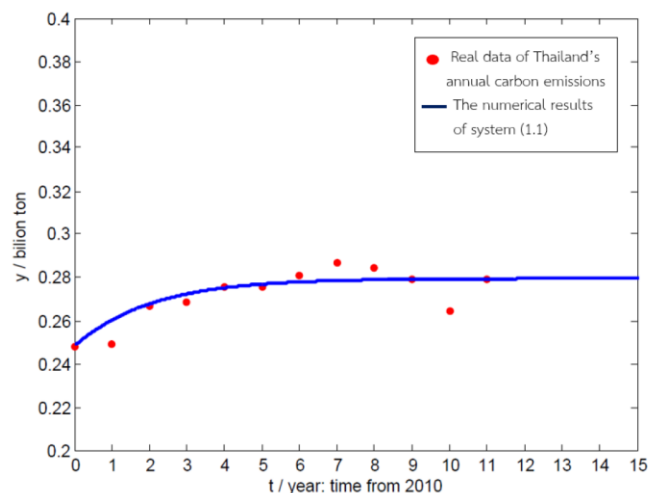

Figure 1. The numerical simulations of carbon emission-absorption model under the influence of urbanization (1.1) compare with real data of real data of Thailand's annual carbon emissions year 2010-2021.
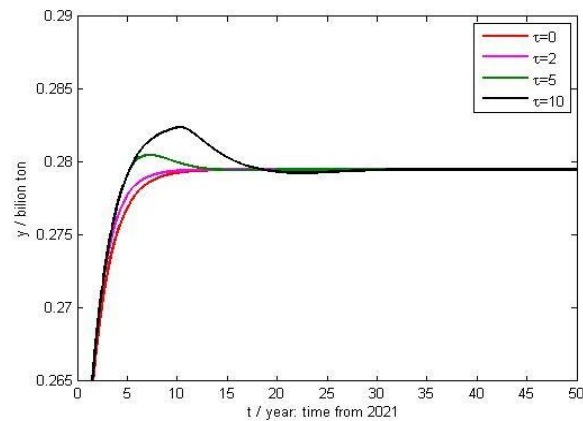
Figure 2. The numerical simulations of carbon emission- absorption model under the influence of urbanization (1.1) when $\tau = 0, 2, 5$ and 10 respectively.

On the Figure 2 we show the total of carbon emissions after the year 2021 follows an upward trend and reaches stability in the year 2037. The rise in carbon emissions is most obvious after 2 years. When $\tau = 0, 2, 5$ and 10 the total carbon emissions reaches its peak at about 0.279, 0.279, 0.2804 and 0.2824 respectively. As the value of τ increases, the maximum total of carbon emissions grows larger as well (2023-2037), meaning that areas with heavy industrial use for long periods of time will emit large amounts of carbon.

4. Conclusion

In this research, we used numerical methods with a carbon emission-absorption model under the influence of urbanization (1.1) to analyze the total values of carbon emissions and absorptions. The results obtained from the mathematical model (1.1) can be summarized as follows;

1. The period of time used for the migration of the population and urbanization is a factor that affects the total amount of carbon emissions.

2. We discovered that the total amount of carbon absorptions is a lot less than the total amount of carbon emissions. Therefore, to achieve carbon neutrality, some measures should be taken to control the growth rate of carbon emissions, such as, developing new technology for carbon capturing or promoting more renewable energy forms.

References

1. Thai Meteorological Department, (2024), Monthly weather forecasts in infographic format. Retrieved 15 May 2024, from https://www.tmd.go.th/forecast/monthly/032024.
2. Fei, X., Hou, Y., & Ding, Y. (2023). Modeling and analysis of carbon emission - absorption model associated with urbanization process of China. *Electronic Research Archive*, *31*(2), 985-1003.
3. BP. (2022). Statistical Review of world energy 2022.
4. Han, L., Sui, H., & Ding, Y. (2022). Mathematical modeling and stability analysis of a delayed carbon absorption-emission model associated with China's adjustment of industrial structure. *Mathematics*, *10*(17), 1-21.
5. Sui, H., Han, L., & Ding, Y. (2022). Dynamic analysis of a delayed carbon emission-absorption model for China's urbanization and population growth. *Mathematics*, *10*(17),1-13.
6. Donald, P., Mayengo, M., & Lambura, A. G. (2024). Mathematical modeling of vehicle carbon dioxide emissions. *Heliyon*, *10*(2).

CFD-ANN coupling model simulation of gas–solid feeding design for ternary biomass mixtures in bubbling fluidized bed gasifier

Chaiwat S.[1], Pornpote P. [1,2] and Benjapon C.[1,2,3]*

[1]*Department of Chemical Technology, Faculty of Science, Chulalongkorn University, Bangkok, 10330 (Thailand)*
[2]*Centre of Excellence on Petrochemical and Materials Technology, Chulalongkorn University, Bangkok, 10330 (Thailand)*
[3]*Advanced Computational Fluid Dynamics Research Unit, Chulalongkorn University, Bangkok, 10330 (Thailand)*
*Benjapon.c@chula.ac.th

Introduction

The design of continuous feeding fluidized bed reactors significantly influences their performance, which is critical for the effective utilization of biomass mixtures in energy production. Proper design of the gas distributor plate and solid tube inlet is essential to ensure stable fluidization and uniform distribution of fluidizing gas and solid particles within the reactor. This study aims to investigate the impact of gas–solid feeder design in bubbling fluidized bed gasifiers on system hydrodynamics using a coupling model of Computational Fluid Dynamics (CFD) and Artificial Neural Networks (ANN).

Methodology

A 2^k factorial experimental design was employed to examine the effects of various gas and solid feeding configurations on key performance parameters, including the gas–solid mixing index and solid residence time. The CFD-ANN model was developed to simulate the hydrodynamics of a scaled-down bubbling fluidized bed gasifier, incorporating ternary biomass mixtures (wood chip, rice husk, palm shell waste) with silica sand as an inert material. The CFD model utilized the Gidaspow drag coefficient and an ANN trained with experimental data to predict system behavior under different feeder designs.

Results and Discussion

The simulation results revealed several critical findings regarding the influence of feeder design on reactor performance. The position and length of the solid inlet tube were found to significantly affect the solid residence time, with optimal configurations enhancing the residence time and improving the uniformity of particle distribution. Specifically, a faraway inlet position from the reactor center and shorter tube length facilitated better mixing and longer residence times, which are essential for efficient gasification. The design of the gas distributor plate also played a vital role. A well-designed distributor plate improved turbulence and mixing within the reactor, leading to more uniform gas and solid distribution. Enhanced turbulence promoted better contact between the biomass particles and the fluidizing gas, which is crucial for efficient conversion processes in gasification. The integration of ANN into the CFD model proved highly effective, offering precise predictions while reducing computational load. The ANN was adept at capturing the complex nonlinear relationships between feeder design variables and reactor performance metrics, enabling the identification of optimal design parameters without extensive computational resources. This approach allowed for rapid evaluation and optimization of various feeder designs, demonstrating the practical utility of combining CFD and ANN in industrial applications.

Table 1. The ANOVA result of gas-solid mixing

Source of variation	SS	DF	MS	F0	p-value
DF2	0.0049	1	0.0049	4.58	0.0581
SF1GF1	0.0028	1	0.0028	2.55	0.1412
SF1GF2	0.0042	1	0.0042	3.92	0.0760
SF1SF2GF1	0.0076	1	0.0076	7.09	0.0238
SF1SF2GF1GF2	0.0047	1	0.0047	4.33	0.0642
Residual	0.0108	10	0.0011		
Total	0.0350	15			

SF1: Solid tube inlet position; SF2: Solid tube inlet length; GF1: Gas distributor opening area; GF2: Gas distributor flow pattern

Significance

This study underscores the importance of optimizing gas and solid feeder designs to improve the efficiency and performance of fluidized bed reactors. The integration of ANN into CFD simulations proved to be a powerful approach, reducing computational resources while maintaining high accuracy. The findings provide valuable guidelines for designing more effective gas–solid feeding systems for biomass gasification, contributing to advancements in sustainable energy production technologies.
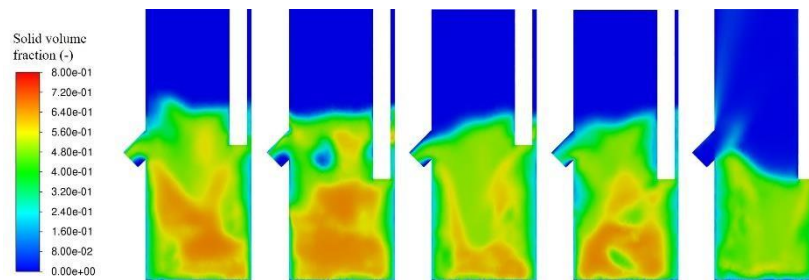

Figure 1. The solid distribution contour of different reactor designs.

References

1. Chaiwat S., Vishnu P., Pornpote P., and Benjapon C. *Can J Chem Eng.* 1 (2024).

CFD-DEM simulation of fluidization of mixed biomass mixtures in a bubbling fluidized bed

Krittin K.[1], Pornpote P.[12] and Benjapon C.[123]*

[1]Department of Chemical Technology, Faculty of Science, Chulalongkorn University, Bangkok 10330 (Thailand)
[2]Centre of Excellence on Petrochemical and Materials Technology, Chulalongkorn University, Bangkok, 10330 (Thailand)
[3]Advanced Computational Fluid Dynamics Research Unit, Chulalongkorn University, Bangkok, 10330 (Thailand)
*benjapon.c@chula.ac.th

Introduction

Fluidized bed combustion technology has gained prominence in promoting electricity production from biomass. However, a significant challenge arises when there is a scarcity of biomass in a specific location or during certain seasons. Using a single type of biomass can lead to low thermal efficiency. To address this issue, mixed biomass is considered a potential solution. Nevertheless, the mixing behavior and heat transfer of mixed biomass particles in a bubbling fluidized bed have not been extensively studied. This research focuses on investigating the mixing behavior and heat transfer characteristics of various biomass combinations within a bubbling fluidized bed. The results aim to provide guidelines for efficiently utilizing mixed biomass and identifying optimal conditions for operation.

Methodology

This study simulates a bubbling fluidized bed with dimensions of 20 cm in width, 3 cm in depth, and 100 cm in height. Spherical silica sand and cylindrical biomass particles, including wood chips and sugarcane bagasse, which vary in size and aspect ratios, are used in this system. The study categorizes bagasse into coarse, fine, and all sizes based on granulometric analysis. It examines various biomass types, loadings (2.5%, 5%, and 7.5% by weight), and blending ratios of wood chips to bagasse (1:1, 3:1, and 1:3) to assess their effects on mixing and heat transfer. During initial packing, with a total particle mass of 400 g at 30 °C, hot air enters the bed from the bottom inlet at 1.8 m/s. The Lacey mixing index is used to measure mixing quality. The study uses a two-way coupling approach of Computational Fluid Dynamics-Discrete Element Method (CFD-DEM) simulations, with Ansys Fluent (2020 R2) for fluid flow and Rocky DEM (4.5.1) for particle interactions, using time steps of 1×10^{-4} s and 2×10^{-5} s, respectively, over a total simulation time of 30 s for each case.

Results and Discussion

The developed CFD-DEM model was validated using experimental data from Ma and Zhao[2], which investigated the fluidization behavior of biomass and silica sand. The parameterized Syamlal and O'Brien drag model used for validation showed good agreement with the experimental results. The study concludes that coarse bagasse provides the most efficient mixing behavior and highest mixing index for single biomass mixtures. For mixed biomass mixtures, the optimal condition is a blending ratio of 1:3 (wood chips to coarse bagasse) with 5% biomass loading using 1 mm silica sand due to the difference in aspect ratio and equivalent diameter of some biomass particles aiding in the mixing behavior. The use of smaller silica sand particles enhances fluidization intensity and mixing efficiency. However, varying biomass loadings have no noticeable effect on mixing. Additionally, differences in equivalent particle diameters are identified as the most crucial factor in selecting suitable biomass sizes for fluidized bed systems. Furthermore, in the case of mixed biomass, the average temperature of all particles slightly increases over time due to improved fluidization intensity when using different silica sand sizes. Variations in silica sand sizes also result in differing particle convective heat transfer rates, which influence the temperature within individual particles. Therefore, improving the mixing of biomass and silica sand by using smaller silica sand particles can correspondingly enhance the heat transfer of mixed biomass.

Significance

- Coarse bagasse size provides efficient mixing behavior for a single biomass mixture.
- A blending ratio of 1:3 (wood chips to coarse bagasse) with 5% biomass loading, using 1 mm silica sand, is identified as an appropriate condition.
- Biomass size differences play a significant role in mixing, while biomass loadings had minimal influence.
- The enhancement of mixing through the use of smaller silica sand particles (with a size of 1 mm) improves the heat transfer of mixed biomass.

This study provides valuable guidelines for optimizing biomass conditions for operation in industrial fluidized bed applications.
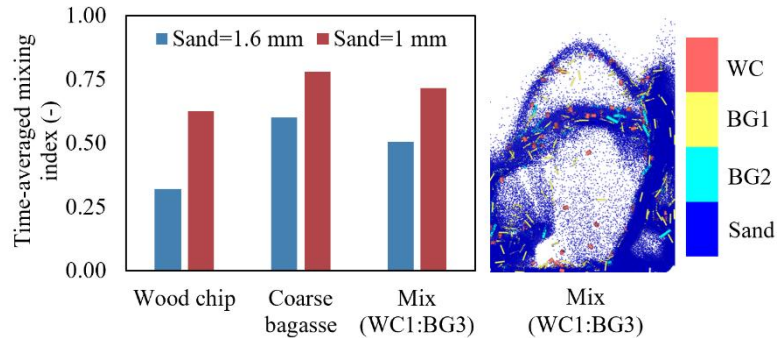

Figure 1. Comparison of the time-averaged mixing indexes across various biomass mixtures and silica sand sizes, along with the solid distribution contour of the mixed biomass mixture.

References
1. Korkerd, K., Zhou, Z., Zou, R., Piumsomboon, P., and Chalermsinsuwan, B. *Powder technology* 433 (2024).
2. Ma, H., and Zhao, Y. *Powder Technology* 336 (2018).

Influence of Air-to-Fuel Ratio on Co-firing Circulating Fluidized Bed Boiler Operation Using Computational Fluid Dynamics

Sorathan T.[1], Nuttima R.[2], Warunee N.[2], Pitakchon W.[2], Pornpote P.[1], and Benjapon C.[1]*

[1]*Department of Chemical Technology, Faculty of Science, Chulalongkorn University, 254 Phayathai Road, Wangmai, Pathumwan, Bangkok 10330, Thailand*
[2]*Integrated Research Center Company Limited, 122 Moo 2 Si Maha Phot, Prachinburi 25140, Thailand*
*benjapon.c@chula.ac.th (corresponding author designated with a star)

Introduction

According to the increasing global population, total energy consumption is also increasing. Most vital energy sources come from electricity generated through power plants. In power plant operations, there are two main types of combustion processes in boiler power plants: coal and biomass. The benefit of coal as a combustion material is its higher heating value, but it has environmental drawbacks. Due to environmental concerns, biomass, a renewable fuel, plays an important role in pollution reduction. Therefore, this research focuses on the variation of operating conditions in co-firing circulating fluidized bed boilers using computational fluid dynamics.

Methodology

A three-dimensional model of the boiler was constructed by using the commercial software Ansys design modeler as a computational domain and validated with industrial data. The study on the variation of operating conditions uses the 2^k factorial design of experiments to evaluate results. Three parameters were investigated in this work: wood blending ratio, mixed fuel flow rate, and inlet air temperature. In addition, there are 3 response parameters in the environmental and performance aspects, Global warming potential (GWP), acidification potential (AP), and heat duty.

Results and Discussion

As the wood blending ratio increases, the global warming potential (GWP) and acidification potential (AP) decrease due to the lower carbon content in the biomass fuel and reduced NOx and SO2 formation potential. In contrast, the heat duty from the heat exchanger decreases when the wood blending ratio increases because the heating value of biomass is lower than that of coal. For mixed solid fuel, the AP increases as the amount of solid fuel increases due to higher flue gas and pollutant emissions. Additionally, the heat duty increases with the amount of solid fuel due to the higher rate of heat transfer from the increased flue gas. Regarding air temperature, an increase in air temperature leads to an increase in heat duty due to the higher temperature gradient, which enhances heat transfer potential. Finally, the optimum condition for low-emission and high-efficiency (LEHE) operation is proposed: an air-to-fuel ratio of 5.89 and an inlet air temperature of 188°C.

Significance

- The research focuses on optimizing operating conditions in co-firing circulating fluidized bed boilers using computational fluid dynamics (CFD).
- The study employed a 2^k factorial design to evaluate the effects of three parameters: wood blending ratio, mixed fuel flow rate, and inlet air temperature.
- Increasing the wood blending ratio reduces environmental impact. However, the heat duty from the heat exchanger decreases as the wood blending ratio increases.
- Higher amounts of mixed solid fuel increase environmental, but the heat duty rises with more mixed solid fuel.
- Higher air temperature enhances heat duty due to a higher temperature gradient.
- For low-emission and high-efficiency (LEHE) operation, the optimal conditions are an air-to-fuel ratio of 5.89 and an inlet air temperature of 188°C.
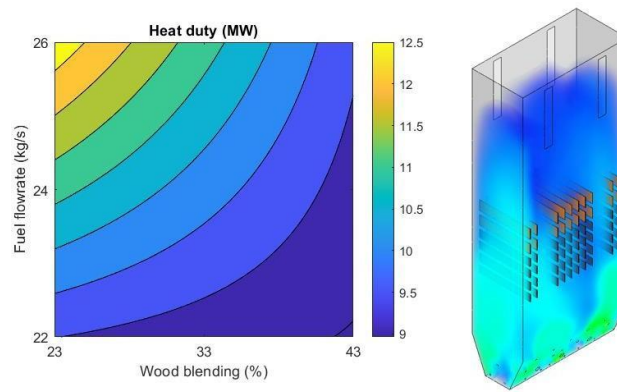
Figure 1. Heat duty contour as a function of wood blending and fuel flowrate.

References
1. Tanprasert, S., Rangton, N., Nukkhong, W., Wises, P., Piumsomboon, P., and Chalermsinsuwan, B. *Journal of Advanced Research in Numerical Heat Transfer*. 17(1) (2024).
2. Xie, J., Zhong, W., Shao, Y., Liu, Q., Liu, L., and Liu, G. *Energy & Fuels*. 31(12) (2017)

Biogas Integration with Biomass Fuel in Bubbling Fluidized Bed Boiler

Varudom S.[1], Phongpapop K.[1], Tanakorn P.[2], Sittiporn P.[2], Benjapon C.[1*], and Pornpote P.[1]**

[1]*Department of Chemical Technology, Faculty of Science, Chulalongkorn University, Bangkok, 10330 (Thailand)*
[2]*Integrated Research Center Company Limited, Prachinburi, 25410 (Thailand)*
*benjapon.c@chula.ac.th and **pornpote.p@chula.ac.th

Introduction

Alternative energy remains a challenge in recruiting sustainable resources for electricity generation. Biogas is a product from anaerobic digestion and has the potential to be a key player in the sustainable energy transition by producing green electricity [1]. In pulp and paper industry sector, biomass is used to produce electricity. Biogas is then integrated to improve combustion in the system. However, there are many factors that make the efficiency of biomass combustion unstable which needs to investigate.

Computational Fluid Dynamics (CFD) is a method derived from several domains of fluid dynamics and heat transfer, to solve difficult issues [2], particularly in chemical reactions like combustion.

In this study, CFD is used to study the usability of biogas in bubbling fluidized bed boiler by co-firing biogas with biomass with two feeding positions: the load burner and the first row of secondary air inlets to study the potential of biomass reduction, thermal duty, and finding the proper position to feed the biogas without modifying the boiler.

Methodology

To study hydrodynamics, and chemical reaction kinetics, the momentum, energy, and mass conservation need to be used in the Ansys Fluent, including the two-fluid model with kinetic theory of granular flow (KTFG). The model was constructed with 3D and studied grid independent with size of 0.8, 0.6, 0.5, and 0.4 meters. The most proper cell size was 0.5 meter with 860,000 cells in total. There were 3 material phases in this simulation: sand phase, gas phase, and biomass phase. To ensure accuracy in heat exchange and phase interaction, Gidaspow's drag model, Gunn's heat transfer, and the standard k-$\square$ viscous model were employed.

Results and Discussion

The biogas co-combustion with biomass in fluidized bed boiler could affect thermal duty, hydrodynamics by increasing the furnace temperature significantly and decreasing the bed temperature without changing the flue gas composition. The temperature gradients above the bed of two cases were higher than the base case. As a result, the furnace temperatures were increased. This is the result of feeding biogas with the assisting of volatile combustion. The firing position in the base case shows fuel burning at the bed surface and slightly above the bed. But in the other two scenario cases, biogas was added above the bed. This causes the combustion reaction to be occurred at higher position.

The feeding at load burner case offered the temperature of 898.52 K at the furnace while the base case provided the temperature of 864.85 K. The furnace temperature of the feeding at load burner case was higher than the base case about 30 ˚C. In addition, the distribution of internal temperatures was not as even as it ought to be because of high temperature at load burner shift the overall temperature to the left side. Poor heat exchange occurs in the water pipe on the right side. Additionally, interior materials may erode because of the high temperature around the load burner. The temperature at the furnace for the feeding at first row of the secondary air inlet case was 906.02 K, which was approximately 40 ˚C higher than the base case. Comparing to the other two cases, the interior temperature distribution was better. The feeding at load burner case and the feeding at the secondary air inlet case had bed temperature about 20 °C lower than the base case. This is because all the fuel in the base case burns on the bed's surface while the biogas fuel for the feeding at load burner case and the feeding at secondary air inlet case are located above the bed. As a result, there is no heat buildup on the bed. The burning of volatile materials will assist the system combustion. In this study, the internal heat dispersion in the

boiler of the feeding at the secondary air inlet case was better. This leads to improved heat exchange at the water pipes. Furthermore, there may be a problem with internal material erosion from heat accumulated at the feeding at load burner. For this reason, the feeding at secondary air inlet is a more suitable location to feed the biogas to improve the steam boiler without modifying the boiler.

Significance

To improve the power generation process using biogas combined with biomass in a bubbling fluidized bed boiler without modifying the boiler.
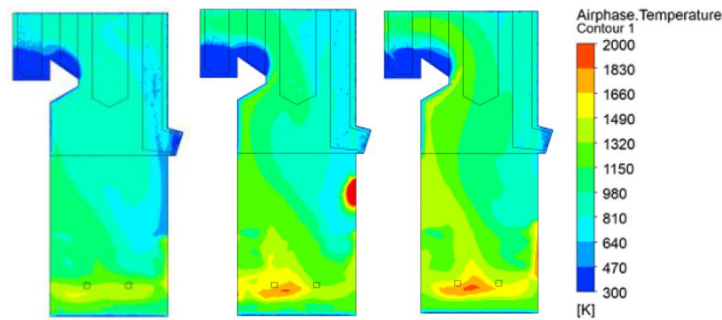

Figure 1. Temperature Profile of (a) base Case, (b) load burner case, and (c) first row of secondary air inlet case.

References

1. Marta G., Biogas Resource Potential and Technical Exploitation, in Comprehensive Renewable Energy (Second Edition), T.M. Letcher, 2022, p. 91-125.
2. Shamoon J., Introduction to CFD, in Using HPC for Computational Fluid Dynamics, 2015, p. 1-20

CFD-Driven Validation of a Customized Particle Filtration Efficiency Tester for ASTM F2299 Compliance

Muhammad Amer [1], Kritchart Wongwailikhit *[2], Ratthapol Rangkupan *[1,3]

[1] *Nanoscience and Technology Interdisciplinary Program, Graduate School, Chulalongkorn University, Bangkok 10330 (Thailand)*
[2] *Department of Chemical Engineering, Faculty of Engineering Chulalongkorn University, Bangkok 10330 (Thailand)*
[3] *Metallurgy and Materials Science Research Institute, Chulalongkorn University Bangkok 10330, (Thailand)*
* kritchard.w@chula.ac.th; *ratthapol.r@chula.ac.th

ABSTRACT

Particulate filtration efficiency (PFE) assessment is a crucial aspect of testing filter media. Several PFE testing protocols are standardized for specific applications; for example, ASTM-F2299 for disposable medical masks, NIOSH-STP-0059 for N types respirators, and ISO-29463-3 for HEPA and ULPA filter media evaluation. Several PFE testers on the market that claim to be in ASTM- F2299 and the cost of purchasing these commercial PFE testers is notably high, and the recommended testing labs for example Nelson lab often have long lead times. This situation highlights the need for a more accessible and compliant testing solution. In this study, we designed and fabricated a customized MMRI PFE tester mounting assembly prototype for the ASTM-F2299 test. The filter holder assembly consists of two fluid domains: upstream and downstream. The airstream, uniformly mixed with particles, enters the upstream domain, passes through the filter material, and exits via the downstream domain. To validate our prototype, we used computational fluid dynamics (CFD) software (ANSYS FLUENT 2024R LNC) to study airflow behavior in the sample holder. A laminar physics model was used at various airflow rates of 5, 10, 15, and 19.5 L/min. The simulation results confirmed that the airflow before entering the upstream sampling region and after leaving the downstream sampling region was laminar, with face velocities ranging from 2.98 to 11.70 cm/s and Reynolds numbers below 1,000. Every flow rate is within the criteria specified in the ASTM F2299 standard. Furthermore, we also conducted experimental validation of our custom MMRI PFE tester with melt-blown and glass fiber filters as reference media. The experimental data and the simulated results were in good agreement, there was only a 0.3%-4.8% difference in pressure drop between these results. These findings clearly showed that our custom sample holder and PFE testing system comply with the ASTM-F2299 standard.

Keywords: computational fluid dynamics (CFD), particulate filtration efficiency (PFE), ASTM-F2299, filter holder, face mask

1. Introduction

The World Health Organization (WHO) declared COVID-19 a pandemic in March 2020, following its rapid global spread and thousands of deaths [1]. As of September 18, 2021, about 227 million cases and 4.67 million deaths were confirmed, resulting in one of the most severe pandemics in history[2]. Health authorities recommend the use of masks as a preventive measure against COVID-19 and other illnesses that are transmitted through droplets and aerosols [3]. Therefore, the WHO strongly suggests critical preventive measures involving social distancing, wearing face masks in public, hand washing, and so on, to self-protect from potential infection[4]. The demand for certified medical masks and respirators among health care and other frontline workers has increased dramatically, putting existing manufacturing and supply chains under strain and demanding rapid testing and certification of new materials by new producers[5]. Several companies have launched

filter and mask testing instruments into the market, especially for particulate filtration efficiency (PFE) testing, the most critical aspect of air filter and mask testing and development.

Standardized performance classification and testing procedures of PFE testing for disposable medical masks, respirators and other air filter media exist from organizations such as American Society for Testing and Materials (ASTM), International Organization for Standardization (ISO) and National Institute for Occupational Safety and Health (NIOSH) of the United States of America. Since the classification and intended use of articles in each standard are different, the specifics of these testing processes vary greatly. For example, the PFE testing protocol for N-series respirator NIOSH 42 CFR Part 84, which is the standard for respirator devices, such as N95 and N99 respirators, employed salt particles with mean diameter of 0.075 um under specific testing condition using specific instrument design. The PFE testing protocol per ASTM F-2299-2019, the PFE testing for disposable medical face per ASTM F2100 classification, use polystyrene latex (PSL) spheres with a mean diameter of 0.1 μm and specific testing condition. While these standards employ similar testing concepts in general, their testing condition differ and are often not interchangeable [3, 6]. During the pandemic crisis, the shortage of personal protective equipment (PPE) was severe, particularly in terms of the supply of N-types and surgical masks. [7].

In response, we have designed and built a custom MMRI PFE testing system per ASTM-F2299 guidelines, with an interchangeable sample holder for ISO-29463-3 testing capability extension in the future. The filter holder assembly consists of two fluid domains: upstream and downstream. The airstream, uniformly mixed with particles, enters the upstream domain, passes through the filter material, and exits via the downstream domain. In this study, we use computational fluid dynamics (CFD) as mean to gain a better understanding of an air flow behavior in the PFE tester. A filter holder that accurately replicates the actual system was designed using a design modeler. The airflow characteristics inside the test rig at various volumetric flow rates were examined through computational fluid dynamics (CFD) simulations using ANSYS FLUENT 2024R. The simulation results were assessed against ASTM F-2299 criteria, i.e. Reynolds number, face velocity, and flow behavior. Lastly, we validated the simulation results with experimental result by measuring a pressure drop reference materials; i.e. melt blown and glass filter material media, at 5, 10, 15, and 19.5 L/min flow rates.

2. Methodology

This study was conducted in two stages: experimental work and ANSYS Fluent simulations. In the results and discussion section, both models were validated using experimental data of pressure drop and key testing parameters face velocity, Reynolds number, and flow behavior, as specified by the ASTM F2299 standard.

2.1. Experimental
2.1.1 Filter material characteristics: Porosity determination

This section of the study examined the porosity of different filter materials: melt-blown and glass fiber. The filter material diameter was 3.8 cm, and the thicknesses of melt-blown and glass fiber were 0.01 cm and 0.042 cm, respectively. The liquid displacement method was used to determine the porosity using equation 1 [8] and the ethanol density was 0.789 g/cm^3. A micrometer was used to measure the thickness of the filter materials, and their weights were measured using a precision balance.

$$\varepsilon = \frac{w_w - \frac{w_d}{\rho_I}}{w_w - \frac{w_d}{\rho_I} + \frac{w_d}{\rho_p}} \qquad\qquad Eq.1$$

w_w and w_d denote the weight in grams of wet and dry filter samples respectively, ρ_I shows the density of the ethanol (g/cm3), and ρ_p is filter material density(g/cm^3)

2.1.2 Filter material characteristics: Material resistance coefficient determination

Material resistance coefficients, i.e. inertial resistance, viscous resistance, and permeability of the filter materials are critical input parameters for porous zone condition in CFD simulation. These parameters were determined from a pressure drop across filter media at various air velocity.

The pressure drop of the reference filter media, were measured using a customized MMRI PFE testing system. The MMRI tester, with a schematic diagram as shown in Figure 1, was designed and assembled together using ASTM F2299 and ISO 29463-3 standard as guideline. In short, the system consisted of a filter-dried air source, a particle generator (Lighthouse Worldwide Solutions, USA), upstream and downstream air flow meter (MF 5706, Silicon Micro-Electro Mechanical System, China), a differential electrical mobility classifier (DEMC 2000, PALAS, Germany) coupling with neutralizer unit, a MMRI custom designed test rig, upstream and downstream condensation particle counters (UF-CPC-50 PALAS, Germany), a pressure differential gauge (PAT 420D, Ventilation Control Products Sweden AB, Sweden), temperature and humidity sensor (Lighthouse Worldwide Solutions, USA) and vacuum pump. In typical PFE test, the filtered dry air was used to generated PSL aerosol, which then homogenized, classified and neutralized and passes through a filter material at specific velocity before exited through the outlet.

In this particulate study, the pressure drop was measured using a clean dried air without PSL particles. Before commencing the experiment, triplicate samples of both melt-blown and glass fiber filters were prepared, each cut into a circular shape with a diameter of 8 cm. Pressure drop measurements were obtained from air differential pressure transmitter at flow rates ranging from 1 L/min to 19.5 L/min.
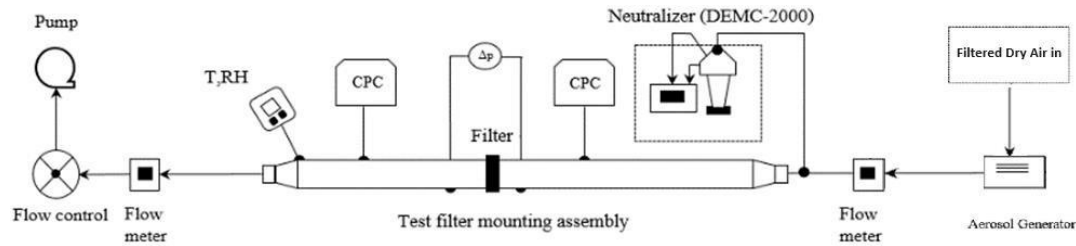

Figure 1. Schematic diagram Customized MMRI PFE Tester

2.2. Computational Fluid Dynamics (CFD) simulation by ANSYS FLUENT 2024R
2.2.1. Governing Equations for gas flow

The airflow through the fibrous medium was considered a steady-state laminar flow in the filter material. The flow was determined using the conversion of the momentum equation and the two-dimensional continuity equation Eq. (2) and Eq. (3).

$$\frac{\partial \rho}{\partial t} + \rho \left(\frac{\partial \mu}{\partial x} + \frac{\partial v}{\partial y} \right) = S_m \qquad Eq.2$$

$$\frac{\partial V}{\partial t} + (\vec{U} \cdot \nabla)V = f - \frac{1}{\rho}\nabla p + \frac{\mu}{\rho}\nabla^2 V \qquad Eq.3$$

ρ- Fluid density, Kg/m^3, S_m-Mass source term, f- External force on unit volume fluid, $\vec{U}$- Velocity vector, μ- Dynamics viscosity, Pa.s.

2.2.1. Geometry and Meshing

The evaluation of pressure drop in the MMRI PFE tester sample holder as shown in (Figure 2A) was conducted via CFD study using Ansys Fluent 2024R. Two geometries were created in the design modeler melt-blow (Model 1) and glass fiber filter (Model 2) thicknesses of 0.01 cm and 0.042 cm respectively as shown in Figure 2B and 2C. Unstructured meshing with smaller element sizes was generated to enhance convergence and reduce the time required to obtain results. We conducted a grid independence test by decreasing the element size from 1.70 mm to 1.60 mm. Within the range

of 1.65 mm to 1.60 mm, the simulation results for pressure drop and face velocity remained unaffected by changes in grid size. We established a mesh with a total of 998,932 elements for the sample holder assembly and mesh quality matrices as shown in Table 1. Both models were simulated at the flow rate of 5, 10, 15, 19.5 L/min.
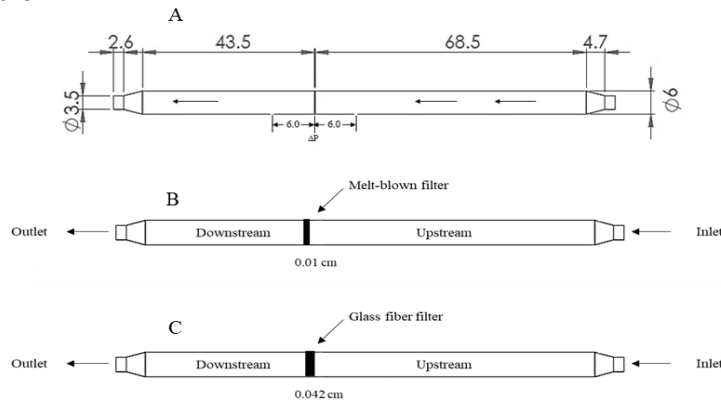

Figure 2. (A) Sample holder mounting assembly (dimensions in cm), (B) Model 1 Melt-blown (C) Model 2 Glass fiber

Figure 3. Sample holder meshing

Table 1: Mesh matrices quality

Quality Matrices	Average Skewness	Average Orthogonal Quality	Average Elements Quality	Element Size(mm)	Number of Elements
Mesh Quality	0.091	0.986	0.925	1.65	998,932

2.2.1. Boundary condition and Solver Setting

A 3D model was configured in this study as shown in Figure 4A. The sample holder model was simulated in two conditions with a melt-blown filter (Model 1) and glass fiber filter (Model 2) and filter thicknesses were changed by 0.01 cm and 0.042 cm respectively. The model's wall motion was stationary and had no shear stress on it. The inlet velocity is calculated by dividing the experimental discharge by the area of the inlet pipe [9]. The inlet velocity was set within a range of 8.7 cm/s to 33.8 cm/s and 0 pressure at the outlet. P1 and P2 were the actual locations of the pressure probes in our testing system we aimed to determine the pressure on these points in the simulation and also calculate the filter face velocity (cm/s) upstream. The Reynolds number was determined using the formula specified in the ASTM F2299-2019 standard [10]. Calculations were performed at upstream planes ranging from 0.5-u to 11-u, and at downstream planes from 0.5-d to d-7, where the distance between each plane (1d) was 6 cm. The following equation was employed to calculate the inlet velocity, filter face velocity, and Reynolds number.

Inlet velocity (cm/s) and Face velocity (cm/s):

$$v = \frac{Q}{A} \qquad\qquad Eq.4$$

v is velocity (cm/s), Q is denoted volumetric flow rate (cm^3/s) and A is cross-sectional area(cm^2)

Reynolds Number:

$$Re = \frac{\rho z D}{\mu} \qquad\qquad Eq.5$$

Here, air density (kg/cm^3), □ is the velocity of air (cm/s), D is inside the sampling diameter line (cm), and μ is the viscosity of air (kg/m-s).
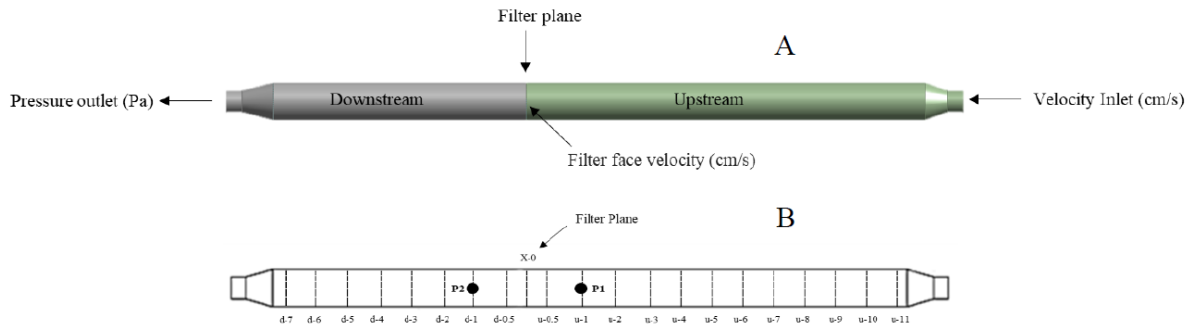

Figure 4. (A) computational domain in this study (B) Average Reynolds number determination

Table 2. Solver setting summary

Solver	Viscous model	Material	Boundry conditions		Porous zone condition			solution method	Iterations	Convergence
			inlet	outlet	x	y	z			
Pressure-based	Laminar	Air	Velocity (cm/s)	Pressure (Pa)	1	0	0	SIMPLE	500	1.00E-04
			8.7, 17.3, 26, 33.8	0						

2.2.1. Porous Zone Condition

A porous medium simulation examines the behavior and transport of molecules and particles through structures such as packed beds, perforated plates, and filter sheets [11]. In ANSYS Fluent, this simulation integrates the velocity, viscous, and inertial resistance terms from the Navier-Stokes equations, along with an additional pressure drop to accurately represent the flow through the porous medium. The porous medium represents the filter material so that the air streamline is utilized in a particular direction where the Darcy-Forcheimer equation is used in the ANSYS Fluent as the external body force term.

$$\frac{\Delta p}{\Delta x_i} = -\frac{\mu}{\alpha} v_i + 0.5 \cdot C_2 \cdot \rho \cdot |v| \cdot v_i \qquad\qquad Eq.6$$

The variables $\frac{1}{a}$ and C_2 represent the viscous and inertial resistance coefficients, respectively, in the direction i (aligned with the air streamline through the filter material) based on the pressure drop across the porous medium. To determine these coefficients, a curve-fitting graph of pressure drop versus velocity should be constructed, with the function derived by comparing two equations and Eq. (6) and (7). The viscous resistance coefficient $\frac{1}{a}$ and the inertial resistance coefficient C_2 can then be calculated using Eq. (8) and Eq. (9).

$$\Delta p = \alpha v_i^2 + b v_i + c \qquad\qquad Eq.7$$
$$\frac{1}{a} = \frac{b}{\mu \cdot \Delta x} \qquad\qquad Eq.8$$
$$C_2 = \frac{2a}{\rho \cdot \Delta x} \qquad\qquad Eq.9$$

Where Δx represents the thickness of the filter material parallel to the direction of the air streamline, and ρ and μ denote the density and viscosity of the fluid flow, respectively.

3. Result and Discussion

3.1.1 Filter material characteristics: Porosity

The porosity of the melt-blown and glass fiber filter materials was measured using the liquid displacement method, and the results show that the melt-blown filter had a porosity of 0.80, suggesting that empty spaces account for 80% of its volume. This high porosity indicates that the melt-blown filter allows for higher airflow and a low-pressure drop. [12], decreasing material

resistance and increasing permeability. In comparison, the glass fiber material had a lower porosity of 0.70 and a considerable high-pressure drop due to its strong resistance.

3.1.2 Filter material characteristics: Material resistance coefficient

In this section, the material resistance properties of filters were determined by analyzing the pressure drop and velocity experimental data. The pressure drop across both filter materials was measured at air flow rate from 1 L/min to 19.5 L/min. As the airflow rate increased from 1 L/min to 19.5 L/min pressure drop and face velocity of both material melt-blown and glass fiber filter also increased from 2.50 Pa to 70.65 Pa and 0.66 cm/s to 11.60 cm/s respectively. This behavior is attributed to the fact that higher airflow rates impose a greater force on the filter material, resulting in increased resistance and, consequently higher pressure drop. The melt-blown filter consistently shows a lower pressure drop compared to the glass fiber filter due to higher porosity.

The material resistance properties, i.e. inertial resistance, viscous resistance, and permeability of the reference filter media (melt-blown and glass fiber filters) were determined by a curve fitting analysis from the relationship between the pressure drop versus velocity utilizing a quadratic Eq. (7) to account for a viscous and inertial resistance components. The variables $\frac{1}{a}$ and C_2 represent the viscous and inertial resistance coefficients, respectively. Eq.(8) and Eq.(9) were used to calculate these coefficients and results as shown in Table 3.

Table 3. Filter materials resistance

Filter material	$\frac{1}{a}$, Viscous resistance (m²)	C_2, Inertial resistance (m⁻¹)	Permeability (m⁻²)	Porosity	Thickness (cm)
Melt blown	1.45781E+11	688500.68	6.86E-12	0.80	0.010
Glass fiber	83731178847	514441.20	1.19E-11	0.70	0.042

3.3 CFD simulation
3.3.1 Air Flow Behavior

In this section of the study, the flow behavior within the test rig was observed and compared with the ASTM F2299 standard. According to the standard, the flow must be in laminar region with Reynolds number not exceeding 1,000. Figures 5, and 6 present the velocity contour from the simulation inside the entire test rig domain for the melt-blown filter and glass fiber filter, respectively. The results indicate that airflow velocity is highest at the center of the sample line, while it decreases near the walls due to frictional effects. At flow rates ranging from 5 L/min to 10 L/min, the flow behavior was confirmed to be laminar for both the melt-blown and glass fiber filters. The velocity contours further illustrate the laminar nature of the flow within the sample section line, and the calculated Reynolds numbers also validated this flow behavior. When the airflow increased to 15 L/min and 19.5 L/min for both melt-blown and glass fiber filters, while the airflow in the testing chamber still is the laminar flow, the velocity contours close to the entrance revealed higher air velocity regions and large velocity difference between the center and the wall region. This discrepancy suggests that the flow may demonstrate transitional behavior in certain areas at these higher flow rates. Further studies are currently ongoing to investigate this issue, and the findings will be reported in future work.
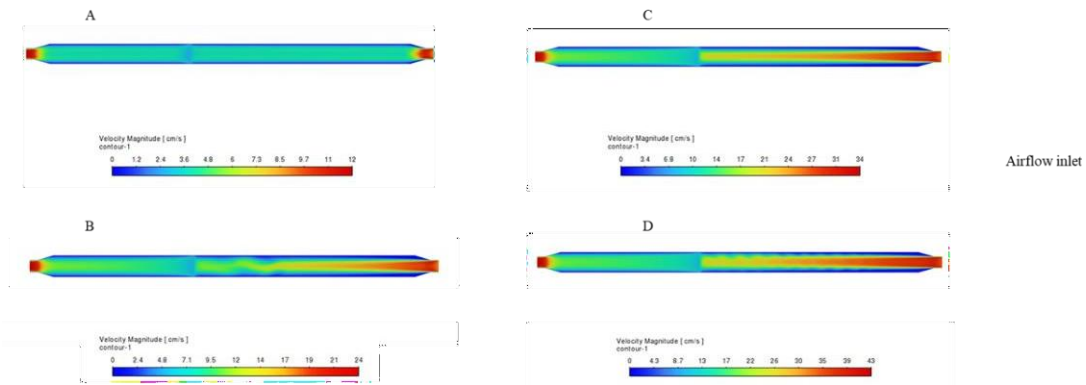
Figure 5. Velocity contours of sample holder with melt-blown filter at flow rates (A) 5 L/min (B) 10 L/min (C) 15 L/min (D) 19.5 L/min and validation with ASTM F2299-19 Standard
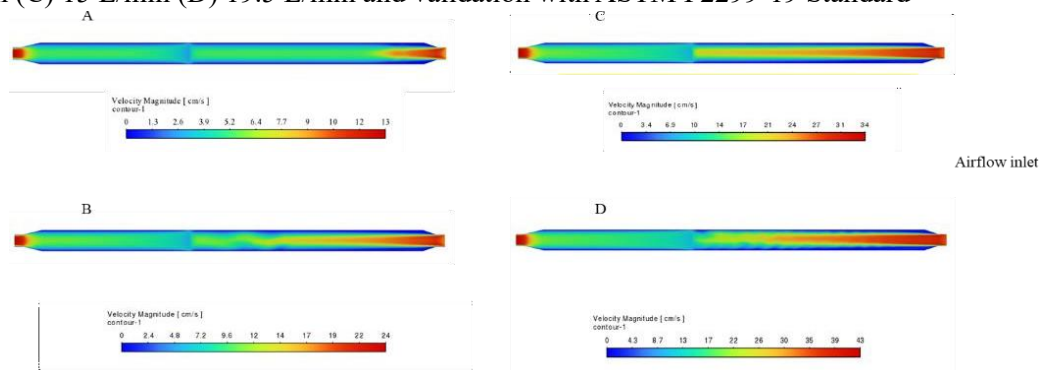

Figure 6. Velocity contours of the sample holder with glass fiber filter at flow rates (A) 5 L/min (B) 10 L/min (C) 15 L/min (D) 19.5 L/min and validation with ASTM F2299-19 Standard

3.3.2. Average Reynolds Number

According to the ASTM F2299 standard, the Reynolds number in the testing condition must be less than 1000 throughout the sample section line to ensure the laminar flow of the testing aerosol stream. The average Reynolds number of air streams at different positions in the test rig and different flow rates were calculated using Equation 5, as shown in Figure 7. The average Reynolds number for the melt-blown sample at a flow rate of 5 L/min was 121. The planes ranged from u-0.5 to u-11 upstream and d-0.5 to d-7 downstream. A higher Reynolds number of 122 was observed at the melt-blown sample plane (x-0) due to the increased velocity at that location. Similarly, at 19.5 L/min, the Reynolds number at the melt-blown filter plane (x-0) was 474. The u-11 plane had a higher Reynolds number of 481 due to the high airflow velocity in this region. The average Reynolds number across the upstream and downstream planes ranged between u-10 and d-7 planes, with an overall average of 472 shown in Figure 7A. The simulation results for the Reynolds number of the glass fiber filter were similar to those of the melt-blown filter, except for a higher Reynolds number of 487 at the u-11 plane. The Reynolds number ranged from 121 to 472 in the upstream and downstream planes for flow rates ranging from 5 L/min to 19.5 L/min. These results indicate that the airflow inside the MMRI PFE test rig at all velocities are laminar and conforms to the ASTM F2299 standard.
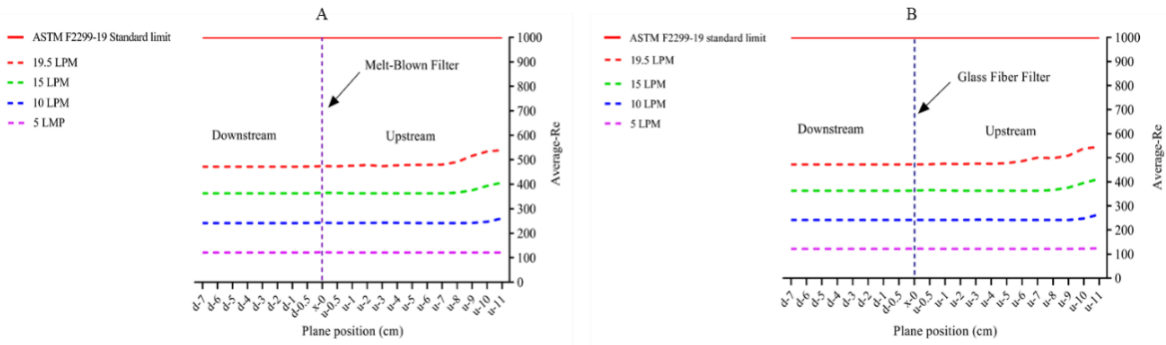
Figure 7. Validation of Simulation average Reynolds number (A) Melt Blown Filter (B) Glass Fiber Filter with ASTM F2299 Standard.

3.3.2. Face Velocity

ASTM F2299 stated that the face velocity of filter material should not exceed 25 cm/s. This section examined the face velocity results from experimental measurements and simulations of melt-blown (MB) and glass fiber (GF) filters at various air flow rates (5, 10, 15, and 19.5 L/min). There is a positive correlation between airflow and face velocity; as the airflow increases, the face velocity also increases [13]. Figure 8A indicates that the melt-blown filter's face velocity values ranged from 2.95 cm/s to 11.70 cm/s, instead the simulation values were nearly the same, ranging from 3.02 cm/s to 11.70 cm/s, with a percentage difference of 0.17% and 2.44%. Similarly, in Figure 8B, with the glass fiber filter, experimental face velocities ranged from 3.0 cm/s to 11.70 cm/s, while simulation values were nearly comparable, showing a 2% to 3% difference. These findings confirm that the MMRI PFE tester sample holder complies with the ASTM F2299-19 standard. Simulation and experimental data of face velocity within the limit of the standard as shown in Figure 8.
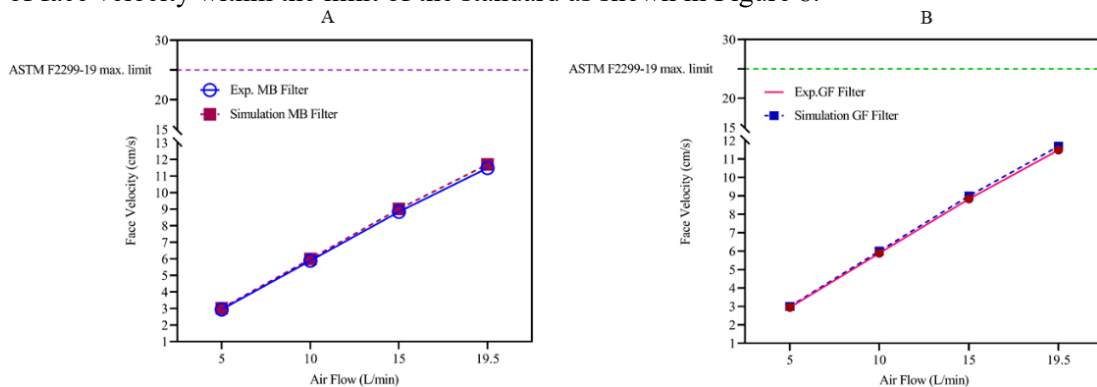

Figure 8. Validation of Experimental and Simulation Face Velocity (A) Melt Blown (MB) Filter (B) Glass Fiber (GF) Filter

3.4. Validation of Pressure Drop Predictions

The model validation was done first, by comparing experimental pressure drop data to simulation findings. The pressure drop across the melt-blown and glass fiber filters was analyzed both experimentally and through CFD simulation. The experimental data for the melt-blown filter demonstrated a linear increase in pressure drop with increasing flow rate, as is characteristic of the porous medium [14]. At an airflow rate of 5 L/min, the recorded pressure drop was around 12 Pa, whereas at 19.5 L/min, it was 46 Pa. The CFD results closely matched these experimental numbers, with a pressure drop of 11.82 Pa at 5 L/min and 45.93 Pa at 19.5 L/min as shown in Figure 9. Similarly, for the glass fiber filter, the experimental pressure drop value increased linearly with the flow rate, from 18.33 Pa at 5 L/min to 70.67 Pa at 19.5 L/min. The simulation findings were nearly identical, with values of 18.74 Pa and 74.12 Pa at the respective flow rates. The simulation predicts a slightly larger pressure drop at higher velocities, suggesting that the model is slightly more cautious in anticipating filter resistance. The percentage difference between experimental and simulation

results for melt-blown and glass fiber filters was carefully investigated across a range of 5 L/min to 19.5 L/min. The investigation found that the simulation model keeps a high degree of accuracy, with percentage differences ranging from a minimum of 0.32% to a maximum of 4.8%.
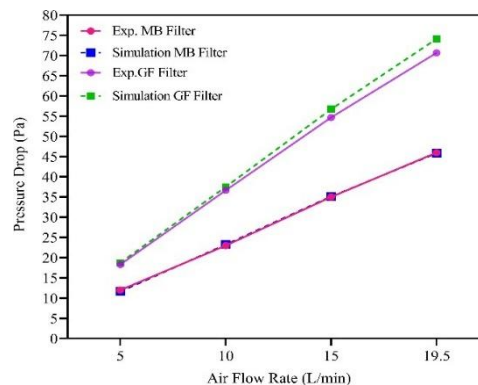

Figure 9. Experimental vs simulated value of pressure drop for (A) Melt Blown (MB) Filter (B) Glass Fiber (GF) Filter

4. Conclusion

This study successfully designed, fabricated, and validated a custom particulate filtration efficiency (PFE) testing system that was compliant with the ASTM F2299-19 standard. Computational Fluid Dynamics (CFD) simulations using ANSYS Fluent 2024R demonstrated that the airflow within the sample holder remained laminar, with face velocities and Reynolds numbers within the acceptable range specified by the ASTM F2299 standard. Experiments validation using the melt-blown and glass fiber filter media produced good agreement with CFD simulation results, with pressure drop differences ranging from 0.3% to 4.8%. The melt-blown filter had a higher porosity of 0.80 and a lower pressure drop than the glass fiber filter, which had 0.70 porosity. The filter material resistance analysis showed that the melt-blown filter had lower viscous and inertial resistance, resulting in higher permeability when compared to the glass fiber filter. The assessment of the Reynolds number, face velocity, and flow behavior inside the test rig confirm the sample holder design conformity with the ASTM F2299 standard. Our design offers a low-cost alternative PFE test rig with ASTM F2299 compliance for accurately assessing the filtration efficiency of various filter media.

References

1. Ciotti, M., et al.,*Crit. Rev. Clin. Lab. Sci*, 2020. 57(6): p. 365-388.
2. Liao, M., et al., *Curr. Opin. Colloid Interface Sci*, 2021. 52: p. 101417.
3. Organization,W.H.,*: interim guidance, 6 April 2020*. 2020, World Health Organization.
4. Forouzandeh, P., K. O'Dowd, and Pillai S.C., *Saf. Sci.*, 2021. 133: p. 104995.
5. Rowan, N.J. and J.G. Laffey, *Sci. Total Environ.*, 2021. 752: p. 142259.
6. ASTM, *Standard test method for determining the initial efficiency of materials used in medical face masks to penetration by particulates using latex spheres*. 2017, West Conshohocken PA, USA.
7. Pourdeyhimi, B.*. J. Med. Sci*, 2020. 2(3): p. 1-11.
8. Yadav, P., R. Farnood, and Kumar V.,*. Chemosphere*, 2022. 287: p. 132092.
9. Banerjee, A., et al.,*. Energies*, 2018. 11(2): p. 320.0
10. F/FM, A.S., *Standard test method for determining the initial efficiency of materials used in medical face masks to penetration by particulates using latex spheres*. 2017.
11. Wang, Y., et al.,*. J. Membr. Sci.*, 2010. 363(1-2): p. 57-66.
12. Liu, X., Shen H., Nie X.,*. Int. J. Environ. Res. Public Health*, 2019. 16(2): p. 247.
13. Xia, T., et al.,*. Energy and Buildings*, 2018. 158: p. 987-999.
14. Jeon, W., et al., . *HVACR Res.*, 2020. 26(6): p. 835-843.

Effect of feeding operation on microplastics separation in hydrocyclone

Dulyapat T.[1], Pornpote P.[1,2] and Benjapon C.[1,2*]
[1]*Department of Chemical Technology, Faculty of Science, Chulalongkorn University*
254 Phayathai Road, Wangmai, Pathumwan, Bangkok 10330, Thailand
[2]*Center of Excellence on Petrochemical and Materials Technology Chulalongkorn University, 254*
Phayathai Road, Wangmai, Pathumwan, Bangkok 10330, Thailand
*Benjapon.C@chula.ac.th (corresponding author designated with a star)

Introduction

Microplastics have become a significant environmental concern, impacting both freshwater and marine ecosystems. In response, extensive research has been conducted to explore methods for separating microplastics from water. One area of investigation involves the use of Computational Fluid Dynamics (CFD) models to study hydrocyclones and their intricate flow patterns. In this study, CFD was systematically employed to examine the separation of microplastics in hydrocyclones. The efficiency of these hydrocyclones was evaluated based on key performance metrics, including the percentage of microplastics recovered, the water split percentage, and the pressure drop. As a result of this comprehensive investigation of feed velocity and inlet type in hydrocyclone.

Methodology

In this study, the liquid-gas-solid system was analyzed using the Eulerian-Eulerian CFD model to investigate the hydrodynamics and separation of microplastics in hydrocyclones. The mixture model was employed to solve a single set of mass and momentum conservation equations for the liquid-gas-solid mixture and utilized an algebraic model for particle-liquid phase interactions. Water and solids were fed into the hydrocyclone, with the outlet condition set to 1 atm pressure and air backflow. Initially, the hydrocyclone was filled with air. The effect of the feed inlet was investigated in a mini hydrocyclone with a body diameter (Db) of 20 mm and inlet diameters (Di) of 4 mm. The cylindrical section (H) and conical section (Hc) have heights of 16 mm and 152 mm, respectively. The vortex finder (Hv) has a length of 10 mm and a thickness of 2 mm. The overflow (Do) and underflow (Du) have diameters of 4 mm, designed to enhance the separation efficiency of the hydrocyclone, including the recovery of microplastics and the water split. The water containing PET particles with a diameter of 10 μm was introduced into hydrocyclones with 3-12 m/s of velocity and a concentration of 0.1% by volume. The system's outlet pressure was maintained at 1 atm. This work aims to study effect of feeding operation to achieve high microplastics recovery and low water split.

Results and Discussion

The hydrodynamic effects of the ratios of underflow diameter to cylindrical diameter, overflow diameter to cylindrical diameter, cone height to cylindrical height, and inlet angle were examined. The efficiency of the hydrocyclone was assessed based on the percentage of microplastics recovered and the percentage of water split as can be seen in Fig. 1A. The results indicate that a higher inlet velocity enhances microplastics recovery for both inlet types and improves water split for the two-inlet type. Energy consumption, represented by pressure drop, is shown in Fig. 1B. The findings reveal that higher inlet velocities result in increased pressure drops. When comparing systems with equal mass flow rates (3 m/s two-inlet compare with 6 m/s one-inlet), the two-inlet configuration demonstrates a lower pressure drop in the hydrocyclone system that relate to lower energy consumptions in the system.

Significance

The increasing inlet velocity improves microplastics recovery and can reduce water split in two-inlet configurations. The two-inlet feed type hydrocyclone consumes less energy compared to the one-inlet configuration at the same mass flow rate.
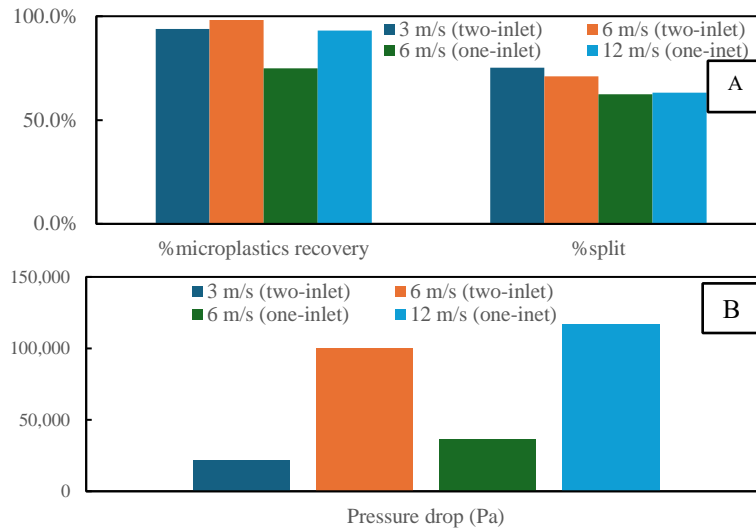
Figure 1. Computational result of microplastics in hydrocyclone with different feed inlet (A) %microplastic separation, (B) Pressure drop (Pa)

References
1. Thiemsakul D.,Piemjaiswang R., Sema T.,Feng Y.,Piumsomboon P. and Chalermsinsuwan B., *Results in Engineering*, 22 (2024).
2. He L., Ji L., Sun X., Chen S. and Kuang S., *Particuology journa*, 71 (2022).

Improving Human Sequential Decision-Making with Reinforcement Learning

Park Sinchaisri

Workers often spend significant time learning to make good decisions, which affects service quality due to initial suboptimal decisions. Observing peers can help, but this isn't always possible, especially in gig economies where workers operate independently. Over the past two decades, many domains have accumulated large amounts of trace data on human decisions and outcomes (e.g., physicians' lab orders, Uber drivers' locations). This data implicitly encodes the collective knowledge acquired by numerous workers about how to effectively perform their jobs. In this paper, we study whether machine learning can be used to mine this high-volume data and extract interpretable insights that can help workers improve their performance at sequential decision-making tasks.

We devise a novel algorithm for automatically learning decision-making rules or "tips" that, if correctly followed by the human worker, most improves their performance. It does so in two steps. First, our algorithm uses imitation learning to learn a model of the current strategy employed by the human workers. In particular, we learn a neural network, called the Q- network, that approximates the long-term value of the actions taken by humans and encodes how changes to their strategy affect performance. Then, we derive a novel objective that captures the discrepancy between the actions taken by the human strategy compared to the optimal policy. Our algorithm selects the tip that minimizes this discrepancy in a way that accounts for which actions are consequential for achieving higher performance. We also design the search space of tips to consist of if-then-else rules and use an approach based on interpretable reinforcement learning to learn the best tips, so that humans can understand and correctly follow them. An extensive behavioral study involved participants managing a virtual kitchen game, requiring them to optimize task assignments among virtual workers with varying skills. Challenges included unknown worker skills and task dependencies. We leverage our algorithm to learn interpretable tips from experimental data, and then demonstrate how providing them improves the performance of a new set of participants, compared to the control group, as well as those who are shown alternative tips derived from natural baselines.

Our results (N = 2,328) demonstrate that our algorithm can generate novel insights that enable human participants to substantially improve their performance compared to counterparts that are not shown the tip (p < 0.0001) or are shown tips suggested by previous participants (p = 0.006) or a baseline algorithm that naively tries to match the optimal policy (p < 0.0001). Our tip can speed up learning by up to three rounds of in-game experience, demonstrating that our tip can significantly reduce the cost of learning. Furthermore, our results suggest that our tip enables the participants to unlearn preconceived notions about the optimal strategy and discover additional strategies beyond the given tip. Interestingly, participants do not merely adjust their actions by blindly following the tip. Instead, as they gain experience with the game, they increasingly understand the significance of the tip and improve their performance in ways beyond the surface-level meaning of the tip. In conclusion, our findings suggest that our algorithm infers interpretable and useful insights about the underlying task, and successfully conveys these insights to human participants. Ultimately, we demonstrate how machine learning can be used to better understand human behavior, and how to leverage this knowledge to improve human decision-making.

Unlocking Synergies: Sufficiency Economy Philosophy for Sustainability

Sirimon Treepongkaruna,[a,b] Pattarake Sarojti,[a,#] Chaiyuth Padungsaksawasdi[c]
[a]Sasin School of Management, Chulalongkorn University, Thailand
[b] UWA Business School, The University of Western Australia.
[c] Thammasart Business School, Thammasart University, Thailand

Abstract

The *Sufficiency Economy Philosophy (SEP)*, initiated by *His Late Majesty King Bhumibol Adulyadej* in the early 1970s to address poverty problems in the rural areas and was initially adopted for sustainable farming. However, *His Late Majesty the King* emphasized that the SEP can be applied to all types of projects at all levels to achieve ultimate goals of sustainability. This paper sets out to demonstrate that the SEP is a unified framework for sustainability. Using data at corporate levels and the Refinitiv ESG rating with its three core pillars as proxies for corporate sustainability performance, we document that Thai firms practicing the SEP tend to have a better sustainability performance, especially in the environmental and governance dimensions. Our two-stage least square instrumental variable analyses imply a causal relationship between the SEP and corporate sustainability performance. We document that a one standard deviation increase in the SEP score enhances the corporate sustainability performance by 35%. This validates our proposed hypothesis of *stakeholders and long-term value creation.* The SEP presents a pragmatic pathway for businesses to achieve sustainability while advancing the Sustainable Development Goals (SDGs). By integrating SEP principles into their strategies, companies can drive positive change, leading the way towards a more sustainable and inclusive future.

The Role of Computational Science and Engineering in Promoting Sustainable Industry

Arthit Vongachariya[1]*

[1]*Industrial Digital, SCG Chemicals Public Company Limited (SCGC),
Rayong, 21150 (Thailand)*
*arthitvo@scg.com

Abstract

This presentation highlights the role of Computational Science and Engineering (CSE) in promoting sustainability within industries. By utilizing tools such as Computational Fluid Dynamics (CFD) and Computer-Aided Engineering (CAE) in conjunction with other digital technologies, we support SCG Chemicals (SCGC)'s four key green polymer concepts: Reduce, Recyclable, Recycle, and Renewable. CAE integrates with material development and product design to reduce material usage in final products, design recyclable packaging to replace non-recyclable materials in the existing market, maximize recycled content in packaging, and develop processes that utilize renewable resources. Additionally, CFD improves process efficiency and energy use, significantly reducing losses from plant trials and scale-ups. CFD simulations optimize fluid dynamics and thermal processes, resulting in more efficient systems and lower operational costs. We will showcase real-world case studies demonstrating how CSE drives innovation and sustainability in industrial sectors.

From TARA to LANTA: A Journey of Thailand's HPC Development

Manaschai Kunaseth[1]*

*[1]NSTDA Supercomputer Center (ThaiSC), National Science and Technology Development Agency
(NSTDA), Pathumthani, 12120 (Thailand)*
*manaschai.kunaseth@nstda.or.th

Introduction

Over the past decade, High-Performance Computing (HPC) has grown rapidly in response to the increasing demands of computational science and engineering research, accelerated by the rise of deep learning and artificial intelligence. In this talk, I will present Thailand's initiative to develop a robust computational infrastructure ecosystem to support national R&D needs. First, the journey from the pilot system TARA to the production infrastructure LANTA will be showcased, highlighting key milestones in design, implementation, and service operation. Next, the major role of collaborations with academic institutions, government agencies, and industry partners will be discussed, along with the challenges related to funding, skill development, and technological barriers. Finally, I will provide insights into future HPC developments in Thailand. This comprehensive overview aims to share our ongoing experience to inspire further advancements in Thailand's HPC and computational science landscape.

Figure 1: LANTA Supercomputer at Thailand Science Park, NSTDA

References

1. P. Sakdhnagool, **M. Kunaseth**, A. Piyatumrong, C. Rungnim, V. Jarerattanachat, W. Udomsiripinij, K. Tharatipayakul, T. Suwan, P. Srichaikul. TARA: A Year in Review. *Thai Journal of Mathematics* **19(3)** (2021) 739-751
2. NSTDA Supercomputer Center (ThaiSC). https://thaisc.io

Microscopic Investigation of the Slurry Drying Process and Binder Migration in Li-ion Battery Anodes using Multiscale-Simulation Methods

Tanongsak Sukkasem [1*], Sowmya Indrakumar [2], Jonas Breitenbach [3],
Jan-Willem Handgraaf [2],Larisa von Riewel [3]
[1]*Digital Transformation Engineering Co., ltd., Chamnan Phenjati Business Center Building Floor 23,*
Huaykwang, Bangkok 10320, Thailand
[2]*Siemens Industry Software Netherlands B.V., Pr. Beatrixlaan 800,*
BN Den Haag 2595, Netherlands
[3]*Heraeus Noblelight GmbH, Heraeusstraße 12, Hanau 63450, Germany*
*tanongsak@dtethai.com

Introduction

Lithium-ion batteries (LiB) are essential electrochemical energy storage systems widely utilized in portable devices like mobile phones and laptops, as well as increasingly in vehicles due to their high power and energy density. However, the intricate manufacturing processes, particularly the slurry drying process for electrode films, pose significant challenges. The drying process is pivotal in determining battery performance and durability, as it influences crucial electrode properties such as porosity and conductivity. This study focuses on the anode side, where slurry containing active materials, conductive carbon, binders, and solvents is cast onto a copper substrate. While traditional organic solvents like N-methyl-2-pyrrolidone (NMP) are effective, they come with environmental and safety concerns, alongside high costs. To address these issues, water-based slurries are being explored as a greener alternative. Additionally, optimizing the drying process is vital for enhancing energy efficiency and reducing production costs. In this study, we investigate the drying process of lithium-ion battery anodes, analyzing film solidification, binder migration, and adhesion forces between the electrode and current collector. Through a combination of experimental tests and multiscale simulation methods like dissipative particle dynamics (DPD) and molecular dynamics (MD), we gain insights into the underlying mechanisms. Our findings, compared with previous experimental results, highlight the impact of drying rates on binder distribution and electrode properties, shedding light on crucial factors influencing battery performance.

Methodology

Starting Structures: Atomistic representations of slurry components were generated using Simcenter Culgi. Binder polymers, including styrene butadiene rubber (SBR) and carboxymethyl cellulose (CMC), were constructed with specified lengths. Active materials such as silicon dioxide (SiO_2) and active carbon, along with conductive additives like graphite sheets and carbon nanotubes, were represented as colloidal entities with fixed coordinates.

Automated Fragmentation and Parameterization: The atomic structures underwent automated fragmentation and parameterization (AFP) using a novel potential energy function incorporating both attractive and repulsive intermolecular forces. This approach enables modeling of all phases at physiologically representative conditions. Heavy atoms were mapped to coarse-grained beads at a three-to-one ratio.

Computational IR Spectra: IR spectra were calculated using the NWChem plugin within Simcenter Culgi. Initial geometry optimization was performed using the Hartree Fock (HF) ab-initio method with a 6-31G* basis set, followed by IR spectrum calculation alongside energy optimization using the same basis set.

Dissipative Particle Dynamics (DPD): DPD simulations were conducted using Simcenter Culgi software. The system was equilibrated using canonical (NVT) and isothermal-isobaric (NPT) ensembles before undergoing slow and fast heating to mimic drying processes. Various parameters including time step, pressure, and box size were set accordingly. Binder diffusion coefficients were calculated post-simulation.

Molecular Dynamics Simulations: Classical all-atom MD simulations were performed in explicit solvent to validate the developed coarse-grained model. The system, including a copper crystal surface and slurry components, was equilibrated and subjected to production simulations at different drying rates.

Slurry Production and Drying Experimental Setup: A speed mixer was used to produce a homogenized electrode slurry, which was then applied to a current collector using an automatic laboratory coater. Dynamic drying with infrared radiation was employed, with varying power densities tested. After drying, the electrode layers were calendered and subjected to peel tests using a universal testing machine to assess adhesion force.

Results and Discussion

Infrared Spectra Analysis: Comparison between experimental and NWChem-generated infrared spectra provided valuable insights into the chemical composition of the water-based slurry. NWChem's individual molecule calculations facilitated precise identification of functional groups, enhancing our understanding of bond vibrations and molecular interactions. The observed peaks in experimental spectra, such as those corresponding to O-H stretching and bending in water molecules, were accurately reproduced in NWChem simulations. Furthermore, NWChem's ability to resolve distinct vibrations allowed for detailed characterization of various functional groups within the slurry, contributing to a comprehensive understanding of its molecular structure (Fig. 1).
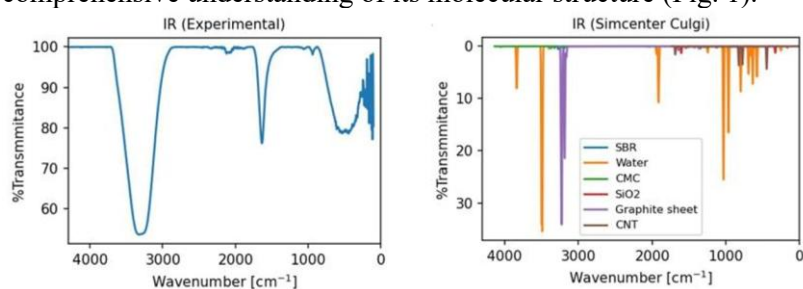

Figure 1. ATR-FTIR transmission spectrum of the aqueous slurry (experimental), the IR spectra of individual components obtained from the NWChem plugin.

Peel Force Analysis: Examination of adhesion strength via peel force tests revealed a clear relationship between drying conditions and electrode layer integrity. Increasing power density during drying resulted in reduced peel strength, indicating weakened adhesion between the electrode layer and current collector. Conversely, lower power output and slower drying speeds led to enhanced adhesive strength, emphasizing the significance of drying parameters in determining the mechanical properties of the electrode (Fig. 2).
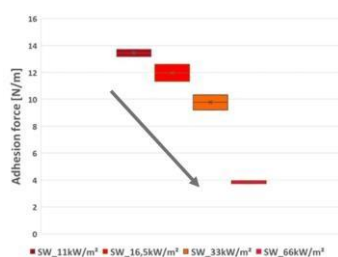

Figure 2. Box plot showing a decrease of the adhesion force with increasing power density for four different drying intensities.

Dissipative Particle Dynamics (DPD) Simulations: DPD simulations provided microscopic insights into the drying process of the slurry under different heating rates. Variation in drying rates resulted in distinct behaviors, particularly in the distribution of the SBR binder. Slower heating led to the accumulation of SBR on the copper substrate, attributed to reduced diffusion under slow drying conditions. This accumulation influenced the interaction between the binder and copper, affecting electrode adhesion. The observations from DPD simulations were consistent with experimental findings, highlighting the importance of drying conditions in shaping slurry morphology and performance (Fig. 3-4).
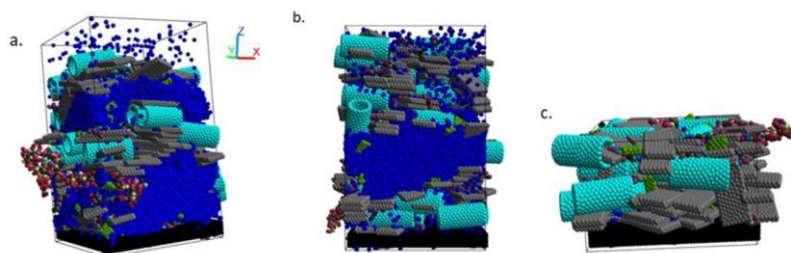
Figure 3. (a) slurry drying snapshot taken from the start of the DPD simulations, (b) snapshot taken during the slurry state, (c) dried slurry snapshot of the coarse-grained system. The component of the slurry is assigned the following colors: blue of water, and multicolored beads for SBR and CMC.
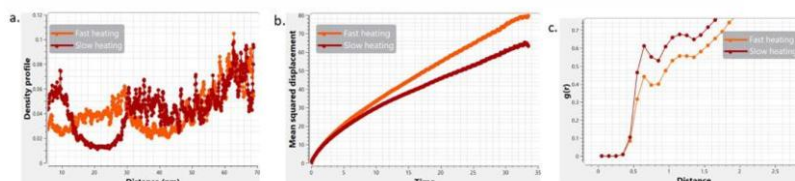

Figure 4. (a) density profile of SBR binder in the z-direction at different heating rates, (b) mean squared displacement of SBR binder under different heating conditions, and (c) paired correlation function between SBR binder and copper substrate for the different heating rates.

Molecular Dynamics (MD) Simulations: MD simulations focused on elucidating the migration of the SBR binder at the molecular level under different drying rates. Despite computational constraints limiting the size of the system and slurry components, MD simulations provided valuable insights into binder dynamics. Faster heating rates were associated with accelerated SBR migration, indicating a dependency of binder behavior on drying conditions. However, limitations in observing significant morphological changes were noted, emphasizing the need for longer length and time scales in MD simulations to capture complex slurry dynamics accurately (Fig. 5).
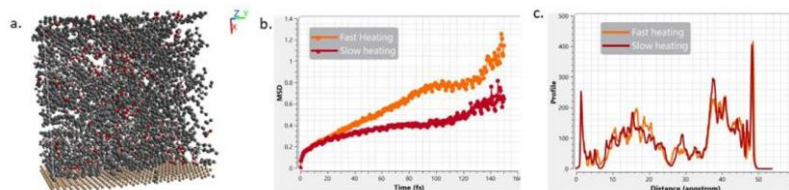
Figure 5. (a) MD snapshot of the dried slurry system, (b) mean squared displacement of SBR binder under different heating conditions, (c) SBR binder density profile in the x-direction at different heating rates.

Significance

This work holds significance in its holistic exploration of water-based slurry drying for electrode fabrication in lithium-ion batteries. By integrating experimental analysis and computational modeling, it offers insights into drying dynamics, binder migration, and adhesion mechanisms. The findings not only advance our understanding of electrode manufacturing processes but also provide a versatile framework applicable across multiple industries, facilitating optimization of drying processes and enhancing battery performance and durability.

Study of CO₂ adsorption on Cu-Based high-entropy-alloy catalysts via density functional theory and machine learning

Pisit Khamloet[1, 2], Meena Rittiruam[1, 2] and Supareak Prasertdam[1, 2]*
[1] High-Performance Computing Unit (CECC-HCU), Center of Excellence on Catalysis and Catalytic Reaction Engineering (CECC), Chulalongkorn University, Bangkok, 10330, (Thailand)
[2] Department of Chemical Engineering, Faculty of Engineering, Chulalongkorn University, Bangkok, 10330, (Thailand)
*supareak.p@chula.ac.th

1. Introduction

The demand for energy and the issue of global warming have shown a significant upward trend over time, largely driven by industrial and technological advancements in sectors like transportation, electricity, and heat[1]. The bulk of our energy is obtained from fossil fuels, resulting in the release of carbon dioxide (CO_2), a significant greenhouse gas that contributes to global warming[2]. Various methods have been employed to reduce CO_2 emissions, including using CO_2 capture materials and reducing CO_2 into high-value-added chemicals through catalytic materials via electrochemical process[3]. The electrochemical CO_2 reduction reaction (CO_2RR) offers a potential method to reduce CO_2 into compounds that are valuable at the cathode such as formic acid ($HCOOH$), methane (CH_4), methanol (CH_3OH), etc. Investigating catalyst selectivity is crucial for optimizing the collection of the target product while minimizing the hydrogen evolution reaction (HER), which competes with CO_2RR. Hori et al. [4] conducted the pioneering experimental study on CO_2RR selectivity using monometallic electrocatalysts. The first group of metals, which primarily facilitate CO formation, includes Zn, Cu, Pd, Ga, Ni, Au, Ag, and Pt. The second group, responsible for the formation of $HCOO^-$, consists of Pb, Tl, In, Sn, Cd, and Hg. However, monometallic catalysts have shown low selectivity, and some metals pose environmental concerns, alongside being costly and having low stability, making them less suitable for large-scale industrial applications[5]. Consequently, there is a pressing need for research and development of electrocatalysts that offer higher activity, selectivity, and stability. This includes investigating alternative metal-based catalysts or enhancing the performance of current ones to improve the efficiency of CO_2RR while making it more environmentally sustainable.

High entropy alloy (HEA) catalysts is the mostly interesting material catalyst, which define as multi-metal elements composed of more metal species as configurational entropy of mixing (S_{mix}) greater than or equal to to1.36R for quaternary alloy and S_{mix} greater than or equal to 1.5R for 5 or more than element[6]. These materials have collected significant interest for development and application in various reactions, making them one of the most promising candidates for catalysis[6]. The unique and distinctive structure of HEAs contributes to their exceptional properties, including high activity and selectivity in reactions of relevance, such as hydrogen evolution reaction[7], oxygen reduction reaction[8], and many others[9]. Therefore, HEAs have been a challenging material for CO_2RR. However, the crucial step in CO_2RR is the adsorption of CO_2 on the surface of the electrocatalyst, as it marks the initial stage in the production process. Additionally, the CO_2 molecule is highly inert and stable, making it difficult to bind to the catalyst surface and requiring significant energy input to initiate a spontaneous reaction. The density functional theory (DFT) is widely used in computational chemistry and materials science to investigate the selectivity and efficiency of catalysts by analyzing adsorption energies. However, studying all active sites in HEA catalysts for CO_2 adsorption requires significant computational time and resources due to the vast number of possibilities. Rittiruam et al.[10] investigated an active site model to represent the active site and its neighboring elements on a minimized model for HEA catalysts. The results showed that the active site model successfully represented the active sites on the HEA surface based on the special quasi-random structure (SQS). Additionally, the adsorption energy and electronic properties were found to be consistent with those of the HEA surface derived from SQS. Machine learning (ML) is a method that reduces both computational time and resource requirements, while also achieving high prediction accuracy. It can utilize a small amount of training data to build models that accurately predict the remaining data.

In This study present the CO_2 adsorption energy of all possible active site in Cu-based HEA catalyst via active site model and combined the DFT calculation and supervised ML model from from Scikit-

learn package[11]. By combining DFT calculations with machine learning techniques, it is possible to greatly decrease computational time and resource requirements. Furthermore, this innovative methodology shows significant potential for enhancing industrial catalysis, specifically in the field of environmental and energy-focused applications.

2. Methodology
2.1 Computational detail and density functional theory calculations

Density functional theory (DFT) calculations were performed using the Vienna Ab-initio Simulation Package (VASP). The pseudopotential was based on the generalized gradient approximation (GGA) with the Perdew-Burke-Ernzerhof (PBE) exchange-correlation functional. A cutoff energy of 500 eV was applied for all DFT calculations, with an energy convergence criterion of 1×10^{-6} eV for geometry optimization to ensure accurate total energy calculations. For vibrational frequency calculations, energy convergence of 1×10^{-8} eV was used to enhance accuracy. The k-point sampling was determined using the Monkhorst-Pack method: $3\times3\times1$ for surfaces, $11\times11\times11$ for bulk systems, and $1\times1\times1$ for isolated molecules. The force tolerance was set at 0.03 eV/Å. Van der Waals interactions were incorporated using the DFT-D3 dispersion correction method[12, 13], and spin polarization was included to improve the adsorption structure. The adsorption energy (E_{ads}) was calculated according to equation (1).

$$E_{ads} = E_{system} - E_{slab} - E_{molecule} \tag{1}$$

Where E_{system} is total energy of adsorption structure, E_{slab} is the total energy of clean surface and $E_{molecule}$ is total energy of isolated molecules. CO_2 molecules can be calculated as the total energy of isolated molecule used by $15\times15\times15$ Å^3 vacuum box.

2.2 Active site model

In general, CO_2 molecules preferentially adsorb at bridge sites in CO_2RR method[14]. Figure 1 illustrates a bridge active site model, divided into three regions based on the host element. The active site model is constructed from a Cu surface with a face-centered cubic (FCC) structure, oriented along the (111) plane, and uses a $4\times4\times1$ supercell dimension. This work uses Cu as the host element because it is a common catalyst and active in CO_2RR[15-17]. The 1st region represents the active site, consisting of two atoms configured. The 2nd and 3rd region were configured two and one atoms, respectively. For geometry optimization, ISIF = 4 was initially used to relax all atoms within the simulation box and the box also optimized. This was followed by ISIF = 2, where the two bottom layers were fixed, while the remaining layers were allowed to relax. The number of bridge active site in HEA catalyst can be calculated follow by equation 2

$$P_{active-site\ models} = \frac{(r_1+n-1)!}{r_1!(n-1)!} \times \frac{(r_2+n-1)!}{r_2!(n-1)!} \times \frac{(r_3+n-1)!}{r_3!(n-1)!} \tag{2}$$

Where r_1, r_2, and r_3 represent the total number of atomic sites on first, second, and third region respectively, n is the number of elements for HEAs surface. Therefore, all possible active site models of bridge can be calculated follow in equation 3

$$P_{bridge} = \frac{(2+4-1)!}{2!(4-1)!} \times \frac{(2+4-1)!}{2!(4-1)!} \times \frac{(1+4-1)!}{1!(4-1)!} = 400 \tag{3}$$

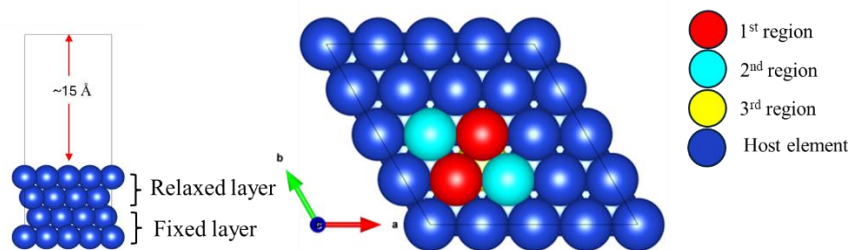**Figure 1** The active site model of bridge site on FCC (111) surface.

2.3 machine learning procedure

Supervised ML, a key branch of ML, uses labeled input data to train a model by identifying relationships between input and output data. This trained model is then used to make predictions or inferences on new, unknown datasets. In this study, the input dataset features are constructed based on

the number of metal atomic configurations in each region, while the output is the CO2 adsorption energy on the active site model. The example data set as shown in table 1. The training dataset consists of 40 data points, with an additional 10 data points used for validating the ML model. The performance of the ML model is typically evaluated using a loss function, which quantifies the difference between the predicted outputs of the algorithm and the actual target values. This helps to measure the accuracy and effectiveness of the model in making predictions. The root mean square error (RMSE) as the loss function was studied, that calculated using the following equations (4)

$$RMSE = \sqrt{\frac{1}{n}\sum_{i=1}^{n}(y_i - y_i')^2} \qquad (4)$$

Where y is actual value, and y' is a predicted value.

Table 1 Example of input feature for CO_2 adsorption on Cu-based HEA catalyst.

1st Region				2nd Region				3rd Region				E_{ads}
M1_1	M2_1	M3_1	M4_1	M1_2	M2_2	M3_2	M4_2	M1_3	M2_3	M3_3	M4_3	
0	2	0	0	1	0	1	0	0	0	0	1	-0.24
0	2	0	0	0	2	0	0	0	0	1	0	-0.28
0	1	0	1	0	2	0	0	1	0	0	0	-0.25
0	1	0	1	1	0	0	1	1	0	0	0	-0.20
1	0	1	0	1	1	0	0	0	1	0	0	-0.17
1	0	1	0	0	0	0	2	0	0	1	0	-0.12

3. Results and Discussion
3.1 Feature correlation

The Pearson correlation coefficient is a commonly employed metric for examining correlations between input and output data, offering significant insights prior to the development of machine learning models. Figure 2 illustrates a heatmap of Pearson correlations, displaying the relationships between various elements. Additionally, it highlights the correlations between CO_2 E_{ads} and the elements within each region. The correlation of all elements in the first section is uniformly -0.33, indicating an important feature as it illustrates the configuration of the active site model. Moreover, the relationship between E_{ads} and M1, M2 in the first region (M1_1, M2_1) and M2 in the second region (M2_2) shows values of -0.16, -0.53, and -0.53, respectively. This suggests a trend toward more negative CO_2 E_{ads} values, indicating strong adsorption. In contrast, M3_1, M4_1, M1_2, M3_2, M1_3, and M3_3 exhibit positive values, leading to more positive E_{ads} values, which indicate weaker adsorption.
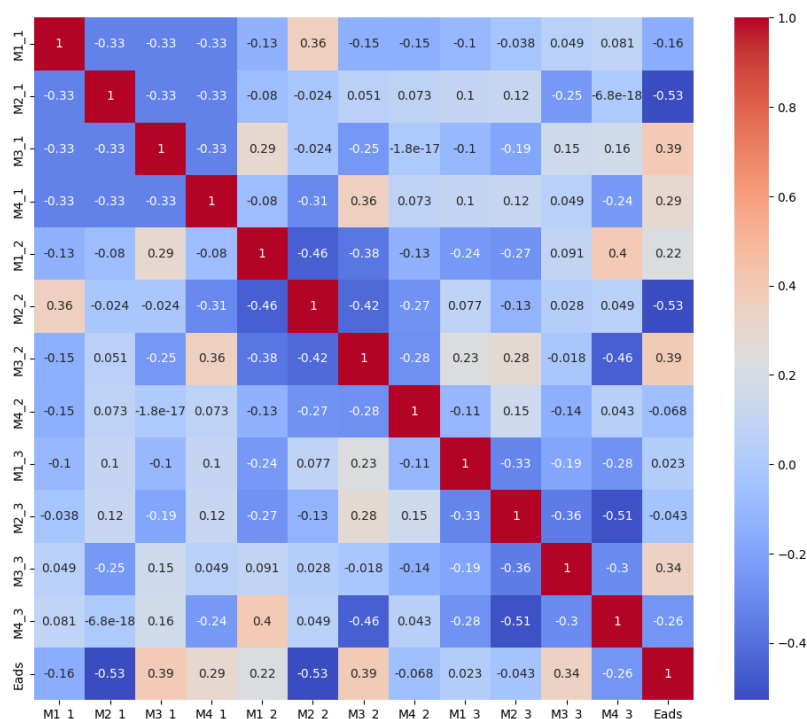
Figure 2 Pearson correlations heatmap between input-input and input-output data

3.2 Performance ML model

The linear regression ML model is a simple supervised learning method. A regression plot of CO_2 E_{ads} values calculated by DFT versus those predicted by the ML model is shown in Figure 3, demonstrating the relationship between actual and predicted values. The plot reveals the high accuracy of the ML model, as most data points lie close to the line where predicted values equal calculated ones. The RMSE values for the training, testing, validation, and overall datasets are 0.0311, 0.0216, 0.1930, and 0.0294 eV, respectively. Smaller RMSE values indicate a closer match between actual and predicted values, signifying the high performance and efficiency of the ML model. Table 2 compares the CO_2 adsorption energy values obtained from DFT calculations and ML predictions. The adsorption energies from both methods are very similar, with only minor differences, further demonstrating the reliability of the ML model. Moreover, the CO_2 adsorption energy distribution data of only DFT method and DFT combined ML method express in Figure 4. The result can be exhibited same trend, that indicated ML model has a high efficiency to unknown data but not alters the pattern of data distribution.
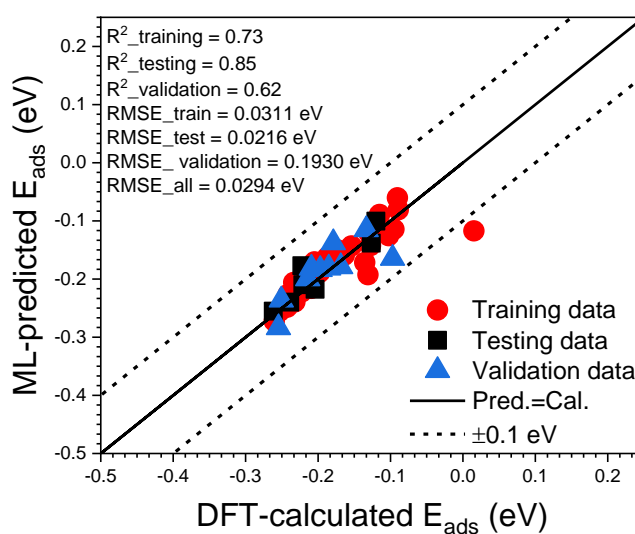

Figure 3 The regression plot between DFT calculation and ML prediction in linear regression ML model for E_{ads} of CO_2.

Table 2 Comparison CO_2 adsorption energy from DFT calculations and ML prediction.

Feature	Adsorption energy (eV)		
	DFT	ML	error
0, 2, 0, 0, 1, 1, 0, 0, 0, 0, 1, 0	-0.25	-0.24	-0.01
1, 1, 0, 0, 0, 0, 0, 2, 0, 0, 1, 0	-0.20	-0.18	-0.02
0, 1, 1, 0, 1, 0, 1, 0, 1, 0, 0, 0	-0.18	-0.14	-0.04
0, 1, 0, 1, 0, 2, 0, 0, 0, 0, 0, 1	-0.25	-0.28	0.03
2, 0, 0, 0, 0, 0, 0, 2, 0, 1, 0, 0	-0.19	-0.18	0.01
1, 0, 1, 0, 1, 1, 0, 0, 0, 0, 0, 1	-0.21	-0.18	-0.03
1, 0, 0, 1, 1, 1, 0, 0, 0, 1, 0, 0	-0.21	-0.20	-0.01
0, 0, 2, 0, 0, 2, 0, 0, 1, 0, 0, 0	-0.10	-0.16	0.06
0, 0, 1, 1, 2, 0, 0, 0, 1, 0, 0, 0	-0.13	-0.12	-0.02
0, 0, 0, 2, 0, 1, 0, 1, 0, 0, 1, 0	-0.17	-0.18	0.01
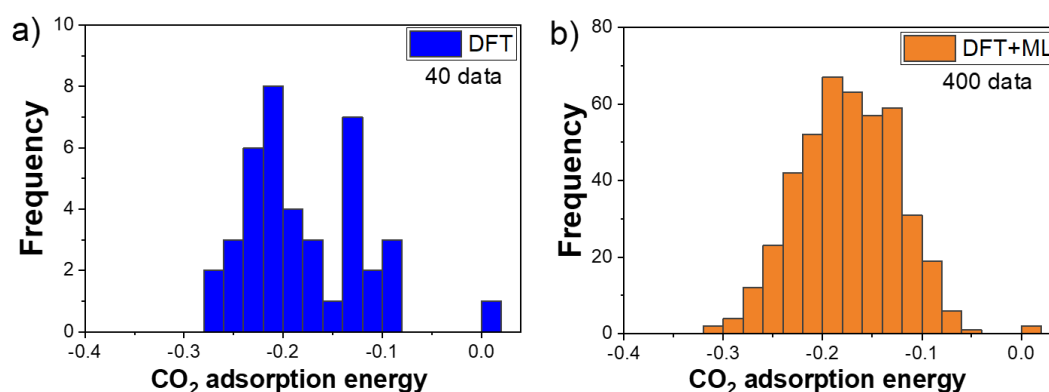
Figure 4 The CO_2 adsorption energy distribution from a) DFT calculation and b) DFT+ML method via 0.2 for bin size

4. Conclusion

The integration of DFT and ML has demonstrated a highly efficient and accurate approach for predicting CO_2 adsorption energy on Cu-based HEA catalysts. The ML model significantly reduces computational time and resources, while maintaining high accuracy when compared to traditional DFT calculations. This hybrid methodology not only provides precise predictions but also exhibits great potential for industrial applications, particularly in environmental and energy sectors where CO_2 reduction is critical. The results highlight the effectiveness of using ML to explore the vast number of possible active sites in HEA catalysts, thereby accelerating the discovery and optimization of efficient catalysts for CO_2RR. Moreover, this study sets a foundation for further exploration into the use of advanced computational techniques in catalysis research, potentially enabling more sustainable and cost-effective solutions for tackling global environmental challenges such as carbon emissions. Future work could involve expanding this framework to other catalytic materials and reactions, further enhancing the environmental and industrial impact of this research.

References

1. Ritchie, H. and P. Rosado, *Fossil fuels.* Our World in Data.
2. Hannah Ritchie, P.R., and Max Roser, *CO_2 and Greenhouse Gas Emissions.* Our World in Data, 2023.
3. Garg, S., et al., *Advances and challenges in electrochemical CO2 reduction processes: an engineering and design perspective looking beyond new catalyst materials.* Journal of Materials Chemistry A, 2020. **8**(4): p. 1511-1544.
4. Hori, Y., et al., *Electrocatalytic process of CO selectivity in electrochemical reduction of CO2 at metal electrodes in aqueous media.* Electrochimica Acta, 1994. **39**(11): p. 1833-1839.
5. An, X., et al., *Common strategies for improving the performances of tin and bismuth-based catalysts in the electrocatalytic reduction of CO2 to formic acid/formate.* Renewable and Sustainable Energy Reviews, 2021. **143**: p. 110952.
6. Xin, Y., et al., *High-Entropy Alloys as a Platform for Catalysis: Progress, Challenges, and Opportunities.* ACS Catalysis, 2020. **10**(19): p. 11280-11306.
7. Wang, Q., et al., *Recent Progress in High-Entropy Alloy Electrocatalysts for Hydrogen Evolution Reaction.* Advanced Materials Interfaces, 2024. **11**(14): p. 2301020.
8. You, J., et al., *Research of high entropy alloys as electrocatalyst for oxygen evolution reaction.* Journal of Alloys and Compounds, 2022. **908**: p. 164669.
9. Huang, X., et al., *Noble-metal-based high-entropy-alloy nanoparticles for electrocatalysis.* Journal of Energy Chemistry, 2022. **68**: p. 721-751.
10. Rittiruam, M., et al., *First-Principles Active-Site Model Design for High-Entropy-Alloy Catalyst Screening: The Impact of Host Element Selection on Catalytic Properties.* Advanced Theory and Simulations, 2023. **6**(11): p. 2300327.
11. Fabian Pedregosa, G.V., Alexandre Gramfort, Vincent Michel, Bertrand Thirion, Olivier Grisel, Mathieu Blondel, Peter Prettenhofer, Ron Weiss, Vincent Dubourg, Jake Vanderplas, Alexandre Passos, David Cournapeau, Matthieu Brucher, Matthieu Perrot, Édouard Duchesnay, *Scikit-learn: Machine Learning in Python.* Journal of Machine Learning Research 2011. **2825-2830**.
12. Grimme, S., et al., *A consistent and accurate ab initio parametrization of density functional dispersion correction (DFT-D) for the 94 elements H-Pu.* The Journal of Chemical Physics, 2010. **132**(15).
13. Díaz, C., Y. Wang, and F. Martín, *Including London Dispersion Forces in Density Functional Theory (DFT + D): Applications to Molecule(Atom)/Surface Phenomena.* 2017.
14. Ou, L., et al., *Theoretical insight into effect of doping of transition metal M (M = Ni, Pd and Pt) on CO2 reduction pathways on Cu(111) and understanding of origin of electrocatalytic activity.* RSC Advances, 2017. **7**(20): p. 11938-11950.
15. Chang, Q., et al., *Electrochemical CO2 Reduction Reaction over Cu Nanoparticles with Tunable Activity and Selectivity Mediated by Functional Groups in Polymeric Binder.* JACS Au, 2022. **2**(1): p. 214-222.
16. Woldu, A.R., et al., *Electrochemical CO2 reduction (CO2RR) to multi-carbon products over copper-based catalysts.* Coordination Chemistry Reviews, 2022. **454**: p. 214340.
17. Tabassum, H., et al., *Surface engineering of Cu catalysts for electrochemical reduction of CO2 to value-added multi-carbon products.* Chem Catalysis, 2022. **2**(7): p. 1561-1593.

DENSITY FUNCTIONAL THEORY OF CO2 REDUCTION USING NICKLE-COMPLEX ELECTROCATALYSTS

**Wilasinee Santiwarodom[1], Pavee Apilardmongkol[1], Thanawit Kuamit[1]
and Vudhichai Parasuk[1]***
[1]Department of Chemistry, Faculty of Science, Chulalongkorn University, Pathumwan, Bangkok 10330 Thailand
*Corresponding address (Email: Vudhichai.P@chula.ac.th)

Introduction

Carbon dioxide (CO_2) is a significant greenhouse gas, and its emissions have surged over the past 150 years due to population growth. The burning of fossil fuels, industrial activities, and other human actions have substantially increased the amount of CO_2 released into the atmosphere. This rise in greenhouse gases, particularly CO_2, is a primary driver of global climate change. Researchers are actively seeking methods to reduce CO_2 emissions, with carbon capture and conversion being a prominent strategy. Due to the stability of CO_2, catalysts are essential for its conversion, typically requiring high temperatures and pressures, which can increase the carbon footprint. An alternative approach involves the electrochemical conversion of CO_2 using electrocatalysts. Recent studies have focused on the electrocatalytic conversion of CO_2 using metal complexes like cobalt and nickel. Nickel, in particular, is favored as an electrocatalyst because it is inexpensive, exhibits a variety of electronic states, and demonstrates high performance. Understanding the mechanism of CO_2 conversion by nickel-complex electrocatalysts is crucial for enhancing catalytic efficiency. In this study, we utilized density functional theory (DFT) calculations to investigate the mechanism of electrochemical CO_2 conversion into higher-value chemicals using nickel complexes. Our findings aim to contribute to the design of more effective electrocatalysts.

Methodology

The model was developed using GaussView and computed with Gaussian16. The mechanism of CO_2 conversion by the Ni-complex catalyst was investigated using the DFT method with the M06-2X functional. For the nickel atom, the LANL2DZ basis set and effective core potential were utilized, while the 6-31G(d,p) basis set was applied for all other atoms. The calculations were conducted in an aqueous solution.

Results and Discussion

A mechanism for the conversion of CO_2 to CO using nickel complex catalysts was proposed. There are two potential pathways for the hydrogenation of CO_2 to CO by the Ni complex: external and internal proton transfer, designated as pathway A and pathway B, respectively, as illustrated in Figure 1. Both pathways involve three steps: initial CO_2 absorption, subsequent proton transfer, and finally, CO formation.

Significance

The findings offer valuable insights for optimizing and designing catalytic systems to achieve greater efficiency in future research efforts.
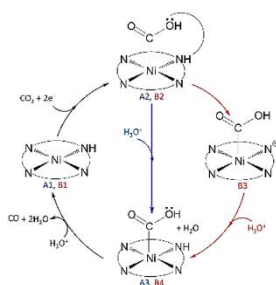
Figure 1. Reaction mechanism of external(A) and internal(B) proton transfer process.

References

[1]   B. Xiong, J. Liu, J. Ding, Y. Yang, Electrochemical conversion of CO_2 to syngas over Cu- M (M = Cd, Zn, Ni, Ag, and Pd) bimetal catalysts, Fuel 304 (2021) 121341.

[2]   Y. Li, S.H. Chan, Q. Sun, Heterogeneous catalytic conversion of CO_2: a comprehensive theoretical review, Nanoscale 7 (2015) 8663-8683.

[3]   M.Z. Iqbal, S. Imteyaz, C. Ghanty, S. Sarkar, A review on electrochemical conversion of CO_2 to CO: Ag-based electrocatalyst and cell configuration for industrial application, Journal of Industrial and Engineering Chemistry 113 (2022) 15-31.

[4]   R.-P. Ye, J. Ding, W. Gong, M.D. Argyle, Q. Zhong, Y. Wang, C.K. Russell, Z. Xu, A.G. Russell, Q. Li, M. Fan, Y.-G. Yao, CO_2 hydrogenation to high-value products via heterogeneous catalysis, Nature Communications 10 (2019) 5698.

[5]   F.-Y. Gao, R.-C. Bao, M.-R. Gao, S.-H. Yu, Electrochemical CO_2-to-CO conversion: electrocatalysts, electrolytes, and electrolyzers, Journal of Materials Chemistry A 8 (2020) 15458-15478.

[6]   M. Juthathan, T. Chantarojsiri, K. Chainok, T. Butburee, P. Thamyongkit, T. Tuntulani, P. Leeladee, Molecularly dispersed nickel complexes on N-doped graphene for electrochemical CO_2 reduction, Dalton Trans. 52 (2023) 11407-11418.

[7]   H. Kim, D. Shin, W. Yang, D.H. Won, H.-S. Oh, M.W. Chung, D. Jeong, S.H. Kim, K.H. Chae, J.Y. Ryu, J. Lee, S.J. Cho, J. Seo, H. Kim, C.H. Choi, Identification of single-atom Ni site active toward electrochemical CO_2 conversion to CO, Journal of the American Chemical Society 143 (2021) 925-933.

Investigation on enzyme-ligand interactions in PfATP4at multiple putative binding sites

Boonsita Sirison[1], Nontanat Yolsirivat[1], and Somsak Pianwanit[2]*
[1]*International School Bangkok (ISB), Nonthaburi 11120 Thailand* [2]*Department of Chemistry, Faculty of Science, Chulalongkorn University, Bangkok 10330 Thailand*
*somsak.t@chula.ac.th

Introduction

Malaria remains a severe public health problem in many countries around the world. One of the main reasons is the widespread of antimalarial drug resistance, especially on *Plasmodium falciparum*, which is responsible for the most virulent form of human malaria. Therefore, researchers are seeking for novel effective drug targeting at new enzyme. PfATP4 is one of the attractive enzyme targets. It is responsible for maintaining Na^+ homeostasis in parasites to make a suitable environment for the parasite living. Although there are some known promising antimalarial PfATP4 inhibitors [1], its mechanism of action is not yet fully understood. Thus, data on enzyme-ligand interactions is needed.

Methodology

As the structure of PfATP4 is experimentally not available, homology modeling technique using two different web servers, AlphaFold [2] and SWISS-MODEL [3], was employed to construct its structure. Moreover, its binding site is not yet known. The GRaSP program [4] was thus used to predict the binding sites. In addition, the G358 residue was also considered for the binding site as it was proposed to involve in the inhibitor binding [5]. For the inhibitors, 11 active compounds were obtained from the literature [6] and 9 inactive compounds were randomly selected from the database provided in the MMV website [7]. The MMV codes for these 20 compounds are given in Table 1. All molecular docking calculations were performed using AutoDock Vina with a box size of 30x30x30 $Å^3$ and an exhaustiveness of 32. Interaction data was analyzed using BIOVIA discovery studio visualizer.

Table 1. List of active and inactive compounds against PfATP4.

Active compounds			Inactive compounds		
MMV000858,	MMV001059,	MMV006239,	MMV004168,	MMV012074,	MMV024311,
MMV020081,	MMV020136,	MMV020391,	MMV045105,	MMV658993,	MMV676406,
MMV020520,	MMV020623,	MMV020710,	MMV688416, MMV688771, MMV1198433		
MMV085210, MMV688980					

Results and Discussion

Homology models constructed from AlphaFold (AF) and SWISS-MODEL (SM) are quite different as shown in Figure 1 (A). Therefore, it is necessary to investigate enzyme-ligand interaction using both models. The top 3 possible binding sites predicted from GRaSP and the G358 binding site were selected for AF and SM models as shown in Figure 1(B) and 1(C). Comparing the binding modes between the two models, the enzyme-ligand interactions are significantly different, which is clearly because of differences in their conformations. At each binding site of AF and SM models, active compounds bind with PfATP4 in a similar manner to inactive compounds with slight and insignificant differences. Ther are several applicable points for further improvement. For example, (i) including more properties to fully explain its biological activity, (ii) exploring more possible binding sites to find the real binding site, and (iii) performing molecular dynamics (MD) simulation to incorporate flexibility of enzyme.
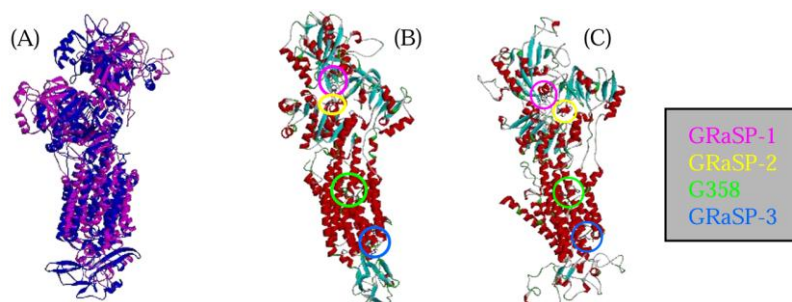
Figure 1. (A) Comparison between homology model from AlphaFold (blue color) and SWISS-MODEL (magenta color); Four putative binding sites in (B) AF model and (C) SM model.
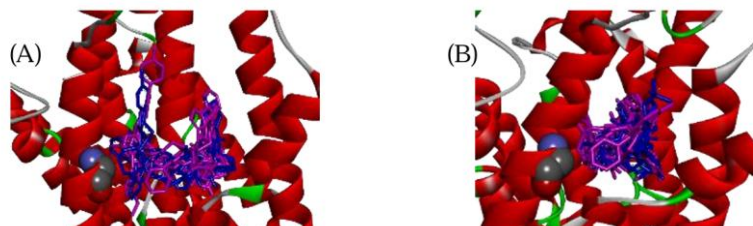

Figure 2. Comparison of binding modes between active (blue color) and inactive (magenta color) compounds at G358 binding site in (A) AF model and (B) SM model.

Significance

The binding modes of active compounds at each of the 4 putative binding sites are not clearly distinguishable from those of the inactive compounds. However, homology model constructed from AlphaFold and SWISS-MODEL yield different binding modes.

References

1. Looker, O., Dans, M.G., Bullen, H.E., Sleebs, B.E., Crabb, B.S., and Gilson, P.R. *Traffic* 23, 442 (2022).
2. AlphaFold Protein Structure Database, https://alphafold.ebi.ac.uk/
3. SWISS-MODEL web server, https://swissmodel.expasy.org/
4. Santana, C.A., Izidoro, S.C., de Melo-Minardi, R.C., Tyzack, J.D., Ribeiro, A.J.M., Pires, D.E.V., Thornton, J.M., and Silveira, S.A. *Nucleic Acids Res.* 50, W392 (2022).
5. Qiu, D., et al. *Nature Communications* 13, 5746 (2022).
6. Dennis, A.S.M., Rosling, J.E.O., Lehane, A.M., and Kirk, K. *Sci. Rep.* 8, 8795 (2018).
Medicines for Malaria Venture (MMV), https://www.mmv.org/

Theoretical Design of Novel Nickel Catalysts for Ethylene Polymerization

Pavee Apilardmongkol[1], Manussada Ratanasak[2,3], Jun-ya Hasegawa[2],
Tatiya Chokbunpiam[4]*, and Vudhichai Parasuk[1]*,
[1]Center of Excellence in Computational Chemistry, Department of Chemistry,
Faculty of Science, Chulalongkorn University, Bangkok 10330 (Thailand)
[2]Institute for Catalysis, Hokkaido University, Hokkaido 001-0021 (Japan)
[3]Center for Computational Sciences, University of Tsukuba, Ibaraki 305-8577 (Japan)
[4]Department of Chemistry, Faculty of Science, Ramkhamhaeng University,
Bangkok 10240 (Thailand)

*vudhichai.p@chula.ac.th and tatiya@ru.ac.th

Introduction

The α-diimine nickel catalysts are capable of polymerizing conjugated monomers through catalyst-transfer polymerization and are well-known for catalyzing olefin polymerization via the coordination-insertion mechanism [1]. The Brookhart group [2] made significant contributions by introducing a series of α-diimine nickel/palladium complexes capable of catalyzing ethylene (ET) polymerization, resulting in high molecular weight polyethylene. This breakthrough paved the way for late transition metal catalysts to become significant contributors to ethylene polymerization processes. In this work, we studied the reaction mechanism of ET polymerization catalyzed by α-diimine nickel complexes using DFT calculations. We constructed α-diimine nickel catalysts based on X-ray data obtained from experimental reports [3]. Then, we explored the reaction mechanism of α-diimine catalyzed ET polymerization by analyzing the relative Gibbs free energy profile, considering both the structural and electronic characteristics at the rate-determining step the reaction. Moreover, we calculated the coordination free energy (G_c), activation free energy ($\Delta G^{\ddagger}$), and reaction free energy (ΔG_r) to assess binding ability and reaction process. We then performed Gibbs free energy profiles for ET polymerization catalyzed by M-α-diimine with the different metal (M) substitutions (M = Mn, Fe, Co, Ni, Cu, Zn, Ru, Rh, Pd, Ag, and Cd). Finally, The calculated energies were used for comparison with the parent Ni-α-diimine complex.

Methodology

All the calculations were carried out using the Gaussian16 software. DFT calculations were performed by using the ωB97XD functional with 6-31G(d) basis set for non-metal atoms and with the Stuttgart/Dresden (SDD) effective core potential for transition metals. The Gibbs free energies were used to elucidate the reaction energy profile. All the optimized local energy minimum structures and transition state structures were confirmed by zero and one imaginary frequency, respectively. The processes from reactant π-complex–TS–product were verified by intrinsic reaction coordinate (IRC) calculations. The structures were calculated under gas phase condition. We assessed the solvent effect with the implicit SMD solvation model using toluene as a solvent.

Results and Discussion

The reaction mechanism of Ni-α-diimine catalysts for ethylene (ET) polymerization were investigated using DFT calculations. The relative Gibbs free energies profile for ET polymerization catalyzed by Ni-α-diimine were elucidated as shown in Figure 1. Our results indicated that the interactions between the Ni-α-diimine complex and ET monomer were strongest during the first ET insertion, which is related to the rate-determining step of this reaction. Then, the relative Gibbs free energy profiles of the different transition metals (M= Mn, Fe, Co, Ni, Cu, Zn Ru, Rh, Pd, Ag, and Cd) were employed for comparison with parent Ni-α-diimine. Among these transition metals, utilizing M = Pd, Rh, Mn, and Ru appears to be a promising choice for catalysts in ET polymerization.
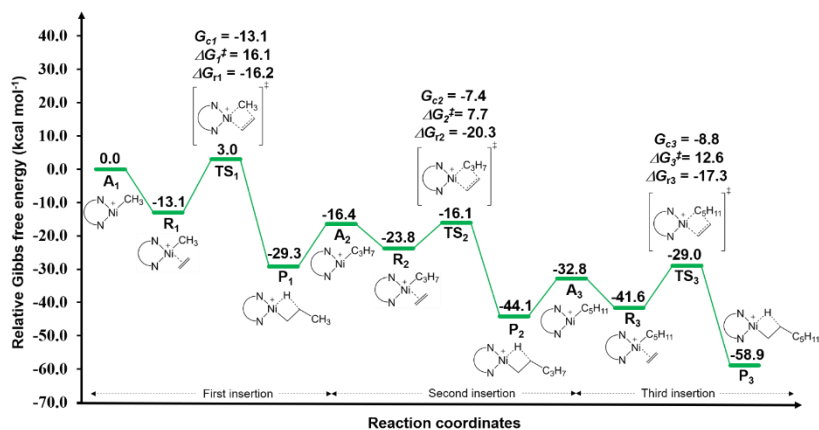
Figure 1. The relative Gibbs free energies profile for ET polymerization catalyzed by Ni-α-diimine.

Significance

The mechanism for ethylene polymerization catalyzed by Ni-α-diimine was investigated by DFT calculations. The activation free energies and coordination free energies were elucidated for different metal substitutions. Utilizing M = Pd, Rh, Mn, and Ru appears to be a promising choice.

References

1. M. D. Leatherman, S. A. Svejda, L. K. Johnson, M. Brookhart, *J. Am. Chem. Soc.* **2003**, *125*, 3068-3081.
2. L. K. Johnson, C. M. Killian, M. Brookhart, *J. Am. Chem. Soc.* **1995**, *117*, 6414-6415.
3. D. Liao, S. Behzadi, C. Hong, C. Zou, M. Qasim, M. Chen, *Appl. Organomet. Chem.* **2021**, *35*, e6406

Aldol condensation of acetone and furfural on H-Beta zeolite: An ONIOM study

Bundet Boekfa[1]*, Thana Maihom[1], Rungtiwa Chidthong[2], Sasiwadee Boonya-udtayan[1], and Piti Treesukol[1]

[1]Division of Chemistry, Department of Physical and Material Sciences, Faculty of Liberal Arts and Science, Kasetsart University, Kamphaeng Saen Campus, Nakhon Pathom, 73140, Thailand
[2]Chemistry Program, Faculty of Science and Technology, Nakhon Pathom Rajabhat University, Nakhon Pathom 73000, Thailand
*bundet.b@ku.ac.th

Introduction

Aldol condensation is an important chemical reaction in transforming biomass into valuable chemicals. Several researchers have investigated various catalysts, including bases and zeolites, to facilitate the formation of carbon-carbon bonds. The use of zeolites as catalysts can improve the efficiency and selectivity of the process, making it more economically feasible. Beta and Faujasite zeolites are effective catalysts for the aldol condensation of furfural and acetone, exhibiting high conversion rates even at low temperatures.

In the study, the aldol condensation reaction of acetone and furfural over H-Beta zeolite was investigated using the ONIOM(MP2:M06-2X) approach. The reaction mechanism was found to consist of three steps: tautomerization, aldol condensation, and dehydration. The study aimed to provide a better understanding of the reaction mechanism for the conversion of biomass over heterogeneous catalysts, specifically H-Beta zeolite. The results from this study can be useful for the design and optimization of catalytic systems for converting ketones into valuable chemicals.

Methodology

The aldol condensation reaction of acetone and furfural over H-Beta zeolite was studied using the ONIOM approach. For the inner layer, the 5T (T representing tetrahedral Si and Al atoms), representing the Brønsted active site of the zeolite, was optimized with the MP2 method. To account for the confinement effect from the framework, the 34T quantum cluster was expanded and analyzed using DFT, specifically the M06-2X functional. The 34T quantum cluster of H-Beta zeolite had previously been studied for adsorption and condensation reactions. The basis set used was the 6-31G(d,p) level of theory. Only the active site and probe molecules were allowed to relax, while the rest were kept fixed according to crystallographic data. All calculations were performed using the Gaussian 09 program.

Results and Discussion

The aldol condensation of acetone and furfural over H-Beta zeolite was investigated using the ONIOM (MP2:M06-2X) approach. The adsorption energy of acetone on H-Beta zeolite was found to be -25.2 kcal/mol as shown in figure 1. The first step of the reaction involves the tautomerization reaction of acetone, which occurs over the H-Beta zeolite through double proton transfer. This step yields the enol product of acetone, with the Brønsted hydrogen atom transferring to the carbonyl group, while the hydrogen atom of the methyl group transfers back to the zeolite. The second step of the reaction involves the aldol condensation of the enol and furfural, resulting in the formation of a C-C bond. Finally, the last step of the reaction is dehydration to be a furfuryl acetone product. The activation energies for these steps are 22.6, 6.1, and 32.7 kcal/mol, respectively. The reaction of acetone to diacetone is also studied. The energy pathways are presented in Figure 2.

Significance

We studied the aldol condensation reaction of biomass conversion within the H-Beta zeolite with ONIOM(MP2:M06-2X) approach.
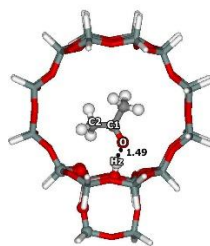
Figure 1. The adsorption of acetone on H-Beta zeolite optimized with ONIOM(MP2:M06-2X) approach. The model is a 5T:34T quantum cluster. Distance is in A.
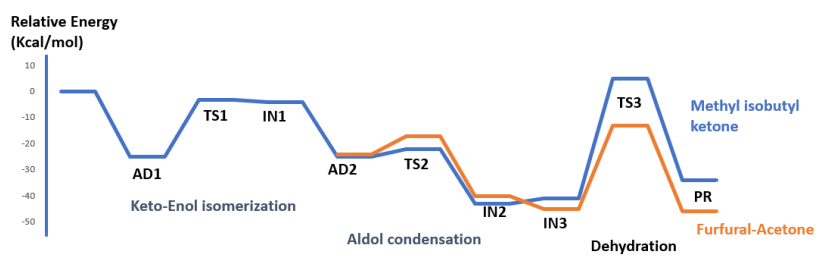
Figure 2. Reaction pathway for the aldol condensation of acetone and furfural on H-Beta zeolite calculated with ONIOM(MP2:M06-2X) approach

References

1. Maeboonruan, N, Boekfa, B., Maihom, T., Treesukol, P., Kongpatpanich, K., Namuangruk, S., Probst, M., and Limtrakul J. *J Mol. Model.* 27, 254 (2021).
2. Boekfa, B, Pantu, P., Probst, M., and Limtrakul. J., *J. Phys. Chem. C*, 114,15061-15067 (2010).

Theory-based design principles for two-level CO_2 utilization in CO_2-derived metal-organic frameworks

Poobodin Mano [1] and Supawadee Namuangruk[1]*
[1]National Nanotechnology Center (NANOTEC), National Science and Technology Development Agency (NSTDA), Pathum Thani, 12120 (Thailand)
*supawadee@nanotec.or.th

Introduction

As awareness of carbon capture, utilization, and storage (CCUS) increased, the development targeted for CO_2 capture and CO_2 conversion has been intensively focused. To make use of CO_2, the synthesis of organic functional polymer materials, for example, polycarbonates and polyesters, from CO_2 as raw material were actively reported. However, the synthesis of metal organic frameworks (MOFs) directly from CO_2 is still limited to the work by Horike and co-workers only [1]. The importance of MOFs is ascribed to its high capability as CO_2 adsorbent. If one could synthesize such MOFs with high *CO_2 content* embedded in structures as well as with high performance toward *CO_2 adsorption capacity*, the degree of CO_2 utilization in total can be maximized in two level. In this study, we proposed new design principles for constructing MOFs together with the concept "two-level" CO_2 utilization for MOFs. The theoretical design was conducted to surpass the limitation of an experiment to find the high-performance MOFs. We delivered not only the new 1,511 MOFs but also the theoretical insight for CO_2 derived MOFs synthesis [2].

Methodology

The theoretical design of MOFs was conducted as follows. We started from the construction of MOFs from existed metal nodes (15 nodes), the existed and hypothetical topology (40 topologies) and new-designed CO_2-derived ligands (14 carbamate ligands). The assembly was done using ToBaCCo package. The structural optimizations were done in classical force field level using LAMMPS package. The physical properties were obtained from Zeo++ software. To estimate the CO_2 adsorption capacity, the grand canonical Monte Carlo (GCMC) simulations were applied using RASPA package with charge equilibrium method. To validate the simulation conditions, the adsorption isotherm of well-established MOF-5 was simulated and confirmed a well agreement with the experimental reports. *CO_2 content* is defined as the content of CO_2 in the host framework in wt% unit, while the *CO_2 capacity* was defined as the CO_2 adsorption capacity at 1 bar using the value from GCMC simulations.

Results and Discussion

1,511 MOF structures were generated. Compared to the well-known carboxylate-type of ligands, carbamate-type shows a more flexible character. For the CO_2 content maximization, against the expectation from stoichiometry, those MOFs with high-coordinated nodes did not show a benefit due to the large steric repulsion and rigidity of the ligand orientation, while those low-coordinated MOFs show the higher values. The 4-coordinated $[V_2(CO_2)_4]$ node in combination with $[-CO_2NHNHCO_2-]$ ligand shows the highest performance with over 50 wt%. For the CO_2 capacity maximization, we found that the key to high performance is the zeolite-like structure in usf-topology, whose paddlewheel metal node fully exposed to the inner cavity, resulting in the efficient host-guest interaction and yield high capacity at low pressure. To further increase the adsorption capacity, we demonstrated that fluorination is one of the promising strategies to effectively enhance CO_2 capacity up to 20 wt% in our best candidate in usf-topology. The effectiveness is ascribed to the existence of both electrophilic and nucleophilic centers which act to both oxygen and carbon in CO_2 respectively.

All generated 1,511 MOFs were collected as database, providing the optimized structures, the theoretically predicted isotherm, and the fundamental physical properties. We believe that the design principles and this database will provide opportunities and challenges for experimentalists in synthesizing new MOFs with breakthrough CO2 utilization.

Significance

- Design principles for "two-level" CO_2 utilization were theoretically developed
- Over 1,500 carbamate type MOFs derived from CO_2 were theoretical proposed

- MOFs with the zeolite-like usf topology show large CO_2 content and CO_2 capacity
- Fluorination was found to be a promising strategy in enhancing CO_2 adsorption in usf-topology
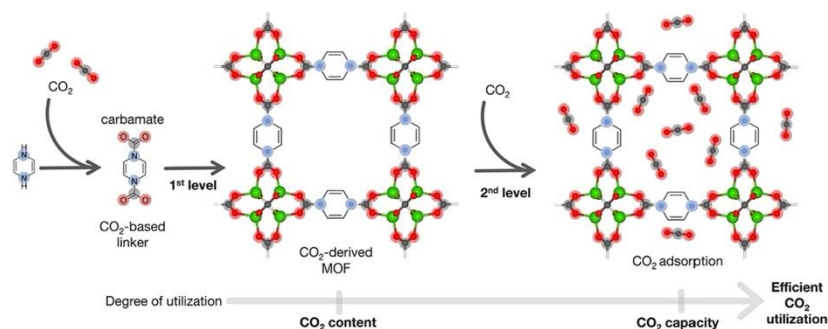
Figure 1. The concept of "*two-level*" CO_2 utilization: the synthesis of MOFs from CO_2 as raw material (benchmarked with CO_2 content) and the application of those MOFs in CO2 adsorption (benchmarked with CO_2 capacity)

References

1. Kadota, K., Hong, Y.L., Nishiyama, Y., Sivaniah, E., Packwood, D., Horike, S. J. Am. Chem. Soc., 143, 16750-16757 (2021)
2. Mano, P., Namuangruk, S. J. Chem. Eng. 486, 150248 (2024)

Theoretical Insight into Formic Acid Production from CO_2 through Hydrogenation on the Pt Cluster Decorated Carbon Nanocones

Yuwanda Injongkol[1,2], Siriporn Jungsuttiwong[3] and <u>Nuttapon Yodsin</u>[4,*]
[1]Futuristic Science Research Center, School of Science, Walailak University, Nakhon Si Thammarat 80160, Thailand
[2]Functional Materials and Nanotechnology Center of Excellence, Walailak University, Nakhon Si Thammarat, 80160, Thailand
[3]Department of Chemistry and Center of Excellence for Innovation in Chemistry, Ubon Ratchathani University, Ubon Ratchathani, 34190, Thailand
[4]Department of Chemistry, Faculty of Science, Silpakorn University, Nakorn Pathom 73000, Thailand
*yodsin_n@su.ac.th

Introduction

The process of converting CO_2 into formic acid through hydrogenation holds significance in environmental catalysis, offering a dual benefit of mitigating the greenhouse effect while yielding valuable chemicals. However, the exploration of platinum-based catalysts is imperative for advancing widespread adoption, given their costly and limited availability. In this study, we utilized density functional theory (DFT) calculations to investigate the reaction mechanism on defective carbon nanocones decorated with Pt_4 clusters (Pt4/dCNC) on the CO_2 hydrogenation process. Two reaction pathways were explored based on the reaction mechanism: one involving co-adsorption and the other involving H spillover combined with co-adsorption.

Methodology

All density functional theory (DFT) calculations were conducted using the Gaussian 16 program package. Geometry optimization and frequency calculations were performed for all complexes utilizing the B3LYP functional, which combines Becke's three-parameter gradient-corrected exchange potential with the Lee−Yang−Parr gradient-corrected correlation potential. In the DFT calculations, a basis set of 6-31G(d,p) was employed for all atoms, except for the Pt atom, for which the LANL2DZ basis set was utilized. The energies of all structures were adjusted through single-point calculations using the B3LYP functional, which incorporated Grimme's D3BJ dispersion correction (B3LYP-D3BJ) to account for dispersion interactions. The 6-311G(d,p) basis set was used for C, O, and H atoms, while the cc-pVTZ-PP basis set was employed for the Pt atom.

Results and Discussion

Our computational investigation focuses on CO_2 adsorption and hydrogenation to FA on Pt4/dCNC, employing density functional theory (DFT). The proposed reaction mechanisms for the CO_2 hydrogenation to FA suggest progression through co-adsorption pathways involving significant intermediates, such as carboxylate or formate, as shown in **Fig. 1**. The co-adsorption mechanism involved in the CO_2 hydrogenation process to produce formic acid on Pt4/dCNC begins with the adsorption of two hydrogen atoms (2H) at an active Pt4 site. Subsequently, a CO_2 molecule co-adsorbs on the surface, forming a co-adsorption complex. After that, the conversion to formic acid can proceed through either a formate pathway or a carboxylate pathway. Form the calculation, the reaction proceeded via co-adsorption mechanisms are thermodynamically and kinetically unfavorable. Therefore, we have suggested an alternative pathway based on our prior research for CO_2 hydrogenation to FA over Pt/dCNC, incorporating a hydrogen spillover mechanism. This proposed pathway follows the introductory reaction step outlined by Sirijaraensre and Limtrakul in 2016.[1] Our results suggest that the pathway combining H spillover with co-adsorption is favored over Pt4/dCNC, with the rate-determining step being the formation barrier of formate intermediate at 1.30 eV. Our study sheds light on the favorable reaction pathway for the hydrogenation of CO_2 to formic acid over Pt4/dCNC catalysts

Significance

We employed DFT calculations to examine the process of CO_2 adsorption and its subsequent hydrogenation reduction to formic acid (FA) using a Pt_4 cluster-doped defective carbon nanocone (Pt_4/dCNC) as the catalyst. In our findings, we have provided a comprehensive analysis of the geometry, electronic structure, and catalytic performance of Pt_4/dCNC materials. Furthermore, we have compared these results in detail with other carbon-based materials that have been previously reported. Our computational simulations reveal that the curvature of CNC plays a beneficial role in augmenting the population of active Pt_4/dCNC sites. The findings from this research significantly contribute to the understanding of the chemical and catalytic characteristics of metal-doped dCNC materials. These insights will facilitate the development of carbon-based catalysts with exceptional efficiency for the conversion of CO_2 into valuable chemical compounds. As a result, this study holds the potential to contribute to global environmental protection efforts by advancing our knowledge and strategies for sustainable CO_2 conversion, thus mitigating the impact of greenhouse gas emissions.
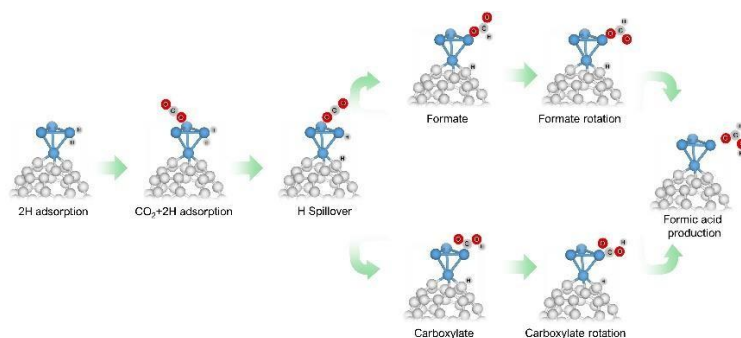

Figure 1. All possible reaction mechanism of CO_2 hydrogenation to formic acid on Pt_4/dCNC

References

1. Sirijaraensre, J. and Limtrakul, J. *Appl. Surf. Sci.* 364, 241 (2016).

Reaction Mechanism and Structure-Activity Relationships of Tertiary Amines in CO$_2$ Capture: A DFT Study

Chalakon Pornjariyawatch[1*], Krit Assawatwikrai[1], Pakanan Leepakorn[1] and Thana Maihom[2]

[1]*Kasetsart University Laboratory School, Kamphaeng Saen Campus, Educational Research and Development Center, Nakhon Pathom 73140, Thailand*
[2]*Department of Physical and Material Sciences, Faculty of Liberal Arts and Science, Kasetsart University, Kamphaeng Saen Campus, Nakhon Pathom 73140, Thailand.*
*chalakon.k@ku.th

Introduction

Nowadays, the utilization of amine-based solutions, especially primary and secondary amines has been widely recognized for their effectiveness in conventional carbon dioxide (CO$_2$) capture. Tertiary amines offer advantages over primary and secondary amines as they exclusively yield bicarbonates instead of carbamates. Nevertheless, a detailed understanding of the reaction mechanism and structural influences remains lacking at the molecular level.

In the present study, to gain insight into the reaction mechanism and structure-activity relationships of tertiary amines in CO$_2$ capture, we used density functional theory (DFT) calculations. We also used the Sure Independence Screening and Sparsifying Operator (SISSO) method [1] to develop informative descriptors to predict CO$_2$ loading, which enables quick screening of promising amines for this capture process.

Methodology

All calculations were performed using the M06-2X density functional as implemented in Gaussian 16 Revision B.01. The def2-SVP basis set was used to perform the geometric optimization. The single point calculations with the def2-QZVP basis set were carried out to obtain more accurate interaction energies. Solvation effects were modeled using the Polarizable Continuum Model (PCM) with water. The tertiary amines [2] employed in this study were depicted in Figure 1a.
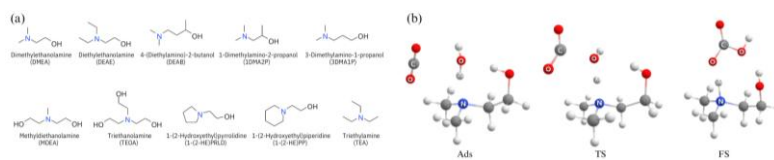
Figure 1. Tertiary amines employed in this study (a) and reaction mechanism for CO$_2$ capture by DMEA (b).

Results and Discussion

The reaction mechanism study, using DMEA as an example, is shown in Figure 1b. The reaction starts with the co-adsorption between CO$_2$ and H$_2$O on DMEA (Ads). In transition state (TS), the H of H$_2$O is shifted to the N of the amine, and the bond between the O of H$_2$O and the C of CO$_2$ is formed in a concerted manner. After the TS, the bicarbonate bound to the protonated amine through hydrogen bonds is formed (FS). The relative enthalpy for all amine cases are tabulated in Table 1. The results suggest that amines containing ethyl group and a single hydroxyl group substitutions, and also cyclic structures exhibit good activity for CO$_2$ capture.

Table 1. Relative enthalpy (ΔH) for CO_2 capture via the base-catalyzed hydration mechanism.

Amines	Relative enthalpy (kcal/mol)			
	Ads	**TS**	**FS**	**Ea**
DMEA	-7.0	3.7	-12.9	10.7
DEAE	-7.8	1.8	-14.4	9.5
DEAB	-4.2	5.1	-11.3	9.2
1DMA2P	-7.1	3.1	-13.9	10.2
3DMA1P	-2.9	6.2	-10.0	9.1
MDEA	-6.9	3.8	-11.5	10.7
TEOA	-6.4	6.0	-10.5	12.4
1-(2-HE)-PRLD	-7.5	1.7	-13.1	9.3
1-(2-HE)-PP	-7.9	1.4	-13.8	9.3
TEA	-5.7	4.0	-13.4	9.7

As shown in Figure 2a, we obtain a good correlation between Ea and CO_2 loading. Therefore, Ea can be used as a descriptor for predicting CO_2 loading. Moreover, the best performing SISSO descriptor used for predicting CO_2 loading is found to be $0.915 + 16.418 \, (1/(\Delta H_{FS\text{-}Ads})^3)*(Dipole)^{1/2}$ as shown in Figure 2b.
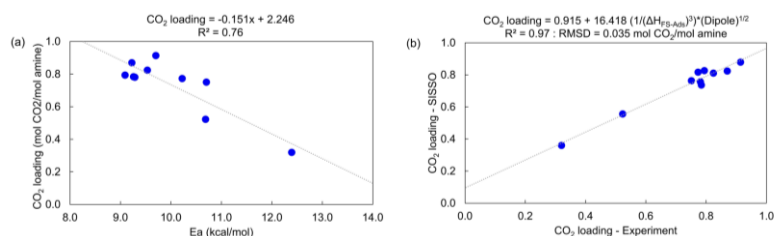
Figure 2. (a) Linear scaling relations between Ea and CO_2 loading and (b) comparison between CO_2 loading from experiment and the predicted CO_2 loading from SISSO.

Significance

Our research uncovers a key reaction mechanism and structure-activity relationships of tertiary amines in CO_2 capture. Additionally, we propose predictive descriptors for CO_2 loading, which support in the quick screening and design of active amines for CO_2 capture.

References

1. Ouyang R, Curtarolo S, Ahmetcik E, Scheffler M, Ghiringhelli LM. *Phys Rev Mater.* 083802 (2018).
2. Xiao M, Liu H, Idem R, Tontiwachwuthikul P, Liang Z. *Appl Energy* 219, 229 (2016).

The Influence of Curvature and External Electric Fields on Graphene Quantum Dots

Thanawit Kuamit[1] and Vudhichai Parasuk[1]*

[1] *Center of Excellence in Computational Chemistry, Department of Chemistry, Faculty of Science, Chulalongkorn University Phyathai Rd., Patumwan, Bangkok 10330, Thailand*
* Vudhichai.P@chula.ac.th

Introduction

Graphene, a two-dimensional monolayer consisting of a single atom thick layer of graphite [1], finds widespread applications, particularly in semiconductors like personal and notebook computers, among others.[2] Indeed, the direct bandgap of semiconductors largely dictates their applications, as it determines their electrical conductivity. The alteration of graphene through bending or curving alters its electronic properties, a topic that has recently garnered significant attention.[3] One method involves controlling the curvature of graphene quantum dots (GQDs) using an external electric field.[4] This study explores the deformation (curvature) and electronic properties of GQDs under vertical electric fields through DFT calculations. The findings could propose a new method for manipulating graphene's curvature, thereby modifying its electronic properties for semiconductor applications.

Methodology

Density functional theory (DFT) calculations utilizing the M06-2x functional and 6-31g(d) basis set were conducted to investigate the impact of external electric fields on three GQD structures: coronene ($C_{24}H_{12}$), circumcoronene ($C_{54}H_{18}$), and circumcircumcoronene ($C_{96}H_{24}$). External electric fields ranging from -0.035 to +0.035 atomic units perpendicular to the molecular plane were applied to these structures. All computations were carried out using the Gaussian 09 package.

Results and Discussion

Our analysis has demonstrated that strong external electric fields (EEFs) induce curvature or bending in GQD structures, as shown in **Figure 1A, B,** and **C**. Additionally, our findings unveil a clear relationship between electric field intensity, GQD size, and curvature, with the curvature effects following this order: $C_{96}H_{24} > C_{54}H_{18} > C_{24}H_{12}$. Furthermore, we observed that increasing the curvature of GQDs leads to a reduction in the HOMO-LUMO gap, indicating that external electric fields can indeed alter the electronic properties of graphene, as displayed in **Figure 1D**. The potential of external electric fields to modulate the electronic properties of GQDs could be advantageous in semiconductor applications.

Significance

• The degree of curvature in GQDs is contingent upon both their size and the intensity of the field.
• The HOMO-LUMO energy gap of GQDs is modified by EEF and relies on their curvature.
• EEF acts as a tool for modifying the electronic properties of graphene-based materials, thereby enhancing their suitability for semiconductor technology.
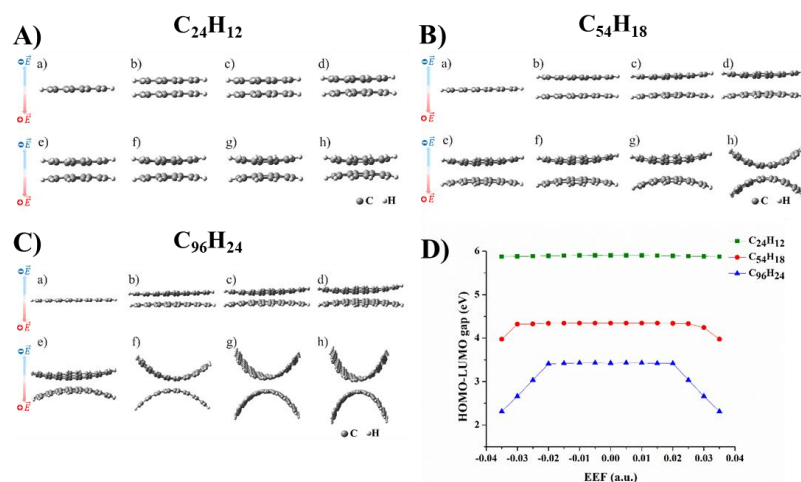
Figure 1. the optimized structures for $C_{24}H_{12}$ **(A)**, $C_{54}H_{18}$ **(B)**, and $C_{96}H_{24}$ **(C)** under various electric fields: a) = 0.0 a.u., b) = 0.005 a.u., c) = 0.0100 a.u., d) = 0.015 a.u., e) = 0.020 a.u., f) = 0.025 a.u., g) = 0.030 a.u., h) = 0.035 a.u., the relationship between different electric fields and the HOMO-LUMO gap energies of $C_{24}H_{12}$, $C_{54}H_{18}$, and $C_{96}H_{24}$ **(D)**.

References

1. K. S. Novoselov, A. K. Geim, S. V. Morozov, D. Jiang, Y. Zhang, S. V. Dubonos, I. V. Grigorieva, and A. A. Firsov, *Science* 306, 666 (2004).
2. P. Castro-Villarreal and R. Ruiz-Sánchez, *Phys. Rev. B* 95, 125432 (2017).
3. N. Pattarapongdilok and V. Parasuk, *Comput. Theor. Chem*. 1140, 86 (2018).
4. S. Tang, Y. Zhang, N. Xu, P. Zhao, R. Zhan, J. Chen and S. Deng, *Carbon* 144, 202 (2019)

Antioxidant activity prediction of diphenylamine derivatives usingQSAR-ML approaches

Ayokanmi Aremu[1], Ismail Dwi Putra[2], Borwornlak Toopradab[1],
Phornphimon Maitarad [1,4*], Thanyada Rungrotmongkol [1,3*]
[1]*Program in Bioinformatics and Computational Biology, Graduate School,*
Chulalongkorn University, Bangkok, 10330 Thailand
[2]*Pharmaceutical Sciences and Technology, Faculty of Pharmaceutical Sciences,*
Chulalongkorn University, Bangkok 10330, Thailand
[3]*Center of Excellence in Structural and Computational Biology, Department of Biochemistry, Faculty*
of Science, Chulalongkorn University Bangkok, 10330 Thailand
[4]*Research Center of Nano Science and Technology, College of Science,*
Shanghai University, PR, 200444 China
*Corresponding address (Thanyada.r@chula.ac.th, pmaitarad@shu.edu.cn +66-2218-5426)

Introduction

Diphenylamine (DPA) derivatives have a significant global impact, primarily due to their widespread use as antioxidants in crucial industrial applications such as engine oils and rubber-based products [1]. DPA derivatives behave as autoxidation inhibitors, which relate the hydrogen atom donating ability of the amino group to peroxyl radicals, yielding non-radical and aminyl radical products [2]. Despite the economic importance of DPA derivatives as antioxidants, there are reports of negative environmental impact of these compounds [3]. Therefore, this study aims to investigate the antioxidant and environmental activity of DPA derivatives.

Methodology

14 DPA derivatives were collected from relevant literature, including their environmental properties and $logK_{OW}$ values [4]. The structure of these compounds was optimized using Density Functional Theory (DFT) with the B3LYP/6-31G (d, p) basis set in Gaussian 09 program [5]. The structural molecular properties were extracted after optimization. These descriptors serve as the independent variables for the Quantitative Structure-Activity Relationship using machine learning (QSAR-ML). Kennard Stone Algorithm was used to divide the data into train set and test set, while the fitness of the models for the prediction of $logK_{OW}$ activity of DPA derivatives was measured by R-squared (R^2) and the root mean square error (RMSE). Important descriptors for the Gradient Boosting Regression (GBR) model were selected through permutation importance. New compounds will be designed based on the QSAR-ML model and the newly designed compounds will be analyzed using quantum chemical calculation.

Results and Discussion

This study developed predictive models for the $logK_{OW}$ of DPA derivatives to explore their antioxidant and environmental activities. The Random Forest (RF) model ($R^2 = 0.958$) as well as the GA-MLR model with linear spline ($R^2 = 0.998$) showed good fitness with high accuracy. However, $RMSE_{test}$ for the GBR model is likely lower (0.693) than other models. Hence, when applied to new, unseen data, the GBR model is expected to provide more accurate predictions of $logK_{OW}$ for DPA derivatives. The key descriptors identified from the GBR model are electron N, electron C_2 and molecular weight, providing valuable insights into the molecular properties influencing $logK_{OW}$.

Significance

- Exploring the relationship between $logK_{OW}$, antioxidant activity and environmental behavior of DPA derivatives can provide valuable insights into the design and assessment of new compound with desired antioxidant activity while minimizing environmental risks.
- The research outcomes hold the potential to influence market dynamics, guiding industries in adapting to regulatory changes, optimizing production, and minimizing economic risks associated with environmental contamination.
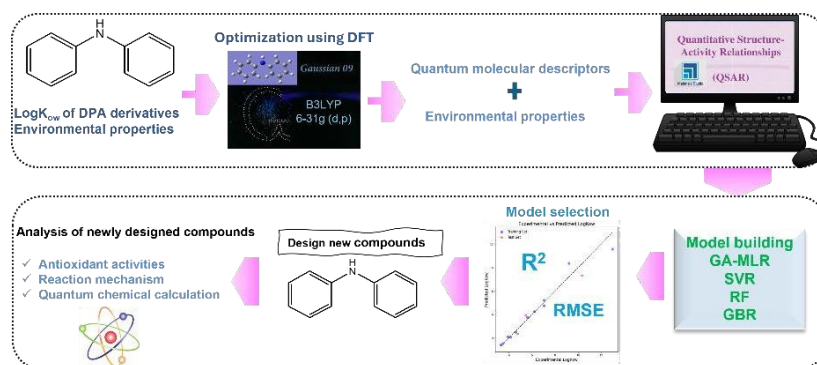
Figure 1. An overview of QSAR-ML approaches applied in this study.

Keywords: Antioxidant**,** DPA derivatives, QSAR-ML, Support Vector Regression, Random Forest, Gradient Boosting Regression.

References
1. Zhang, Z., *et al., Wat. Res*. 189, 116-602 (2021).
2. Jin *et al*., *Chem*. 317 137-913, (2023).
3. Lu, Z*., et al., Sci. Total Environ*. 647, 182–190 (2019).
4. Zhang, Z., *et al., Environ. Sci. Technol. Lett*. 7, 102–110 (2020).
5. Pham, P. T. T., *et al., Viet. J. Chem.,* 58(6), 742-751, (2020).

First-Principles Calculations of Sn-Based Double Perovskite Solar Cell Materials Analysis of Defect Structure

Mai Otake[1], Suzune Omori[1], Masanori Kaneko[2], Giacomo Giorgi[3], Koichi Yamashita[2] and Azusa Muraoka[1]*

[1] Japan Women's University, 2-8-1, Mejirodai, Bunko-ku, Tokyo (Japan)
[2] Yokohama City University, 22-2, Seto, Kanazawa-ku, Yokohama city, Kanagawa (Japan)
[3] The University of Perugia, Piazza dell'Università, 1, 06123 Perugia PG (Italy)
* muraokaa@fc.jwu.ac.jp

Introduction

Perovskite solar cells which use perovskite crystals in the light-absorbing layer, are expected to become the next-generation solar cells because they have achieved high photoelectric conversion efficiency comparable to that of silicon-based solar cells. Currently, among perovskite solar cells, lead halide perovskite has achieved the highest photoelectric conversion efficiency [1], but the toxicity of lead has become a problem from the viewpoint of practical use, and lead-free solar cells are required. Therefore, Sn-based perovskite solar cells are attracting attention as a lead-free perovskite because of their high stability and resistance to heat and light [1]. However, Sn-based perovskite solar cells suffer from low photoelectric conversion efficiency. One of the main reasons for this is "defects". The presence of defects in the crystal causes the appearance of deep levels in the band gap (defect levels), which trap carriers and induce carrier recombination, leading to low photoelectric conversion efficiency [2]. In this study, we analyze the defect structures of FA_2SnGeI_6 and MA_2SnGeI_6, double perovskites doped with germanium, which are promising lead-free materials after tin, to find clues for improving energy conversion efficiency [3].

Methodology

In FA_2SnGeI_6 and MAS_2SnGeI_6, we focused on a series of point defects [4], namely atomic vacancies, self-interstitial atoms, and anti-site defects, and considered the defect levels that are formed (Figure 1 (a)). First-principles calculations were performed using the DFT calculation package VASP (Vienna ab initio package) under the condition that the cutoff energy of the plane- wave expansion is 520 eV. DFT calculations were performed using the PBE (Perdew-Burke- Ernzerhof) exchange-correlation functional along with Grimme's D3 dispersion correction [5]. Defect structures for FA_2SnGeI_6 and MA_2SnGeI_6 were created using 2×2×2 supercells containing 8 stoichiometric units. The point-defect calculations were conducted using Pydefect, a robust and open-source Python library [6].

Results and Discussion

We carried on structural optimization of FA_2SnGeI_6 and MA_2SnGeI_6 in primitive cell. The space groups of FA_2SnGeI_6 and MA_2SnGeI_6 are Pmm2 and P1. The band gaps of FA_2SnGeI_6 and MASnI3 are 0.57 eV and 0.89 eV, respectively, confirming a direct transition band gap in both cases. In the chemical potential phase diagram, a situation where the chemical potential of tin is small and the chemical potential of iodine is large is called "Sn-poor, I-rich" and a situation where the chemical potential of tin is large and the chemical potential of iodine is small is called "Sn-rich, I-poor. In FA_2SnGeI_6, germanium vacancy V_{Ge} (2-/1-), tin vacancy V_{Sn} (2-/0), and anti- site defect I_{Sn} (1-/0) (Figure 1 (b)), in which tin is removed and iodine enters, are easily formed in the Sn-rich, I-poor condition. However, under Sn-rich and I-poor conditions, these defect levels were hard to form. Similarly, in MA_2SnGeI_6, I_{Sn} (2-/1-) is easily formed in the Sn-poor, I- rich condition, but not in the Sn-rich, I-poor condition.

In conclusion, it is found that in SnGe double perovskite, the Sn-rich, I-poor condition can control the formation of defect levels, which has a significant influence on the photoelectric conversion efficiency [7].

Significance

Perovskite solar cells indeed hold significant promise for advancing towards a carbon- neutral society due to their unique properties and potential for cost-effective, widespread deployment. Their lightweight, thin, and flexible nature opens possibilities for installation on a wide array of surfaces, which was previously impractical with conventional silicon solar cells. Additionally, their production using coating technology offers a more accessible and potentially greener manufacturing process compared to traditional methods. However, the issue of defects within the perovskite crystal structure remains a challenge. These defects can significantly impact both the efficiency and stability of the solar cells. Understanding and mitigating these defects are crucial steps in realizing the full potential of perovskite solar technology.
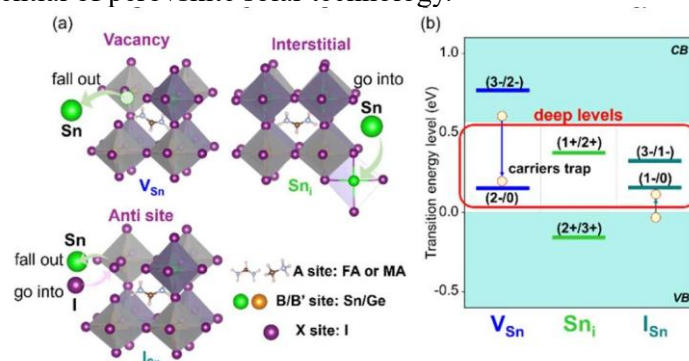
Figure 1. (a) The point defect structure (Vacancy, Interstitial, Anti-site), (b) The defect levels of FA_2SnGeI_6

References

1. D. Nasti, A. *Abate, Adv. Energy Mater.*, 10, 1902467 (2020).
2. N. Liu et al., *Phys. Chem. Chem. Phys.*, 20, 6800 (2018).
3. D. Meggiolaro et al., *J. Phys. Chem. Lett.*, 11, 3546-3556 (2020).
4. I. Yonenaga, *OYO BUTURI*, 86, 12, 1040-1050 (2017).
5. S. Grimme, J. Antony, S. Ehrlich, S. Krieg, *J. Chem. Phys.*, 132, 154104 (2010).
6. Y. Kumagai, N. Tsunoda, A. Takahashi, F. Oba, *Phys. Rev. Mater.,* 5, 123803 (2021).
7. M. Otake, et al., *J. Comp. Chem. Jpn.*, in press (2024).

Molecular encapsulation of fengycin with β-cyclodextrin: A computational study

Aamir Aman[1], Alisa Vangnai[2], Thanyada Rungrotmongkol[1,2]*

[1]*Program in Bioinformatics and Computational Biology, Graduate School, Chulalongkorn University, Bangkok 10330, Thailand*
[2]*Center of Excellence in Structural and Computational Biology, Department of Biochemistry,*
* thanyada.r@chula.ac.th

Introduction

Fengycin, a lipopeptide class initially discovered in Bacillus subtilis [1], has demonstrated potential as an antifungal agent for limiting plant diseases [2]. Naturally occurring fengycin from various bacterial strains has been effectively employed to treat a range of agricultural infections. These include clubroot disease caused by *Plasmodiophora brassicae* in cruciferous plants [3], and maize rot induced by *Fusarium moniliforme* [4]. β-Cyclodextrin (βCD) is a cyclic oligosaccharide characterized by a hydrophilic exterior and a lipophilic interior cavity. Due to its unique structure and nonpolar interior cavity, βCD and its derivatives are extensively utilized as pharmaceutical excipients. They primarily enhance the solubility and stability of various drugs by forming inclusion complexes [5]. The main objective of this work aimed to shed light on the structural and energetic features of fengycin complexation with βCD and the effect of amino acids (AA: arginine, lysine and proline) as third components on the complexation of fengycin with βCD.

Methodology

Fengycin consists of an anionic cyclic decapeptide with a β-hydroxy fatty acid attached at the N-terminus [6]. Fengycin has some unusual moieties that are not found in the standard Amber force field, including the β-hydroxyl on the acyl chain and the ester bond connecting the C-terminus to Tyr. The HF/6-31G* level of theory was used to create parameters for those unusual moieties using the Gaussian09. The inclusion complex of βCD and optimized structure of fengycin and fengycin/βCD-Arg/Lys/Pro ware created using AutoDock Vina. The Glycam-06 and the general AMBER force fields were employed to simulate the behavior of βCD and fengycin, respectively. Initially, the complexes were heated from 10 K to 298 K for 100 ps, followed by three individual all-atom molecular dynamics simulations in the NPT ensemble, with a temperature of 298 K and pressure of 1 atm, utilizing the AMBER22. Three replicates of all-atom MD simulations were conducted for each system, with a duration of 1 μs.

Results and Discussion

The docking study directed that fengycin can make inclusion complex by inserting its acyl chain into βCD. Analysis of MD simulations trajectories shows stable RMSD for all complexes, however, some complexes show fluctuation which means fengycin went out of the βCD cavity. After carefully examining the ternary complexes, fengycin/βCD-Lys shows higher atomic interaction of fengycin with βCD while maintaining its acyl chain inside βCD, compared to fengycin/βCD-Arg and fengycin/βCD-Pro. The higher energy value of ternary complex fengycin/βCD-Lys also favors that the addition of amino acids specifically lysine can enhance the stability of fengycin inside βCD.

Significance

- This study addresses molecular mechanics (MM) of fengycin structure.
- It also focuses on a binary complex of fengycin/βCD and shows the importance of the addition of amino acids to binary complex to make it a ternary complex.
- The computational study of molecular encapsulation of fengycin with βCD holds significance in biomedical, environmental, and green chemistry applications, with the potential to advance the development of novel antimicrobial agents and environmentally friendly technologies.
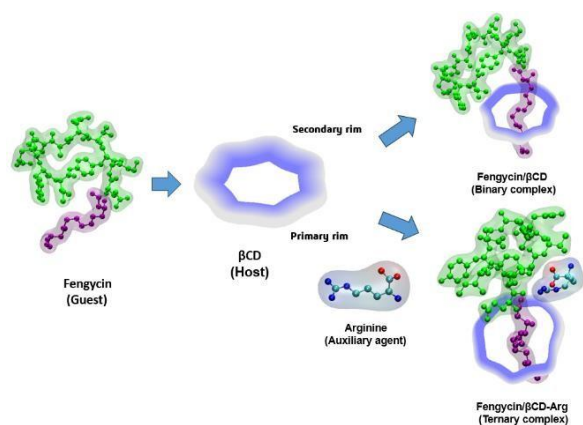
Figure 1: A graphical representation of inclusion complexation of fengycin/βCD-AA

Keywords: Fengycin, β-cyclodextrin, Inclusion complex, Molecular mechanics, MD simulation.

References
1. Ogawa, N., C. Takahashi, and H. Yamamoto, J Pharm Sci, 2015. 104(3): p. 942-54.
2. Vanittanakom, N., et al., J Antibiot (Tokyo), 1986. 39(7): p. 888-901.
3. Ongena, M. and P. Jacques, Trends Microbiol, 2008. 16(3): p. 115-25.
4. Li, X.Y., et al., J Microbiol Biotechnol, 2013. 23(3): p. 313-21.
5. Hu, L.B., et al., FEMS Microbiol Lett, 2007. 272(1): p. 91-8.
6. Horn, J.N., T.D. Romo, and A. Grossfield, Biochemistry, 2013. 52(33): p. 5604-10.

Theoretical studies on the reaction mechanism ofLi-mediated ammonia synthesis

Chinami Okamura[1], Azusa Muraoka[1], Koichi Yamashita[2]
[1]Japan Women's University, 2-8-1, Mejirodai, Bunkyo-ku, Tokyo (Japan)
[2] Yokohama City University, 22-2, Seto, Kanazawa-ku, Yokohama-city, Kanagawa (Japan)

Introduction

Ammonia has recently attracted renewed interest as an energy carrier for renewable energy sources. However, the high dissociation energy of triple-bonded nitrogen molecules represents a major activation barrier to the production of ammonia. The conventional Haber-Bosch process, which is used to produce ammonia, occurs under high temperatures and pressures and emits large amounts of CO_2. Therefore, there is a need to develop an alternative technology to produce ammonia on a small scale in a decentralized process. Of particular significance is the promising Li-mediated electrochemical nitrogen reduction method (Figure 1) proposed by Tsuneto et al. [1], which uses an electrochemical cell with a platinum anode and a metal cathode to dissociate nitrogen

Figure 1. (a) Schematic diagram of the reaction on the Li_xN_y layer. (b) Diagram of reaction.

easily and selectively for ammonia synthesis via lithium, the only element in the periodic table that can react with nitrogen molecules at room temperature. This prosess is based on the reduction of Li ions to metal at the cathode by electrolysis and their reaction with N_2 to form a $Li_xN_yH_z$ layer, which reacts with protons to form NH_3. Currently, this is the only paradigm that can unambiguously perform electrochemical ammonia synthesis[2]. Recently, Fu et al. reported that Ca can mediate the reduction of nitrogen at room temperature as a promising alternative element to Li [3]. The electrolyte is $Ca[B(hfip)_4]_2$, and the process is analogous to that of Li in Figure 1(a). Furthermore, Ca exhibits a mechanism that remains unresolved, and the structural changes that occur during the mediation of the nitrogen reduction reaction remain poorly understood.
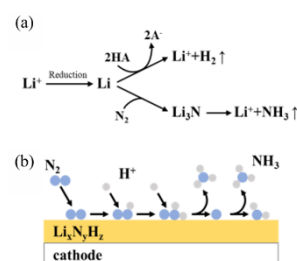
Methodology

The catalyst ions are reduced and deposited as metal on the cathode. Nitrogen molecules adsorb onto the deposited metal to form a lithium nitride surface, where NH_3 is formed by direct addition of a proton donor. Based on this reaction model [4], in this study, Li_3N is formed by the reaction of metallic lithium and nitrogen molecules, and the thermodynamic stability and catalytic activity of various lithium nitride (Li_xN_y) phases formed under different reaction conditions are also examined. Additionally, the reaction pathway of the triple bond breaking process of nitrogen molecules is investigated using density functional theory calculations. The structure of ammonia molecules synthesized by adsorption of hydrogen atoms on lithium nitride was also investigated using the B3LYP/6-31G(d).

Results

The initial stage of the reaction in the case of the Li catalyst was investigated by studying, the process of adsorption of an N_2 molecule onto a Li cluster and breaking of the N_2 triple bond within the Li cluster. A structure was obtained in which a Li atom was adsorbed on N≡N, surrounded by N≡N, and incorporated into the Li cluster. Figure 2 shows the change in potential energy as the N-N distance is increased by 0.2 Å. Based on this structure, the structure of the adsorbed (Li)10 cluster is optimized at each N-N distance. At a distance of 2.2 Å to 2.4 Å, the energy decreases significantly and the structure changes drastically. This indicates that the structural change between 2.2 and 2.4 Å is important for the N≡N bond breaking. This is due to significant changes that the N-N bond as the N2 atom enters the interior of the Li cluster and the three Li atoms are inserted between the nitrogen atoms. Furthermore, structural optimization was performed by placing a hydrogen atom in proximity to each nitrogen atom, acting as a proton donor. This process revealed that, when the Li
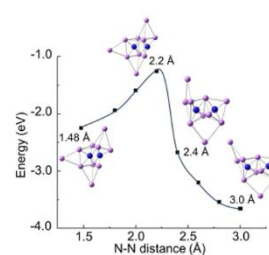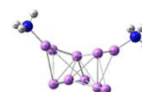

Figure 2. N ≡ N breaking process in $(Li)_{10}$

Figure 3. Ammonia structure formed by adsorption of hydrogen atoms onto $Li_{10}N_2$.

cluster serves as the nucleus, hydrogen atoms form bonds with the nitrogen atoms that are coordinated to the outer Li, forming an ammonia molecule (Figure 3)[4].

Similar calculations were performed on the reaction structure between nitrogen molecules and Ca clusters as shown in Figure 4. The results indicated a difference in the magnitude of the energy barrier is observed between Ca and Li. In particular, Ca exhibited a lower energy barrier, indicating that the nitrogen triple bond is broken at a lower energy.
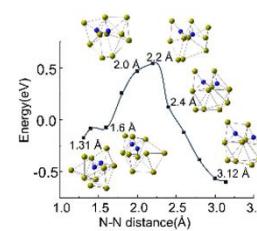
Figure 4. N ≡ N breaking process in $(Ca)_{10}$

Significant

The theoretical studies of the nitrogen reduction reaction using metal catalysts such as Li and Ca, which is considered promising for ammonia production, will enable us to propose a new ammonia production method and nitrogen reduction reaction to replace the conventional production method, and is expected to be the only paradigm that can clearly perform electrochemical ammonia synthesis.

References
1. A. Tsuneto, et al., *Chem. Lett.,* **22**, 851 (1993)
2. H.-L. Du, et al., *Nature*, **609**, 722 (2022)
3. X. Fu, et al., *Nature*, **23**, 101 (2023)
4. J. McEnaney, et al., *Energy. Environ. Sic.*, **10**, 1621 (2017)

Experimental and Theoretical studies of coupling reaction with heterogeneous catalysts

Deekakaew Puttaruksa[1], Patchayamon Thongtan[1*], Tunchaok Petsrjun[1]
and Bundet Boekfa[2]

[1]*Kasetsart University Laboratory School, Kamphaeng Saen Campus, Educational Research and Development Center, Nakhon Pathom 73140, Thailand*
[2]*Department of Physical and Material Sciences, Faculty of Liberal Arts and Science, Kasetsart University, Kamphaeng Saen Campus, Nakhon Pathom 73140, Thailand.*
*patchayamon.t@ku.th

Zeolite, a crystalline microporous aluminosilicate, stands out as an exceptional catalyst in the green chemistry synthesis. The utilization of Palladium zeolite catalysts in cross-coupling reactions, synthesizing unsymmetrical biaryls from aryl halides and boronic acid, has gained interested. Pd-Beta zeolite, owing to its specific pore sizes, exhibits remarkable shape selectivity for coupling reactions, demonstrating superior catalytic activity and recyclability compared to other catalysts. The larger pores of Pd-Beta zeolite facilitate efficient encapsulation of aggregated Pd species, thereby enhancing catalytic performance. In this study, we focus into the cross-coupling reaction between Bromobenzene and aryl boronic acid using Pd-H-Beta zeolite, employing both experimental and theoretical approaches, as illustrated in Scheme 1.
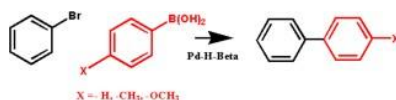
Scheme 1. The cross-coupling reaction of Bromobenzene and aryl boronic acid catalyst by Pd-H-Beta zeolite

Methodology

Part 1: Pd-H-Beta zeolite preparation process in the laboratory.

rt 48hrs — Evaporate THF — After evaporation — Washed with diethyl ether
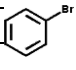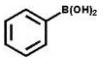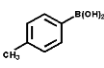
Part 2: Biphenyl synthesis process using Pd-H-Beta zeolite catalyst.
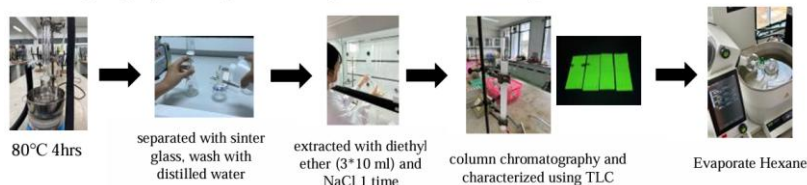
80°C 4hrs — separated with sinter glass, wash with distilled water — extracted with diethyl ether (3*10 ml) and NaCl 1 time — column chromatography and characterized using TLC — Evaporate Hexane

Results and Discussion

The cross-coupling reaction involving bromobenzene and aryl boronic acid was studied with Pd-H-Beta zeolite. The coupling reaction was performed employing Pd-H-Beta under diverse conditions, as outlined in Table 1.

Table 1. Screening for the cross-coupling reaction between Bromobenzene and phenyl boronic acid with various catalysts at reaction time 4 hrs.

Entry	Aryl halides	Aryl boronic acid	Catalysts	Temp (^{0}C)	Yield (%)
1	(bromobenzene)	(phenylboronic acid, B(OH)₂)	Pd(OAc)2	Room temp	41
2			H-Beta	80	8
3			Pd-H-Beta	80	60
4			Pd-H-Beta (reuse)	80	43
5		(p-tolylboronic acid, CH₃–C₆H₄–B(OH)₂)	Pd-H-Beta	80	61
6		(4-methoxyphenylboronic acid, H₃CO–C₆H₄–B(OH)₂)	Pd-H-Beta	80	85
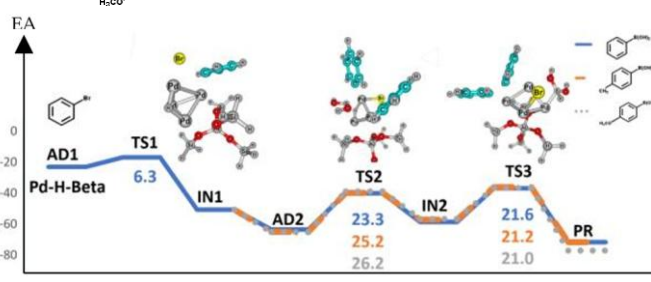
Figure 2. Reaction Pathway for the coupling reaction of bromobenzene with phenylboronic acid, p-tolylboronic acid, and 4- methoxyphenylboronic acid over Pd-H-Beta zeolite. The structures were calculated using the M06L/LANL2DZ functional. Energies are in kcal/mol.

Significance

In our research, the optimal synthesis conditions are studied. The catalyst's reusability further underscores its practicality and economic viability. Additionally, theoretical insights provided by DFT calculations elucidate the reaction mechanism.

References

1.   García-melchor M, Lledos A, Ujaque G, Maserati F. Computational perspective on pd-catalyzed cc cross-coupling reaction mechanisms. Acc. Chem. Res. 2013;11:2626-2634.
2.   Boekfa, B; Maihom, T, Ehara M, Limtrakul. J., Investigation of the Suzuki-Miyaura cross-coupling reaction on a palladium H-beta zeolite with DFT calculations. Scientific Reports 2024;14:611.

Development of combined plane wave and localized basis sets method toward analysis of molecular adsorption on metal surface: a CH₄/CD₄ adsorption on Rh(111) surface

Hiroki Sakagami[1] Makito Takagi[1], Takayoshi Ishimoto[2], Tomomi Shimazaki[1], and Masanori Tachikawa[1]*

[1] *Graduate School of NanoBioScience, Yokohama City University, Seto 22-2, Kanazawa-Ku, Yokohama 236-0027, Kanagawa, Japan*
[2] *Department of Applied Chemistry, Graduate School of Advanced Science and Engineering, Hiroshima University, 1-3-2 Kagamiyama, Higashihiroshima 739-8511, Japan*
*tachi@yokohama-cu.ac.jp

Introduction

The H/D isotope effects of the molecules adsorbed on metal surfaces play an important role in fundamental physics and catalytic activity. Recently, Yoshinobu et al. reported that in experiments on the adsorption of cyclohexane (C_6H_{12}/C_6D_{12}) on Rh(111), the adsorption energy of C_6D_{12} was 0.084 eV smaller than that of C_6H_{12}. They also observed that the adsorption distance for C_6D_{12} was approximately 0.02 to 0.03 Å longer than that of C_6H_{12}.[1] Despite many studies, the adsorption mechanism between H/D and metal surfaces is still unclear due to the difficulty of direct experimental analysis of the H/D isotope effect on the metal surface. In computational chemistry, it is important to include the nuclear quantum effects (NQEs) to treat H/D isotope effects accurately. One

Fig.1. Schematic illustration of the CPLB method for CH_4 adsorption on a Rh(111) surface. The PW and LO methods are applied to the green and pink balls, respectively.

of the powerful methods to include NQE is our multicomponent density functional theory (MC_DFT).[2] Although the MC_DFT method based on localized (LO) basis set is useful for cluster systems, it is not suitable for surface systems. Meanwhile, plane wave (PW) basis set in the framework of periodic boundary condition is well known for such a surface system with delocalized electrons. Recently, we have developed the combined plane wave and localized basis sets (CPLB) method,[3] which is a new approach to incorporate both the advantages of the LO and PW. Furthermore, to consider molecular structural changes on metal surfaces, we have implemented a structural optimization program in the CPLB method. Using this program, we demonstrated the possibility of accurate calculations for local chemical phenomena on metal surfaces.[4,5] In this study, we analyzed the molecular adsorption mechanism of CH_4/CD_4 as a small molecule, on Rh(111).

Computational Method

The CPLB method divides the system into surface and cluster systems. The effect of delocalized electrons is treated as the surface system consisting of the whole system using PW (E(PW, surface). The cluster system consisting of a few metal atoms with adsorbates is used as an accurate calculation by the quantum effect of nuclei using LO (E(LO, cluster)), and eliminated the excess part (E(PW, cluster)). Then, the total energy (E(CPLB)) is calculated from each computational result by eq. (1).

$$E(\text{CPLB}) = E(\text{PW, surface}) - E(\text{PW, cluster}) + E(\text{LO, cluster}) \qquad (1)$$

Additionally, by differentiating each term in eq. (1), we calculate the force on each atom (eq. (2)). In this study, we implemented a structural optimization in the CPLB method.

$$\mathbf{F}(\text{CPLB}) = \mathbf{F}(\text{PW, surface}) - \mathbf{F}(\text{PW, cluster}) + \mathbf{F}(\text{LO, cluster}) \qquad (2)$$

For the PW-based calculations, we used the Vienna ab initio simulation package (VASP). For the LO-based calculations, we used the modified Gaussian16 program package embedded with the MC_DFT method.

Results and Discussion

We performed structural optimization calculations in the CPLB method for the adsorption of a CH_4/CD_4 molecule on the on-top site of the Rh(111) surface. The C-H/D bond length and the distance between C and the Rh(111) surface is shown in Fig. 2. The C-H bond length within the molecule was 0.006 Å shorter than that of CD_4. This is similar to the H/D isotope effect of covalent bonds due to the anharmonicity of the potential. On the other hand, the distance between C and the Rh(111) surface for CH_4 was 0.009 Å longer than that for CD_4. This result follows the same trend as the experimental adsorption distance reported by Yoshinobu et al. Additionally, the adsorption energy of CH_4 was 0.069 eV larger than that of CH_4. These results suggest that the interaction between the Rh(111) surface and CH_4/CD_4 is opposite to the C-H/D covalent bond trend.

Based on these results, our CPLB approach is effective in reproducing the H/D isotope effects on small molecules, such as CH_4/CD_4, that are adsorbed on metal surfaces.

On the day, we will also present reports including other computational results, as well as the development of vibrational analysis using the CPLB method.

Fig.2. Optimized adsorption structure, charge, and adsorption energy of CH_4/CD_4 on Rh(111) surface.

References

[1]   T. Koitaya, S. Shimizu, K. Mukai, S. Yoshimoto, and J. Yoshinobu, J. Chem. Phys., 136, 214705 (2012).
[2]   T. Udagawa and M. Tachikawa, J. Chem. Phys., 125, 244105 (2006).
[3]   T. Ishimoto and H. Kai, Int. J. Quant. Chem., 118, e25452 (2018).
[4]   H. Sakagami, M. Tachikawa, and T. Ishimoto, Int. J. Quant. Chem., 120, e26275 (2020).
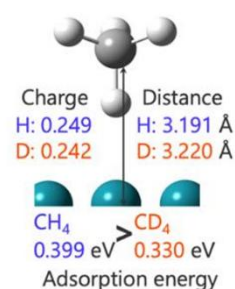[5]   H. Sakagami, M. Tachikawa, and T. Ishimoto, RSC Adv., 11, 10253 (2021).

Theoretical Study on Surface Defects and the Molecular Passivation Effect for SnGe mixed Perovskite

Emi Kino[1], Takumi Naitou[1], Makito Takagi[1], Masanori Tachikawa[1], Koichi Yamashita[1], Tomomi Shimazaki[1]*

[1]*Graduate School of NanoBioScience, Yokohama City University, Seto 22-2, Kanazawa-ku, Yokohama 236-0027, Kanagawa (Japan)*
*tshima@yokohama-cu.ac.jp

Introduction

Perovskite solar cells (PSCs) have been attracting attention because of their low cost, lightweight, and high power conversion efficiency (PCE). Perovskite structures are represented by ABX_3 (**Fig. 1**), where A, B, and X representing an organic cation, a metal cation, and a halide anion, respectively. The perovskite material with Pb cation has higher PCE than those using other metals.1 However, due to the environmental toxicity of Pb, Pb-free perovskites have been developed in recent years. Sn-based perovskite is expected as Pb free perovskites.[2] However, Sn-based perovskite is unstable in air and is reported to be stabilized by the addition of Ge.[3,4]
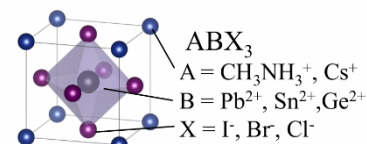

Figure 1. Crystal structure of ABX_3 perovskite.

One of a factor of decreasing the PCE of PSCs is that defects on perovskite traps the electron/hole and act as recombination of carriers. In particular, defect levels located within the bandgap as centers of carrier recombination. Additionally, it has been reported that defects are concentrated at the interface of the perovskite. To reduce the number of trapping sites, a passivation technique using the coating of organic molecules onto the interface of perovskites has been proposed. For example, ethylenediamine (EDA) and iodopentafluorobenzene (IPFB) are useful as a passivation molecule.[5,6] Based on theoretical calculations, we have proposed a mechanism of passivation for Sn-based perovskite, where interactions between defect levels and molecular orbitals of the molecules are essential.

Therefore, in this study, serious defects were selected as the cause of trapping for SnGe perovskite of $CH_3NH_3Sn_{0.5}Ge_{0.5}I_3$, and passivation calculations using EDA and IPFB were performed for these defects, and these results were compared with those for Sn-based perovskite.

Methodology

We performed calculations to slab models with defects and passivated defect with a passivation molecule. Electronic structure calculations based on density functional theory (DFT) calculations with PBE functional were performed. The energy cutoff was set to 450 eV *k*-point sampling was set to $2 \times 2 \times 1$ by the Monkhorst–Pack method during the optimization calculations. Thereafter, single-point and DOS calculations were performed with k-point samplings of $4 \times 4 \times 1$ and $5 \times 5 \times 1$ using the Γ-centered mesh, respectively. All calculations were conducted with Vienna Ab initio Simulation Package (VASP) 5.4.4.

Results and Discussion

First, we determined the serious defect structures of SnGe perovskite $(CH_3NH_3Sn_{0.5}Ge_{0.5}I_3)$. According to the conditions of defect formation energy and defect levels in the band gap by density of states (DOS) analysis, we found two types of the serious defect structures: (i) Sn/Ge vacancy defects (V_{Sn}/V_{Ge}), and (ii) Sn/Ge substituted with I defects (I_{Sn}/I_{Ge}). These defects are classified as p-type defects in which no electrons exist in the defect level.
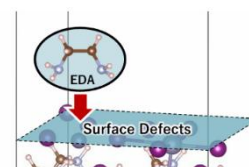
Figure 2. Schematic diagram of passivation by EDA

Next, molecular passivation (adsorption) was calculated for these defects as shown in Fig. 2. Here, EDA was used as a passivation molecule. Fig. 3. shows the DOS of V_{Sn} and after passivation; V_{Sn} defect has a defect level in the band gap (Fig. 3a), which was improved by passivation (Fig. 3b).

In addition to the above p-type defects, we also analyzed n-type defects in which there are electrons in the defect level. Here, we consider a defect that I atom substituted with MA defects (MAI). For these defects, passivation by IPFB was to be effective. Compared with Sn-based, the serious defect structures and effective passivation molecules tend to be similar. Thus, interactions between defect levels and molecular orbitals of the molecules are also important for the passivation of SnGe perovskite.
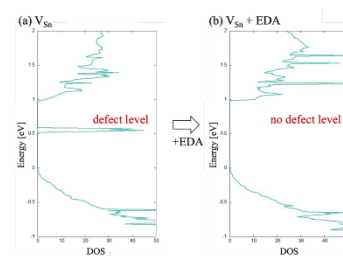
Figure 3. Density of states (DOS) of the SnGe perovskite ($CH_3NH_3Sn_{0.5}Ge_{0.5}I_3$): (a) Vacancy at Sn site (V_{Sn}) defect, (b) V_{Sn} defect passivated by EDA molecule.

Significance

This research is about improving trapping caused by surface defects, which is one of the factors that reduce power conversion efficiency (PCE), on SnGe perovskite without the use of environmentally toxic Pb.

References

1. Jeon, I. *et al. Nanomaterials,* **11**, 2066 (2021).
2. Ke, W. & Kanatzidis, M. G. *Nat Commun,* **10**, 965 (2019).
3. Noel, N. K. *et al. Energy Environ. Sci. 7,* 3061–3068 (2014).
4. Ito, N. *et al. J. Phys. Chem. Lett. 9,* 1682–1688 (2018).
5. Zhang, Z. *et al. Angewandte Chemie International Edition,* **61**, e202210101 (2022)
6. Naito, T. *et al. J. Phys. Chem. Lett.* **14,** 6695–6701 (2023).

Theoretical study of electronic structure calculations for NTz-based acceptor molecules non-fullerene organic solar cells

HARUKA Araragi[1], Seihou Jinnai[2], Yutaka Ie[2], and Azusa Muraoka[1]*

[1]Graduate School of Science, Japan Women's University, 2-8-1,
Mejirodai, Bunkyo, Tokyo, 112-8681 (Japan)
[2] The institute of Scientific and Industrial Research, Osaka University, 8-1,
Mihogaoka, Ibaraki, Osaka, 567-0047 (Japan)
* muraokaa@fc.jwu.ac.jp

Introduction

The current research focus in the development of bulk heterojunction organic solar cells is on non-fullerene acceptors. In contrast to the widely used fullerene acceptors, the optical properties and electronic energy levels of non-fullerene acceptors can be easily modified [1]. Naphtho[1,2-c:5,6-c']bis[1,2,5]thiadiazoles (NTz) as the central unit (NTz-DCI) are also non-fullerene π-conjugated acceptor molecules with polycyclic acceptor-donor-acceptor-donor-acceptor (A-D-A-D-A) type, a high energy gap between HOMO and LUMO and high charge mobility [2]. In a related study, Ie et al. fused an alkyl-substituted thiophene to NTz to form alkyl-substituted dithienonaphtho[1,2-c:5,6-c']bis[1,2,5]thiadiazole (TNTz-c8), which resulted in a higher conversion efficiency [3]. In this study, the molecular structure, absorption spectra, and electronic polarization properties of TNTz-c8-DCI with TNTz as the central unit of the main chain molecule are characterized using density functional theory.

Methodology

DFT calculations were performed using Gaussian 16. First, TNTz-c8-DCI and NTz-DCI monomer were optimized, and then excited state calculations for these structures were performed using the TD-DFT method. The computational level is B3LYP/6-31G(d,p). Next, similar calculations were performed for the TNTz-c8-DCI and NTz-DCI dimers to calculate the charge transfer. The calculated levels are B3LYP-D3/6-31G(d,p).

Results and Discussion

Structural optimization of TNTz-c8-DCI revealed a symmetric 30.9° twist around the center TNTz of the main chain (Figure 1). TNTz-c8-DCI is an A-D-A-D-A type molecule. Therefore, we focused on (TNTz-c8-DCI)$_2$ and discussed the intermolecular interactions exhibited by TNTz. The results show that the stacked structure of the ADADA–ADADA type is stabilized in a manner that circumvents the steric barrier of the side chain between the two molecules. Subsequently, a comparison is made between the present results and those obtained for NTz-DCI without alkyl substitution. Excitedstate calculations indicate that TNTz-c8-DCI has a stronger absorption band in the longer wavelength region than NTz-DCI, especially between 500-650 nm. This indicates that TNTz-c8-DCI has complementary optical absorption while increasing the optical absorption of the donor molecule [4].

Table 1 shows the dipole moment, charge transfer and distance, and binding energy for the NTz system. The dipole moment is also smaller in TNTz, and therefore the charge polarization is also smaller. These confirm the effect of the π-expansion. The amount of charge transfer is about the same, the transfer distance and binding energy have smaller values for TNTz. The ideal charge transfer direction is along the acceptor-acceptor stacking axis. However, these results show that the charge transfer distance is extended in the direction along the acceptor molecular axis. Consequently TNTz with smaller one is expected higher crystallinity and improved charge transport properties in the complex. Further details will be presented on the day.

Table 1. Dipole moment, charge transfer and distance, and binding energy of NTz-based acceptor molecules

Acceptor	Dipole moment (Debye)	Amount of charge transfer	Charge transfer distance (Å)	Binding energy (eV)
TNTz-c8-DCI	0.063	0.587	0.022	0.71
NTz-DCI	1.125	0.586	0.400	1.41

Significance

Organic thin-film solar cells are characterized by their utilization of organic compounds, which makes them lightweight, flexible, and enables printing processes. These attributes have prompted consideration of their practical use in applications that are challenging to achieve with silicon solar cells. In order to achieve such high-efficiency organic thin-film solar cells, the following issues remain to be addressed in research, (i) the development of organic semiconductor materials that enable highly efficient light absorption and charge transfer. (ii) the construction of optimized molecular assembly and organization structures in organic thin films.
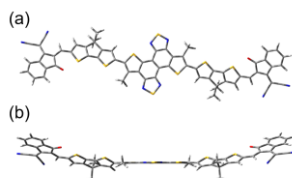

Figure 1. Structure of TNTz-c8-DCI (a) top view, (b) side view

References
1. W. Zhao, D. Qian, et al., *Adv. Mater.*, 10, 1-6 (2016).
2. I. Osaka, et al., *J. Am. Chem. Soc.*, 134, 3498-3507 (2012).
3. Y. Ie, et al., *J. Photopolym. Sci. Tech.*, 34, 285-290 (2021).
4. H. Araragi, et al., 14th Ewha-JWU-Ochanomizu Joint Symposium 2023.

QSAR-ML Study on Darunavir Analogs for HIV-1 Protease Inhibition

Saba Ali[1], Hathaichanok Chuntakaruk[2], Phornphimon Maitarad[3], Muhammad Asad Ur Rehman[4], Tanatorn Khotavivattana[4], Thanyada Rungrotmongkol[2], Supot Hannongbua[1]*

[1]*Center of Excellence in Computational Chemistry (CECC), Department of Chemistry, Faculty of Science, Chulalongkorn University, Bangkok 10330, Thailand*
[2]*Program in Bioinformatics and Computational Biology, Graduate School, Chulalongkorn University, Bangkok 10330, Thailand*
[3]*Research Center of Nano Science and Technology, College of Sciences, Shanghai University, Shanghai 200444, P. R. China*
[4]*Center of Excellence in Natural Products Chemistry, Department of Chemistry, Faculty of Science, Chulalongkorn University, Bangkok, 10330, Thailand*
*supot.h@chula.ac.th

Introduction

The ongoing prevalence of HIV-1 infection remains a critical global public health concern, underscoring the necessity for antiretroviral medications that specifically target viral proteins to diminish viral replication. HIV-1 protease (PR) plays a crucial role in cleaving viral polyproteins, thereby facilitating the maturation of viral proteins. Protease inhibitors (PIs) approved by the FDA are widely used in anti-retroviral therapy to manage HIV-positive patients. Darunavir is a leading PI used as the second-line therapy option to reduce HIV replication [1]. However, darunavir may not be effective against all changes in HIV-1 PR due to multi-drug resistance (MDR). The primary objective of this study is to explore the Quantitative Structure-Activity Relationship-Machine Learning (QSAR-ML) methodologies [2] to link the structural features of darunavir analogs with their inhibitory activity against HIV-1 PR.

Methodology

Thirty-three darunavir analogs with inhibitory activity towards wild-type HIV-1 PR from our previous work were used for the QSAR-ML study. Molecular descriptors for all compounds were calculated using Material Studio software. Using the Kennard-Stone algorithm, the dataset was then divided into a training set comprising 80% of the compounds (26 compounds) and a test set containing the remaining 20% of compounds (7 compounds). This division facilitated the evaluation of the generalization performance of regression models. Three regression models were employed: Artificial Neural Network (ANN), Random Forest (RF), and Group-Fused Adaptive Multivariate Regression (GFA-MLR). These models were utilized to predict the inhibitory activity of the darunavir analogs and assess their potential as HIV-1 PR inhibitors.

Results and Discussion

Using various models, QSAR concepts were employed to correlate the inhibitory activity of darunavirs with their molecular descriptors. Feature selection was performed using descriptors such as atomic selection, E-state keys, Chi (0) (valence modified), Chi (2) (valence modified), and molecular flexibility. The feature selection process played a crucial role in identifying the most relevant molecular descriptors for predicting the inhibitory activity of the compounds. By incorporating descriptors such as atomic selection and molecular flexibility, we were able to capture key structural features that contribute to the interactions between the considered compounds and HIV-1 PR. Furthermore, among these models, the ANN model in Fig. 1 demonstrated superior performance, providing the most accurate prediction for the inhibitory values of the darunavir analogs. The Root Mean Square Error values for both the training and test datasets are used to assess the accuracy and reliability of the QSAR model's predictions. Lower values indicate better predictive performance, with RMSE values closer to zero indicating a better fit of the model to the data. The superiority of the Artificial Neural Network (ANN) model is evidenced by its lower RMSE values for both datasets. This indicates that the ANN model provides more accurate predictions of inhibitory activity than other algorithms, making it the preferred choice for this study.

Significance

The significance of this study lies in the utilization of QSAR analysis, an efficient and cost-effective *in silico* methodology, to explore inhibitory activity. By employing different algorithms, a comprehensive comparative analysis is conducted, offering valuable insights into the molecular mechanisms underlying inhibitory properties. The study can uncover critical structural features that influence the inhibition potency of these analogs, providing valuable theoretical insights and paving the way for the molecular refinement of novel anti-retroviral agents.
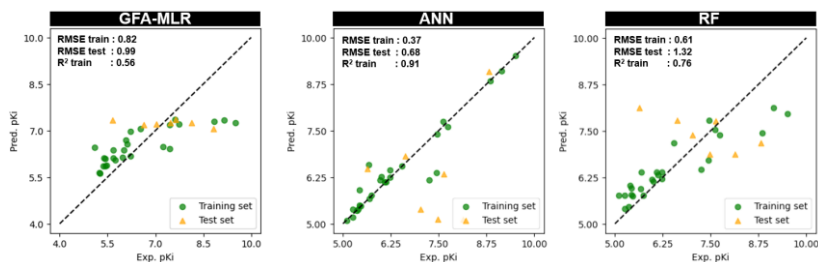
Figure 1 QSAR models including GFA-MLR, ANN, and RF model.

References

1. World Health Organization. (2016). Consolidated guidelines on the use of antiretroviral drugs for treating and preventing HIV infection: recommendations for a public health approach. World Health Organization.
2. Tian, Y., Zhang, S., Yin, H., & Yan, A. (2020). Quantitative structure-activity relationship (QSAR) models and their applicability domain analysis on HIV-1 protease inhibitors by machine learning methods. Chemometrics and Intelligent Laboratory Systems, 196, 103888.

Understanding roles of 2-PAM analogs as antidotes for organophosphate

Phiphob Naweephattana[1], Nalinee Kongkaew[2], Panida Surawatanawong[3], Nawee Kungwan[4], Thanyada rungrotmongkol[1,2], Alisa S. Vangnai[1,*]

[1]*Center of Excellence in Biocatalyst and Sustainable Biotechnology, Department of Biochemistry, Faculty of Science, Chulalongkorn University, Bangkok 10330, Thailand*

[2]*Program in Bioinformatics and Computational Biology, Graduate School, Chulalongkorn University, Bangkok 10330, Thailand*

[3]*Department of chemistry, Faculty of Science, Mahidol University, Bangkok 10400, Thailand*

[4]*Department of Chemistry, Faculty of Science, Chiang Mai University, Chiang, Mai 50220, Thailand*

*Alisa.V@chula.ac.th

Introduction

Demand for food is directly proportional to the population of the world. The global population will increase by roughly eight billion individuals in 2024. Chemical pesticides known as organophosphates (OP) have been employed in agricultural and domestic settings and cause a significant risk of poisoning, with widespread health implications globally. Toxic effects on specific neurological organs can be modulated by OPs given to humans through several routes of absorption, including oral consumption, skin adsorption, and respiratory inhalation. These pesticides function by inhibiting acetylcholinesterase (AChE), an essential enzyme for nerve function, leading to overstimulation of neuronal pathways and fatal outcomes. Current treatments, primarily involving oxime-based reactivators like 2-pralidoxime (2-PAM), have limitations, particularly their inability to cross the blood-brain barrier (BBB) effectively. Oxime is a nucleophile that is highly potent and attacks organophosphate and related hydrogen transfer states. Understanding the reaction mechanisms will elucidate in which the 2-PAM antidote treats organophosphorus nerves agents as well as aid in the development of highly effective molecular design 2-PAM analogs.

Quantum mechanics and molecular mechanics (QM/MM) have become one of the most essential tools to gain insight into the active site of enzymes and contribute to identifying the determinants of reactivity. Understanding key factors affecting treatment is important to the development of 2-PAM.

Methodology

The Gaussian 16 software was used for all quantum mechanical/molecular mechanical (QM/MM) calculations. The geometries were optimized using the B3LYP density functional theory (DFT) method at the high-level layer. The def2-svp basis set was used, which includes Ser203-paraoxon, His447, Glu334, and 2-PAM analog. The molecular fragments within a 5 Å range were addressed using the universal force field (UFF) molecular mechanics methodology. The B3LYP method, along with the D3BJ dispersion correction and the 6-311++G(d,p) basis set, was used for the high-level layer in both the single-point and solvation calculations. The PM7 method was used for the low-level layer. The solvation effects were simulated using a polarizable continuum model (PCM) with parameters specific to water ($\varepsilon = 78.3553$).

Results and Discussion

In our investigation of the reactivation mechanisms of pralidoxime (2-PAM) in the presence of inhibited organophosphate (OP), we delineated two distinct pathways, A and B, through which 2-PAM could potentially reverse the inhibition of acetylcholinesterase by OP compounds such as paraoxon. In Pathway A, the process initiates through a concerted hydrogen transfer involving the protonation of the oxygen atom at Glu334 by a hydrogen from the imidazole ring of His447. Subsequently, this interaction facilitates the capture of a hydrogen atom from 2-PAM, leading to nucleophilic attack on the phosphorous atom of Ser203-paraoxon. This series of actions results in a molecular rearrangement that forms a double bond with phosphorus, releasing the byproducts Ser203-paraoxon and 2-PAM. Conversely, Pathway B begins with a similar hydrogen transfer from 2-PAM to His447 but includes an additional step where a second hydrogen transfer catalyzes further reaction sequences, eventually resulting in comparable molecular rearrangements and byproduct release. The elucidation of these pathways underscores the complexity of 2-PAM's mechanism of action, suggesting that the efficiency of reactivation may depend on the structural dynamics within the enzyme-inhibitor complex.

Significance

    Understanding mechanisms of 2-PAM antidote treats organophosphorus nerves agents could lead to the development of more effective antidotes against OP poisoning by enhancing the reactivation process of inhibited enzymes.
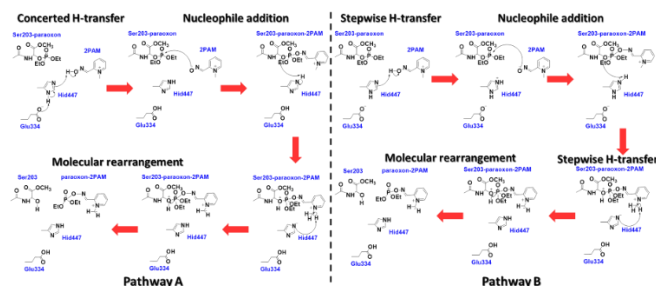
Figure 1. Reactivation mechanism of pralidoxime (2-PAM) inhibited Organophosphate (OP).

References
1. da Silva Gonçalves, A.; França, T. C. C.; Caetano, M. S.; Ramalho, T. C., Journal of Biomolecular Structure and Dynamics 2014, 32 (2), 301-307.
2. Kongkaew, N.; Hengphasatporn, K.; Injongkol, Y.; Mee-udorn, P.; Shi, L.; Mahalapbutr, P.; Maitarad, P.; Harada, R.; Shigeta, Y.; Rungrotmongkol, T.; Vangnai, A. S., RSC Advances 2023, 13 (46), 32266-32275.

Structural and dynamic properties of fully glycated human serum albumin

Prin Tadawattana[1], Deanpen Japrung[2] and Prapasiri Pongprayoon[1]*
*[1]Department of Chemistry, Faculty of Science, Kasetsart University,
Bangkok, 10900, Thailand*
*[2]National Nanotechnology Center, National Science and Technology Development Agency,
Pathumthani 12120, Thailand*
*prapasiri.p@ku.th

Introduction

Human Serum Albumin (HSA) is the most abundant protein carrier in blood. It carries metabolites and drugs. In diabetic patients, HSA gets modified by non-enzymatic glycation due to persistent hyperglycemia. Lysines were found to be the main glycation sites. Abundant blood glucose conjugates with a free amino group of lysines. Multiple glycation sites were experimentally reported. The glycation impairs structure and ligand-binding capability where no molecular detail is available. Such glycated HSA (GHSA) was also reported to be a potential biomarker for diabetes. Many attempts have been made to detect GHSA in order to monitor the diabetic progression. GHSA displays the unique characteristics which can be used to distinguish it from healthy albumin. Recently, the X-ray structure of GHSA with one glycated lysine at position 195 was solved where no structural and dynamic data on fully glycated albumin is available. The understanding of GHSA structure and function is crucial for designing effective GHSA detection strategies. To date, how the full glycation disrupts albumin activity microscopically remains mystery. Therefore, Molecular Dynamics Simulations were performed to explore the nature of fully glycated GHSA. The insights obtained here can be useful for better understanding the effect of glycation on albumin function and designing specific and selective GHSA-detecting strategies.

Methodology

The crystal structure of GHSA (PDB:4IW2) with one glycated lysine at position 195 was downloaded from PDB databank [1]. The configurations were built by modifying glucose-lysine structure using Gaussview -6.1 [2]. The AMBER99SB-ILDN[3], general Amber force field (GAFF)[4], and GLYCAM_06 were used. MD simulations were carried out by GROMACS2020.7 software package [5]. The 5000-step energy minimization, 10-ns equilibration (NPT) at 300K and 1atm were performed. The equilibrated structure was followed by a 500-ns production run with a repeat.

Results and Discussion

The full glycation of HSA disrupts both structure and function. The glycation alters the protein dynamics resulting in:(i) The change in drug binding affinities, (ii) The alternation of ligand-binding pocket sizes, (iii) The enhancement of protein reactivity, and (v) The change in W214 microenvironment. Such unique characteristics found here can be useful for better understanding the effect of glycation on albumin function and designing specific and selective GHSA-detecting strategies.

Significance

The understanding of GHSA structure and function is crucial for designing effective GHSA detection strategies. This insight is also important for GHSA-based diabetes biosensor design.

References

1. Wang, Y., et al., *Structural mechanism of ring-opening reaction of glucose by human serum albumin.* J Biol Chem, 2013. **288**(22): p. 15980-7.
2. Dennington, R., T. Keith, and J. Millam, *GaussView, Version 6.1.* 2016: Semichem Inc., Shawnee Mission, KS,.
3. Lindorff-Larsen, K., et al., *Improved side-chain torsion potentials for the Amber ff99SB protein force field.* Proteins, 2010. **78**(8): p. 1950-1958.
4. Wang, J., et al., *Development and testing of a general amber force field.* 2004. **25**(9): p. 1157-1174.
5. Van Der Spoel, D., et al., *GROMACS: Fast, flexible, and free.* Journal of Computational Chemistry, 2005. **26**(16): p. 1710-1718.

Unveiling a Novel Janus kinase 2 Inhibitors for Cervical Cancer Treatment: Computational Screening and Experimental Validation

Duangjai Todsaporn[1], Kamonpan Sanachai[2], Chanat Aonbangkhen[3],
Athina Geronikaki[4], and Thanyada Rungrotmongkol[1,5*]

[1] Department of Biochemistry, Faculty of Science, Center of Excellence in Structural and Computational Biology, Chulalongkorn University, Bangkok, Thailand
[2] Department of Biochemistry, Faculty of Science, Khon Kaen University, Khon Kaen, Thailand
[3] Center of Excellence in Natural Products Chemistry (CENP), Department of Chemistry, Faculty of Science, Chulalongkorn University, Bangkok, Thailand
[4] Department of Pharmaceutical Chemistry, School of Pharmacy, Aristotle University of Thessaloniki, Thessaloniki 54124, Greece
[5] Program in Bioinformatics and Computational Biology, Graduate School, Chulalongkorn University, Bangkok, Thailand
* Thanyada.r@Chula.ac.th, t.rungrotmongkol@gmail.com

Introduction

Cervical cancer, particularly those associated with high-risk human papillomavirus (HPV) types, poses a substantial burden on women's health globally, with HPV18+ being one of the most prevalent oncogenic strains implicated in the development of this malignancy. Despite advancements in treatment modalities, the efficacy and tolerability of current therapeutic approaches remain limited. A previous study reported that a Janus kinase 2 (JAK2) inhibitor can induce apoptosis in HeLa HPV18+ cancer cell lines, indicating that JAK2 is a promising target for treatment [1]. In this work, we employed a docking-based virtual screening approach to identify JAK2 inhibitors. The screened compounds were evaluated for cytotoxic effects against both cervical cancer and non-cancer cell lines.

Methodology

Molecular docking using the GOLD program was employed to screen candidate compounds. The three-dimension structure of 78 furochochicine derivatives acting as ligands were generated using the GaussView program. The 3D structure of JAK2/tofacitinib (PDB: 3FUP) was obtained from the RCSB database, and hydrogen atoms were added to the protein. The reference ligand (tofacitinib) was designated as the docking center, and a sphere with a 12 Å radius around tofacitinib was generated for docking. Each compound was docked, and 100 docking poses were collected. The screened compounds obtained from virtual screening were then subjected to cell-based assays to study their anti-cancer effects. HeLa HPV18+ cervical cancer cell lines were seeded in 96-well plates, treated with the screened compounds, and incubated for 48 hours. After incubation, MTT solution was added, and the formazan crystals formed by metabolically active cells were solubilized. Absorbance was measured at 570 nm to determine %cell viability.

Results and Discussion

Virtual screening revealed that 31 in-house furochochicine derivatives (94.93-61.38) exhibited GOLD fitness scores superior to that of ruxolitinib (60.48), a known JAK2 inhibitor. Furthermore, these 31 screened compounds demonstrated potent cytotoxic effects against the HeLa cervical cancer cell line, with IC_{50} values reaching the micromolar scale. Consequently, these potent compounds were further investigated to gain insights into their cellular mechanisms using flow cytometry-based apoptosis detection and Western blotting analysis.

Significance

The integration of computational screening with experimental validation has resulted in the discovery of a novel compound scaffold as a potent JAK2 inhibitor for cervical cancer treatment. Some

of the in-house furochochicine derivatives hold significant promise as potential therapeutic agents for further clinical development, offering new hope for patients with cervical cancer.
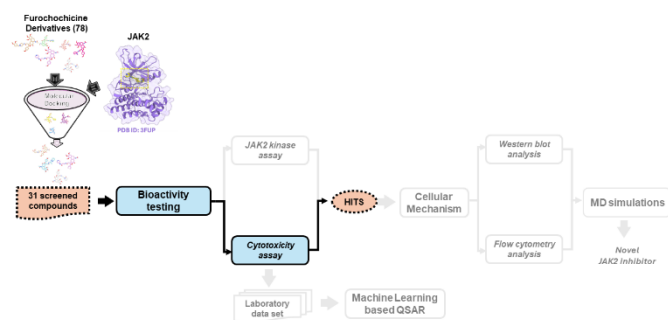

Figure 1: Workflow for the discovery of novel JAK2 inhibitors using *in silico* and *in vitro* studies (black: completed works, gray: future works).

References

1. Morgan, E.L. and A. Macdonald, JAK2 inhibition impairs proliferation and sensitises cervical cancer cells to cisplatin-induced cell death. Cancers, 2019. 11(12): p. 1934.

High-binding Affinity Nanobody Against SARS-CoV-2 XBB.1.5: Computational-based Protein Engineering

Phoomintara Longsompurana[1], Napat Kongtaworn [2], Rungtiva P. Poo-arporn[1], and Thanyada Rungrotmongkol [2,3]*

[1]*Biological Engineering Program, Faculty of Engineering,*
King Mongkut's University of Technology Thonburi, Bangkok, 10140 (Thailand)
2Program in Bioinformatics and Computational Biology,
Graduate School, Chulalongkorn University, Bangkok, 10330 (Thailand)
[3]*Center of Excellence in Biocatalyst and Sustainable Biotechnology, Department of Biochemistry,*
Faculty of Science, Chulalongkorn University, Bangkok, 10330 (Thailand)
*Corresponding author e-mail: Thanyada.r@chula.ac.th

1. Introduction

The appearance of the SARS-CoV-2 variant XBB.1.5 has instigated a global health crisis by exploiting the attachment mechanism of its spike protein, facilitating viral entry into cell. This challenge has inspired an urgent demand for the development of neutralizing molecules to counter viral invasion[1,2]. Antibodies (Abs) are well-known to neutralize SARS-CoV-2 by binding to its spike protein, preventing virus entry into cells and subsequent infection[3]. However, antibody neutralization can be less effective against new SARS-CoV-2 variants due to mutations that reduce antibody binding efficacy[4,5]. Moreover, therapeutic monoclonal antibodies can be expensive and challenging to produce at scale, limiting their accessibility and widespread use[6]. Alternatively, nanobodies (Nbs), which are the single variable heavy chain domains of antibodies[7], are a promising option due to their small size, high binding affinity, solubility, stability, and effectiveness in neutralizing SARS-CoV-2 by binding its spike protein[8]. However, traditional methods for nanobody screening, such as phage display and immunization of animals (e.g., camelids), have several drawbacks. These include being time-consuming, costly, resource-intensive, necessitating extensive gene library construction, and requiring expertise in molecular biology techniques[9-11]. To address these limitations, we propose an *in silico* approach to select a Nb and improve its binding affinity with the SARS-CoV-2 spike protein receptor binding domain (RBD), circumventing traditional production limitations. We screened 29 Nbs against RBD XBB.1.5 via the HDOCK server to identify a lead Nb and engineered it through computational design for heightened affinity.

2. Methodology

2.1 Selection of lead nanobody for RBD XBB.1.5

The XBB.1.5 RBD structure was engineered by changing P486 to S486 in PDB ID 8IOV. To discover a lead Nb with the highest binding affinity for the XBB.1.5 RBD target, all 29 Nbs from the Protein Data Bank (PDB) (https://www.rcsb.org/)[12] were docked with the RBD XBB.1.5 using a blind docking method in HDOCK (http://hdock.phys.hust.edu.cn/)[13]. Next, the Nb/RBD complexes underwent energy minimization using the AMBER ff14SB force field to achieve the optimal torsion of amino acid side chains[14], ensuring optimal conformations before rescoring with HDOCK. The Nb with the lowest HDOCK scores was selected as a lead Nb. This chosen Nb was then utilized in the subsequent phase of the structure-based engineering process.

2.2 Structural-based engineering of lead nanobody for RBD XBB.1.5

To improve binding affinity of the lead Nb to RBD XBB.1.5, site-directed mutagenesis was performed on the lead Nb. The HDOCK score of the Nb/RBD complex from the lead Nb selection process was recorded as HDOCK(Nb native). Mutations were prioritized at residues on the Nb interface that either did not interact or had repulsive interactions with RBD XBB.1.5. Prior to redocking, each mutated amino acid was optimized using the CHARM force field within the Discovery Studio

program[15]. The mutated Nb was then redocked to determine the post-mutation score, referred to as HDOCK$_{(Nb\ mutant)}$. The ΔHDOCK value for each Nb mutation was calculated to assess the binding affinity changes for each mutated residue using Equation (1)[16].

$$\Delta HDOCK = HDOCK_{(Nb\ mutant)} - HDOCK_{(Nb\ native)} \quad (1)$$

The ΔHDOCK score indicated the binding affinity of each residue of Nb to RBD XBB.1.5. The mutation that resulted in the lowest ΔHDOCK at a specific position was selected for multi-point mutation [16]. This multi-mutated Nb was then docked with RBD XBB.1.5 to obtain the final HDOCK score. The sequences of the multi-mutated Nb and the lead Nb were aligned using BioEdit software to assess sequence similarity [17].

2.3 Physicochemical properties

The predicted physicochemical properties, including contact surface amino acids, contact surface area, and chemical and physical interactions of the engineered Nb, were determined using the PDBsum server (http://www.ebi.ac.uk/thornton-srv/databases/pdbsum/Generate.html)[18]. Additionally, other properties such as molecular weight, pI value, molar extinction coefficient, instability index, aliphatic index, and grand average of hydropathicity (GRAVY) were predicted using the ProtParam (ExPASy) tool (https://web.expasy.org/protparam/)[19]. Protein solubility was assessed using the Protein–Sol web server (https://protein-sol.manchester.ac.uk/)[20], and total charge was calculated using PROTEIN CALCULATOR v3.4 (https://protcalc.sourceforge.net/)[21].

3. Results and Discussion

3.1 Selection of lead nanobody for RBD XBB.1.5

The selection of lead Nb for RBD XBB.1.5 was based on a docking process. The criteria for selection, the HDOCK score of the lead Nb should be low, indicating high binding affinity. This investigation discovered in Figure 1 that the Nb_7KGK exhibited the highest binding affinity (-464.97) to the targeted RBD XBB.1.5. Therefore, Nb9 was appropriately chosen as the lead Nb for further amino acid engineering. This outcome aligns with earlier studies indicating that the Nb_7KGK exhibits optimal interaction with RBD Variant-of-Concern (VOC)[16].

3.2 Structural-based engineering of lead nanobody for RBD XBB.1.5

To improve the binding affinity and specificity of the Nb_7KGK, the modification of engineered Nb centered on crucial target residues at the interaction site of Nb to RBD XBB.1.5, while considering the non-contact/interaction amino acid(s) and amino acid(s) that caused unfavorable residues upon protein-protein surface contact. In the introduction of single site-directed mutations, each mutation site was altered with various amino acids possessing diverse properties. For instance, Figure 2a-b illustrated that at the intriguing mutation sites of Nb_7KGK, including threonine (T33), glutamic acid (E44), alanine (A50), glycine (G55), alanine (A62), isoleucine (I98) and glutamine (Q104) were considered to mutate. We discovered that the majority
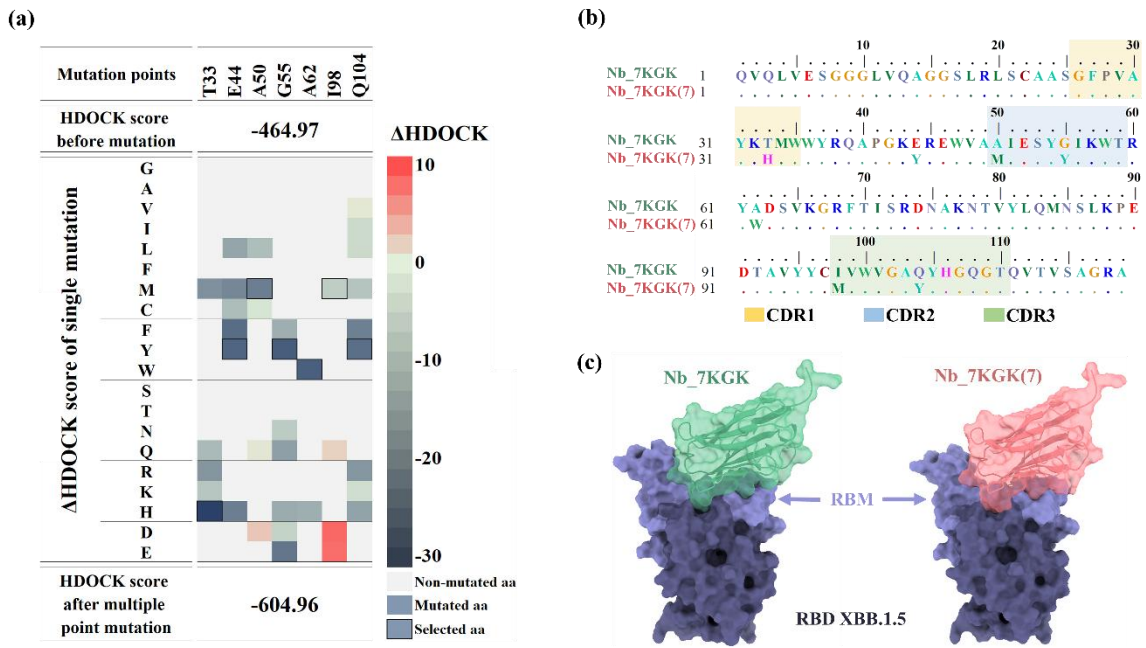
Figure 1. HDOCK score results of the docking of 29 Nbs with RBD XBB.1.5.

of mutated residues in Nb_7KGK were aromatic residues tyrosine (Y), tryptophan (W), and histidine (H) with higher ΔHDOCK scores. Amino acid candidates were selected based on their potential to contribute to hydrophobic interactions with the RBD XBB.1.5. As a result, the engineered Nb_7KGK(7) from the multi-point mutation exhibited a more robust interaction with RBD XBB.1.5. Obviously, the HDOCK score of Nb_7KGK(7) (-604.96) indicated that the engineered Nb provided a higher binding affinity more than native Nb_7KGK. Notably, Figure 1(b) proves that the primary characteristic of the lead Nb_7KGK was its emphasis on the complementarity-determining regions (CDRs), specifically CDRs 1-3, for engaging with the RBM of RBD XBB.1.5[22,23]. As expected, the Nb_7KGK(7) still interact on receptor-binding motif (RBM) of RBD XBB.1.5 consistently to native Nb_7KGK (see Figure 2c). Moreover, Figure 3 exhibits amino acids distribution of the Nb_7KGK(7) on RBM of RBD XBB.1.5, show higher number of interface contacted residues.

In addition, Figure 4 illustrates that Nb_7KGK(7) exhibited more overall interactions (a), interface residues (b), interface area (c), and a greater number of hydrogen bonds and non-bond contacts (d) in terms of chemical interactions. It is evident that the mutation residues significantly enhanced chemical interactions. For instance, T33H, A50M, I98M, and Q104Y significantly improved hydrogen bond interactions, while E44Y, A50M, and A62W meaningfully increased non-bond contact interactions. These findings align with previous studies that identified hydrophobic interactions from aromatic residues as a key interaction of Nb on the RBM of RBD[24,25]. Notably, the mutated residues were predominantly located within CDR1 (T33H), CDR2 (G55Y), and CDR3 (I98M and Q104Y). These are essential structural features facilitating binding to the target ligand[22,23].

Figure 2. Mutation points of Nb_7KGK; (a) ΔHDOCK score, (b) sequence alignment of Nb_7KGK and Nb_7KGK(7), and (c) structure of docking output.
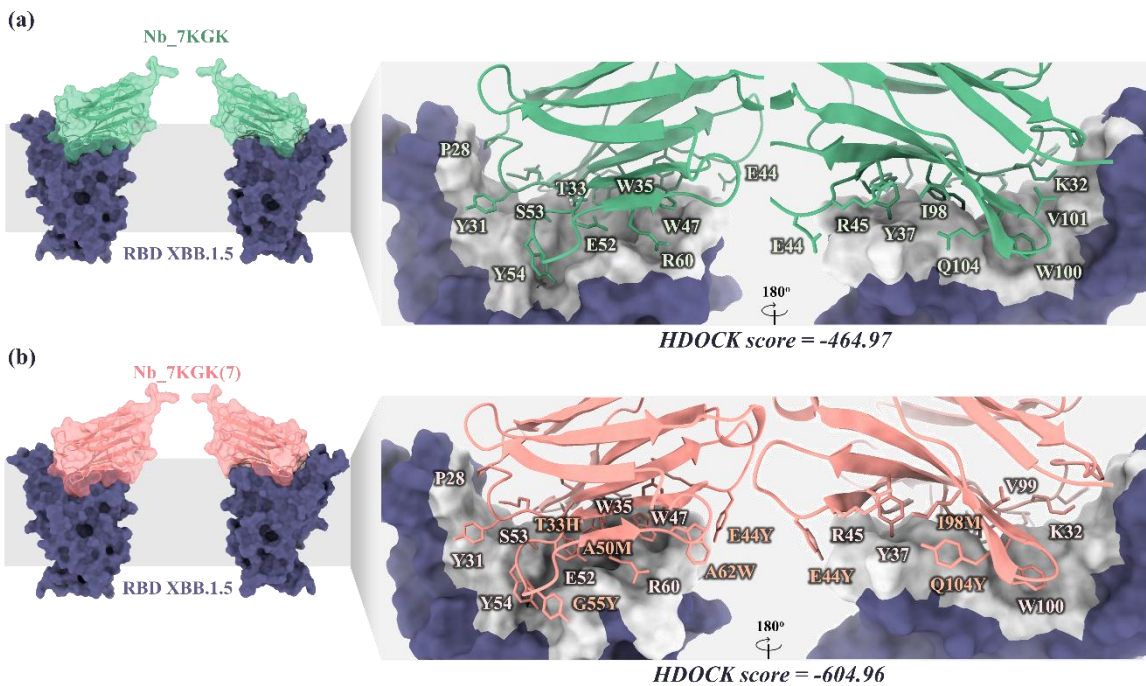

Figure 3. Distribution of interaction residues of Nb_7KGK and Nb_7KGK(7) on RBD XBB.1.5.
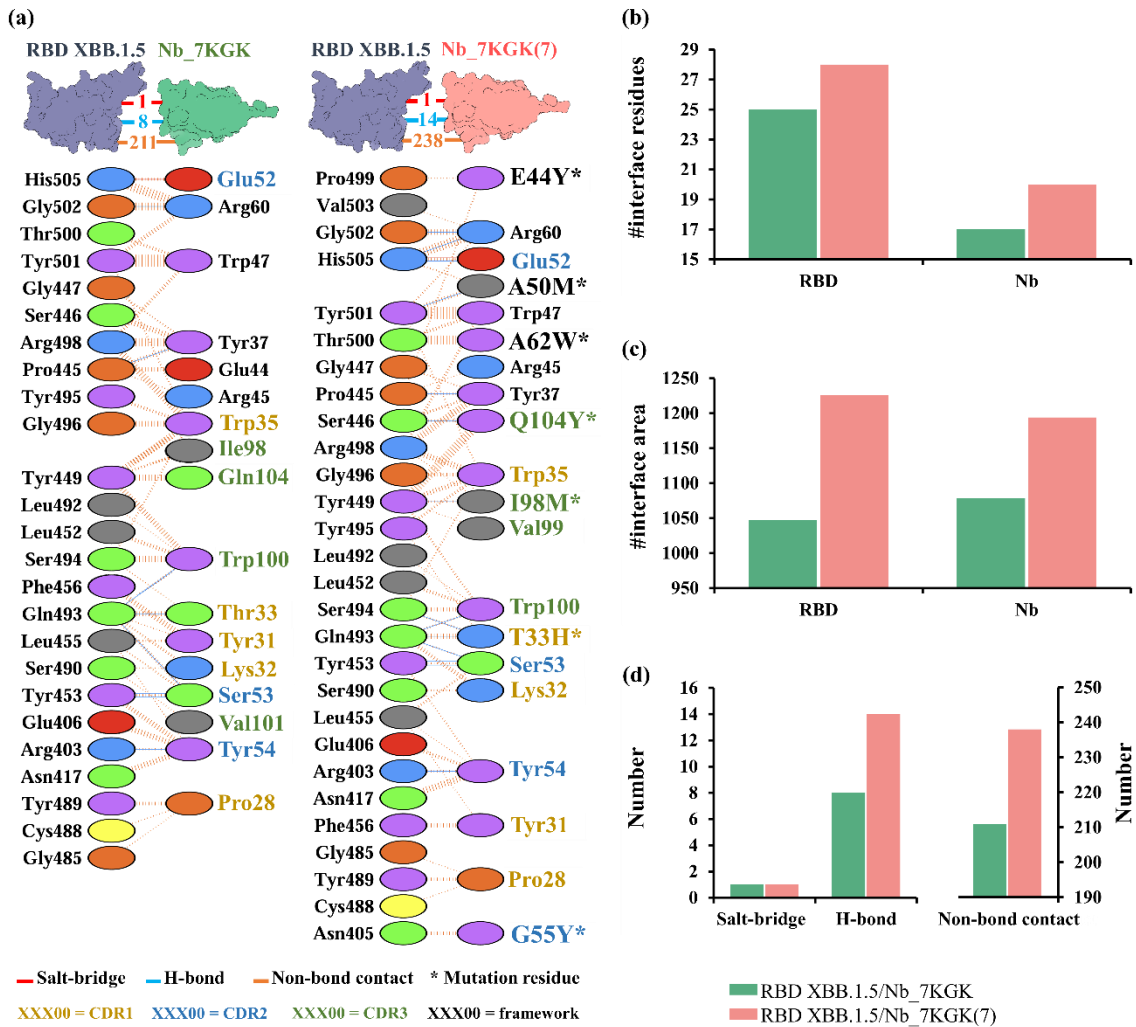
Figure 4. The comparison of protein-protein interactions of (a) Nb_7KGK and Nb_7KGK(7) with RBD XBB.1.5, (b) interface residue, (c) interface area, and (d) chemical interactions of RBD XBB.1.5/Nb_7KGK and RBD XBB.1.5/Nb_7KGK(7).

Furthermore, Figure 5 demonstrates that Nb_7KGK(7) (HDOCK score -604.96) interacts more strongly with RBD XBB.1.5 than human ACE2 (HDOCK score -305.14). This discovery indicated that Nb_7KGK(7) exhibits a robust interaction with RBD, surpassing its interaction strength with ACE2[26,27]. We suggest that the engineered Nb could potentially be developed as a new neutralizing Nb for the protection or treatment of SARS-CoV-2 XBB.1.5 infection[28,29].
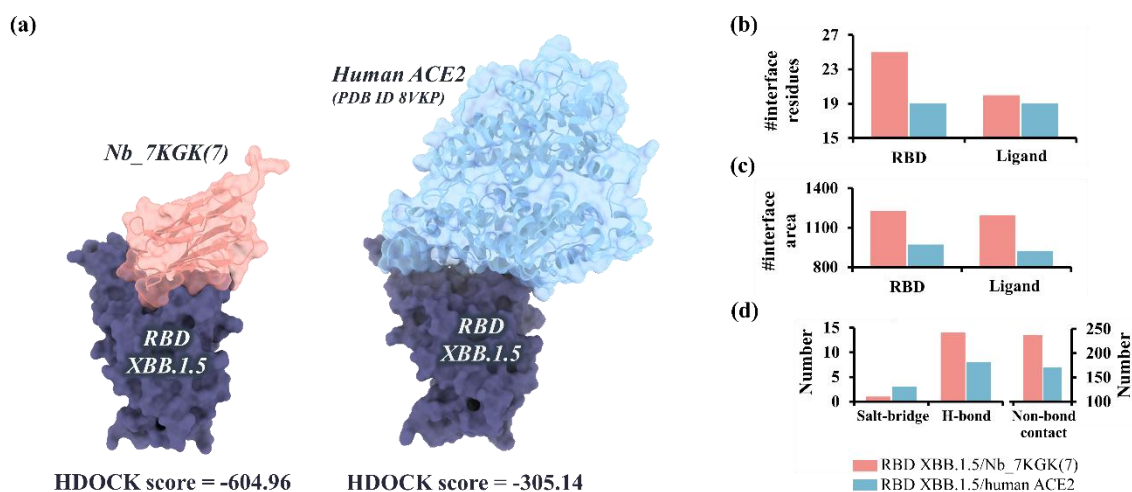
Figure 5. The comparison of (a) HDOCK score and binding posture, and the protein-protein interaction parameters; (b) interface residue, (c) interface area, and (d) chemical interactions of RBD XBB.1.5/Nb_7KGK(7) and RBD XBB.1.5/human ACE2

3.3 Physicochemical properties

According to predictions of physicochemical properties in Table 1, the engineered Nb_7KGK(7) exhibited only minor alterations in its overall characteristics compared to its original form, Nb_7KGK. Replacing the aliphatic residues in the native Nb with aromatic residues (G55Y and A62W) led to a slightly decrease in the aliphatic index. In contrast, aromatic mutations (T33H, E44Y, G55Y, A62W, and Q104Y) increased the molar extinction coefficient at 280 nm, thereby imparting a distinctive trait to the novel Nb[30]. Although the engineered Nb_7KGK(7) has a higher aromatic residue content, the histidine substitution at T33H enhanced polarity (resulting in a more negative GRAVY) and total charge at biological pH, thereby increasing the pI value[31]. Typically, nanobodies exhibit a basic pI value and a high positive charge as a common trend, strategically designed to mitigate self-aggregation[22]. Since mutations were distributed across seven residues, all mutation residues preserved the solubility of Nb_7KGK(7).

Table 1. Physicochemical properties of Nb_7KGK and Nb_7KGK(7)

Physicochemical properties	Nb_7KGK	Nb_7KGK(7)
Number of amino acids	119	119
Formula weight	13144.88	13549.42
Aliphatic index	72.94	67.98
Ext. coefficient (at 280 nm, disulfide forms)	39420	49515
Grand average of hydropathicity (GRAVY)	-0.274	-0.309
Total charge at pH 7.4	4.7	5.8
pI value	9.36	9.42
Solubility	0.61	0.61

4. Conclusion

The selection of the lead Nb for RBD XBB.1.5 was based on a docking process, aiming for a low HDOCK score indicating high binding affinity. Nb_7KGK exhibited the highest binding affinity, making it the lead Nb for further engineering. The Nb_7KGK(7) was engineered through multiple point mutations focusing on key residues, showing enhanced interaction with RBD XBB.1.5 and surpassing the native Nb_7KGK in binding affinity. This engineered Nb displayed stronger interaction

with RBD XBB.1.5 compared to human ACE2, indicating its potential as a neutralizing agent against SARS-CoV-2 XBB.1.5. The physicochemical property predictions of Nb_7KGK(7) showed improved properties, such as an increased molar extinction coefficient and pI value, while maintaining good solubility.

References

1. Parums, D. V. *Medical science monitor: international medical journal of experimental and clinical research* **29**, e939580-939581 (2023).
2. Sugano, A. *et al. bioRxiv*, 2023.2001. 2018.524660 (2023).
3. Ju, B. *et al. Nat.* **584**, 115-119 (2020).
4. Ray, D., Quijano, R. N. & Andricioaei, I. *Chem. Sci.* **13**, 7224-7239 (2022).
5. Zhou, T. *et al. Sci.* **376**, eabn8897 (2022).
6. Capela, E. V., Aires-Barros, M. R., Freire, M. G. & Azevedo, A. M. *Front Clini Drug Res Anti Infect* **4**, 142 (2017).
7. Ackaert, C. *et al. Front. immunol.* **12**, 632687 (2021).
8. Huo, J. *et al. Nat. Struct. Mol. Biol.* **27**, 846-854 (2020).
9. Zhong, G. *et al. Small* **15**, 1904881 (2019).
10. Salema, V. & Fernández, L. Á. *Microb. Biotechnol.* **10**, 1468-1484 (2017).
11. Che, Y.-J. *et al.* in *The 9th IEEE International Conference on Nano/Micro Engineered and Molecular Systems (NEMS).* 440-443 (IEEE).
12. Burley, S. K. *et al. Protein crystallography: methods and protocols*, 627-641 (2017).
13. Yan, Y., Tao, H., He, J. & Huang, S.-Y. *Nat. Protoc* **15**, 1829-1852 (2020).
14. Maier, J. A. *et al. J. Chem. Theory Comput.* **11**, 3696-3713 (2015).
15. Best, R. B. *et al. J. Chem. Theory Comput.* **8**, 3257-3273 (2012).
16. Longsompurana, P. *et al. PLoS ONE* **18**, e0293263 (2023).
17. Tippmann, H.-F. *Briefings in bioinformatics* **5**, 82-87 (2004).
18. Laskowski, R. A., Jabłońska, J., Pravda, L., Vařeková, R. S. & Thornton, J. M. *Protein Sci* **27**, 129-134 (2018).
19. Gasteiger, E. *et al. Protein identification and analysis tools on the ExPASy server.* (Springer, 2005).
20. Hebditch, M., Carballo-Amador, M. A., Charonis, S., Curtis, R. & Warwicker, J. *Bioinformatics* **33**, 3098-3100 (2017).
21. Deller, R., Carter, B., Zampetakis, I., Scarpa, F. & Perriman, A. *Biochem Biophys Res Commun* **495**, 1055-1060 (2018).
22. Zhong, Z. *et al. Biochem Biophys Res Commun* **572**, 1-6 (2021).
23. Fernández-Quintero, M. L., DeRose, E. F., Gabel, S. A., Mueller, G. A. & Liedl, K. R. *IJMS* **23**, 5419 (2022).
24. Lan, J. *et al. Nat.* **581**, 215-220 (2020).
25. Wang, Y., Liu, M. & Gao, J. *Proceedings of the National Academy of Sciences* **117**, 13967-13974 (2020).
26. Wagner, T. R. *et al. EMBO reports* **22**, e52325 (2021).
27. He, S. *et al. Vaccines* **11**, 371 (2023).
28. Wu, X. *et al. Cell reports* **37** (2021).
29. Entzminger, K. C. *et al. Antib. Ther.* **6**, 108-118 (2023).
30. Pawar, P. P. & Bichile, G. K. *Archives of Physics Research* **2**, 50-59 (2011).
31. Huyghues-Despointes, B. M. *et al. J. Mol. Biol.* **325**, 1093-1105 (2003).

Evaluation of Pyrazalone Derivatives as a Potential EGFR Inhibitor

Yazdaniyar Fajri Halimi[1], Duangjai Todsaporn[1], Athina Geronikaki[2], and Thanyada Rungrotmongkol[1,3]*

[1]Department of Biochemistry, Faculty of Science, Chulalongkorn University, Bangkok, 10330, Thailand
[2]Department of Pharmaceutical Chemistry, School of Pharmacy, Aristotle University of Thessaloniki, Thessaloniki 54124, Greece
[3]Program in Bioinformatics and Computational Biology, Graduate School, Chulalongkorn University, Bangkok 10330, Thailand
*thanyada.r@chula.ac.th

Introduction

The Epidermal Growth Factor Receptor (EGFR), a transmembrane glycoprotein with tyrosine kinase activity, plays a pivotal role in regulating various signaling pathways.[1] Overexpression of EGFR is reported to be associated with several cancers including non-small- cell lung cancer (NSCLC) metastasis and survival prognosis.[2] Erlotinib and gefitinib as the first- generation EGFR drugs have demonstrated promising results in NSCLC patients.[3] However, with extended use, treatment involving first-generation EGFR drugs can result in the development of L858R-T790M and exon 19 deletion mutations, which have the potential to diminish drug sensitivity.[4] In response, researchers have developed irreversible second- generation medications, such as afatinib and dacomitinib. Nevertheless, clinical trial experiments reported side effects, including skin disorders and gastrointestinal issues.[5] The development of the 3rd generation, osimertinib, to overcome T790M secondary mutation exhibits excellent inhibitory activity and safety profile improvement. However, the C797S mutation developed after treatment with osimertinib. This mutation had caused drug binding interference, leading to drug resistance.[6] Therefore, the development of efficacious alternative EGFR inhibitors remains a formidable challenge in the field.

Molecular docking emerges as a valuable tool for assessing the inhibitory activity of potential candidates targeting EGFR. Here, we employed molecular docking to screen a series of pyrazalone derivatives, a five-membered ring containing an adjacent diaza structure with a ketone group, aiming to study their potential towards both wild-type (WT) and L858R-T790M (DM) EGFR inhibitors, aiming to contribute to the ongoing efforts in the search for effective therapeutic options for EGFR-driven cancers.

Methodology

The crystal structures of wild-type and double mutant EGFR tyrosine kinase (TK) were retrieved from the Protein Data Bank with PDB ID:6VHN and PDB ID:5UGC, respectively. The missing residues were built using the Modeller 10.5 program.[7] Fifty-nine pyrazalones from our in-house library were independently docked into the ATP binding site using the Chemscore- kinase template with the following parameters: a 10Å sphere and 100 docking poses. The compound with the highest PLP-score was then visualized using the Discovery Studio program.

Results and Discussion

A molecular docking experiment was performed to study the binding mode of the screened compound against EGFR-TK. Erlotinib and gefitinib were used as standard references for WT- EGFR-TK, while for DM EGFR-TK, osimertinib was used as a positive control. A molecular docking study on WT EGFR-TK showed that there are 5 compounds that possess a higher score than gefitinib. While for DM EGFR-TK, there are 4 compounds that have a higher score than osimertinib. The highest-scored compound in WT EGFR-TK is PRL6, while for DM EGFR-TK, PRL11 is identified as the most potential compound. Interestingly, PRL57 exhibits dual inhibition activity against both WT and DM strains.

The binding analysis of the WT-gefitinib shows one Hbond interaction at Met98, while the WT-PRL6 complex indicates four Hbonds: 3 Hbonds found at Arg53 and one at Asp160, which contribute to increased binding affinity better than gefitinib. The DM-ligand interaction analysis of osimertinib exhibits Hbond interaction at Met92, while PRL11 forms Hbond at Cys96. However, further

experimental validation of the predicted inhibitory activity of the ligands is crucial step for confirming their potential activity as EGFR inhibitors.
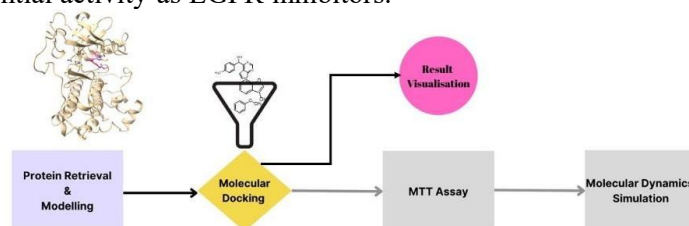

Figure 1. Workflow for the discovery of novel EGFR inhibitors (black: completed work and grey: future work)

Significance

This study contributes to the understanding of potential EGFR-TK inhibitors by identifying novel compounds with a binding affinity better than gefitinib and osimertinib, which are commonly used EGFR-TK inhibitors. The discovery of compounds PRL6, PRL11, and PRL57 may improve further exploration and optimization of EGFR-targeted inhibitors. The discovery provides considerable implications for advancing the development of more efficacious inhibitors for EGFR-related illnesses, such as NSCLC.

References
(1)   Uribe, M. L.; Marrocco, I.; Yarden, Y. Cancers EGFR in Cancer: Signaling Mechanisms, Drugs, and Acquired Resistance. **2021**. https://doi.org/10.3390/cancers.
(2)   Mukohara, T. Expression of Epidermal Growth Factor Receptor (EGFR) and Downstream-Activated Peptides in Surgically Excised Non-Small-Cell Lung Cancer (NSCLC). *Lung Cancer* **2003**, *41* (2), 123–130. https://doi.org/10.1016/S0169- 5002(03)00225-3.
(3)   Kris, M. G.; Natale, R. B.; Herbst, R. S.; Lynch, T. J.; Prager, D.; Belani, C. P.; Schiller, J. H.; Kelly, K.; Spiridonidis, H.; Sandler, A.; Albain, K. S.; Cella, D.; Wolf, M. K.; Averbuch, S. D.; Ochs, J. J.; Kay, A. C. *Efficacy of Gefitinib, anD Inhibitor of the Epidermal Growth Factor Receptor Tyrosine Kinase, in Symptomatic Patients With Non-Small Cell Lung Cancer A Randomized Trial*; 2003; Vol. 290. www.jama.com.
(4)   Morgillo, F.; Della Corte, C. M.; Fasano, M.; Ciardiello, F. Mechanisms of Resistance to EGFR-Targeted Drugs: Lung Cancer. *ESMO Open* **2016**, *1* (3), e000060. https://doi.org/10.1136/esmoopen-2016-000060.
(5)   Barron, F.; de la Torre-Vallejo, M.; Luna-Palencia, R. L.; Cardona, A. F.; Arrieta, O. The Safety of Afatinib for the Treatment of Non-Small Cell Lung Cancer. *Expert Opin Drug Saf* **2016**, *15* (11), 1563–1572. https://doi.org/10.1080/14740338.2016.1236910.
(6)   Lazzari, C.; Gregorc, V.; Karachaliou, N.; Rosell, R.; Santarpia, M. Mechanisms of Resistance to Osimertinib. *J Thorac Dis* **2020**, *12* (5), 2851–2858. https://doi.org/10.21037/jtd.2019.08.30.
(7)   Šali, A.; Blundell, T. L. Comparative Protein Modelling by Satisfaction of Spatial Restraints. *J Mol Biol* **1993**, *234* (3), 779–815. https://doi.org/10.1006/jmbi.1993.1626.

Theoretical analysis of the influence of residues around the chromophore on Enhanced Green Fluorescent Protein

Mio Takakuwa, Yukiumi Kita, Tomomi Shimazaki, Masanori Tachikawa*

Graduate School of NanoBioScience, Yokohama City University, Seto 22-2, Kanazawa-Ku, Yokohama 236-0027, Kanagawa, Japan
*tachi@yokohama-cu.ac.jp

Introduction

Green Fluorescent Proteins (GFPs) emit a green glow, and their variant, Enhanced GFP (EGFP), shines even brighter, making it extensively used in bio-imaging applications[1]. Both GFP and EGFP have their chromophore centrally located, which is crucial for luminescence. These proteins autonomously synthesize their chromophores, which emit light upon excitation, proving crucial for bio-imaging purposes. Typically, internal residues within proteins form hydrogen bonds with adjacent residues, influencing each other's interactions. In EGFP, residues surrounding the chromophore, such as Arg96 and Thr203, have been experimentally shown to play significant roles, as depicted in Figure 1. Previous studies suggest that Arg96 has been implicated in the charge delocalization of the EGFP chromophore[2] and Thr203 is able to stabilize the anionic form of the chromophore by forming hydrogen bonds between its side chain to the chromophore[3]. However, the theoretical details of their individual impacts remain poorly understood. Thus, this study theoretically investigates the influence of these residues on the chromophore, their hydrogen-bonded structures, and fluorescence spectra, aiming to clarify the roles of Arg96 and Thr203.

Methodology

From the structure of EGFP (PDB ID: 6L26), obtained via neutron crystallography which includes deuterium atoms, we created the "EGFP model". This model incorporates residues and heavy water molecules directly hydrogen-bonded to the chromophore, so it has total of 13 residues: chromophore (CRO), Val61, Thr62, Gln94, Arg96, Asn146, His148, Thr203, Ser205,
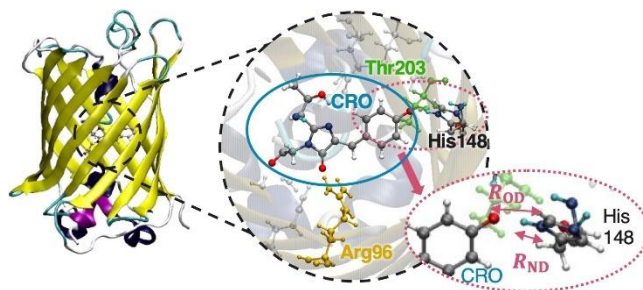

Figure 1. The location of CRO, Arg96, Thr203 and His148 in EGFP.

Glu222, DOD301, DOD306, DOD323. Further, we created the "model without Arg96", consisting of 181 atoms and the "model without Thr203", consisting of 191 atoms excluding only Arg96 or Thr203, respectively. Given the presence of deuterium in the PDB file, we use the multi-component density functional theory extended to density functional theory (MC_DFT), which extends the quantum effects of light-mass particles to particles other than electrons, such as protons and deuterons[4]. In MC_DFT calculations, B3LYP/6-31++G(d,p) were used for electrons, and all protons and deuterons are expressed as 1s Gauss type functions. During the calculations, we enforced the constraints that heavy atoms, except for CRO and heavy water molecules, are fixed to preserve the relative molecular orientation between the CRO and residues under the protein environment.

Results and Discussion

Figure 1 shows the definitions of the distance between the oxygen atom of the CRO and the deuterium atom of His148 (R_{OD}) and the distance between the nitrogen atom and the deuterium atom in His148 (R_{ND}). The values of R_{OD} and R_{ND} for all models and experimental values are summarized in Table 1. In the absence of Arg96 or Thr203, R_{OD} becomes shorter than R_{ND}, whereas it becomes longer in the hydrogen-bonded model and experimental value. These results indicate that Arg96 and Thr203 have a crucial role in stabilizing the deprotonated state of the CRO. Additionally, it has been found that these two residues also influence the charge of CRO, as well as its absorption and fluorescence spectra. More complete results have been reported in our recent paper[5].

Table 1. R_{OD} and R_{ND} bond length in each model. (Units in Å.)

Model	R_{OD}	R_{ND}
Experimental Value[6]	1.767	1.029
EGFP model	1.546	1.103
Model without Arg96	1.048	1.646
Model without Thr203	1.030	1.772

Significance

This study delves into the physicochemical origins of the emission properties of EGFP, an essential tool for bioimaging applications. Employing quantum chemical calculations, we specifically investigate the structural roles, charge, and fluorescence spectra of Arg96 and Thr203, which are directly hydrogen-bonded to the CRO. This approach provides deeper insights into how particular protein residues affect the behavior, stability, and fluorescence of the CRO. Our findings offer significant contributions to the understanding of protein structure and its fluorescence properties, paving the way for the development of more accurate and controlled bioimaging techniques.

References

1. R. Y. Tsien, *Annu. Rev. Biochem.* 67, 509 (1998).
2. J. A. Sniegowski, *et al. Biochem.Biophys. Res. Commun.* 332, 657 (2005).
3. J. Kaur*, et al*. *Photochem. Photobiol.* 95, 543 (2019).
4. T. Udagawa, *et al*. *J. Chem. Phys.* 125, 244105 (2006).
5. M.Takakuwa, *et al*. *Bull. Chem. Soc. Jpn.* 96, 711–716 (2023).
6. C. Shibazaki, *et al*. *J. Phys. Chem. Lett.* 11, 492(2020).

AI Harmony: Integrating Hormonal Mechanisms into LLMs for Improved Decision-Making

Kasidis M. and Taechasith K.
Ratchasima Witthayalai School, Nakhon Ratchasima, 30000 (Thailand)
*rs59253@rajsima.ac.th and rs62617@rajsima.ac.th

Introduction

In the pursuit to enhance artificial intelligence (AI) by mirroring human cognitive processes, this study explores the integration of hormonal mechanisms into the Chat-GPT 4 model to improve decision-making and problem-solving abilities. The research hypothesizes that hormonal principles, crucial for regulating human mood, cognition, and productivity, can significantly boost AI performance when simulated within AI systems (Wise R.A. et al., 2004; Florian et al., 2012).

Methodology

We focus on four key hormones: Dopamine, Endorphin, Serotonin, and Cortisol, which are crucial in regulating human mood, cognition, and productivity. Our methodology involves a detailed analysis of these hormones' roles and mechanisms, followed by adapting and integrating these mechanisms into the Chat-GPT 4's workflow. The effectiveness of this hormone-inspired AI model is assessed using standardized tests such as the SAT to measure improvements in decision-making accuracy and speed. (Sonne et al., 2023; SAT Suite, n.d.).

Results and Discussion

Initial testing showed that the Hormone-Inspired GPT model, termed Monkan Kankoon, outperformed the standard Chat-GPT 4 in both decision-making accuracy and problem-solving speed on simulated SAT exams. We did no specific training for these exams. Exams were sourced from publicly available materials. Exam questions included both multiple-choice; we designed separate prompts for each format, and images were included in the input for questions that required it. Notably, Monkan Kankoon achieved a 1.1% higher score in the SAT Reading & Writing section and an 8.5% increase in the SAT Math section compared to the baseline model.

Exam	GPT-4	Monkan
SAT Evidence-Based Reading & Writing	1:38 minutes (98.6 seconds)	1:59 minutes (119 seconds)
SAT Math	2:14 minutes (134 seconds)	2:07 minutes (127 seconds)

Table 1: Time Taken by Monkan's (GPTs) and Chat-GPT 4 on Each Exam

Exam	GPT-4	Monkan
SAT Evidence-Based Reading & Writing	723.3 (~ 91%)	730 (~ 92%)
SAT Math	566.6 (~ 65%)	603.3 (~ 71%)

Table 2. Monkan's (GPTs), and Chat-GPT 4 performance on academic and professional exams. We report GPT-4's final score graded according to exam-specific rubrics, as well as the percentile.

As shown in Table 2 Monkan Kankoon (GPTs) demonstrates superior performance compared to GPT-4 in both exams. Monkan Kankoon scored approximately 1.1% higher on the SAT Reading & Writing section and approximately 8.5% higher on the SAT Math section.
However, as shown in Table 1, it took longer for Monkan to respond, with a delay of 21.1 seconds on the SAT Reading & Writing section and 7 seconds on the SAT Math section.

While the results are promising, the reliance on standardized tests for validation presents limitations regarding the model's application in real-world scenarios. Future research will expand testing to include

a broader range of cognitive tasks and explore additional hormonal influences to provide a more comprehensive assessment of the model's capabilities.

Significance

The integration of hormonal mechanisms into AI represents a novel approach to enhancing cognitive computing technologies, offering substantial improvements in AI-driven decision- making processes. This interdisciplinary endeavor not only bridges biological insights with AI development but also paves the way for future innovations in neuro-inspired AI applications.

References

1. Wise, R. A. (2004). Dopamine, learning and motivation. *Nature Reviews. Neuroscience*, 5(6), 483–494. https://doi.org/10.1038/nrn1406
2. Florian, R.P., et al. (2012). 'The Role of Serotonin in Cognitive Function: Evidence from Recent Studies.' *Journal of Psychopharmacology*, 26(7), 1020–1026. https://doi.org/10.1177/0269881112440613
3. *Full-Length Linear SAT Practice Tests (Nonadaptive) – SAT Suite.* (n.d.). https://satsuite.collegeboard.org/sat/practice-preparation/practice-tests/linear
4. Sonne, J., Goyal, A., & Lopez-Ojeda, W. (2023, July 3). *Dopamine.* StatPearls -NCBI Bookshelf. https://www.ncbi.nlm.nih.gov/books/NBK535451/
5. Chaudhry, S. R., & Gossman, W. (2023, April 3). *Biochemistry, endorphin*. StatPearls - NCBI Bookshelf. https://www.ncbi.nlm.nih.gov/books/NBK470306/

A Graph Convolutional Deep Learning Model for Identifying Potential Aromatase Inhibitors

Teeraphan Laomettachit[1]* and Monrudee Liangruksa[2]
[1]Bioinformatics and Systems Biology Program, School of Bioresources and Technology, King Mongkut's University of Technology Thonburi, Bangkok 10140 (Thailand)
[2] National Nanotechnology Center (NANOTEC), National Science and Technology Development Agency (NSTDA), Pathum Thani 12120 (Thailand)
*teeraphan.lao@kmutt.ac.th

Introduction

Aromatase inhibitors play a crucial role in the treatment of hormone-sensitive breast and lung cancers by blocking the conversion of androgens to estrogens.[1, 2] However, there is a need for more effective and selective aromatase inhibitors. Recent advancements in deep learning devoted to drug discovery are the application of graph convolutional neural networks to predict the properties of small molecules represented as graphs. In this study, we utilize the inhibitory activities of experimentally tested compounds against aromatase from the PubChem database. We develop a graph convolutional deep neural network capable of predicting molecules with aromatase inhibitory properties. The model with the most optimal hyperparameter set exhibits an AUC of 0.83. Our model serves as a good starting point for further development and for screening potential aromatase inhibitors, which can help save time and resources that would otherwise be spent on trial-and-error experiments.

Methodology

We retrieved a list of compounds tested for inhibitory activity against aromatase from PubChem (https://pubchem.ncbi.nlm.nih.gov/) (Gene ID: 1588). After removing duplicates, the compounds were split into two categories: 2474 'active' compounds (inhibitory effect observed) and 3129 'inactive' compounds (no inhibitory effect observed). The classification was based on PubChem's criteria, where compounds with IC50 ≤ 10 µM were classified as 'active'.

Using the DeepChem library (https://deepchem.io/), we implemented a graph convolutional neural network model that leverages compounds' atomic features and structural information.[3] The model's performance in predicting the active or inactive properties of the compounds was evaluated by the AUC. This evaluation was carried out by comparing 16 different hyperparameter sets with the 3-fold cross-validation method. The hyperparameter set with the highest AUC after being averaged among the 3-fold was chosen (Fig. 1A).

Results and Discussion

Based on our method, the most optimal model with the highest AUC is comprised of the following layers: a 64-node graph convolutional layer with ReLU activation, a batch normalization layer, a graph pool layer, a 128-node dense layer with ReLU activation, another batch normalization layer, a graph gather layer with tanh activation, and an output node that uses the SoftMax function to assign a probability of a compound being "active" (i.e., having an inhibitory effect on aromatase).

Figure 1B compares the AUC from our deep learning model with the most optimal hyperparameter set (AUC = 0.83) to five other machine learning algorithms (AUC ranging from 0.76 to 0.79).

Significance

Recently, graph convolutional neural networks have been successfully used to extract information from small molecules in the form of graphs. This technique has proven effective in learning molecular features and fingerprints. The current work focuses on the use of the technique in predicting molecules with aromatase inhibitory properties, which can be used in the treatment of hormone-sensitive breast and lung cancers.

The developed model, achieving the AUC of 0.83, offers a promising further study to screen novel aromatase inhibitors from extensive databases, especially with compounds from natural products. The

ability to predict molecular properties using deep learning techniques provides an exciting opportunity to accelerate the drug discovery process.
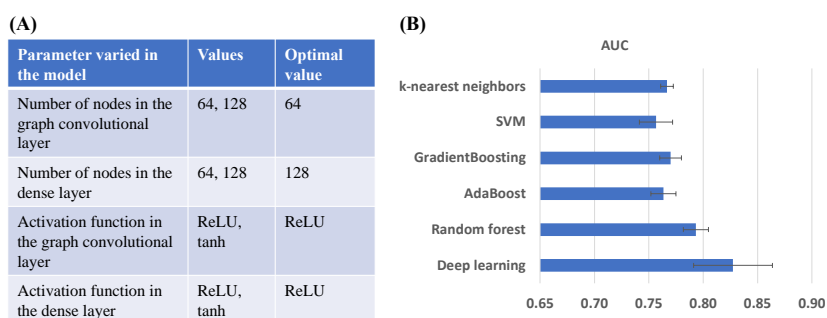
(A)

Parameter varied in the model	Values	Optimal value
Number of nodes in the graph convolutional layer	64, 128	64
Number of nodes in the dense layer	64, 128	128
Activation function in the graph convolutional layer	ReLU, tanh	ReLU
Activation function in the dense layer	ReLU, tanh	ReLU

(B)

Figure 1. (A) Hyperparameters considered in this study and the optimal values obtained from the 3-fold CV method. (B) Comparison of the AUC between the deep learning model and five other machine learning models.

References

(1) Brueggemeier, R. W.; Hackett, J. C.; Diaz-Cruz, E. S. Aromatase inhibitors in the treatment of breast cancer. *Endocr Rev* **2005**, *26* (3), 331-345. DOI: 10.1210/er.2004-0015.
(2) Weinberg, O. K.; Marquez-Garban, D. C.; Fishbein, M. C.; Goodglick, L.; Garban, H. J.; Dubinett, S. M.; Pietras, R. J. Aromatase inhibitors in human lung cancer therapy. *Cancer Res* **2005**, *65* (24), 11287-11291. DOI: 10.1158/0008-5472.Can-05-2737.
(3) Duvenaud, D. K.; Maclaurin, D.; Iparraguirre, J.; Bombarell, R.; Hirzel, T.; Aspuru-Guzik, A.; Adams, R. P. Convolutional networks on graphs for learning molecular fingerprints. *Adv Neural Inf Process Syst* **2015**, *28*.

Unlocking Methanol Production from Carbon Dioxide: The Crucial Role of Amine in Ru-PNP Catalysis

Sirilak Kongkaew[1], Maneeporn Puripat[1], Thanawit Kuamit[1], Waraporn Parasuk[2], Vudhichai Parasuk[1,*]

[1]*Center of Excellence in Computational Chemistry, Department of Chemistry, Faculty of Science, Chulalongkorn University, Bangkok 10330, Thailand*
[2]*Department of Chemistry, Faculty of Science, Kasetsart University, Bangkok 10900, Thailand*
*Vudhichai.P@chula.ac.th

Introduction

Fossil fuel combustion emits carbon dioxide (CO_2), harming human health and air quality. Capturing and converting CO_2 into useful compounds offers a practical solution to reduce atmospheric CO_2 levels. Among the various CO_2-recycling products, methanol is the most desirable. Its prominence is since the chemical industries employ it as a feedstock and "green" liquid fuel. The experimental research has reported CO_2 can convert to methanol at 36% and side product at 64% by Ru-complex catalyst and morpholine co-catalyst; unfortunately, it cannot convert to methanol without the amine involvement [1]. In this study, we use DFT calculations to investigate how the ruthenium complex (Ru-PNP) catalyst with ethylenediamine (EDA) assistance, can convert CO_2 to methanol.

Methodology

The Gaussian 09, Revision E.01 software was applied to perform the density functional theory (DFT) computations [2]. The calculations employed the B3LYP-D3 hybrid functional with a mixed 6–31g(d) basis set for C, H, O, P, and N, and the SDD basis set for Ru [3]. Energetic refinements were performed at the B3LYP-D3/SDD (Ru), 6–31+g(d,p) (C, H, O, P, and N) level of theory. Thermochemical data were computed under experimental conditions of 74.019 atm, 428.15 K and tetrahydrofuran solvent.

Results and Discussion

The concept of energetic span (δE) is employed to elucidate the process. The CO_2 conversion to methanol is explored using Ru-PNP catalysis with amine assistance through three potential routes. Route A, with $\delta E > 60$ kcal mol^{-1}, comprises three steps: the synthesis of formic acid, formamide, and methanol. While Route B, with $\delta E = 35.07$ kcal mol^{-1}, consists of four steps: the formation of formic acid, formamide, formaldehyde, and methanol. Lastly, Route C, with $\delta E = 39.14$ kcal mol^{-1}, involves sub-pathways of formic acid, formaldehyde, and methanol. Route B has the lowest δE; thus, it is the most favorite route. In the case of EDA absence, CO_2 hydrogenation to formic acid cannot form, since the formate is trapped by the catalyst. This observation explains why CO_2 conversion to methanol is unattainable without the presence of amine.
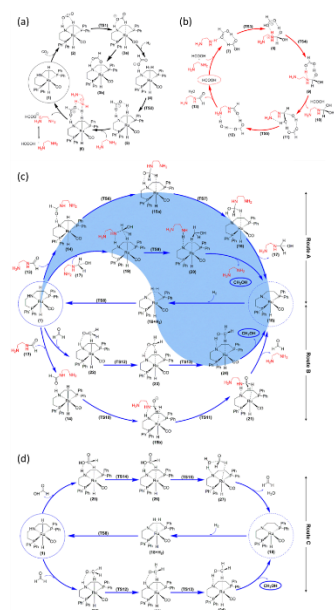
Figure 1. CO$_2$ hydrogenation to methanol via sub-pathways: (a) formic acid formation, (b) formamide formation, (c) methanol formation from alkanolamine/formaldehyde, and (d) methanol formation from formic acid
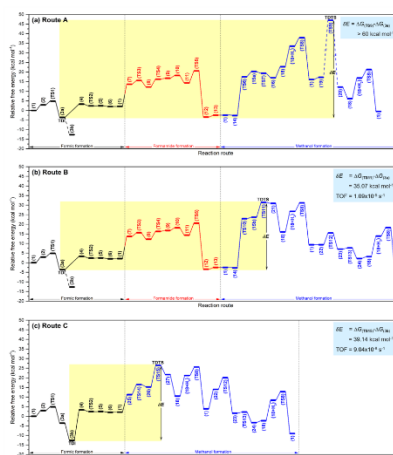

Figure 2. Relative free energy profiles are plotted continuously for sub-pathways of Route A, B and C.

Significance

The key intermediate of CO$_2$ conversion to methanol using Ru-PNP catalyst and amine assistance is formamide.
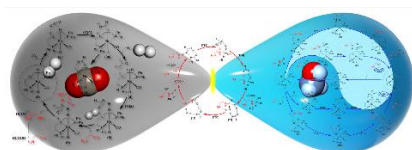

Figure 3. Reaction mechanism of Ru-PNP catalyst and amine-assisted CO$_2$ hydrogenation to methanol.

References

1. Kar, S., Sen, R., Kothandaraman, J., et al., *J. Am. Chem. Soc.* 141 (2019).
2. Becke, A.D., *Phys. Rev. A* 38 (1988).
3. Sieffert, N., Bühl, M., *J. Am. Chem. Soc.* 132 (2010).

Effect of Pore Geometries on the Ion Transport through Solid-State Nanopores

Prapasiri Pongprayoon[1], Deanpen Japrung[2] and Attaphon Chaimanatsakun [3]*

[1] *Faculty of Engineering at Sriracha, Kasetsart University Sriracha Campus,*
Chonburi 20230, Thailand
[2]*National Nanotechnology Center, National Science and Technology Development Agency,*
Pathumthani 12120, Thailand
[3]*Department of Chemistry, Faculty of Science, Kasetsart University,*
Bangkok, 10900, Thailand
*attaphon.ch@ku.th

Introduction

Solid-state nanopore is one of promising molecular biosensors because they offer adjustable properties and enhanced thermal and chemical stability. The selectivity and sensitivity of nanopores depend on their geometries and surface properties. Nanopores detect their analytes by measuring the level of current blockage when single molecule passes through them. As a molecule moves through a nanopore, it temporarily obstructs the flow of ions, leading to detectable fluctuations in the ionic current. Various designs of solid-state nanopores have been explored for sensing applications, including cylindrical (CY), hourglass (HG), and conical (CO) shapes, each offering distinct ion transport properties. Most nanopores were used for DNA sequencing where protein sequencing becomes of interest for medical applications. Our previous work shows that the pore geometries affect the current level when using subnano-sized pore. Thus, in this work, the effect of pore geometries and surface properties of nanopore that are compatible to protein sequencing are revealed. Three key pore geometries (CY, HG, and CO) are investigated here. The continuum models (finite element) are used to observe ion transport properties.

Methodology

The nanopore system, as shown in Figure 1(a), consists of two reservoirs of equal size that are separated by a membrane thickness of $t = 3.2$ nm that contains nanopores. We consider the three types of the difference pore shape (cylindrical (CY), hourglass (HG) and conical (CO)), as shown in Figure 1(b). Both the nanopore and the reservoirs are filled with an aqueous KCl solution with bulk salt concentrations are 0.01, 0.1, 1 M. To simulate ionic current through nanopores, the COMSOL Multiphysics software is used to numerically solve the coupled Nernst-Planck-Poisson (NPP) and Navier-Stokes (NS) equations. The finer meshes are used inside pore area and smaller than Debye length to accurately capture the region of the electric double layer. (EDL) [1].

Results and Discussion

In this work, the three types of pore shapes are used to investigate the effect of pore geometries on the ion transport. The current-voltage (*I-V*) curves of three types of pore shapes at different applied voltage +1V to -1V are shown in Figure 2. At the low concentration of 0.01 M and 0.1 M shows nonlinear behavior, while the higher concentration of 1 M has ohmic behavior. The result is because of the Debye layer inside nanopore. Low concentration results in a large Debye layer, whereas high concentration causes it to be small. The I-V curve of a CO pore shows that the current is smaller when a positive voltage is applied compared to when a negative voltage is applied. This indicates that the ion transport behaviors vary depending on the direction of the voltage bias, and the presence of an asymmetric pore leads to ion rectification. The nanopore conductance of CY is highest follow CO and HG.
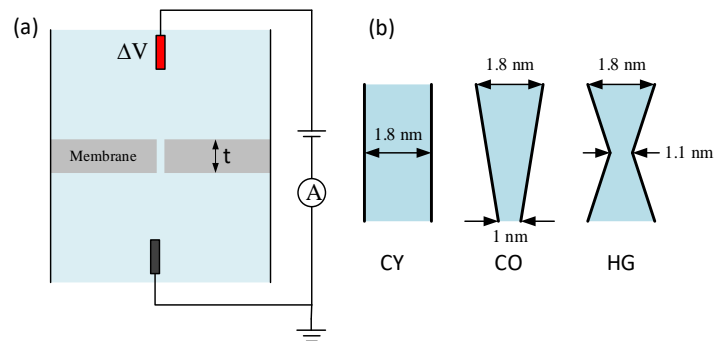
Figure 1. Schematics of (a) the nanopore system and (b) pore geometries.

Significance

The results here will be useful for nanopore design for protein sequencing.

References

1.   Laohakunakorn, N. and U.F. Keyser, *Electroosmotic flow rectification in conical nanopores.* Nanotechnology, 2015. **26**(27): p. 275202.

Leveraging Generative Pre-trained Transformers (GPT) for ESG Integration in Thai Stock Investment Management

**Nutdanai Wangpratham[1], Teerasit Termsaithong[1, 2]*, Pasin Marupanthorn[1],
Jutha Koryanyong[1], Chanon Chanpiwa[1], Carat Pathomsathit[1]**
[1]QuantCorner Laboratory, Thailand
[2]Learning Institute, King Mongkut's University of Technology Thonburi, Bangkok, Thailand
*teerasit.ter@kmutt.ac.th

Introduction

The integration of Environmental, Social, and Governance (ESG) factors into investment decision-making is becoming increasingly important due to the impact of ESG on financial performance and risk profiles. In Thailand, regulatory changes such as the Securities and Exchange Commission's (SEC) "One Report" mandate further emphasize the necessity for companies to disclose comprehensive ESG information. Despite the benefits, the complexity and volume of ESG data present significant challenges to investors. This study explores the application of Generative Pre-trained Transformers (GPT) to enhance the processing and integration of ESG considerations in investment management, particularly for Thai stocks.

Methodology

Our approach utilizes advanced natural language processing capabilities of GPT models to analyze and interpret large volumes of contextual ESG data. The methodology involves equipping GPT with the various sources of the ESG knowledge repositories, including regulator's guidance documents. The GPT model is then applied to perform ESG materiality assessments, comprehensive data analysis, and risk management. Users can access the software via the ChatGPT platform, which allows for uploading and analyzing the "One Report" format used by Thai companies.

Results and Discussion

The application of GPT models has shown significant potential in simplifying the analysis of ESG data, providing more accessible and actionable insights for investors. Key results include the model's ability to extract complex ESG information and its effectiveness in enhancing investment decision-making processes. The discussion highlights the challenges related to data quality and biases in ESG reporting, as well as the evolving nature of ESG factors. Despite these challenges, GPT models have demonstrated a substantial capability to adapt and provide valuable insights, positioning them as a critical tool for sustainable investing.

Significance

This study underscores the transformative potential of GPT models in the realm of sustainable finance. By improving the integration of ESG factors into investment processes, GPT models contribute to more informed and responsible investment strategies. This advancement not only aids investors in navigating the complexities of ESG data but also promotes the broader objective of sustainable financial markets, aligning with global sustainability goals and regulatory standards.
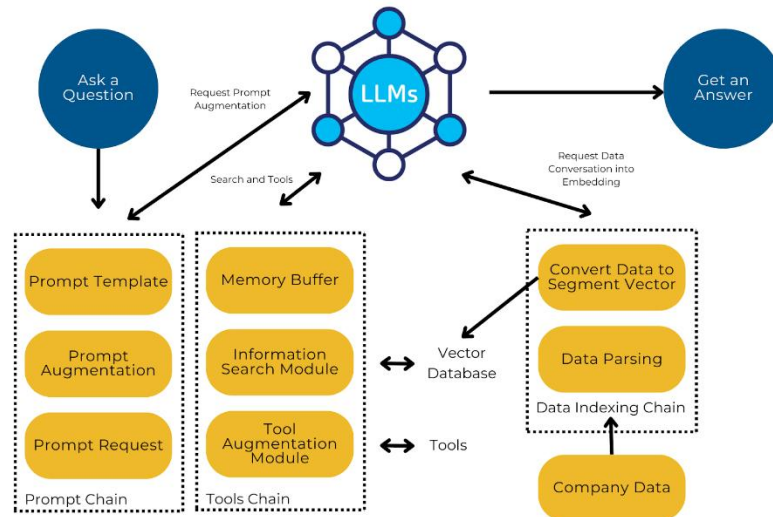
Figure 1. Conceptual Workflow for ESG Analysis Using GPT Models

References
1. Bolton, P., Despres, M., Da Silva, L. A. P., Samama, F., & Svartzman, R. (2020). The green swan. *BIS Books*.
2. Brown, T. C., et al. (2020). Language models are few-shot learners. *Advances in Neural Information Processing Systems*.
3. Schramade, W. (2016). Bridging sustainability and finance: The value driver adjustment approach. *Journal of Applied Corporate Finance*, 28(2), 17-28.
4. Clark, G. L., Feiner, A., & Viehs, M. (2015). From the stockholder to the stakeholder: How sustainability can drive financial outperformance. Available at *SSRN 2508281*.

Gamified Education for Chemical Engineering student

Naesara Kitsawat[1, 2] and Supareak Prasertdam[1, 2]*

[1] *Gamified Engineering Education Research Center (GAMER), Department of Chemical Engineering, Faculty of Engineering, Chulalongkorn University, Bangkok, 10330, (Thailand)*
[2] *Department of Chemical Engineering, Faculty of Engineering, Chulalongkorn University, Bangkok, 10330, (Thailand)*

*supareak.p@chula.ac.th

1. Introduction

Traditional education has predominantly used teacher-centered approaches, with instructors presenting content while students passively listen, limiting engagement and interaction. The most effective learning is a mix of teacher-centered and student-centered approaches [1]. Recognizing this, we developed a gamified board game for chemical engineering students, specifically for the course Unit Operation I, to increase engagement and knowledge retention.

Unit Operation I is a subject that all students of the Department of Chemical Engineering, Faculty of Engineering, Chulalongkorn University must study because its content is an important foundation for studying in the Department of Chemical Engineering. Students must understand the content of this subject to apply it to study other subjects and work.

2. Methodology

Gamification, defined as integrating game elements into non-game contexts, aims to motivate desired behaviors. Techniques like point systems, goal setting, competition, and emotional connection create engaging learning experiences.

We applied the gamification principle as a teaching medium for the Unit through board games. Our objectives were to study the game-playing technique to enhance learning, examine the effects of game-playing on students' behavior, and develop a prototype board game for Unit Operation I, covering fluid properties, flow dynamics, and related devices.

This strategic board game is set in 1887 England, where players take on the roles of chemical engineers pioneering the field of chemical engineering education. Suitable for 2-6 players and lasting 1-2 hours, the game requires participants to leverage their knowledge of Unit Operation I to develop and utilize equipment.

The game ends when a player fulfills their mission card by acquiring all required equipment. Points are earned through completing tasks and accumulating coins and star tokens. Players engage in four main actions:

  • Answering knowledge-based questions to earn coins.
  • Developing equipment by answering knowledge-based questions about that equipment.
  • Purchasing completed equipment.
  • Negotiating deals to borrow equipment when supply runs out.

With elements of competition, cooperation, and academic challenge, this game offers a unique blend of strategy and education. It tests players' problem-solving skills and understanding of engineering concepts.
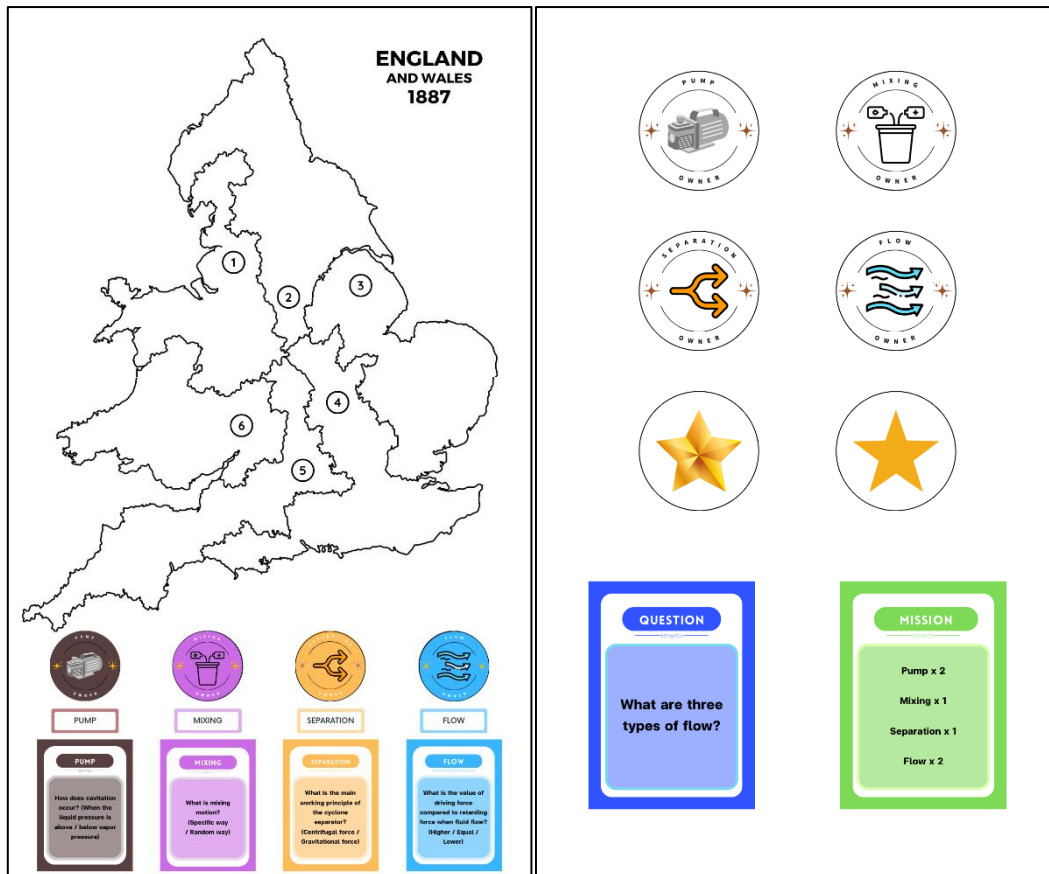
Figure 1. Prototype of board game a) The board is designed to resemble an 1887 map of England. At the bottom are question cards about equipment. and b) Other components of the game board include medals, general question cards, and mission cards.

3. Results and Discussion

Using a gamified board game as an educational tool for teaching Unit Operations in Chemical Engineering has proven highly effective in enhancing the learning experience. Traditional teaching methods often rely on lectures that can lead to passive learning and limited student engagement. In contrast, a gamified approach transforms the classroom into a dynamic and interactive environment where students actively participate in their learning process. The board game, designed specifically for the subject, immerses students in real-world scenarios where they apply theoretical knowledge to solve practical problems. This innovative method bridges the gap between theory and practice and stimulates curiosity and a deeper understanding of the material.

Students report increased motivation and enthusiasm when learning through gamification. The competitive and collaborative aspects of the game encourage them to engage more deeply with the subject matter. As they navigate challenges, answer questions, and strategize to win, they reinforce key concepts and develop a firmer grasp of fluid mechanics, heat transfer, and separation processes. Additionally, the gamified environment fosters a sense of accomplishment and satisfaction as students progress, making the learning process enjoyable and rewarding.

Beyond academic benefits, the gamified board game enhances soft skills such as teamwork, communication, and critical thinking. The game's interactive nature requires students to discuss strategies, collaborate with peers, and make decisions under time constraints, which mirrors real-world professional scenarios. Moreover, the relaxed and engaging atmosphere of the game alleviates the stress often associated with traditional assessments, allowing students to focus on learning without fearing failure.

In summary, integrating a gamified board game into the teaching of Unit Operations significantly enriches the educational experience. It improves knowledge retention and comprehension and cultivates essential skills that prepare students for their future careers in engineering. This approach

represents a modern and effective way to make complex subjects accessible, engaging, and enjoyable for students.

4. Significance

Developing a board game as an educational tool for Unit Operation I significantly enhances the learning experience. This interactive medium transforms complex engineering concepts into engaging, hands-on activities. By simulating real-world industrial scenarios in a simplified format, the board game fosters a deeper understanding of theoretical principles through experiential learning.

As a supplemental teaching tool, it supports instructors in delivering content effectively while creating a stimulating and enjoyable learning environment. This innovation aligns with modern pedagogical strategies, emphasizing active and student-centered learning, thus enhancing overall educational outcomes.

References

[1] Murphy, L., Eduljee, N. B., & Croteau, K. (2021). Teacher-Centered Versus Student-Centered Teaching: Preferences and Differences Across Academic Majors. *Journal of Effective Teaching in Higher Education, 4*(1). https://doi.org/10.36021/jethe.v4i1.156

SPONSORS

DIAMOND SPONSOR

RUBY SPONSORS

SAPPHIRE SPONSORS

JADE SPONSOR